

© 2009

JAMES E. MAY

ALL RIGHTS RESERVED

NON-LINEAR VIBRATION CONTROL OF LONG, FLEXIBLE STRUCTURES EMPLOYING
INTER-MODAL ENERGY TRANSFER [MODAL DAMPING]

A Dissertation

Presented to

The Graduate Faculty of The University of Akron

In Partial Fulfillment

of the Requirements for the Degree

Doctor of Philosophy

James E. May

August, 2009

NON-LINEAR VIBRATION CONTROL OF LONG, FLEXIBLE STRUCTURES EMPLOYING
INTER-MODAL ENERGY TRANSFER [MODAL DAMPING]

James E. May

Dissertation

Approved:

Accepted:

Advisor
Dr. Craig C. Menzemer

Department Chair
Dr. Wieslaw Binienda

Committee Member
Dr. Wieslaw Binienda

Dean of the College
Dr. George K. Haritos

Committee Member
Dr. Robert Liang

Dean of the Graduate School
Dr. George R. Newkome

Committee Member
Dr. D. Dane Quinn

Date

Committee Member
Dr. Kevin L. Kreider

ABSTRACT

In the not too distant past, the design philosophy for tall civil structures could be summarized as LARGE MASS-LARGE STIFFNESS. The information age has brought about advances in material science and design technologies that provide the means to explore and construct high-reaching, expansive and much lighter-duty geometries. Current design trends require not only extensive strength-based engineering, but also carefully executed motion-based analysis. Tall, flexible civil structures have long been known to be prone to low frequency transverse vibrations. To further complicate matters, the associated natural damping properties are small leading to drawn out settling times. Motion-based augmentations offer enabling solutions. This research develops, evaluates and demonstrates a modal-based motion control strategy that may be viable for a select grouping of flexible structures. ‘Modal Damping’ exploits damping mechanisms inherent in structures by capitalizing on distinctive dynamic properties existing among the structures vibration modes. An automated, non-linear control scheme was developed to transfer energy from the fundamental vibration mode, where most vibration energy of the civil structures of interest resides, to higher order modes where vibration impedance was shown to be more effective. To achieve this objective, Modal Damping employs motion control forces self-powered by the redistribution of fundamental mode kinetic energy making the strategy highly efficient. The Modal Damping concept was developed and analyzed via dynamic simulation. The analytical findings were then applied to design an experimental model that was constructed and utilized to conduct a concept demonstration and evaluation.

DEDICATION

This dissertation is dedicated to my parents, Walter and Johanna May. Their life stories were probably not too dissimilar from others of their generation raised in the rust belt of the United States during the depression era of the early twentieth century. In many ways it was a world extremely different from the one most of us are fortunate to experience today. A basic public education through grade 12 was generally thought to be a notable achievement... even so it was not necessarily a requirement among the working class families to which they belonged. Those conditions allowed for a high school diploma for my mother, and nearly one for my father. Neither had the opportunities, the means, nor the support to pursue higher education; it was never a consideration. Regardless, they successfully negotiated the roads that life laid out before them. Their journey together was fruitful, but not without challenges. Together though, they raised seven children; none of us ever had to do without.

Because of their efforts and sacrifices each of their children was free to pursue individual opportunities and dreams. They inspired me personally to set goals, work toward those goals, and to make the best of life and the subsequent hand dealt. Although neither will be able to share this particular moment with me in person, I believe they share it in spirit. Thank you mom and dad... I love you both!

ACKNOWLEDGEMENTS

It's a fact: I would not have completed this project without the love and support of my beautiful wife. Sharon, you have been an infinite source of encouragement, energy and most importantly... smiles. When I needed emotional support, there you were; when I needed to be motivated, you obliged. Throughout these and all other daily challenges you worked to keep me grounded, and my focus on what is truly important in life. Thanks dear... love ya!

I owe a note of gratitude to our children. Rybo and Kybo, thanks for your interests and contributions... "darn-it men, I'm a doctor, not an engineer...". Nathan and Cindy, you have and continue to be an influential force in my life.

A special thanks to Dr. Craig Menzemer for agreeing to serve as my doctoral advisor in spite of my limitations... I began as a convert from a very different engineering discipline. Some might have described it as a mid-life thing. Dr. Menzemer never failed to provide the necessary technical direction when required, which was often. But more importantly, he patiently listened to my ramblings for the many years it took to complete this degree. Thanks Dr. M.

Much thanks to Messrs Dale Ertley and Dave McVaney, both senior engineering technicians at the University of Akron. Both played key roles transitioning my paper ideas to real-world implementations. I benefitted greatly from their many lessons. Their time, efforts, and friendships will always be held in high regard.

I thank God for family, the opportunities presented me, and whatever abilities I might claim to hold; I have been undeservingly blessed.

TABLE OF CONTENTS

	Page
LIST OF TABLES	x
LIST OF FIGURES	xi
CHAPTER	
I. INTRODUCTION.....	1
1.1 Modal Damping Introduced.....	4
1.2 Research Plan and Objectives	5
II. LITERATURE RESEARCH SUMMARY	8
2.1 Modal Damping Strategic Overview.....	13
2.2 Damping in Structures	14
2.2.1 Damping Mechanisms	15
2.2.2 Damping Devices/Components and Systems	24
2.2.3 Passive Damping.....	25
2.2.4 Active Damping.....	36
2.2.5 Semi-Active Damping	45
2.3 Feedback Theory and Practice for Control of Structural Dynamics.....	49
2.3.1 Linear Feedback Control	50
2.3.2 Non-Linear Feedback Control	66
2.3.3 Distributed Control	70
2.3.4 Stability.....	71
2.4 Modal Control and Inter-Modal Energy Transfer.....	76

III. MODAL DAMPING... AN ALTERNATIVE CONTROL STRATEGY	79
3.1 Modal Damping Basis.....	79
3.1.1 Motivation and Objective	81
3.1.2 Mode Shape Fundamentals.....	86
3.1.3 Linear Modal Analysis (LMA)	89
3.1.4 Exciting Targeted Vibration Modes	101
3.1.5 Modal Deformation Energy	105
3.1.6 Modal Energy Redistribution Risks	109
3.1.7 Control Forces.....	125
3.2 Automated Control Implementation Strategy.....	130
3.2.1 Control Logic	131
3.2.2 Control Sequence.....	133
3.2.3 Simulation Specifications for the Cantilever-Tendon Geometry.....	135
IV. MODAL DAMPING SIMULATION AND ANALYSIS.....	137
4.1 Dynamic Modeling of the Baseline Flexible Cantilever Structure.....	137
4.1.1 Model Formulation	139
4.1.2 MATLAB/SIMULINK Implementation	150
4.1.3 Model Validation	152
4.1.4 Impulse Test Results.....	153
4.2 Coupled Tendon/Cantilever Phenomenological Model Design	155
4.2.1 Cantilever/Tendon Pair Dynamic Model... The Philosophical Approach.....	157
4.2.2 Tendon Geometric Algorithm.....	159
4.2.3 Tendon Feedback Force Algorithm.....	163
4.2.4 Damping Control Law.....	186
4.3 Simulation and Analytical Results	186

4.3.1 Pluck Test Description and Analytical Test Results.....	187
4.3.2 Wind Gust Test Description and Results	202
4.3.3 Damping Augmentation — Summary Analysis of the Simulation Findings	207
V. EXPERIMENTAL TESTING	218
5.1 Anelastic Damping Parameter Assessment	218
5.1.1 Technical Discussion	219
5.1.2 Test Results	226
5.1.3 Damping Coefficient Modeling.....	233
5.2 Modal Damping Concept Demonstration	235
5.2.1 Concept Demonstration Work Plan.....	236
5.2.2 Hardware Design and Fabrication	238
5.2.3 Fabrication and Assembly	248
5.2.4 Electrical Interface Design and Fabrication	250
5.2.5 Circuit Design	252
5.2.6 Control Algorithm Design.....	253
5.2.7 Software Design and Coding	255
5.2.8 The Pluck Test	259
5.2.9 Characterization Test.....	259
5.2.10 Formal Test Overview	262
5.2.11 Formal Test Results	263
5.3 Simulation Validation	270
VI. CONCLUSION	275
6.1 Recommendations	278
BIBLIOGRAPHY	280
APPENDICES	288

APPENDIX A. LIST OF VARIABLES, DEFINITIONS AND USAGE	289
APPENDIX B. CONCEPT DEMONSTRATION TEST PARAMETERS AND RESULTS.....	292

LIST OF TABLES

Table	Page
2-1 TMD Sample Design Parameters.....	59
3-1 Modal Strain Energies Given Equivalent Deflections [1 ft].....	109
3-2 Modal Deflections Given Equivalent Energies	110
4-1 Predicted Baseline Luminaire Cantilever Modal Frequencies.....	154
4-2 Simulation Damping Performance Summary (10 sec mark)	211
5-1 Parameter Test Specimen Design Specifications	222
5-2 Aluminum Damping Parameter (ADP) Data Sampling Specification	225
5-3 Anelastic Damping Parameter Assessment Summary	232
5-4 Damping Model Prediction Accuracies [RMS].....	235
5-5 Cantilever/Tendon Connection Specifications	242
5-6 Concept Demonstration General Design Requirements.....	242
5-7 Concept Demonstration Modal Frequencies	243
5-8 Concept Demonstration Control Tendon Selection Criteria	244
5-9 Concept Demonstration Control Tendon Design Specifications	245
5-10 Concept Demonstration Actuation Subsystem Dynamic Properties	247
5-11 Concept Demonstration Accelerometer Performance Specifications.....	250
5-12 Concept Demonstration Actuator Specifications	252
5-13 Concept Demonstration Data Acquisition Specifications	255
5-14 Modal Damping Settling Time Summary	265

LIST OF FIGURES

Figure	Page
1-1 Cantilever Pole Schematic Diagram and Characteristic Time Response	2
1-2 Failed Roadside Luminaire Poles.....	3
1-3 Modal Damping Research Plan	5
2-1 Conceptual Freedom Tower Renderings.....	8
2-2 Structural Design Evolution.....	9
2-3 Damping Augmentation Hierarchy	15
2-4 Measured Building Natural Period Properties (a) Steel structures (b) Reinforced concrete structures.....	17
2-5 Measured Building Damping Ratio Properties (a) Steel structures (b) Reinforced concrete structures	17
2-6 Material Damping Rheological Model.....	18
2-7 Sample Response Characteristics of Natural Damping Mechanisms (a) Viscous/exponential damping (b) Coulomb damping (c) Drag	19
2-8 Engineered Viscous Component.....	20
2-9 Stress-Deformation Cycle [Viscous & ViscoElastic Damping]	21
2-10 Stress-Deformation Cycle [Coulomb Damping]	23
2-11 Stress-Deformation Cycle [Hysteretic Damping].....	23
2-12 Structural Damping Roadmap.....	25
2-13 Structure & Augmentation (Damping) Feedback Loop.....	26
2-14 TMD Schematic Model.....	28
2-15 TMD Time Responses	30
2-16 Secondary Damper Effectiveness.....	30

2-17	CITICORP Center on Stilts.....	31
2-18	Tuned Liquid Column Damper Schematic Model	32
2-19	Free Body Model of an Impact Damper.....	35
2-20	Active Control Functional Block Diagram.....	38
2-21	AMD Schematic Model	39
2-22	Kyobashi Building [AMD Subsystem]	40
2-23	Kajima Active Variable Stiffness Building Schematic	43
2-24	Triton Square Physically Coupled Buildings	44
2-25	Semi-Active Mass Damper Schematic Model	46
2-26	Semi-Active Damping Functional Block Diagram.....	46
2-27	Standard Control System Block Diagram	50
2-28	Standard Regulator Block Diagram.....	52
2-29	Tuned Mass Damper Control Block Diagram.....	57
2-30	TMD Root Locus Sample Design.....	60
2-31	Standard Regulator Block Diagram.....	64
2-32	Modeling Structural and Disturbance Uncertainties	65
2-33	Simple Feedforward Neural Configuration	69
3-1	Space-Based Flexible Topology.....	81
3-2	Typical Vibration Impedance Modulus for the Anelastic Rheological Model.....	82
3-3	Sample Proportional Damping Curves	84
3-4	Cantilever Vibration Mode Shapes 1&2	87
3-5	Free Body Diagram for the Simplified Vibrating Cantilever.....	88
3-6	Baseline Aluminum Pole Mode Shape Functions [Linear Modal Analysis]	101
3-7	2nd Vibration Modal Excitation Test Response.....	105
3-8	Material Damping Rheological Model.....	111

3-9	Typical Vibration Impedance Modulus for the Anelastic Rheological Model...	112
3-10	Stress Components During Elastic Harmonic Deformation.....	114
3-11	Damped Power Temporal Modulation Function	117
3-12	Modal Deflection Functions [Before & After Energy Transfer Event]	120
3-13	Peak Damped Power Density Function.....	120
3-14	Energy Dissipation Density Function.....	121
3-15	% Energy Dissipation versus Structural Height	123
3-16	Energy Dissipation Density Contour [0→99% energy transfer]	124
3-17	Generalized Cantilever/Tendon Configuration.....	126
3-18	Control Tendon Geometry and Projection to Lumped Mass Model.....	127
3-19	3-Point Tendon Configuration Effectiveness [Impulse Control Force]	129
3-20	Vibration Energy Trajectories	
	(a) Energy versus displacement [without Modal Damping]	
	(b) Energy versus velocity [without Modal Damping]	
	(c) Energy versus displacement [with Modal Damping]	
	(d) Energy versus velocity [with Modal Damping]	132
3-21	Tendon Control Sequence.....	133
4-1	Baseline Cantilever Pole and Lumped Mass Model	
	(a) Schematic drawing (b) Nodal lumped mass spatial distribution.....	138
4-2	Gravity Force Contribution.....	140
4-3	Discretized Mass Model.....	144
4-4	Complimentary Virtual Work Schematic	146
4-5	SIMULINK State Space Function Block	151
4-6	Unit Impulse Test Simulation Results	
	(a) Nodal displacements and FFT [without top mounted luminaire]	
	(b) Nodal displacements and FFT [with top mounted luminaire]	155
4-7	Generalized Cantilever/Tendon Configuration (repeated)	156
4-8	Closed-Loop Cantilever/Tendon Block Diagram.....	158

4-9	Generalized Cantilever/Tendon Geometric Parameters	160
4-10	Specific 3-Pt Tendon/5-DOF Cantilever Connection Geometry.....	162
4-11	Control Tendon Force Set.....	163
4-12	Cantilever/Tendon Rigid Body Truss Model.....	165
4-13	Angle Rate Feedback [Geometric Version 1] Block Diagram.....	167
4-14	Tendon Model Performance [Geometric Version 1].....	170
4-15	Angle Rate Feedback [Geometric Version 2] Block Diagram.....	171
4-16	Tendon Model Performance [Geometric Version 2].....	173
4-17	Angle Feedback [Geometric Version 3] Block Diagram	174
4-18	Tendon Model Performance [Geometric Version 3].....	175
4-19	Length Feedback Control [Geometric Version 4] Block Diagram	176
4-20	Tendon Model Performance [Geometric Version 4].....	177
4-21	Deformed Cantilever/Tendon Geometric Parameters.....	179
4-22	Energy Conservation Control [Version 5] Block Diagram.....	181
4-23	Cantilever/Tendon Geometric Parameters.....	184
4-24	Pluck Test Initial Conditions	194
4-25	Pluck Test Nodal Responses [NO Augmentation].....	195
4-26	Pluck Test DFT [Node-1 Displacement/NO Augmentation].....	195
4-27	Pluck Test Nodal Responses [With Augmentation]	196
4-28	Pluck Test DFT [Node-1 Displacement/Augmentation].....	197
4-29	Nodes 2 & 4 State Trajectories [Pluck Test]	198
4-30	Animated Sequence of Pluck Test Simulation Results.....	201
4-31	Wind Gust Forcing Function and Distribution	202
4-32	Wind Gust Test Nodal Responses [NO Augmentation].....	203
4-33	Wind Gust Test DFT [Node-1 Displacement/NO Augmentation].....	203

4-34	Wind Gust Test Nodal Responses [With Augmentation].....	205
4-35	Wind Gust Test DFT [Node-1 Displacement/Augmentation]	205
4-36	Wind Gust Test DFT [Node-1 Velocity/With Augmentation]	206
4-37	Nodes 2 & 4 State Trajectories [Wind Gust Test/Augmentation].....	207
4-38	Energy Dissipation Trajectories - Pluck Test (a) NO augmentation (b) Modal Damping augmentation	209
4-39	Energy Dissipation Trajectories – Wind Gust Test (a) NO augmentation (b) Modal Damping augmentation	210
4-40	BD Errors - Pluck Test (a) BD variation without feedback control (b) BD variation with feedback control	211
4-41	BD Errors – Wind Gust Test (a) BD variation without feedback control (b) BD variation with feedback control	212
4-42	Energy Trajectory Discrepancies (a) Pluck test (b) Wind gust test	214
4-43	Base Moment [Pluck Test][NO Augmentation vs. Augmentation]	216
4-44	Base Moment [Wind Gust Test][NO Augmentation vs. Augmentation]	216
5-1	ADP Experimental Model Schematic and Design Parameters	222
5-2	ADP & SDP Test Specimens	222
5-3	Mounted Steel Damping Parameter (SDP) Experimental Specimen.....	222
5-4	Node-5 Acceleration.....	223
5-5	Node-5 Spectral Content.....	223
5-6	Damping Parameter Experimental Configuration Schematic	224
5-7	Butterworth Filter Transient Effect (a) Unfiltered response (b) 2 nd order Butterworth (c) 6 th order Butterworth.....	227
5-8	Accelerometer Modal Components [Emulated Impulse Test] (a) Aluminum damping parameter specimen [Node 5] (b) Steel damping parameter specimen [Node 5].....	227

5-9	Mode-2 Damping Coefficient Analysis [Emulated Impulse Test] (a) Aluminum damping parameter specimen (b) Steel damping parameter specimen.....	230
5-10	Exponential Decay Fit (a) Noticeable drag effect (b) Minimal drag effect	231
5-11	Measured Modal Damping Coefficient Summary [ADP/SDP]	232
5-12	Measured Modal Frequency Summary [ADP/SDP].....	233
5-13	Steel Damping Coefficient Model Comparison.....	235
5-14	Aluminum Damping Coefficient Model Comparison	235
5-15	Concept Demonstration Developmental Work Plan	237
5-16	Generalized Cantilever/Tendon Configuration.....	238
5-17	The Concept-Demo Model Design Evolution.....	241
5-18	Dynamic Comparison of Concept Demo versus Baseline Cantilever (a) Measured modal frequency comparison (b) 1 st and 2 nd mode shape comparison	243
5-19	Tendon Length Variation [time 0→5 sec]	244
5-20	Tendon Length Variation Rate [time 0→5 sec]	245
5-21	Tendon Tension Force [time 0→5 sec]	245
5-22	Control Tendon Actuation System (a) Braking actuation system (b) Electro-magnetic disc brake (c) Mounted wind-up mechanism (d) Wind-up pulley.....	248
5-23	Concept Demo Experimental Model (a) Final concept demonstration assembly (b) Story ‘Node’ with hinge connection (c) Multi-story design (d) Story hinge (bearing) connection.....	249
5-24	Concept Demo Accelerometers (a) PCB accelerometer (b) ACH-01 accelerometer	251
5-25	Pluck Test Positioning Actuator	251
5-26	Sensor Conditioning Circuits [PCB and ACH-01].....	252
5-27	Actuator Driving Circuits [Pluck and Braking]	253

5-28	Modal Damping Control Sequence.....	254
5-29	Software Functional Flow Diagram.....	257
5-30	Modal Damping Actuator Control Logical Flow Diagram.....	258
5-31	Pluck Test Implementation [Pre-Positioning] (a) Analytical model (b) Experimental model	259
5-32	Damping Mechanisms of Interest (a) Viscous damping (b) Coulomb damping (c) Drag.....	260
5-33	Natural System Response to Pluck Input (a) Natural response [no tendon] (b) Natural response [with tendon]	260
5-34	Modal Damping Performance Summary (a) Relative settling time [full evaluation set] (b) Relative settling time [demonstration set]	264
5-35	Demonstration Tests Scatter Chart.....	265
5-36	Measured Test Data [Single MD Event] (a) No MD events [test: feb04091516] (b) One MD event [test: feb04091528]	266
5-37	Modal Damping Control Sequence.....	267
5-38	Settling Time Improvement [Single MD Event]	268
5-39	Modal Damping DFT Effect [2 to 3.5 sec] (a) Without Modal Damping [test: feb04091516] (b) With Modal Damping [test: feb04091531]	269
5-40	Measured Test Data [Three MD Events] (a) No MD events [test: feb04091516] (b) Three MD events [test: feb04091531]	269
5-41	Simulation Validation [Natural Damped Without Control Tendon] (a) Nodal accelerations [SIMULINK] (b) Experimental data [test: feb04091531]	272
5-42	Simulation Validation [Natural Damped With Control Tendon] (a) Nodal accelerations [SIMULINK] (b) Experimental data [test: feb04091531]	272
5-43	Simulation Validation [Modal Damping Energy Transfer Event] (a) Simulated nodal acceleration [SIMULINK] (b) Experimentally measured acceleration [test: feb04091531]	274

CHAPTER I

INTRODUCTION

Tall, or long, flexible structures have long been known to be prone to low frequency, slowly decaying transverse vibrations that can be brought on by simple external disturbances such as a gust of wind. Vibrations eventually decay naturally due to one or more physical mechanisms such as friction or drag. Unfortunately, the natural damping mechanisms inherent to such structures or those attributed to its environment are relatively small; consequently decay often occurs painfully slow. Equivalent damping ratios for these long and flexible structures are often less than one percent ^[1,2]. By comparison, damping ratios for tall, steel and concrete buildings governed by serviceability conditions generally range from 1% to 2%. ISO 4354:1997 suggests 1% to 1.5% ^[3].

For most simple and uninhabited structures, the lightly damped dynamic behavior is inconsequential. In some cases however, the extended settling time is undesirable and costly even for the un-inhabited structure. An interesting example is the luminaire support structure; a tall aluminum pole found adjacent to most major highways. One of the more common is the 42 foot HAPCO tapered luminaire support often used by Departments of Transportation and shown diagrammed in Figure 1-1 ^[4]. Such poles have long been known to vibrate in both the fundamental and the 2nd mode. A Feb 17, 2003 storm in the New Jersey area that contained violent winds estimated to be 50 MPH incited the failure of 50 light poles erected in the Atlantic City area. All of

the failed poles were physically comparable. Failures were generally found to be in the base support where the greatest moment forces are developed. Example failures are pictured in Figure 1-2. Forensic analysis found that the multitude of stress cycles required to have had occurred to reach failure occurred over surprisingly short life spans. Although the environment was harsh, the problem was no doubt exacerbated by the pole's 'dynamic' personality. Post failure analysis indicated that the pole design was afflicted by more than one motion-based problem: a potential resonant coupling to vortex shedding^[5] and its under-damped dynamic nature. One problem introduces vibration energy, the other sustains it.

The measured damping ratio of the typical pole was again found to be no more and often less than 1%. Dynamic modeling of the aluminum cantilever revealed the ringing behavior shown in Figure 1-1.

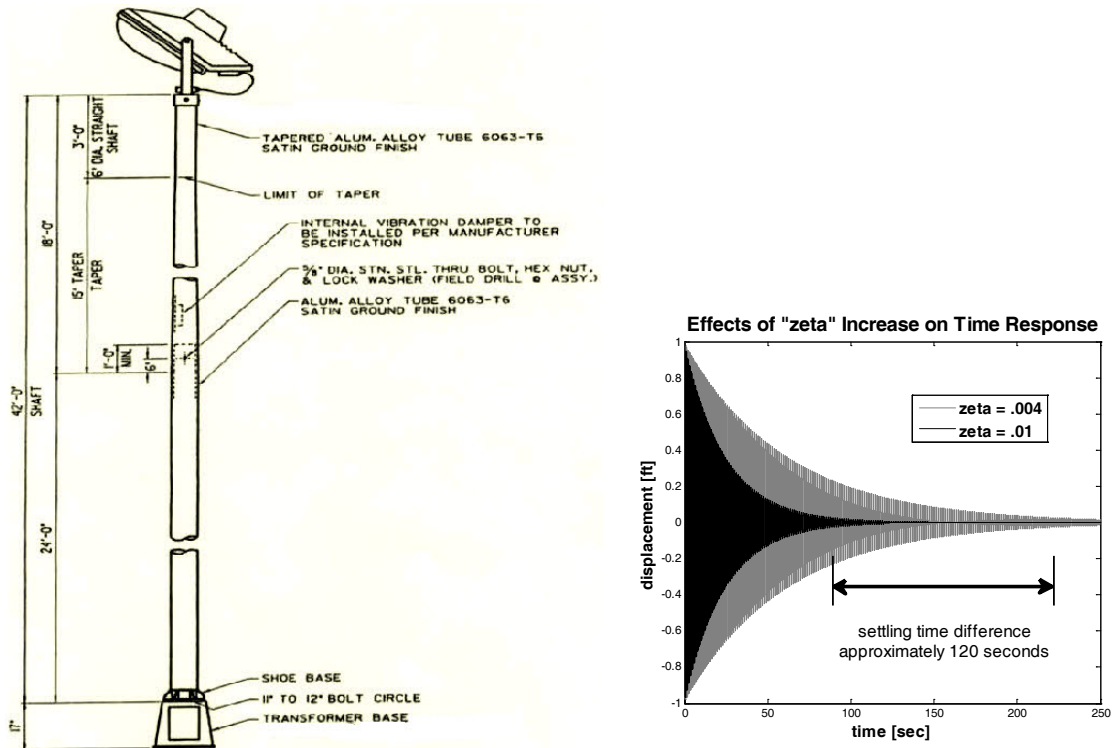


Figure 1-1 Cantilever Pole Schematic Diagram and Characteristic Time Response

When excited, the simple cantilever pole experiences in excess of a hundred stress cycles before reaching its 4τ dampened state, about 98% decay of its vibration magnitude. Minor improvements in effective damping can significantly improve settling time and reduce stress cycling.

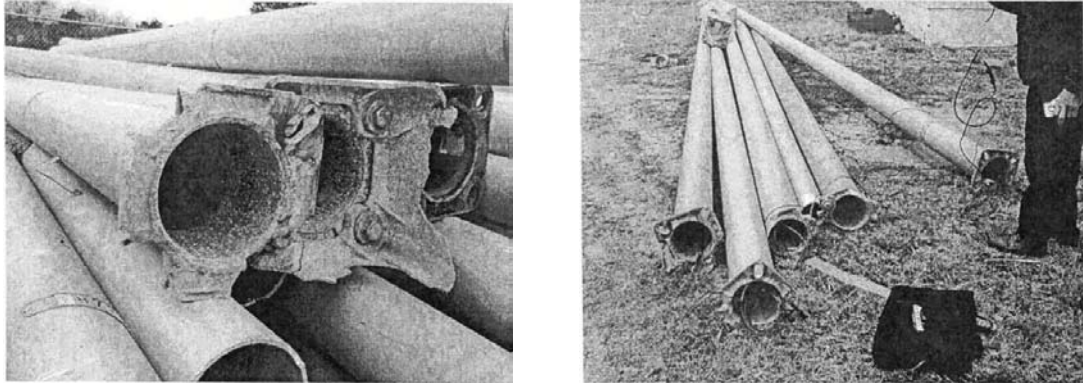


Figure 1-2 Failed Roadside Luminaire Poles

These kinds of structures are prime candidates for damping augmentation. Unfortunately, the physical geometries of long and slender structures do not easily lend themselves to common enhancements. Increasing a structure's mass or its cross-sectional moment of inertia may not be technically or economically practical. Damping improvement by way of technology offers alternative options.

The fact that a simple cantilever pole is prone to underdamped behavior is not difficult to imagine. However, current contemporary trends in the design and construction of high rise structures feature reduced mass, reduced stiffness and subsequently, less effective inherent damping mechanisms all of which encourage similar dynamical behavior. Without augmentation, it's reasonable to assume that such structures will behave similarly to the simple cantilever pole when subjected to lateral excitation forces. Structural engineers should anticipate this design trend to continue into the future.

The advent of dynamically active structures continues to motivate the research and development of damping technology to augment the natural properties inherent in the structure. A summary of current damping technology and state-of-the-art applications is provided in Chapter 2 of this document. Existing damping augmentation options were found to be diverse in their approach. Some were based on the inclusion of simple passive components, while other approaches involve intelligent and active subsystems. Most augmentation technology however, targets more complex structures.

1.1 Modal Damping Introduced

The damping approach proposed herein is directed at highly dynamic, yet structurally simple systems as characterized by aluminum cantilever poles, where overly sophisticated and expensive augmentations are not warranted. These structures of interest can be characterized by the following dynamic properties:

- Structures are tall, or long, with large height to width ratios. They are flexible.
- The majority of energy is coupled into the fundamental vibration mode for most of the natural excitation conditions.
- When compared to the fundamental mode, the higher order modal vibrations produce reduced spatial displacements along the longitudinal axis of the structure given comparable energies. Spatial velocities and accelerations may, or may not increase.
- Maximum and minimum lateral spatial displacements (mode shape nodes and anti-nodes) along the longitudinal axis of the structure occur at different locations for different vibration modes. Some locations may be more ‘convenient’ from a control standpoint when compared to those of the fundamental mode.

- Each vibration mode can generally be found to have different dissipation properties. In general, higher order vibration modes exhibit greater impedances to vibration.

Modal Damping was developed to capitalize on these very properties and tendencies. The approach is ‘modal’ in nature in that it attempts to redirect energy from a vibration condition having minimal energy dissipation capacity to one known to have more effective damping properties. The exact goal was to engineer the transfer of vibration energy from the fundamental mode to the second mode, then to evaluate its affect on dissipation performance.

1.2 Research Plan and Objectives

The subject Modal Damping effort was directed by a program research-plan shown diagrammed in Figure 1-3. The plan was prepared and presented during the initial phase of this study.

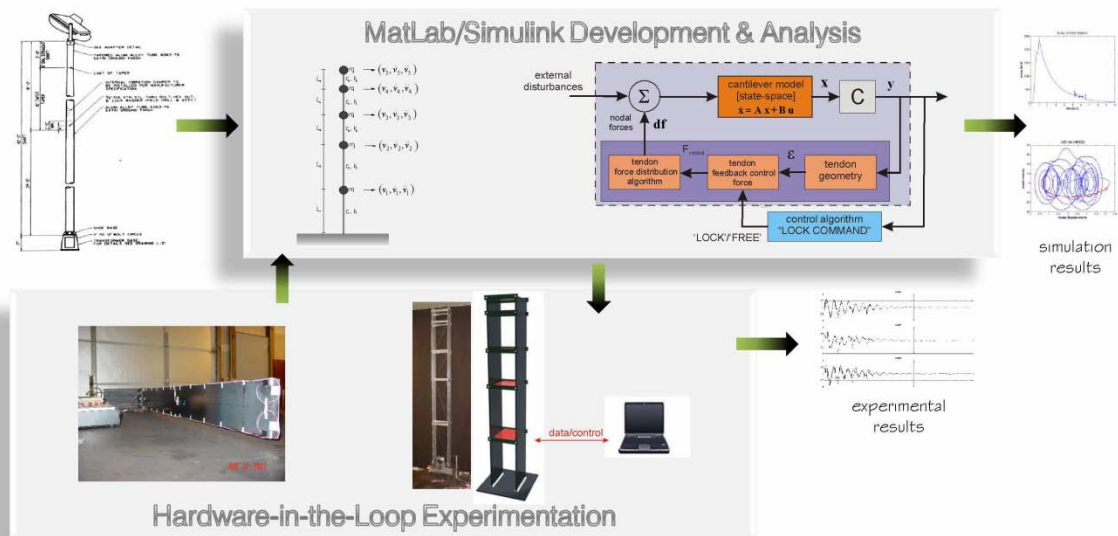


Figure 1-3 Modal Damping Research Plan

The essential elements of the plan included the following:

1. Investigate state-of-the-art and evolving technologies directed to improve structural damping.
2. Develop a theoretical damping augmentation scheme for the baseline structure that capitalizes on its inherent dynamic tendencies. Specifically, transfer vibration energy from the base-line fundamental mode to higher order modes with more effective vibration impedances.
3. Develop specific control strategies and algorithms to effect modal energy transfer.
4. Model and simulate the augmented system using the MATLAB/SIMULINK environment. Demonstrate the implementation and viability of the Modal Damping augmentation concept. Quantify damping behavior of the coupled structure/augmentation systems.
5. Develop a representative experimental model with the integrated damping augmentation device and control system. Develop an experimental test plan to corroborate the simulation results. Conduct a demonstration and collect the necessary data to characterize damping effectiveness of the Modal Damping augmentation scheme.

The diagram illustrates the two major thrusts: the analytical and the experimental. The two elements were coupled and supported each other. Measured damping properties were used to validate and improve simulation fidelity while the analytically developed control scheme and implementation guided the design of the experimental model.

A generalized 42 foot aluminum highway cantilever pole was selected as the baseline structure. It represented a real-world structure with documented dynamical problems. The cantilever was utilized to complete the analytical portion of this study. The highway pole is an extremely simple structure, yet it arguably presents a worse

case condition as a self damping structure. It became an attractive candidate for analytic investigation and development. The analytically developed control configuration took the persona of the base-line structure, it was extremely simple. It proved itself to be adequate for analytical development and analysis but its adaptation will be shown to lack ‘elegance’ and practicality. The analytical configuration was not necessarily a likely contender for real-world application of the Modal Damping augmentation. Consequently, the concept demonstration experimental model evolved and was somewhat more sophisticated taking on a frame-like configuration; possibly a more likely geometry for Modal Damping application.

CHAPTER II
LITERATURE RESEARCH SUMMARY

Advances in material science and design technology have enabled the construction of taller, longer, and lighter-duty structures. These advancements enable visually breathtaking results such as the two conceptual Freedom Tower proposals shown rendered in Figure 2-1 [6, 7].



Figure 2-1 Conceptual Freedom Tower Renderings

Whether it is one of the initial concepts or the latest design upgrades, attention is immediately drawn to the 1776 foot “Freedom Tower”. It is planned to be a largely glass structure. Initial designs included asymmetric grids rising to its 70 stories of office space, after which a light truss and tension cable structure with wind turbines take the tower to approximately 1500 feet. Atop a 276 foot off-center spire was proposed. Redesign efforts have eliminated the asymmetry, light truss, turbines and off-center

spire. Regardless, the Freedom Tower will be awe inspiring. Given the creativity of the proposed ideas to date, its features will most likely lack mass and possibly stiffness and the more comfortable dynamic behavior generally associated with the those two properties.

The decision to build taller and lighter, and having the ability to do so, requires that engineers address increased dynamical responses of the sleek forms that are not present with shorter, stockier and more rigid anatomies. In the past, the primary design process was strength-based oriented. Design philosophies have changed significantly; the evolution is apparent in the simple pictorial timeline shown in Figure 2-2. Although the montage represents but a small set of tall structures designed and constructed over a period of the last 150 years or so, the progression from LARGE MASS/LARGE STIFFNESS designs to those that are LIGHT/FLEXIBLE is apparent.

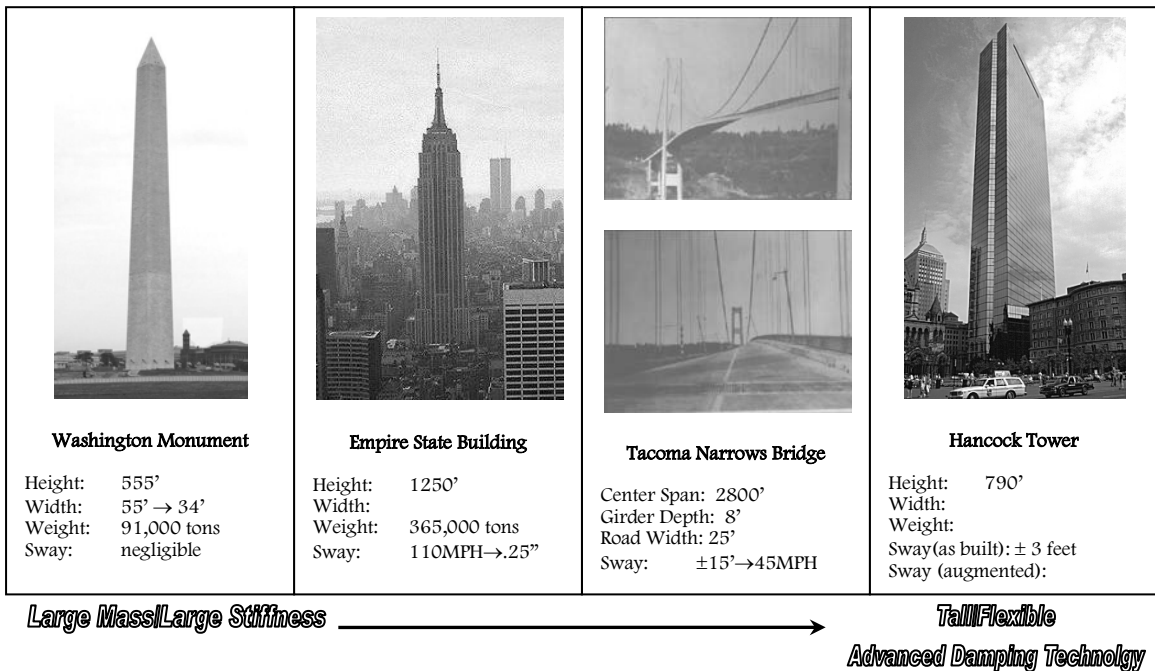


Figure 2-2 Structural Design Evolution

The Washington Monument, circa 1850, is 555 feet 5-1/8 inch in height, certainly a tall structure in its day. Width at its base is 55 feet tapering to 34 feet 5 inch, giving it a slender profile with a height to width slenderness ratio that slightly exceeds 10. It is however constructed of quarried marble and granite blocks with a total weight of 91,000 tons. The thickness of the wall at its base is 15 feet. Although it tapers, the wall thickness at the observation level is still 18 inches. To no surprise, the monuments sway in high wind conditions is less than an inch peak ^[8].

Likewise, the Empire State Building was the state of the art high rise when constructed, circa 1930. It stands 1250 feet in height, the tallest structure in its day, and is still an icon for high rise structures. It weighs in at around 365,000 tons. It has a moment resisting frame consisting of 165,000 tons of steel framing. Furthermore, it is granite and limestone cladded. As tall as it stands, it is estimated to sway less than ± 1 inch during a wind of 110 MPH ^[9, 10] because of its construction.

Steel is a wondrous structural material. Teamed with the advanced design technology, it permits previously unthinkable possibilities to adventurous and creative architects/engineers. It enables ‘tall’ (long) and yet makes possible ‘sleek’... as evidenced by the infamous Tacoma-Narrows suspension bridge, circa 1940. Maybe not the first, but its sleek profile resulted in the classic case of runaway or unbounded dynamics; the video of its 1940 collapse is a famed Kodak moment ^[11] as its deck rolled an estimated ± 25 feet before collapsing. Underdamped and flexible in its vertical direction, the bridge was excited by resonant wind forces leading to its dramatic structural failure. The oscillations in the vertical direction were brought on by a radical roadway design objective: achieve a sleek appearance. A relatively shallow girder approach was adopted in lieu of the usual deep truss design. Although statically capable

in terms of strength, the stiffness and damping properties, or lack thereof, of the 8 foot deep girder became its undoing.

The John Hancock Tower of Boston Massachusetts marked another milestone for U.S. high rise engineering. Its sleek 790 feet tall profile made it the tallest structure in the New England region. It's clad with a lightweight aluminum and mirrored glass exterior that unfortunately offers little in the way of damping. Consequently, after its construction, it was found to have multiple pronounced underdamped vibration modes: one translational mode along its weak axis and one rotational mode. The modes were nearly identical in frequency (.14 Hz) compounding the problem. Energy from the translational mode easily coupled into the rotational mode. Two tuned, 300-ton mass dampers were integrated into opposite ends of its 58th story. They were positioned to respond to lateral motion in a common mode as well as twisting motion in a differential mode. Each mass, a box of steel filled with lead, 17 feet (5.2 m) square by 3 feet (0.9 m) high, slides on a hydrostatic bearing developed by a thin layer of oil forced between the steel plates and the mass damper. The cost of the damper retrofit was \$3 million. It was a statement of things to come.

Current design thrusts, material science innovations and related construction advancements dictate that a motion-based element be included in the overall design process. Dynamic motion inherent to flexible structures may be a concern to the structure itself, to its occupants, or possibly to the type of activity practiced within the structure (space based structures). Structures designed for flexibility can certainly be designed to be extremely tolerant to vibrations as long as material states remain elastic and dynamics remain bounded. In other words, an adequate strength-based design and a dynamically active structural behavior are not necessarily mutually exclusive features.

Improving dynamic responses may not be as simple as stiffening the structure in order to withstand wind excitation forces. Seismic forces represent another form of excitation energy. These forces produce major concern because they are non-stationary and narrow-banded waves with significant uncertainty and most importantly, contain significant energy. If the structures natural frequency is dissonant to that of the core frequency of the seismic energy it becomes more resilient. Correlation tends to improve as the rigidity of the structure increases. Spectrum analyses of the seismic record for El Centro, California for the Imperial Valley earthquake in 1940 indicated that a tall flexible building having lower natural frequency vibration modes is less susceptible to excitation damage ^[12]. Therefore, flexibility is good for structures in active seismic regions. The dichotomy however, is that flexibility is generally disturbing to its occupants. The human element, generally the controlling factor when the structure is to be occupied, experiences discomfort when unexpected or unwanted acceleration reaches about 0.02g ^[13].

The behavior of inhabited structures in view of current design trends has motivated the development of motion-based technological elements. Although controlled by a different standard set, the uninhabited structure is likewise prey to modern day design trends. These structures must withstand the rigors of their dynamic environment. An interesting example is the simple roadside aluminum luminaire support structure whose in-field failure history was discussed briefly in Chapter I. Modern day materials and manufacturing processes have enabled these structures to be produced effectively: tall and slender yet statically strong while meeting economical constraints. A schematic drawing of a representative 42 foot tapered luminaire was shown illustrated in Figure 1-1. Although proven to be sufficiently strong when exposed to worst case static conditions, a number of these relatively simple structures

were found to succumb to their dynamic environmental conditions encountered in the field. Forensic analysis of the failed poles unexpectedly revealed that a multitude of stress cycles must have had occurred over relatively short life spans of the poles. Certainly the environment was harsh. The cantilever's problems however, were exacerbated by their motion-based nature, part of which was their underdamped character.

2.1 Modal Damping Strategic Overview

Whether occupied or uninhabited, the design process of modern day tall/long flexible structure must investigate both the strength-based and the motion-based design elements. In addition to ensuring adequate strength for all possible loadings, static and dynamic, the design engineer has the responsibility to understand and predict structural dynamic characteristics and behavior. If applicable, serviceability requirements must be satisfied (e.g. the John Hancock Building), and effects on accelerated structural aging must be considered (e.g. the roadside aluminum luminaire pole). The structure's damping properties plays a role for both considerations.

If established damping requirements cannot be met naturally by the basic structure, some form of augmentation must be developed and integrated into structure. At present, a design team can choose one or more of the currently acceptable strategies available to improve a structure's dynamic behavior ^[14]:

1. The energy transmission path can be isolated from the disturbance [seismic excitation].
2. Natural frequencies of the structural vibration modes can be displaced from those of the excitation energy of the disturbance [primarily seismic excitation].
3. Energy dissipation devices can be incorporated into the structure.

4. Motion control forces can be produced within the structure to oppose external excitation and internal structural dynamic forces that extend vibration.

The focus of this research leverages from the strategic approach encapsulated by option 4 above, but in a manner that represents an alternative scheme that is based on efficient inter-modal energy transfer. Modal Damping will be shown to alter a structures dynamic character by using self-generating structural motion control forces to govern modal behavior of the structure in such a way as to exploit higher order vibration impedance inherent in the structure. Control forces are self-generated by the redistribution of kinetic energy of the vibrating structure itself.

The science of two distinct engineering disciplines was applied to achieve this goal:

1. Structural Dynamics.
2. Automated Control Theory.

The following sections summarize the state-of-the-art technology for both disciplines concentrating on how these technologies bear on the structural vibration problem.

2.2 Damping in Structures

The science and technology of structural damping can best be summarized and visualized as existing in hierarchically form. Structural damping begins with low level physical mechanisms. When they exist within a given structure, they naturally contribute to energy dissipation at an elementary level. As their physics are understood and their effects reproducible, mechanisms are formed into engineering devices or components that can be mechanically connected to a structure to augment naturally existing damping mechanisms. Finally, engineered devices can be further integrated

into higher level systems that can be intelligently controlled to achieve a tailored dynamic response.

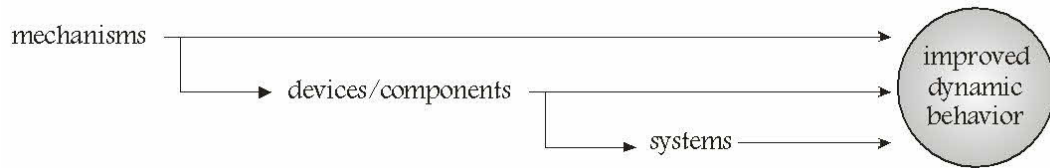


Figure 2-3 Damping Augmentation Hierarchy

Damping can exist in one or more hierarchical levels within any given structure.

2.2.1 Damping Mechanisms

Mechanisms are considered, or assumed herein to refer to the elemental contributors/causes of energy dissipation... first principles of vibration damping if you will. Damping is ultimately a property based upon one or more of these physical mechanisms. These mechanisms generally act to convert kinetic energy. In the context of a vibrating structure, kinetic energy is principally converted to heat. The energy conversion within the structure leads to energy dissipation and consequently vibration decay.

The following five damping mechanism types have been distinguished ^[15, 16] :

1. STRUCTURAL/MATERIAL damping is associated with elastic deformation of the structure or material itself. It sometimes includes or is referred to as ANELASTIC damping.
2. VISCOUS damping is associated with shearing deformation. It is most often produced by liquid, but can also be produced with polymeric materials such as rubber.
3. HYSTERETIC damping is associated with cyclic inelastic deformation.
4. COULOMB damping is associated with frictional forces between displaced elements.

5. EXTERNAL damping is associated with the interaction between the structure and its environment (soil, aerodynamic, etc).

The individual mechanisms are discussed in more detail in the following sections. Common forms of engineered devices for each mechanism are likewise presented.

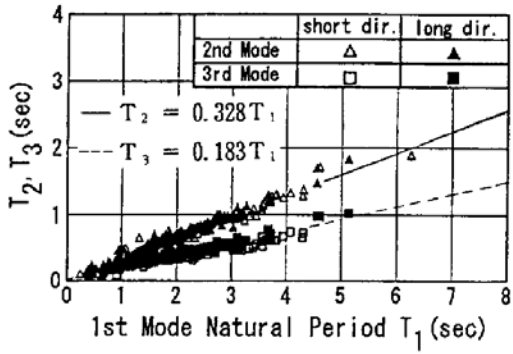
2.2.1.1 Structural/Material (Anelastic) Damping

The term ‘structural damping’ was often found to be used as a catch all for ill-defined damping that naturally occurs in and around the structure itself. Its usage was interpreted to imply dissipation occurring:

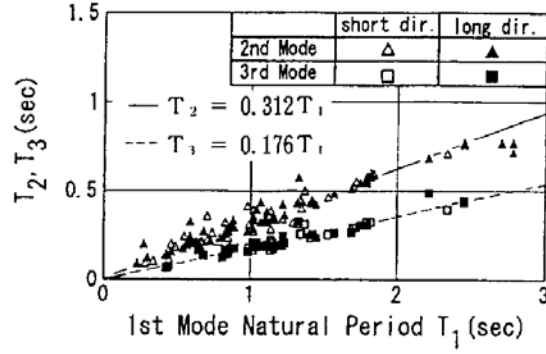
- At the soil interface or from other external effects such as aerodynamic/drag.
- From within structural joints.
- From crack slippage.
- From actual material damping.

When attempting to predict dynamic responses of full scale structures, it is difficult if not impossible to try and separate contributions from specific mechanisms to develop mathematical models. Often, similarity analyses that attempt to predict responses by comparing the candidate structure to observed responses of existing structures is an alternate and reasonable approach.

Satake et al developed a database summarizing measured dynamic properties of over one hundred Japanese structures [17,18]. Measurements were taken post-construction. Two building type categories were established: steel structures and reinforced concrete. Satake determined natural periods, and damping ratios as a function of building heights and types. Figure 2-4^[19] demonstrates relatively good correlation between natural period and building height, while Figure 2-5^[19] reveals significant scatter in the damping ratio measurements.

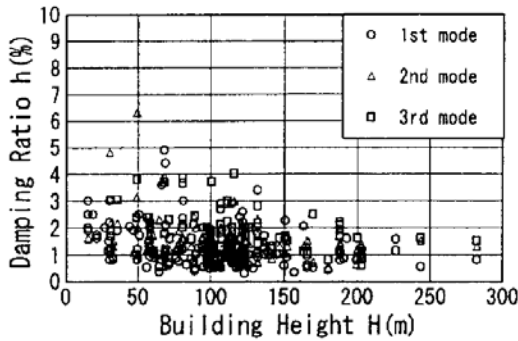


(a) Steel structures

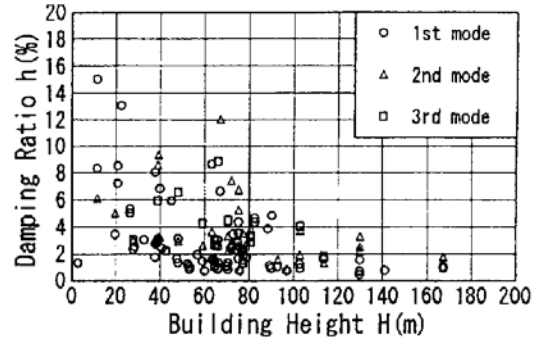


(b) Reinforced concrete structures

Figure 2-4 Measured Building Natural Period Properties^[19]



(a) Steel structures



(b) Reinforced concrete structures

Figure 2-5 Measured Building Damping Ratio Properties^[19]

The more interesting mechanism in the structural damping grouping is the material damping mechanism. Material damping is primarily attributed to internal friction at the molecular level occurring during the deformation cyclic that results in heat generation^[20]. The mechanism is also referred to as ‘anelastic’ damping because it is associated with recoverable small strain deformation. The given first order rheological model is shown diagrammed in Figure 2-6. The parallel spring/viscous-damper pair c_d and E_2 form a tuned couple, with a natural frequency of

$\omega_d = \frac{E_2}{c_d} \text{ rad/sec}$. At frequencies well above ω_d , the material behaves elastically with a modulus of E_1 . At frequencies well below ω_d , it behaves elastically with a modulus of E_2 . Maximum energy dissipation occurs at ω_d .

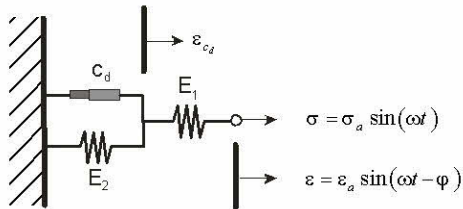


Figure 2-6 Material Damping Rheological Model

This internal/molecular friction damping mechanism is actually one of a variety of mechanisms that is thought to be associated with metal materials. Thermoelastic, magnetoelastic, and the Snoek effect are examples of additional mechanisms that have been identified. They are discussed further by Dowling^[20]. These mechanisms also exhibit visco-elastic like behavior. Each contributes to energy dissipation, usually within specific and unique frequency ranges.

2.2.1.2 Viscous Damping

Viscous damping is the fundamental damping mechanism that is generally assumed to exist in many mechanical systems. Mathematically, it is described by a force versus deformation rate relationship:

$$F_c(t) = c_d \dot{u}(t) \quad (2.1)$$

In more elemental terms it is represented to be a shear related phenomenon,

$$\tau_v = G_v \dot{\gamma}$$

where, the modulus of viscosity G_v is a function of viscosity of fluid/oil.

The relationship of Equation (2.1) is popular not only because it correlates reasonably well with physical observations, but also because it results in linear equation of motion models. The governing equations for a mass/spring/viscous damper system thereupon take the differential form $m\ddot{v}(t) + c\dot{v}(t) + kv(t) = f(t)$ with the homogeneous response $v(t) = a_1 e^{\lambda_1 t} + a_2 e^{\lambda_2 t}$. Because damping is viscous the exponential coefficients can easily be computed as,

$$\lambda_{1,2} = \frac{-c \pm \sqrt{c^2 - 4mk}}{2m} \quad (2.2)$$

The systems of interest are underdamped, so $c^2 \ll 4m \cdot k$. The time response takes on the exponential decaying sinusoidal form shown in Figure 2-7a.

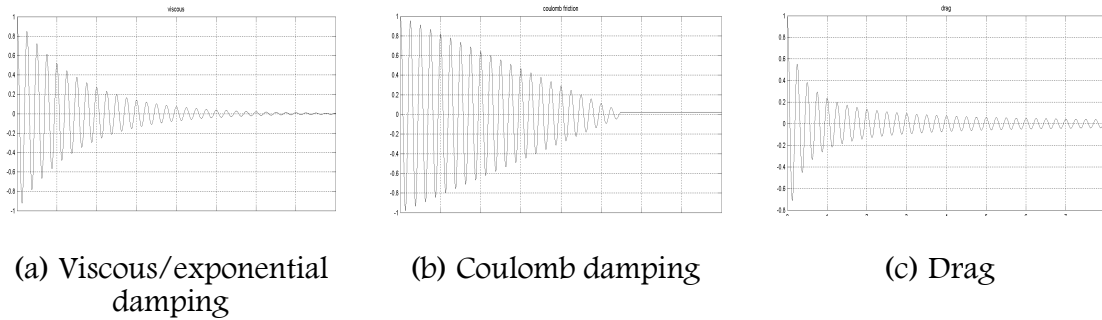


Figure 2-7 Sample Response Characteristics of Natural Damping Mechanisms

Percent of critical damping is often used as a measure of damping effectiveness. Critical damping is achieved when the component values of the system force the radical term of Equation (2.2) to zero, in other words,

$$c_{cr} = \sqrt{4mk} = 2m\omega_n \quad (2.3)$$

The critical damping factor is defined as

$$\zeta = \frac{c}{c_{cr}} = \frac{c}{2m\omega_n} \quad (2.4)$$

Physically, the viscous mechanism can be realized as a dashpot/damper device that consists of an oil filled cylinder/piston arrangement. An orifice in the piston allows the oil to flow through the piston as it is displaced in the cylinder. Fluid shearing resulting from the laminar flow of the oil through the orifice generates damping; kinetic energy is converted to heat. Figure 2-8 illustrates a viscous device engineered as a passive damping component for tall structures; its size is noteworthy.

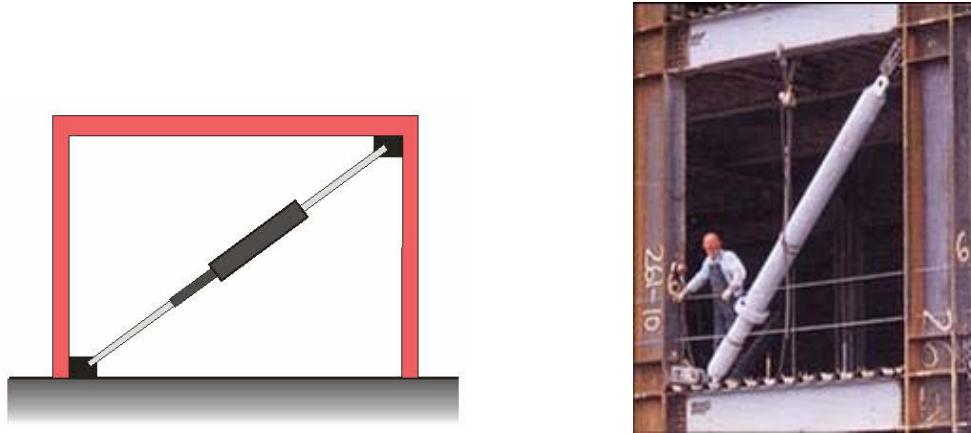


Figure 2-8 Engineered Viscous Component

The viscous stress-deformation relationship diagrammed in Figure 2-9 shows the hysteretic behavior of the device, revealing its dissipative nature. The unit damping energy dissipated in one deformation cycle is:

$$\Delta W_{Viscous} = \int_{u(t_1+T)}^{u(t_1)} F_c du = \int_{t_1+T}^{t_1} c \dot{u}^2 dt \quad (2.5)$$

$$\Delta W_{Viscous} = c \pi \omega \hat{u}^2$$

Often, the behaviors of other damping mechanisms are desired to be modeled using equivalent viscous parameters in order to form a linear model. This is easily accomplished by equating the unit damping energies of the two devices and computing an equivalent damping factor, $c_{eq} = \frac{\Delta W_{non-viscous}}{\pi \omega \hat{u}^2}$.

2.2.1.3 Viscoelastic Damping

Rubber and rubber-like materials demonstrate both elastic and viscous deformation characteristics, shear stresses depend on both deformation magnitudes and rates.

$$\tau = G_e \gamma + G_v \dot{\gamma} \quad (2.6)$$

The rheological model for the viscoelastic device is a spring and damper connected in parallel, the Kelvin-Voigt model^[21]. Deformation of both the spring and damper are equal, the stress each component experiences sum for the device as expressed by Equation (2.6), valid for steady state harmonic motion. The visco-elastic stress-deformation hysteresis loop is diagrammed (labeled) in Figure 2-9.

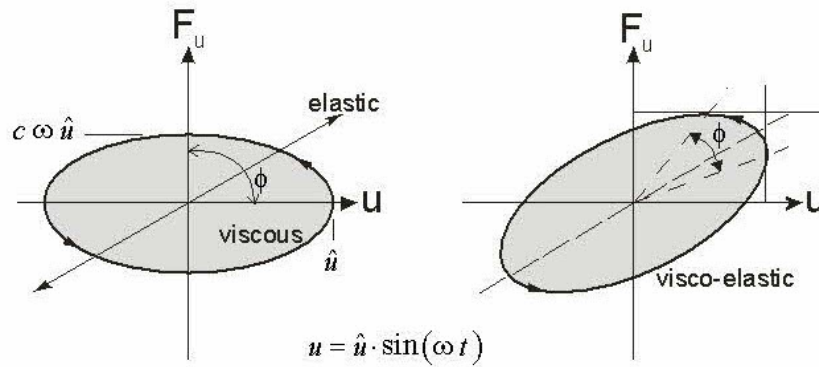


Figure 2-9 Stress-Deformation Cycle [Viscous & ViscoElastic Damping]

The addition of the elastic element causes the elliptical hysteresis trajectory of the purely viscous material to rotate in the stress-strain plane. The phase shift ϕ between strain and stress does not depend on stress magnitude. Rather, it is a function of stress frequency. For purely viscous materials, the phase shift is a constant $\frac{\pi}{2} \text{ rad}$.

2.2.1.4 Coulomb Damping

Coulomb, or frictional damping, is an interfacial mechanism occurring at joints and cracks during displacement. The stress-deformation hysteresis loop is diagrammed in Figure 2-10. The stress- strain relationship is non-linear:

$$F_{coulomb} = \begin{cases} -\mu N & \text{if } \dot{u} > 0 \\ 0 & \text{if } \dot{u} = 0 \\ \mu N & \text{if } \dot{u} < 0 \end{cases} = -\mu N \operatorname{sgn}(\dot{u})$$
$$\Delta W_{Coul} = \int_t^{t+T} F_d du = 4 F_d \hat{u}$$

A linear formulation is generally desired and obtained by equating the unit energy dissipation to that of the viscous damper:

$$\Delta W_{Coul} = \Delta W_{Viscous}$$
$$4 F_d \hat{u} = c_{eq} \pi \omega \hat{u}^2$$
$$c_{eq} = \frac{4 F_d}{\pi \omega \hat{u}}$$

The equivalent viscous transformation yields a linear system representation with exponential decay behavior. The real-world response is not however, viscous-like. Actual coulomb decay behavior is shown in Figure 2-7b for comparison. The decay rate is uniform rather than exponential. This will be shown to be of special interest for the Modal Damping Concept Demonstration experimental model.

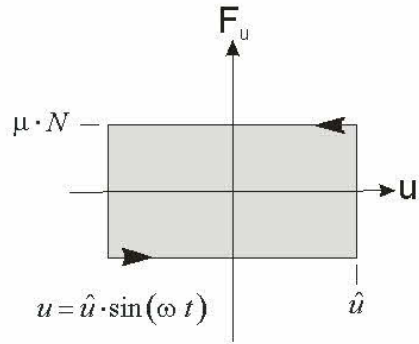


Figure 2-10 Stress-Deformation Cycle [Coulomb Damping]

2.2.1.5 Hysteretic Damping

Inelastic deformation cycles develop hysteretic damping. The stress-deformation cycle represented in Figure 2-11 forms a hysteresis loop relating the amount of energy dissipated in the cycle.

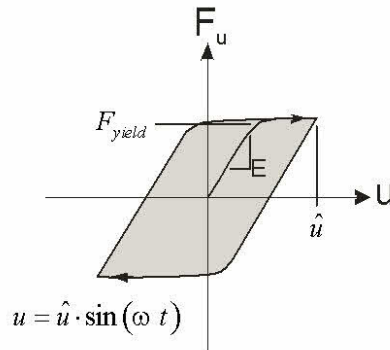


Figure 2-11 Stress-Deformation Cycle [Hysteretic Damping]

The amount of energy is a function of the material yield strength, the materials ductility, and the magnitude of deformation. The approximate unit energy is:

$$\Delta W_{Hysteretic} \approx 4 F_y u_y [\eta - 1] = 4 F_y \hat{u} \left[\frac{\eta - 1}{\eta} \right], \quad \eta = \frac{\hat{u}}{u_y}$$

The equivalent viscous damping coefficient for harmonic deformation is:

$$\Delta W_{hysteresis} = \Delta W_{viscous}$$

$$4 F_y \hat{u} \frac{(\eta-1)}{\eta} = c_{eq} \pi \omega \hat{u}^2$$

$$c_{eq} = \frac{4 F_y}{\pi \omega \hat{u}} \cdot \frac{(\eta-1)}{\eta}$$

or

$$4 E \hat{u}_y^2 (\eta-1) = c_{eq} \pi \omega \hat{u}^2$$

$$c_{eq} = \frac{4 E}{\pi \omega} \cdot \frac{(\eta-1)}{\eta^2}$$

2.2.2 Damping Devices/Components and Systems

These physical damping mechanisms can manifest themselves in various engineered devices, components or systems that can then be directly integrated into a structure. Components and systems have generally been found to be dividable into three major classes or mappings of damping approaches ^[22,23,24] that generally connote design complexities and energy requirements:

1. PASSIVE DAMPING.
2. ACTIVE DAMPING.
3. SEMI-ACTIVE DAMPING.

Several researchers have developed hierarchical diagrams that attempt to serve as logical roadmaps of design options^[25]. Kurata^[24] further showed that the design logic could proceed down one of two conceptual paths, frequency dependency or frequency independency. Frequency dependency dictates the robustness of a given approach with regard to external variables such as excitation forces and building parameters.

Figure 2-12 is a composite roadmap of damping options that was distilled from those found in the literature. Modal Damping is shown added as a possible option providing a new direction an engineer might consider.

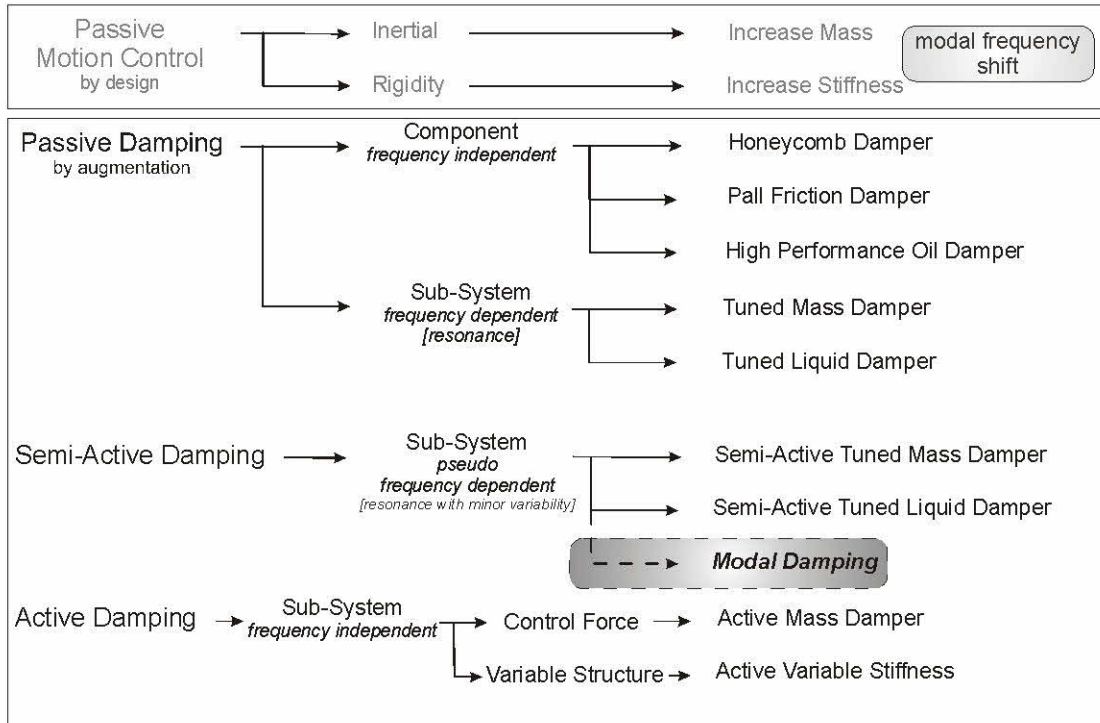


Figure 2-12 Structural Damping Roadmap

2.2.3 Passive Damping

Passive Damping Devices are distinguished by two major characterizing features.

1. They do not depend on external energy sources to achieve the targeted system behavior. They are instead ‘driven naturally’ by the motion of the structure being dampened.
2. Passive devices, for the most part, have fixed properties. Consequently, the augmented structural system cannot adapt itself to unexpected changes in external variables such as excitation or structural parameters. In most cases, the passive

approach offers a reliable and cost effective solution. However, the inability to adapt can possibly impact augmentation effectiveness if external variations become significant.

When integrated, the structure/damper couple forms a closed loop feedback system. The damping devices are driven by the dynamic states of the structure as depicted in Figure 2-13. While being driven, they:

1. Generate equilibrating forces which are fed back to the structure.
2. They dissipate energy.

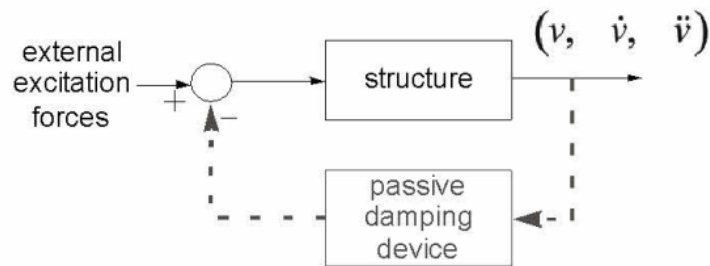


Figure 2-13 Structure & Augmentation (Damping) Feedback Loop

2.2.3.1 Component Level Damping

Examples of passive damping components are the oil viscous damper, the Pall friction damper, and the Honeycomb hysteretic damper each whose respective mechanism was presented above. These components can be directly integrated into the structure as shown in Figure 2-8 for the viscous damper, for an immediately increase the structures effective damping capacity. Large numbers of components, each positioned at one of many locations are generally required. Of course the damping distribution across the structure (both the degree and the location of damping) requires a systems design approach to maximize benefits and minimize costs.

2.2.3.2 System Level Tuned Mass Damper (TMD)

The (TMD) is a frequency dependent subsystem. Its design requires that the TMD subsystem dynamics be tuned to the dynamics of the structure to attain optimal performance. Resonant coupling is imperative. A poor design could serve to exacerbate poor dynamic behavior with the possibility of generating beat phenomenon. The approach involves physically integrating one or more secondary mechanical systems to the primary structure. Each secondary system is most often a single-degree-of-freedom mass-damper-spring configuration. The TMD principle is dependent on the interaction of inertial forces generated between the primary structure and the secondary mass caused by differential relative accelerations. The inertial forces are coupled through the spring-damper pair. TMD component parameter values are chosen to tune its natural frequency to that of the coupled pair (structure/subsystem). The design enables the TMD to vibrate out of phase with the primary structure. Equilibrating forces are generated to help balance structural dynamic forces. The coupled systems orchestrate energy transfer between two separate vibration modes: from that of the structure to that of the TMD with the goal of secondary system energy being dissipated in the secondary damping device.

The TMD design can proceed along a number of different paths, but often a desired effective damping ratio (ζ_{eff}) is chosen as the objective. If this is the case, parameters are chosen such that ^[26]:

$$\zeta_{eff} = \frac{\bar{m}}{2} \sqrt{1 + \left(\frac{2\zeta_p}{\bar{m}} + \frac{1}{2\zeta_d} \right)}$$
$$\bar{m} = \frac{m_d}{m}$$
(2.7)

ζ_p and ζ_d are the damping ratios of the primary structure and the secondary system respectively. The TMD design process has several real-world constraints that govern the design, specifically:

- Maximum allowable mass of the subsystem.
- The size, availability and mechanical compatibility of secondary dampers.
- The allowable relative displacement of the secondary mass.

A simple example demonstrates the significance of the constraints and how they fold into the system design process. Assume a tall structure modeled as a SDOF as diagrammed in Figure 2-14. Let the effective structural mass of the fundamental mode be 5000 tons and the period of the fundamental vibration mode be 6 seconds. Secondary masses typically range 1%-2% of the primary mass. Suppose that the structure will accommodate a secondary mass (m_d) of 2%. The design begins with the equations of motion...

$$m\ddot{u} + c\dot{u} + ku + c_d(\dot{v} - \dot{v}_d) + k_d(v - v_d) = \delta$$

$$m_d\ddot{u}_d + \dot{c}_d(\dot{v}_d - \dot{v}) + k_d(v_d - v) = 0$$

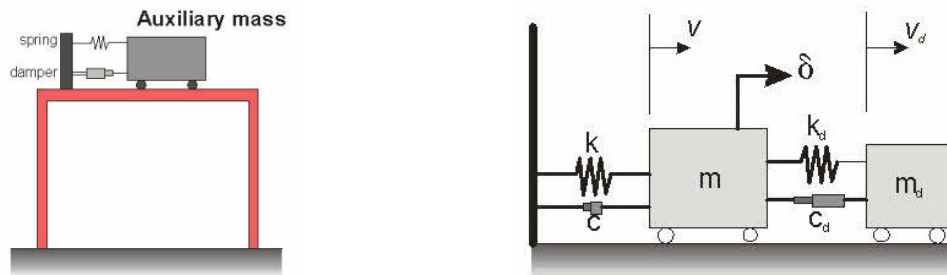


Figure 2-14 TMD Schematic Model

The equations can be re-arranged as shown in Equation (2.8) to facilitate analysis. The eigenvalues of the coefficient matrix are used to help tune the TMD and select the parametric values (described in Section 2.3.1.2) for a thorough system design.

$$\begin{bmatrix} \dot{x}_1 \\ \dot{x}_2 \\ \dot{x}_3 \\ \dot{x}_4 \end{bmatrix} = \begin{bmatrix} 0 & 1 & 0 & 0 \\ -\frac{k+k_d}{m} & -\frac{c+c_d}{m} & \frac{k_d}{m} & \frac{c_d}{m} \\ 0 & 0 & 0 & 1 \\ \frac{k_d}{m_d} & \frac{c_d}{m_d} & -\frac{k_d}{m_d} & -\frac{c_d}{m_d} \end{bmatrix} \cdot \begin{bmatrix} x_1 \\ x_2 \\ x_3 \\ x_4 \end{bmatrix} + \begin{bmatrix} 0 \\ \delta \\ 0 \\ 0 \end{bmatrix}, \quad \begin{bmatrix} x_1 \\ x_2 \\ x_3 \\ x_4 \end{bmatrix} = \begin{bmatrix} v \\ \dot{v} \\ v_d \\ \dot{v}_d \end{bmatrix} \quad (2.8)$$

Equation (2.7) offers a quick look into damping augmentation requirements for this example. If an effective damping ratio of 5% is desired, and the primary system is assumed to have only 1% damping, a damping ratio of 12.8% would be required from the TMD subsystem. The design proceeds by selecting the secondary dampening device that provides the necessary damping value. The secondary coupling spring is then chosen to set the natural frequency of the subsystem. The plots of Figure 2-15 reveal the resulting effectiveness of the TMD. The first plot is a set of traces comparing the building displacement to an impulse response with and without the damping augmentation. The exponential decay of the augmented system represents $\zeta_{eff} = 5\%$

which can be verified by logarithmic decrement $\delta = \ln\left(\frac{u(t)}{u(t+T)}\right)$, $\zeta = \frac{\delta}{\sqrt{4\pi^2}}$.

The relative displacement of the secondary mass to the building is shown as the second plot of Figure 2-15. The maximum displacement is shown to be $u_d \approx \pm 2.5 ft$. Expected secondary mass displacements will have to be compatible with the spring-damper pair physical limitations. Although it might intuitively seem that the TMD subsystem would be more effective if the parametric value of the damper (c_d) were simply increased, analysis indicates otherwise. Arbitrarily increasing c_d would actually have adverse affects on the net effectiveness of the TMD. This is shown in Figure 2-16. The plot of Equation (2.7) indicates an inverse relationship between damping ratio of the TMD

subsystem and the overall effectiveness of the coupled systems. Note however, that the plot fails to show that when increasing the effective structural damping ratio (by decreasing the parametric value of the secondary damper), an increase in relative displacement occurs between the secondary mass and the building.

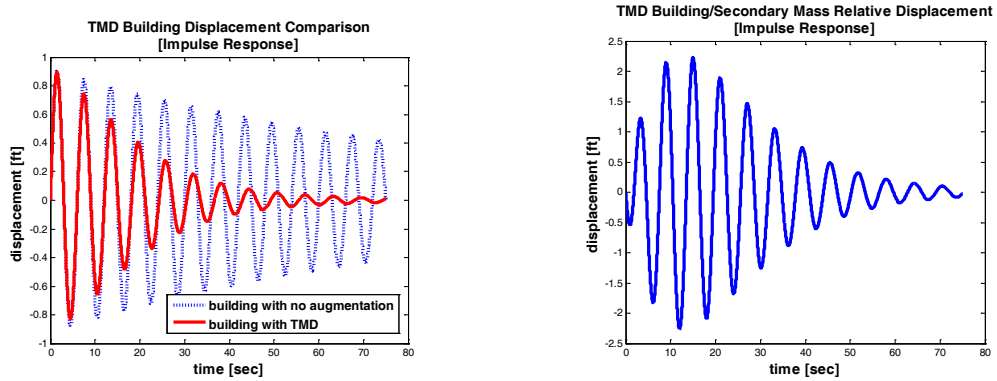


Figure 2-15 TMD Time Responses

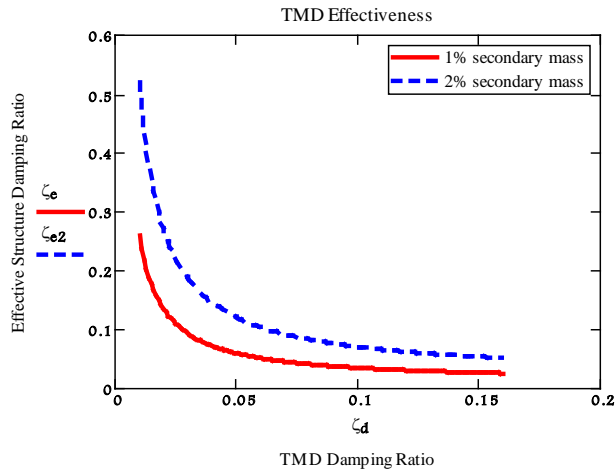


Figure 2-16 Secondary Damper Effectiveness

The CITICORP Center in Midtown Manhattan New York City is a fascinating example of modern day design and construction technology^[27]. One of the design team’s greatest challenges was accommodating a structural constraint levied by the historical nature of the site. The original St. Peter’s Lutheran Church was built on the

site in 1862. Its congregation, was willing to sell a portion of the land for the Citicorp project given that specific conditions were met. A new church was to be built... and it was to maintain free sky rights over its church. The constraints resulted in a 915 feet tall, 59 story structure that essentially stands on 100 feet high stilts (see Figure 2-17 [28,29]). The 'stilts' are four 17.5 foot square columns located at the center of the outside walls. In addition, there is a central core. Because of this unique ground interface, a design goal was established to minimize the overall weight of the structural steel skeleton. Its outside walls were design as vertical trusses with diagonal cross beams configured in a chevron pattern. The vertical trusses carry the wind load and a portion of the gravity load. The remaining gravity load is carried by the core. The building is clad with aluminum and glass.



Figure 2-17 CITICORP Center on Stilts

Because of its design and lightweight nature, a tuned mass damper was required to control sway. The building's natural or inherent damping ratio is 1%. A secondary mass, a 400-ton concrete block, was located at the top of building at the 63rd floor. The damping subsystem is tuned to be biaxially resonant, that is to dissipate vibration in both lateral directions. The TMD activates once sway reaches a displacement of ± 2.6

inches at its natural frequency. The resulting equivalent damping ratio is approximately 5%. In the case of the Citicorp Center, the TMD reduced building sway by 50%, however, the TMD subsystem has limitations. As it interacts with the structure at a single point, its effects are localized. Since its effectiveness is based upon the maximizing differential velocities between the structure and secondary mass, it is generally located high in the structure and serves to primarily mitigate the fundamental vibration mode.

2.2.3.3 Tuned Liquid Damper

The Tuned Liquid Damper (TLD) is a variation of the TMD with the difference being that the auxiliary control mass of the subsystem is in liquid form ^[30]. Several different forms of the TLD exist. A tuned sloshing device, sometimes referred to as a sloshing-slamming damper, is the simplest of the TLDs to implement. It requires no sophisticated components other than the liquid container.

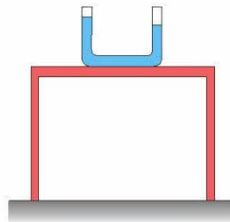


Figure 2-18 Tuned Liquid Column Damper Schematic Model

The motion of the structure causes the contained liquid to slosh. The ‘break-wall’ action of the sloshing liquid against the containment vehicle generates counterbalancing inertia forces. Equilibrating forces are often approximated based upon differential hydrostatic forces generated between both ends of the tank using the following expression ^[31],

$$F = \rho \cdot g \cdot b \cdot \int_0^{\eta_n+h} x \, dx - \rho \cdot g \cdot b \cdot \int_0^{\eta_0+h} x \, dx$$

Yalla points out that the dynamic sloshing and slamming actions is complex. The simple approximation is not linear over all amplitudes of wave motion and cannot be reduced to a static formulation. Another significant drawback of the sloshing damper is the difficulty in tuning it. Damatty has published similar findings, the response to large excitations are not well defined, associated damping parameters become non-linear with excitation amplitude [32].

A friendlier form of the TLD is the Tuned Liquid Column Damper (TLCD). The TLCD is also an enclosed container like the sloshing damper; however it is U-shaped and has a horizontal section with vertical sections at each end. The U-shaped container eliminates the break-wall, slamming action found in a standard TLD. Like the sloshing-slamming damper though, TLCD behavior is inherently non-linear. The advantage of the TLCD is that its dynamic modeling is more straightforward than the sloshing damper. A controllable orifice significantly improves the damping performance of the device. Performance determining features have been found to be:

- The TLCD is tuned by varying its length ratio: the length of the horizontal leg to the total length of water in the U shaped tube. Length ratios are typically 0.6→0.7.
- The natural frequency of the damper is determined by the total length of the liquid column.
- The area ratio is the ratio of cross sectional area of the horizontal part of the U-tube to that of the vertical part.

The free body diagram of the TLD is similar to that of the TMD shown in Figure 2-14. The equivalent component values are more difficult to identify. Tuning and performance optimization was described as being a form of art as well as science.

Liquid dampers offer several advantages over standard TMD subsystems. Initial cost and maintenance costs tend to be lower. Mass associated with TMD systems is strictly dead weight and serves no other function. The containers of the TLDs can be utilized for water supplies within the structure. This can be significant when the required subsystem mass ratio is considered. Mass ratios on the order of 1-2% of the structure's inertial mass are generally necessary.

2.2.3.4 Impact Dampers

S. de Souza et al ^[33] define a vibro-impact damper, aka an impact damper, as a secondary, loose mass utilized to effect the vibration behavior of a primary mass by way of momentum transfer occurring through collisions between the two masses. Souza stated that the momentum transfer event can potentially offer assistance in decreasing oscillation amplitudes of the primary system. De Souza utilized generalized Euler-Lagrange equations of motion to construct a mathematical model of the phenomenon. Parameters of the impact damper were optimized in the neighborhood of the primary system resonance. Even when mass ratios between the impact and primary systems

were small $\left(\frac{m_{impact}}{M_{primary}} = .005 \right)$, the impact damper was shown to have the ability to

control chaotic behavior of the primary system. He concluded that such dampers have utility for improving dynamic behavior of devices such as turbine blades. P. Frantisek's mathematical model developed from his free body diagram similar to that diagram in Figure 2-19 demonstrated that impact behavior is complex, involving pseudo-periodic and chaotic motions ^[34]. Frantisek's model attempted to predict the fundamental motion of the masses. His model recognized two regions of operation; the masses motions were segmented as a piecewise construct composed of:

1. A region described by linear impact-less motion of two systems.
2. A region defined by impact criterion dictated by energy conservation that yielded post impact states.

The impact-less region is defined by standard 2 degree-of-freedom equations of motion:

$$m_1 \ddot{v}_1 + b_1 \dot{v}_1 + k_1 v_1 + b_2 (\dot{v}_1 - \dot{v}_2) + k_2 (v_1 - v_2) = F_0 \cos(\omega t)$$

$$m_2 \ddot{v}_2 - b_2 (\dot{v}_1 - \dot{v}_2) - k_2 (v_1 - v_2) = 0$$

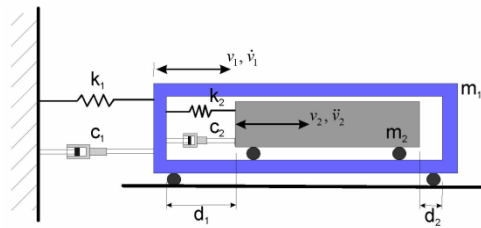


Figure 2-19 Free Body Model of an Impact Damper

Once impact is detected, the mass velocities are adjusted according to the Newton theory of direct centric elastic impacts:

$$\text{kinetic energy}_{t+} = \text{kinetic energy}_{t-}$$

$$\text{momentum}_{t+} = \text{momentum}_{t-}$$

leading to

$$\dot{v}_{1+} = \frac{(m_1 - m_2) \dot{v}_{1-} + 2m_2 \dot{v}_{2-}}{m_1 + m_2}$$

$$\dot{v}_{2+} = \frac{(m_2 - m_1) \dot{v}_{2-} + 2m_1 \dot{v}_{1-}}{m_1 + m_2}$$

The near instantaneous change in velocities of the impacting masses precipitated the complicated bifurcated behavior demonstrated with simulation results.

The impact damper took on special interest because it is one device used to control vibration behavior in the aluminum luminaire poles, the baseline flexible structure. This damper device was investigated by L. Caracoglia and N.P. Jones as a

funded study by the Illinois Department of Transportation [35]. The proposed design was a chain damper with mass per unit length m , of length l , suspended inside the vibrating pole. The specific design is performed via empirical testing and targeted fundamental mode vibrations. Experimental testing showed that chain dampers behave nonlinearly. Their performance is amplitude dependent. Various regimes were observed delineated by full, partial, or no impact of the chain with the pole. Caracoglia noted that: “at large oscillation amplitudes the number of impact usually increased and became irregular, therefore critically diminishing the effectiveness of the device”. Damping evaluations were performed. Damping assessments were unexpectedly difficult due to false beating modulations caused by in-plane and out-of-plane coupling and the low inherent damping. With the top mounted luminaire, the impact damper (chain) increased the critical damping factor from approximately 0.1-0.2% to approximately 2%.

2.2.4 Active Damping

Some of the limitations and constraints of passive mass dampers such as robustness and massiveness can be overcome by the use of active damping systems. The active control approach integrates structural dynamic problem with advanced control theory. Active damping is achieved through the use of an intelligent, real-time controller that monitors system behavior and effects necessary control forces using externally available energy, typically from electrical or hydraulic sources. The controller monitors the dynamic state of the structure using combinations of sampled measurements of displacements, velocities, and accelerations taken at selected points within the structure. The measured state variables become inputs to the control algorithms which apply the appropriate gains and combinatorial formulae dictated by the advanced control laws. The science of designing feedback control laws (of

particular interest to structural motion control) is briefly discussed in following sections.

In general, active control can be designed to respond to wider ranges of conditions. Y. L. Xu ^[36] performed a parametric study of the active mass damper to evaluate its effectiveness to reduce wind excited motion of tall buildings. He compared passive to active system responses for alongwind, crosswind, torsional, and white noise excitation. The active system was found to be more effective in all cases in reducing both displacement and acceleration responses. Performance of the active mass damper is not sensitive to small variations in system parameters (structural mass, structural damping, secondary damping, excitation forces) begetting its robust character. Xu contended that the majority of dynamic vibration energy is found in the fundamental mode; the wind-induced response of tall buildings is primarily attributed to the two orthogonal fundamental sway modes and sometimes the fundamental torsional mode of vibration. He pointed out that this may not be the case when an active control system is integrated. Depending on its configuration, he postulated that the controller may distribute vibration energy into uncontrolled modes. However, his analysis of a 40 story building having been augmented with one active mass damper installed on the top floor and tuned to the fundamental frequency of the building revealed no evidence that other vibration modes were noticeably excited due to control inputs.

A distinctive requirement of the active controller is that it depends on external energy to effect forces to mitigate undesired dynamic forces of the vibrating structure. As shown in Figure 2-20, the external power is introduced in the feedback path. The developed counterbalancing forces can be significant.

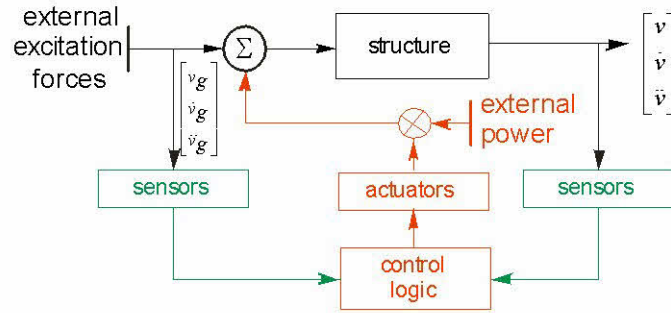


Figure 2-20 Active Control Functional Block Diagram

Unlike passive control systems, instability is a concern for the active design. An active control system has the potential to drive the structural system to failure because it adds energy to the vibrating system. The magnitude, phase and placement of the control forces are key variables in the design effort. Control design criteria are discussed in more detail in later sections. Active Damping systems tend to fall into one of two primary variations: Active Mass Dampers and Active Variable Stiffness Controllers.

2.2.4.1 Active Mass Damper (AMD)

The AMD is an inertial based system. The principle is similar to that of the TMD where equilibrating inertial forces are generated between the primary structure and the secondary mass. In the case of the TMD however, the damping augmentation subsystem is driven by the motion of the structure itself. AMD equilibrating forces between the damping augmentation subsystem and the structure are delivered through an intelligently controlled actuator. The actuator is primarily responsible for the relative acceleration differences between the two platforms. Smaller secondary masses are possible because higher relative accelerations can be generated. Higher associated cost of the AMD operation is due to its external energy requirements. The TMD by

comparison, gets a free ride. The equations of motion describing the AMD can be derived from Figure 2-21:

$$\begin{aligned}
 m\ddot{v} + c\dot{v} + kv + k_d(v - v_d) + F_{active} &= \delta \\
 m_d\ddot{v}_d + k_d(v_d - v) &= F_{active}
 \end{aligned}
 \tag{2.9}$$

$$F_{active} \rightarrow f(v, \dot{v}, \ddot{v})$$

The specific algorithmic control laws executed by the intelligent controller determine the optimal $F_{control}$ given the measured states of the system, v, \dot{v}, \ddot{v} . Control law strategies and algorithms are discussed in later sub-sections.

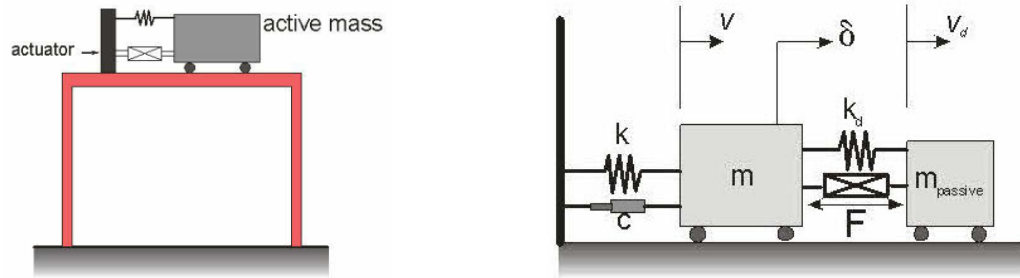


Figure 2-21 AMD Schematic Model

The first application of active structural control in civil engineering was the ten-story office building in Kyobashi, Tokyo, Japan [37,38]. This occurred in 1989. The building was construction using rigidly connected steel framing composed of box columns and H-beams. The building footprint is rectangular in shape, only 3.0 meters in the transverse direction and 12.5 meters in the longitudinal direction. Two AMDs are installed on the top story in order to reduce two distinct vibration modes. The building and one of the AMD are shown in Figure 2-22 [39,40]. One mode is a translational mode caused by the unusually narrow profile along the weak structural axis. The second mode is a torsional mode caused by unbalanced mass distribution

around the center of gravity of the section. Both earthquake and wind excitation forces were a concern.



Figure 2-22 Kyobashi Building [AMD Subsystem]

The AMD is composed of two auxiliary, pendulum-mounted masses accelerated by hydraulic oil actuators. Auxiliary mass-1 is 4200 kg (~9200 lb) and is located near the center of the floor. Auxiliary mass-2 is 1200 kg (~2650 lb) and is located on the same floor as the auxiliary mass-1, but located significantly off center. The fundamental vibration frequency of the translational mode was determined to be 1.065 Hz with a damping ratio of only 0.77%. The frequency for the fundamental torsional mode was determined to be 1.85 Hz. Each auxiliary mass was tuned to 0.4 Hz lower than that of either of the two structural modes for stability purposes.

The multi-state feedback active control logic was developed using a linear quadratic regulator strategy based on acceleration measurements. The feedback consisted of four acceleration states, one taken at each of the mass damper locations, and one taken on each of the mass dampers. Furthermore, these measured acceleration states were used to compute respective accelerations relative to the building's base

acceleration based on a measurement taken at the first basement level. The final control input to the two auxiliary mass dampers took the form:

$$u_1 = g_1 \ddot{y}_1 + g_2 \ddot{y}_{mass_damper1}$$

$$u_2 = g_3 (\ddot{y}_2 - \ddot{y}_1) + g_4 \ddot{y}_{mass_damper2}$$

where $g_{i(i=1 \rightarrow 4)}$ are the feedback gains dictated by the control logic design. The auxiliary masses `mass_damper1` and `mass_damper2` were able to generate 3.4 and 2.2 metric tons of equilibrating control force respectively.

The active controller in the Kyobashi Seiwa Office Building has been *exercised* on numerous occasions from regional earthquake and wind activity. Controlled and uncontrolled responses have been captured. Post analysis of the structures dynamical data indicates that the active control system increased the fundamental vibration mode damping ratio of the controlled structure from approximately 1.7% to 15.2→23.8%. The control system was found to reduce accelerations by a factor of approximately three.

2.2.4.2 Active Variable Stiffness (AVS) Damping

An AVS system can best be described as one that dynamically changes the stiffness properties of the structure based on measured or predicted excitation forces [41]. It is referred to as a non-resonant control strategy. The control logic uses its ‘foresight’ to vary structural stiffness in order to direct the structures natural vibration frequency dissonant from that of the expected forcing function. In doing so, the amount of energy coupled into the structure is minimized. The control strategy is based on feed-forward logic using measurements of external excitation forces, i.e. ground accelerations. Estimations of structural responses are formulated for each of the finite structural stiffness states. Computer technology advancements have enabled estimates

to be accomplished in real-time, allowing the optimal stiffness properties to be selected prior to complete structural excitation. The feed-forward based equations of motion were presented by Tadashi Nasu ^[42] and take the form:

$$\ddot{x}(t) = E(t) \cdot (SF(t) + RF(t - \Delta t))$$

$SF(t)$ represents the estimated seismic forces based on structural masses and measured ground accelerations

$$SF(t) = f(M(t), \ddot{y}_{ground}(t))$$

And, $RF(t)$ represents the predicted structural resonant forces,

$$RF(t - \Delta t) = f(M(t), C(t), K(t), \ddot{x}(t - \Delta t), \dot{x}(t - \Delta t), x(t - \Delta t))$$

$E(t)$ is the dynamically controlled parameter and represents a transfer function based on the selected structural dynamic properties,

$$E(t) = f(M(t), C(t), K(t))$$

The stiffness parameter is continuously evaluated and if necessary varied to achieve the optimal response. Nasu described two strategies for dynamic selection of $K(t)$, the time-varying stiffness parameter. The first is based on spectral filtering of the ground acceleration measurements. The second approach involves parallel simulations that predict in real-time the estimated structural responses for each of the possible stiffness states. Selected parameters from the predicted responses form a cost equation used to determine stiffness optimality. Both strategies have been exercised. The second method has proven to be more effective.

Research supported by the Kajima Technical Research Institute resulted in a 3-story, 400 ton steel structure that has served as the control building for hosting the development of state of the art fundamental AVS technology. The variable stiffness

components are two-ended enclosed hydraulic cylinders that act to lock or un-lock steel races laterally connected between adjacent stories. A simple schematic drawing of the building is shown in Figure 2-23 [43].

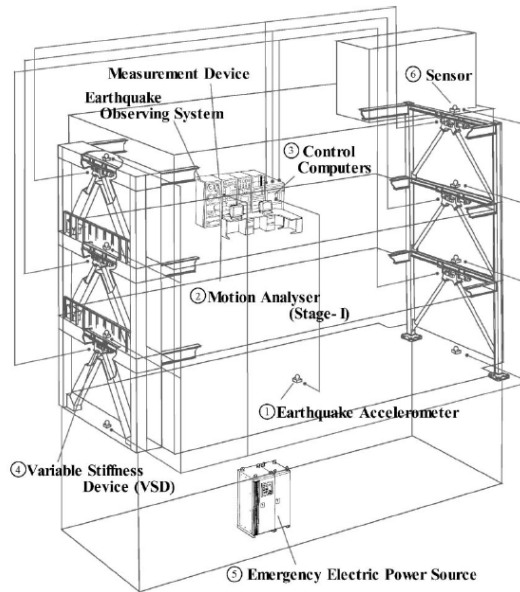


Figure 2-23 Kajima Active Variable Stiffness Building Schematic

The three story structure with each story having two stiffness states results in 8 discrete stiffness states that require dynamic evaluation. In general, AVS is effective during narrow banded disturbances, but is not as effective when disturbances have wide band energy.

2.2.4.3 Triton Square Office Complex

A significantly different approach to structural vibration control can be found in the Triton Square Office Complex shown in Figure 2-24 [44].

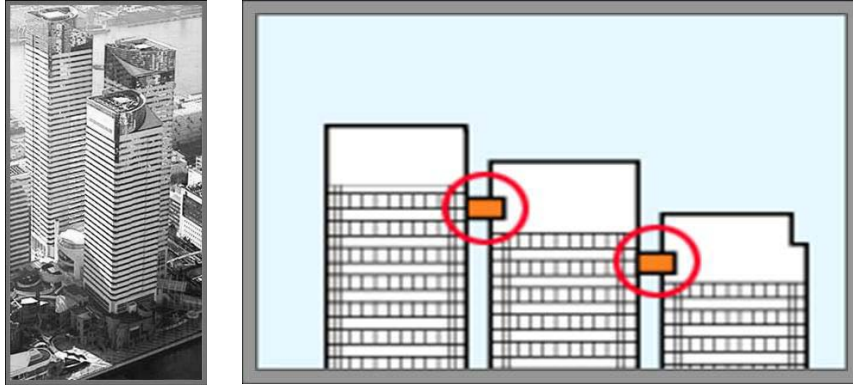


Figure 2-24 Triton Square Physically Coupled Buildings

The engineers of this multi-building complex resolved to reduce structural responses to wind and seismic forces using an active control scheme that physically couples two adjacent buildings with dissimilar dynamic characteristics. R. E. Christenson et al ^[45] showed that actively controlled coupled buildings using acceleration feedback is an effective method to reducing the RMS response of multiple story accelerations for simulated earthquakes.

Christenson experimentally evaluated the controllability of two scaled buildings coupled at the top stories using a controllable linear actuator. Each building was designed to have two degrees of freedom along one lateral direction. In comparison, the Triton Square structure involved 45, 40, and 35 story buildings coupled using two 35-ton active control actuators.

Christensen stated that in order for the control strategy to be effective, the natural frequencies of the individual buildings must not coincide. His objective was to develop a control strategy to reduce maximum story accelerations in both buildings. In Christensen's experiment, there were four regulated acceleration states, two per building, and there was one actuator signal generated by the controller. The control strategy he implemented was a variation of an optimizing Linear Quadratic Gaussian

approach configured to minimize root mean square story accelerations over both buildings. Results indicated that the active control strategy was able to reduce all of the RMS accelerations in the complex 52% → 66% over the uncoupled buildings when tested using a simulated El Centro earthquake excitation.

2.2.5 Semi-Active Damping

Semi-active vibration control offers a compromise between full active control and passive control. Semi-active designs integrate key features from both the passive and active options while attempting to balance performance and operational costs. Semi-active systems are typically designed around passive energy dissipation devices such as viscous shearing of fluids, frictional sliding, or tuned inertial mass mechanisms. The significant difference between the semi-active variation and its passive counterpart is an automated feedback controller coupled to the damping devices that provides for real time adaptation to system behavior. This robustness is the major benefit derived from active damping systems. Unlike active systems however, semi-active systems depend on the passive components themselves to generate the majority of the control forces. Subsequently, a much smaller external energy source is required to power feedback components. And, like their passive associates, semi-active systems will rarely have the capability to drive the building to less stable states regardless of the system failure.

The additional complexity of semi-active systems is embodied in the functional block diagram of Figure 2-26.

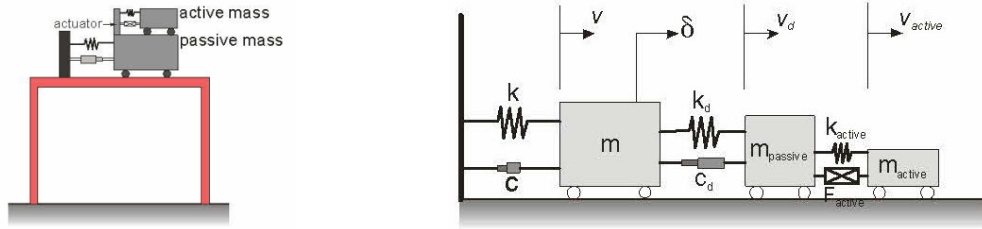


Figure 2-25 Semi-Active Mass Damper Schematic Model

The diagram reveals multiple feedback paths. Each path requires careful design. The composite system must be evaluated for all given excitation conditions to establish and ensure satisfactory system behavior.

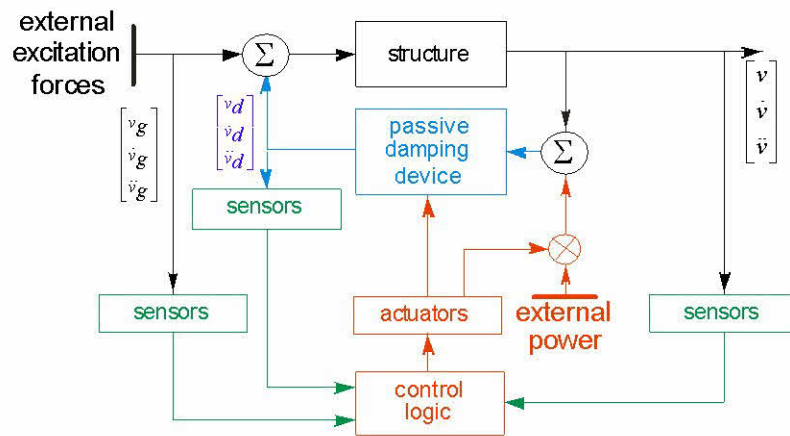


Figure 2-26 Semi-Active Damping Functional Block Diagram

Often times semi-active and hybrid systems are grouped together or are discussed as being equivalent. Both systems can generally be characterized as having intelligent, real-time feedback loops that vary system parameters related to overall performance. Technically, there are differentiating features. Semi-active designs can be distinguished by their external energy requirements and utilization. They tend to direct external energy into the generation of control forces, although to a lesser extent than active systems. An example would be a semi-active tuned mass damper. However, like the passive system, the control energy for hybrids is for the most part sourced by the

motion of the structure itself. Feedback control schemes for the hybrid systems generally optimize specific parameters associated with discrete components such as orifice position. An example would be a tuned liquid column damper. For the purpose of this high level summary, they will not be differentiated to any great extent.

2.2.5.1 Semi-Active Devices/Components

Symans ^[23] provides a thorough review of state-of-the-art devices used to facilitate semi-active control. Included are stiffness control devices, electrorheological dampers, magnetorheological dampers, friction control devices, and fluid viscous dampers.

Stiffness control devices are bi-state in nature. They can be commanded to engage/disengage additional stiffness of secondary bracing systems, modifying the natural vibration characteristics of the primary structure. Stiffness control devices can be hydraulically or electromagnetically actuated.

Electrorheological (ER) dampers are hydraulic-like dampers, but, contain fluid whose viscosity characteristics can be dynamically modulated. Viscous control is achieved by suspending dielectric particles in the damping fluid. The orientation of these particles is sensitive to externally applied electric fields and when aligned can be used to increase the viscosity of the fluid. A phenomenological model referred to as the Bingham model ^[46], consists of a Coulomb friction device in parallel with a linear viscous dashpot. Its behavior is described by the follow stress-strain relationship:

$$\tau(t) = \tau_y(t) \cdot \text{sgn}(\dot{\gamma}) + \eta \dot{\gamma}$$

where, $\tau(t)$ is the current shear stress, $\tau_y(t)$ is the time varying commanded yield stress of the ER fluid, $\dot{\gamma}(t)$ is the current shear strain rate, and $\text{sgn}(\bullet)$ is the signum

function. The dielectric particles suspended in the fluid have been experimentally found to cause the yield stress to vary with electric field strength as a power law function:

$$\tau_y(t) = K[\varepsilon(t)]^p$$

where, K is a scalar relating to the geometry of the particular device, $\varepsilon(t)$ is the time varying commanded electric field strength (kV/mm) and the exponent p is an experimentally determined value ranging from 1.2 to 2.5 [47].

Magnetorheological dampers behave similarly to electrorheological dampers. A magnetic field, rather than an electric field is the controlling variable.

Friction control devices are extensions of the ideal coulomb element described earlier that dissipate energy through frictional mechanisms developed through sliding motion. This controllable variation yields a time varying normal force whose model is an adaptation to the basic coulomb model presented in Section 2.2.1.4, where now,

$$F(t)_{coulomb} = \mu N(t) \cdot \text{sgn}(\dot{x}).$$

Fluid viscous control damping devices are extensions of fixed viscous damping mechanisms described earlier, which dissipate energy through shearing mechanisms developed in the fluid flow motion. The device is typically realized by including a variable orifice between two sides of an oil filled cylinder. The variable orifice is generally formed by using a fixed orifice in the piston head of the damper with an additional bypass circuit between the two sides of the cylinder. The bypass circuit could be a simple on/off type switching action, or it could be a variable modulation. The resisting force of the variable fluid viscous damper is modeled as:

$$F(t) = C(t) \cdot \dot{x}(t)$$

where $C(t)$ is a commanded, time varying damping coefficient and $\dot{x}(t)$ is the piston velocity.

Common applications of semi-active control include the semi-active tuned mass damper (diagrammed in Figure 2-25) and tuned liquid dampers [41,48,49]. The non-linear behavior of the tuned liquid damper, the tuned liquid column damper (TLCD) in particular, results in non-optimal damping over the expected range of excitation. The primary advantage of the TLCD however, is that its dynamic behavior can be enhanced by introducing a flow regulator, or orifice, in the horizontal segment. Using external control logic, the orifice opening can be set to a desired head-loss and in turn, the desired effective damping. The adjustment of the liquid column length tunes the resonant frequency of the subsystem. Coupling the TLCD to external control logic results in a passive-active, or semi-active subsystem.

2.3 Feedback Theory and Practice for Control of Structural Dynamics

Automated control is itself a complex science that bridges the spectrum of engineering disciplines because of its unbiased mathematical nature. It is often featured as the enabling technology used in advance aerospace vehicles (flight control and weapons control) and automotive technologies (anti-lock braking and emissions control). Although less glamorous, or maybe less advertised, automated control also has established a role as an enabling technology for many advanced structural control designs that involve interactive closed-loop, and adaptive algorithms. The following sections summarize the application of this science to the control problem of structural dynamics.

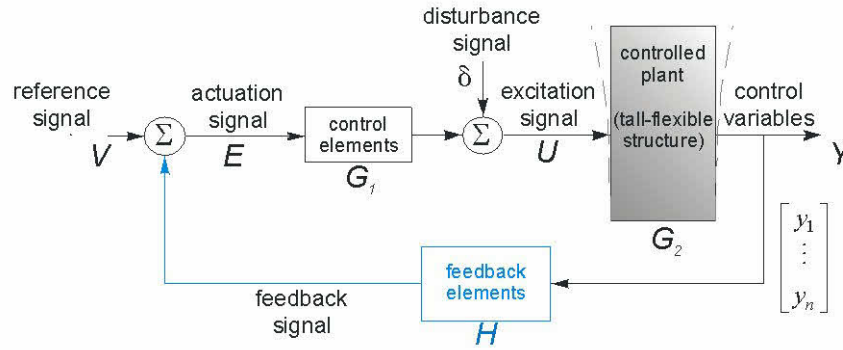


Figure 2-27 Standard Control System Block Diagram

Control discussions typically begin and ground themselves to functional block diagrams. A standard block diagram for a closed-loop feedback control system with control vernacular is shown in Figure 2-27 [50]. The closed-loop nature of the approach implies that output is compared with input before action is effected. Simply put, the control system consists of:

- The plant (mechanical, electrical, chemical, tall-flexible structure, etc.) to be controlled.
- Sensors and actuators as required that interface to the real world system.
- A ‘control-law’ implemented as either component type control elements or as a computer executed algorithm.

2.3.1 Linear Feedback Control

The particulars of the control discipline can be demarcated and approached from a multitude of directions: continuous vs. discrete; classical vs. modern; etc. Understanding this design option hierarchy assists in the identification of viable design candidates. Often times the first step is to determine whether the plant behaves linearly or non-linearly. Control engineers learn very early in their undergraduate curriculum

how to differentiate the two systems... Fundamentally, a linear system is one whose behavior satisfies the principle of superposition [51],

if

$$f(u_1(t)) = y_1(t)$$

$$f(u_2(t)) = y_2(t)$$

then

$$f(au_1(t) + bu_2(t)) = f(au_1(t)) + f(bu_2(t)) = ay_1(t) + by_2(t)$$

for any real numbers a and b .

Because of the many tools available for linear systems it is targeted and when possible achieved through simplifying approximations. In general, the passive damping approaches and many of the semi-active and active damping approaches described earlier in this section assume linear system behavior. If linearity is assumed, the output signal of the closed-loop system diagrammed in Figure 2-27 can be expressed as a Laplace transfer function of the form,

$$Y(s) = \frac{V(s) \cdot G_1(s) \cdot G_2(s)}{1 + G_1(s) \cdot G_2(s) \cdot H(s)} + \frac{\delta(s) \cdot G_2(s)}{1 + G_1(s) \cdot G_2(s) \cdot H(s)}$$

The output signal is shown to be a function of two input signals, the reference $v(t)$ and the disturbance $\delta(t)$. When the controlled plant is an advanced aircraft, the reference signal $v(t)$ might represent the commanded pitch attitude. When the controlled plant is a structure, the controlled variables are more likely to be nodal position or velocities. In this case, the structure is normally desired to be stationary; the reference signal becomes $v(t) = 0$. This simplifies the block diagram to that shown in Figure 2-28.

Absence of a reference signal transforms the problem from one of tracking to one more commonly referred to as a regulator problem. This transformation changes

the nature of the control objective. Regulators are designed to drive a disturbed dynamic system back to a desired equilibrium point. Design attention is given to the closed-loop dynamic response of the control variables $Y(t)$ rather than the behavior of tracking error $E(t)$.

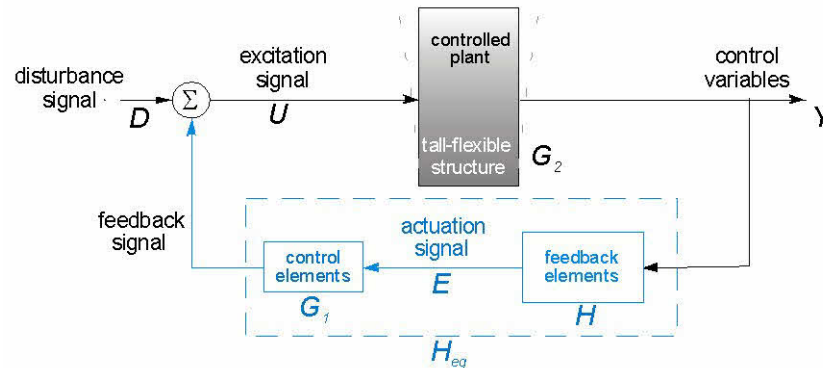


Figure 2-28 Standard Regulator Block Diagram

Structural disturbances generally imply forces generated by wind or seismic activity, but can include internally generated forces as well. Feedback generated by the control system also takes the form of forces that excite the structure. When the system design is effective, responses to feedback forces mitigate or negate the undesired excited responses. For the structural regulator problem, control compensation used to regulate dynamic behavior is found in the feedback path of the closed-loop configuration whose transfer function is:

$$\frac{Y(s)}{\delta(s)} = \frac{G_2(s)}{1 + G_2(s) \cdot H_{eq}(s)} \quad (2.10)$$

The control-law realizes the intelligence or logic of the control strategy. The control-law that is embedded in the feedback loop H_{eq} may be developed to shift natural frequencies of the main structure to pre-specified locations; or, it may be designed to optimize a formulated cost function. The particular form of the selected

control strategy is highly dependent on the personality of the controlled plant. Factors such as linearity, controllability, observability, stability, parameter sensitivity, and fidelity of the plants dynamic model must be included in the control law decision. Likewise, signal properties of external disturbances must be investigated. Finally, closed-loop behavior will furthermore be affected by sensor and actuator dynamics, and processor speed.

2.3.1.1 Linear Control Strategies

For structures, linear feedback control generates excitation forces of the general form:

$$u(t) = \int_{t_0}^{t_i} h(\tau) \cdot y(t-\tau) d\tau + d(t) \quad (2.11)$$

$$U(s) = H_{eq}(s) \cdot Y(s) + D(s)$$

In most cases, feedback gain coefficients are assumed constant and time invariant, particularly over some given piecewise linearized range. The control law of Equation (2.11) applies to single Degree-of-Freedom (DOF) systems as well as Multiple DOF systems when the systems are linear in nature. MDOF systems are hereafter assumed unless otherwise stated. When displacement, velocity, and acceleration feedback (H_d, H_v, H_a) is assumed and gains are constant, the dynamic equations formed from equilibrium requirements becomes:

$$\mathbf{M} \times \ddot{\mathbf{y}}(t) + \mathbf{C} \times \dot{\mathbf{y}}(t) + \mathbf{K} \times \mathbf{y}(t) = -\mathbf{H}_a \times \ddot{\mathbf{y}}(t) - \mathbf{H}_v \times \dot{\mathbf{y}}(t) - \mathbf{H}_d \times \mathbf{y}(t) + \mathbf{G} \times \mathbf{d}(t) \quad (2.12)$$

Rearranging Equation (2.12), and forming the energy balance equation over some time interval $t_0 \rightarrow t_f$ [12] by pre-multiplying each term by $\dot{\mathbf{y}}^T(t)$ and integrating over the positive time interval yields,

$$\begin{aligned}
& \int_{t_0}^{t_f} \dot{\mathbf{y}}^T(t) (\mathbf{M} + \mathbf{H}_a) \ddot{\mathbf{y}}(t) dt + \int_{t_0}^{t_f} \dot{\mathbf{y}}^T(t) (\mathbf{K} + \mathbf{H}_d) \mathbf{y}(t) dt + \int_{t_0}^{t_f} \dot{\mathbf{y}}^T(t) (\mathbf{C} + \mathbf{H}_v) \dot{\mathbf{y}}(t) dt = \\
& = \int_{t_0}^{t_f} \dot{\mathbf{y}}^T(t) (\mathbf{G} \times \mathbf{d}(t)) dt
\end{aligned} \tag{2.13}$$

The right side of the energy balance equation represents the energy introduced into the system by the disturbance $\mathbf{d}(t)$. The left side of the equation represents the change in vibration energy occurring during the time interval $t_0 \rightarrow t_f$ as effected by the inherent dynamic properties of the structure and the control compensation. The equation must balance. The energy change caused by the system can represent increased/decreased dynamic energy as well as energy dissipation.

Equation (2.13) can be used to provide discriminating insight into feedback control strategies conducive to structural motion control:

- As long as the velocity feedback gain (H_v) is positive, then

$$\int_{t_0}^{t_f} \dot{\mathbf{y}}^T(t) (\mathbf{C} + \mathbf{H}_v) \dot{\mathbf{y}}(t) dt > 0.$$

A damping device driven by nodal velocity will always dissipate energy thus reducing total system energy. Velocity feedback laws are often used.

- As long as the acceleration feedback gain (H_a) is negative, the net inertial, or

$$\text{kinetic, energy } \left\| \frac{1}{2} \dot{\mathbf{y}}(t_f) (\mathbf{M} + \mathbf{H}_a) \dot{\mathbf{y}}(t_f) - \frac{1}{2} \dot{\mathbf{y}}(t_0) (\mathbf{M} + \mathbf{H}_a) \dot{\mathbf{y}}(t_0) \right\|$$

will decrease over any time interval. A mass damper driven by negative nodal acceleration gains will always develop inertial forces that oppose dynamic inertial forces of the structure.

- Likewise, as long as the displacement feedback gain (H_d) is negative, the net potential energy $\left\| \frac{1}{2} \mathbf{y}^T(t_f)(\mathbf{K} + \mathbf{H}_d)\mathbf{y}(t_f) - \frac{1}{2} \mathbf{y}^T(t_0)(\mathbf{K} + \mathbf{H}_d)\mathbf{y}(t_0) \right\|$ will decrease over any time interval. Displacement actuation driven by negative nodal displacement gains obviously reduces net nodal displacement. The approach however has inherent limitations. Alone, it ignores the potentially large forces required to develop such displacements. More importantly, it requires an independent nodal location to displace from. Although workable on paper, it is not so practical for large structures.

Linear Control Law designs generally fall into one of the following design approaches:

1. A conventional or classical linear state feedback approach where cascade or feedback compensation is added to improve the system response. Conventional control is generally associated with scalar, or single-input/single-output systems (SISO).
2. A modern linear control theory approach where state variable feedback gains are often designed to minimize optimal performance indices. Modern control generally implies multiple-input/multiple-output systems (MIMO).
3. An alternate modern linear control approach based upon eigen-structure assignment. Eigenvector spaces are identified. The desired contribution of each mode to each state and output response is selected.
4. A robust control approach that explicitly deals with uncertainty embedded within the problem definition.

A brief review of the essentials of each approach as applied to structural control follows.

2.3.1.2 Classical Control

Classical control theory generally infers frequency domain and s-plane analysis. Relying on transform methods, classical control is primarily applicable for linear time-invariant systems^[50]. Frequency domain methods such as Nyquist and Bode investigate magnitude and phase of the spectral response of the system. These methods are practical for a number of reasons. The tools for analyzing linearized systems are well established and structured. Furthermore, frequency response can be experimentally measured from which a transfer function readily synthesized. Root Locus is a graphically oriented design approach that produces multiple solution trajectories rendered in the complex s-plane for design evaluation. The analysis requires a system transfer function represented in Laplace form. Each of these classical methods allows the controls designer a range of design possibilities. That is the resulting control systems are not unique. Although the design approaches are mathematically structured, the act of determining appropriate compensation to achieve the desired behavior viewed by some as engineering art.

The dynamics of the plant are first modeled yielding G_2 . The desired behavior is then specified. The feedback compensation is conceived and modeled yielding H . The dynamics of the control elements are developed and modeled as required yielding G_1 . For Nyquist or Bode analysis, the control ratio (closed-loop transfer function) becomes,

$$\frac{Y(j\omega)}{D(j\omega)} = \frac{G_2(j\omega)}{1 + G_1(j\omega) \cdot G_2(j\omega) \cdot H(j\omega)} \quad (2.14)$$

The control ratio of the system for Root Locus design takes on the general form,

$$\frac{Y(s)}{D(s)} = \frac{G_2(s)}{1 + G_1(s) \cdot G_2(s) \cdot H(s, \kappa)}, \quad \kappa = 0 \rightarrow \infty \quad (2.15)$$

Structures are disturbed by forces that may not be accurately described by mathematics; sensors produce measurement noise; and digital hardwares introduce quantization uncertainties. Classical theory is accommodating for designing control systems that offer ‘robustness’ to such disorders as designs yield acceptable closed-loop performance using techniques to adjust gain and phase margins.

The passive Tuned Mass Damper (TMD) system displayed in Figure 2-14 is a good augmentation candidate for the classical design approach. The auxiliary mass is typically integrated into the structure at a location where the nodal acceleration and velocity are large. The generated inertial control forces and vibration energy dissipation is subsequently maximized. The generalized closed-loop damping augmentation block diagram shown in Figure 2-13 can be tailored for the TMD problem.

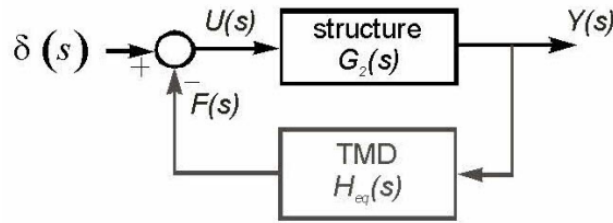


Figure 2-29 Tuned Mass Damper Control Block Diagram

Since the fundamental vibration mode is the primary mode of interest, placement is commonly near the top of the structure. Given that orthogonal translational modes can be decoupled, the transfer function along one vibration axis becomes:

$$G_2(s) = \frac{Y(s)}{U(s)} = \frac{1}{ms^2 + cs + k} = \frac{1}{(s + a_1)(s + a_2)} \quad (2.16)$$

Likewise, the transfer function along the passive mass damper feedback path becomes:

$$H_{eq}(s) = \frac{F(s)}{Y_d(s)} \cdot \frac{Y_d(s)}{Y(s)} = \frac{F(s)}{Y(s)} \quad (2.17)$$

The control variables of the main structure $(\ddot{y}(t), \dot{y}(t), y(t))$ become the excitation variables for the auxiliary mass system. In return, the generated inertial force of the auxiliary structure becomes the control force for the main structure in response to the original disturbance. The Laplace transfer function of the closed-loop system becomes

$$\frac{Y(s)}{D(s)} = \frac{G_2(s)}{1 + G_2(s) \cdot H_{eq}(s)} \quad (2.18)$$

The underlying strength in classical control is the ability to describe closed-loop properties of the system in terms of open-loop properties of its parts which are known or measurable. In particular, when using the root locus method, the poles of the closed loop transfer function are related to the poles and zeros of the open loop transfer function of the system components. The roots of the system characteristic equation are determined by the denominator of the closed-loop transfer function, and establish the behavior of the system transient response. For the TMD example, the transfer functions of Equations (2.16) and (2.17) can be substituted into the closed-loop function of Equation (2.18) yielding a characteristic equation that may look something like:

$$\frac{Y(s)}{D(s)} = \frac{\frac{1}{ms^2 + cs + k}}{1 + \frac{1}{ms^2 + cs + k} \cdot \frac{(m_d s^2 + c_d s + k_d) \cdot (ms^2 + (c + c_d)s + (k + k_d))}{(c_d s - k_d)}} \quad (2.19)$$

$$CE = (ms^2 + cs + k)(c_d s - k_d) + (m_d s^2 + c_d s + k_d) \cdot (ms^2 + (c + c_d)s + (k + k_d))$$

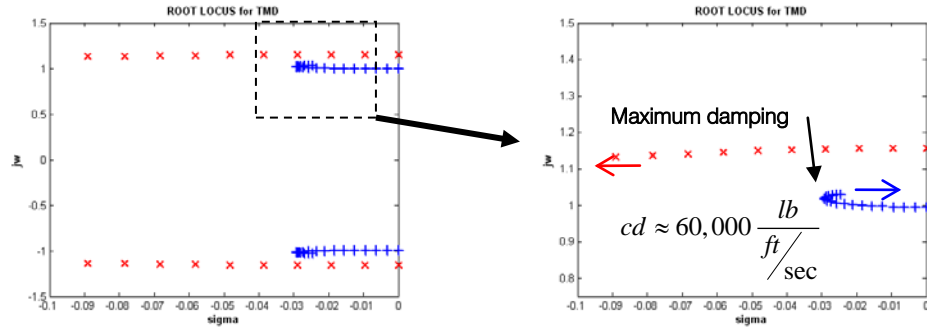
The composite roots of the characteristic equation become the poles of the augmented system. The dominant system poles can be re-located with the proper selection of m_d , c_d and k_d in order to generate a more desirable dynamic response. The natural frequency of the augmented system can be shifted and magnitudes of nodal

displacements, velocities, and accelerations of the structure can be reduced with proper placement. Pole re-location is constrained by the practicality of the auxiliary mass size and physical parameters of the spring and damper. There are a number of design techniques available to predict and adjust the system behavior. Both the root-locus and frequency response methods are viable design approaches for the TMD problem. The TMD sample design task of Section 2.2.3.2 can be used to demonstrate the root locus technique. Recall the design parameters...

Table 2-1 TMD Sample Design Parameters

Structural Mass	5000 tons
Fundamental Vibration Period	6 sec
Allowable Secondary Mass Fraction	2%

The secondary mass m_d , the secondary spring k_d , and the secondary viscous damper c_d are all parameters that must be designer selected. Experience has demonstrated that m_d is determined by economics and practicality, but is generally constrained by the maximum allowable limit of the structure... usually taken as (up to) 2% of the effective mass of the fundamental mode. k_d is chosen so that it, along with the selected secondary mass, sets the natural frequency of the augmentation subsystem to match that of the primary structure. Finally, c_d becomes the ‘control variable’ that is used to attain the specified damping response. m_d , k_d along with a range of c_d values can be substituted into the characteristic equation Equation (2.19). The roots once determined and plotted yield the locus of trajectories shown in Figure 2-30.



The root loci plots shown are for the sample TMD design problem. The plot on the left shows the 4 distinct loci. They exist as conjugate pairs designated by ‘+’ and ‘x’. The right plot is a magnified section of the left. The directions of the loci are shown. Note the ‘+’ pair turns and returns to the $j\omega$ axis as c_d varies. The maximum damping point is noted and identifies the optimal c_d for the given set of secondary system parameters.

Figure 2-30 TMD Root Locus Sample Design

Variations of pole placement techniques have been developed. Chang and Yu described an optimal pole placement technique where closed-loop poles were shifted into a prescribed region in the complex plane using minimum control force [52]. Control force is calculated using displacement and velocity feedback. Feedback gains are computed using the Kuhn-Tucker necessary conditions and four complex plane location constraints that define the desired pole placement space. The technique was applied to two structures, one modeled as a SDOF system, the other an eight DOF system each subjected to base acceleration excitation. In each case, the dominant building mode became the critical controlled mode.

Classical control theory has its limitations. It is difficult to apply in multiple-input/multiple-output (MIMO), or multi-loop systems. Control loops can be expected to interaction in a multivariable system and the coupling permeations can be difficult, if not impossible to investigate using classical approaches.

2.3.1.3 Modern Control

Modern controls design is a time-domain technique. A state-space model formulation of the system to be controlled is required. The state space model is a first-order vector differential equation of the form

$$\begin{aligned}\dot{\mathbf{x}} &= \mathbf{A} \times \mathbf{x} + \mathbf{B} \times \mathbf{u} \\ \mathbf{y}_{out} &= \mathbf{C} \times \mathbf{x} + \mathbf{D} \times \mathbf{u}\end{aligned}\tag{2.20}$$

where $\mathbf{x}(t)$ is a vector of control variables or system states, $\mathbf{u}(t)$ is a vector of control inputs, and $\mathbf{y}_{out}(t)$ is a vector of defined output states.

To achieve desirable closed-loop properties, state-variable feedback control of the form

$$\mathbf{u}_{feedback} = -\mathbf{H} \times \mathbf{x}$$

is often used, where the feedback gain \mathbf{H} is a matrix whose elements are generally time invariant control gains. The state-space model automatically handles MIMO configurations and multiple feedback states.

As with the classical design methods, modern control assumes linear time-invariant system behavior. The objective of modern control theory is to achieve some optimal system performance which meets specified performance criterion generally expressed as an integral performance index ' J '. J can take on many forms. For example, when quality of the transient response of the system is important, the tracking error can be used as the performance parameter,

$$J = \int_0^{\infty} e(t) dt$$

When J is minimized for the specified input, the system response is considered optimal.

If the controller is a regulator type, the performance index typically takes the form,

$$J = \int_0^{\infty} (\mathbf{x}^T \times \mathbf{Q} \times \mathbf{x} + \mathbf{u}^T \times \mathbf{R} \times \mathbf{u}) dt \quad (2.21)$$

This expression represents the most common form of the Linear Quadratic Regulator (LQR) [50,53]. Equation (2.21) represents a compromise between minimal state deviation and minimal energy criteria. For the controlled structure, this is interpreted as minimal displacements, velocities, and/or accelerations while consuming minimal control forces. The minimum is sought over all state trajectories. The optimal control law, $\mathbf{u}^*(\mathbf{t})$, is expressed as an explicit function of the state variables $\mathbf{x}(\mathbf{t})$. \mathbf{Q} and \mathbf{R} are weighting matrices that serve as design parameters.

The results of the second method of Liapunov (see Section 2.3.4.2) are utilized to derive a process for computing the optimal control $\mathbf{u}^*(\mathbf{t})$ [54]. For \mathbf{Q} and \mathbf{R} positive definite, the feedback gain solution that minimizes the performance index J is

$$\mathbf{H}_{LQR} = \mathbf{R}^{-1} \times \mathbf{B}^T \times \mathbf{P}$$

where \mathbf{P} is the Ricatti matrix obtained from the Algebraic Riccati Equation:

$$\mathbf{A}^T \times \mathbf{P} - \mathbf{P} \times \mathbf{B} \times \mathbf{Z}^{-1} \times \mathbf{B}^T \times \mathbf{P} + \mathbf{P} \times \mathbf{A} + \mathbf{Q} = \mathbf{0}$$

The analytical solution to the algebraic Riccati equation is difficult to obtain when the order of the system is large. Numerical solutions such as dynamic programming techniques can be used when analytical solutions do not exist. Once \mathbf{P} is determined, the optimal control law can be formed.

$$\mathbf{u}^*(\mathbf{t}) = -\mathbf{H}_{LQR} \times \mathbf{x}(\mathbf{t})$$

As long as the system of Equation (2.20) is controllable and \mathbf{Q} and \mathbf{R} are suitably chosen, the \mathbf{H}_{LQR} given by these equations guarantees the stability of the closed-loop system

$$\dot{\mathbf{x}} = (\mathbf{A} - \mathbf{B} \times \mathbf{H}_{LQR}) \times \mathbf{x} + \mathbf{B} \times \mathbf{u}$$

The LQR solution is a formal one that gives a unique solution to the feedback control problem once the design parameter \mathbf{Q} has been selected. It is widely used because it is not only explicitly clear, it is robust, and it drives state variables to specified values at specified times. It is optimized for stationary signals however and may not be the proper approach for seismic excitation. Note that \mathbf{H}_{LQR} is computed in terms of the open-loop quantities \mathbf{A} and \mathbf{B} . For the regulator problem, both modern and classical design approaches have this feature of determining closed-loop properties in terms of open-loop quantities in common. However, in modern control, all the entries of \mathbf{H}_{LQR} are determined at the same time by using the matrix design equations. This corresponds to closing all the feedback control loops simultaneously, which is in complete contrast to the one-loop-at-a-time procedure of classical controls design.

The LQR design has many variations, each offering an optimized solution for a tailored condition set. Yamada and Kobari^[55] introduce performance indices that account for short term excitation conditions, constrained control input, and for systems with variable elements. L.L. Chung discretizes the problem and presents an optimal control law based on predictive structural responses^[56].

LQR has some inherent robustness properties, but it requires knowledge of the full state vector \mathbf{x} . A related technique, LQG offers more rigorous treatments for uncertainties on closed-loop stability and for disturbance effects on closed-loop performance. Preumont presents an approach for formulating the LQG solution^[57]. Kim

and Park applies the LQG controller to lightly damped systems with natural frequency variations^[58]. Natural frequency uncertainties might arise during the development of the mass or stiffness matrices involving unusual or extensive approximations.

2.3.1.4 Robust Control

“Robust control refers to the control of unknown plants with unknown dynamics subjected to unknown disturbances” ^[59]. Every real world problem contains uncertainty. Its presence is unavoidable, but too often it is dismissed via simplifying assumptions. For certain control problems the unknowns or randomness cannot be assumed negligible. Its real presence is shown infiltrating the standard closed loop problem diagrammed in Figure 2-31 . In some cases, this uncertainty must be taken into account.

In the not too distant past, the uncertainty problem would have been addressed from a purely stochastic perspective. Radom variable distributions would have been formulated and expected values calculated. The field of Robust Control offers the controls engineer an alternate technique for adapting to the risks of uncertainty. Instead of designing system performance around expected values, uncertainty bounds are established for the unknowns.

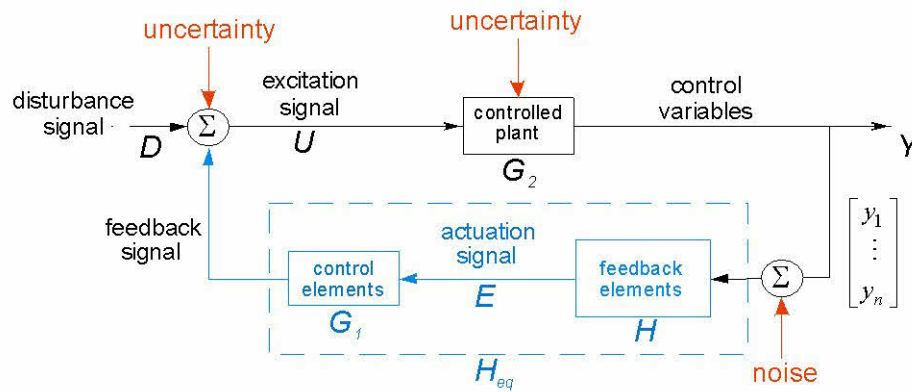


Figure 2-31 Standard Regulator Block Diagram

System design goals include stability and performance for all possible models described by a combination of nominal and uncertainty values. It can best be described as a worst case approach rather than a normalized design approach.

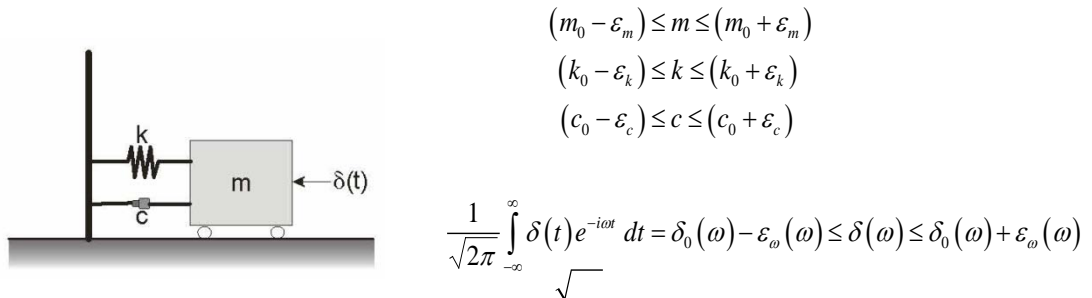


Figure 2-32 Modeling Structural and Disturbance Uncertainties

Consider the free body diagram of a simplified structure shown Figure 2-32. It identifies some fundamental uncertainties associated with that of the plant and its environment. Additional sources can easily be associated with sensor noise and actuator behavior.

Robust control strategies generally take the form of Hankel norms. Two fundamental forms are H_2 and H_∞ . H_2 control attempts to bound the power gain of the system while H_∞ attempts to bound the energy gain of the system. Investigating ‘gains in power’ or ‘gains in energy’ relate to behavior of the system near singularities in the transfer function^[60]. Optimal feedback is designed by formulating the appropriate cost index and then minimizing as was discussed for the LQR design.

J.N. Yang et al. applied H_2 -based control strategy to two benchmark flexible structures: a seismically excited cable-stayed bridge and a wind excited 76 story building ^[61]. Two control strategies were investigated. The first strategy was designed optimized for energy bounded excitations. The second was optimized for peak bounded excitations. In both cases, simulation results indicated that the H_2 design was viable for

civil structures. J.C. Wu et al. utilized an H_∞ control strategy for a simulated wind excited building using reduced ordered system models^[62]. The study focused on dynamic wind load behavior, a stationary random process. Simulation results showed that robust control strategies provided satisfactory results with reduced ordered systems, but sufficient modes were critical. S. Ankireddi and H.T.Y. Yang implemented an H_2 feedback controller centered around a variable parameter sampled data system^[63]. Controller performance was measured with and without time delays at multiple sample times. Sampled data was assumed corrupted by discrete time white noise. Three different building models excited by seismic activity and simulated wind gusts were investigated. Simulation results indicated that the H_2 control strategy driving an active mass damper demonstrated good potential for vibration control in civil applications.

2.3.2 Non-Linear Feedback Control

In general, non-linear systems are those whose behaviors do not follow the law of superposition. Nonlinearities can exist in the damping devices themselves or in the control laws that generate feedback forces for active and semi-active systems. Several damping mechanisms and devices have already been discussed that demonstrate nonlinear behavior: Coulomb devices are based upon frictional mechanisms; and Hysteretic devices are based upon non-elastic stress-strain regions of operation. Often times, these devices can be linearized within established conditions. However, Yamada/Kobori notes that: “the more practical the control system, the more its nonlinearity should be considered”^[64]. The low cost yet powerful digital computer has enabled new techniques for considering non-linearities.

Yamada gives examples of non-linear velocity feedback control laws^[65]. These laws compute feedback that follow the phase of the velocity state variable but whose gains are nonlinearly related. Examples given were:

- $u(y, \dot{y}) = -a|\dot{y}|^\alpha \operatorname{sgn}(\dot{y})$ $-1 \leq \alpha \leq 0$ The gain decreases as the velocity variable increases.
- $u(y, \dot{y}) = -\min(e|\dot{y}|, u_0) \operatorname{sgn}(\dot{y})$, $e > 0$ The gain is linearly related to the velocity variable but is constrained in magnitude by saturation.
- $u(y, \dot{y}) = -u_0 \operatorname{sgn}(\dot{y})$ The gain is full positive or negative depending on the phase of the velocity variable, often referred to as BANG-BANG control.

2.3.2.1 Fuzzy-Logic Control

Battaini et al. investigated the potential for fuzzy-logic based control strategies as an active structural control option^[66]. Fuzzy-logic, introduced by Zadeh^[67], is proposed to be able to handle imprecise or highly stochastic information as well as hysteretic structural behavior. The fuzzy logic strategy can best be described in the steps of the design procedure...

1. Pseudo-precise (precision limited with noise) variable measurements of the real system are mapped or ‘fuzzified’ into linguistic terms. This step is referred to as fuzzification.
2. The measured (fuzzified) state information is evaluated using knowledge-based rules that take the form of ‘IF-THEN’ evaluations.
3. The knowledge-based evaluations produce a reasoned solution.
4. The solution is ‘de-fuzzified’ into precise control inputs or actions for the controlled system.

Battaini coupled a fuzzy logic based algorithm with an active mass damper and applied the design to a three story structure. Two designs were analytically compared. The first design used only 3 and 5 membership functions for the input and output signals respectively. The second design used a 5 membership function input signal was also investigated. In either case, the membership function sets were relatively small. A knowledge based rule set was constructed using linear regression model that was a function of control input. The completed designs were evaluated using simulated earthquake excitation. Stable responses were obtained that reduced structural response behavior.

M. Aldawod et al. developed a fuzzy controller, coupled it with an active tuned mass damper and analytically applied the approach to a 76 storey structure^[68]. The fuzzy controller design consisted of a two-variable, seven membership-function input structure, an LQR associated knowledge base structure, and a center-of-gravity defuzzification scheme. The system was evaluated using a 24 degree-of-freedom structure model. Stiffness of the building was given a $\pm 15\%$ uncertainty. Furthermore, the fuzzy controller performance was compared to that of an LQR controller whose design details were not given. The fuzzy controller performed as well as the LQR design. In most cases it was more robust than the LQR design with regard to the uncertainty.

2.3.2.2 Neural Net Control

Neural network controllers have been investigated for application to structures with significant non-linear and poorly modeled dynamics. Neural networks mimic biological neural pathways using a matrix of connective pathways. Connective weights

are assigned to represent relative strengths of pathways between artificial neurons, or perceptrons. A general feedforward configuration is shown in Figure 2-33.

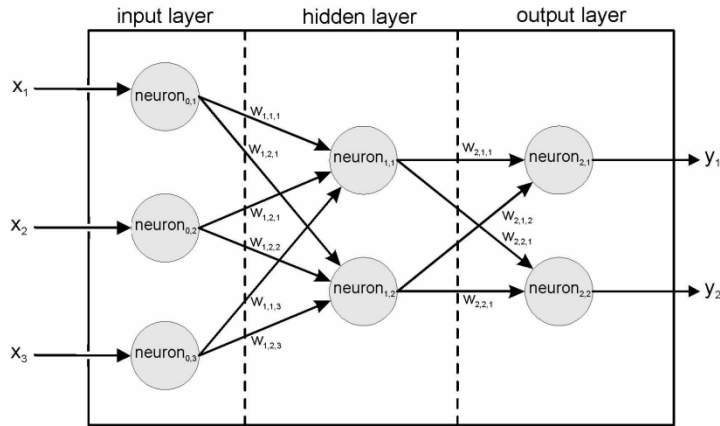


Figure 2-33 Simple Feedforward Neural Configuration

The network is characterized as an n dimensional input, an m dimensional output, with one or more hidden layers. The basic neuron function takes the form,

$$y_k = \varphi \left(\left(\sum_j w_{k,j} \cdot x_j \right) + b_k \right)$$

$\varphi(\cdot)$ represents a transfer function that can take a simple linear to a non-linear form.

Neuron gains are determined through supervised training typically via a back-propagation learning algorithm.

G.G. Yen developed the theoretic foundation of a distributed neural control system for flexible multi-bodied structures^[69] with highly non-linear dynamics. Yen was able to experimentally demonstrate the viability of such a control system on a two segmented body.

S.M. Yang et al, experimentally demonstrated the ability of a 3-layer artificial neural networks to perform system identification and vibration suppression on a modeled building structure^[70]. A 3-layer neural network controlling a hydraulically driven mass damper was investigated and demonstrated to effectively reduce vibrations

of the model. Peak-to-peak vibrations were shown to have been reduced by approximately 75%.

2.3.3 Distributed Control

Udawadia et al, investigated the methodology of using a distributed architecture to actively control large structures^[71]. In this study, multiple and independent controllable devices were distributed within a large structure. The specific active element was a bracing member that could generate a commanded force between its two connection points. This study demonstrated that global dynamic behavior of a large structure can be improved, and equally important, that the global stability can be ensured by using local control of the individual active elements. Axial force across the active member and relative velocity between its endpoints were selected as feedback states used in the control logic. This control configuration has always been attractive to the aerospace industry because of its fault tolerance features. Ensuring robust global behavior is difficult however because of potential unstable interaction, or beat modes between local controllers.

Equations of motion were developed showing complex dependencies of feedback gains. A MDOF model was developed to investigate interaction between active members. Global stability was shown to exist using eigenvalue analysis given local feedback gains remained in prescribed ranges. The MDOF model demonstrated that the proposed control scheme stiffened the structure and in general, resulted in an increased rate of energy dissipation using a given, simple set of connection criteria.

J.P. Lynch and K.H. Law developed and evaluated an extremely unique control concept that is modeled as a market place of buyers and sellers^[72]. Market-Based Control is a decentralized approach where localized controllers used to supply power

represent market sellers while control devices/actuators represent buyers. Rules observed in a free market scenario are used to construct local cost functions formulated as functions of power produced and a time-varying market price for that power. Sellers and buyers attempt to maximize profit and production respectively,

$$\begin{aligned} \text{seller} &\rightarrow \max J_{S_i}(P_{S_i}, p) \\ \text{buyer} &\rightarrow \max J_{B_i}(P_{B_i}, Y(t), p) \end{aligned}$$

Where, S_i and B_i represent the seller and buyer at the i^{th} locale respectively. P_{S_i} represents the seller produced power and p its current market price. The sellers cost function represents his profit at that price. P_{B_i} represents the buyers (local control device) sought power, $Y(t)$ is a function of the desired forced system response at the i^{th} subsystem. The buyers cost function is described as his utility (production) function which he is trying to maximize. The aggregate of all localized cost functions are constrained by the conservation of total energy in the system.

Lynch compared the Market Based Control approach with that of the LQR on both a five storey and a twenty storey structure using hydraulic damper devices as buyers. His simulation results indicated that the Market Based approach was as effective as a typical LQR design. The Market Based Control was used with a linearized system, but appeared to have utility for non-linear systems as well.

2.3.4 Stability

A poorly designed and/or implemented active controller that introduces energy into the system can actually exacerbate the vibration problem and at worst case, transform an otherwise stable, albeit under-damped system to an unstable system. The fundamental premise of a stable system can be summarized as:

$$\int_{-\infty}^t |g(t, \tau)| d\tau \leq \beta < \infty, \quad u(t) \leq \varepsilon < \infty, \quad -\infty < t < \infty$$

$$y(t) = \int_{-\infty}^t g(t, \tau) u(\tau) d\tau$$

Where $g(t, \tau)$ is the system response to an impulse at time τ , and β and ε are finite numbers [73]. In other words, bounded input must yield bounded output (BIBO) for all time. How is this stable performance assured, or tested for? The stable nature of each control design approach is typically based upon deep-rooted mathematical examination and established criterion. A multitude of textbooks and literature exists that investigate and establish criteria for different closed-loop control design approaches. It is extremely important to be able to establish stability for each and every motion control design for a civil structure. But an extensive treatise on stability is neither practical nor necessary in this discourse. However, a summary description relative to the control classifications introduced earlier is given below.

2.3.4.1 Stability in the Classical Design Case

As discussed in Section 2.3.1.2, classical control design is primarily accomplished in the frequency domain. The complex s -plane ($\sigma, j\omega$) is often used to graphically investigate system response. For a stable system, the criterion is straightforward. Roots of the system's characteristic equation: $CE = 1 + G(s)H_{eq}(s)$, must lie in the left half s -plane... $\sigma < 0$.

Nyquist stability criterion is an alternate approach based upon complex-variable theory[74]. This technique is likewise a graphical procedure, but results in a phase vs. magnitude polar plot of the system characteristic equation. Stability becomes a function of the phase-magnitude trajectory. The computer is now an efficient tool for the

generation of detailed Nyquist plots as they are cumbersome to generate manually. This technique not only offers stability assessments, but also provides insight into phase and gain margins.

Other techniques available for single-input-single-output (SISO) systems include the Routh-Hurwitz Test^[75] for continuous systems and the Jury Stability Test^[76] for discrete systems. Both tests provide the means to identify right half plane roots of a characteristic equation, but offer little in terms of the degree of stability or specific response dynamics.

2.3.4.2 Stability in the Modern Design Case

The fundamental premise of stability in the classical design case extends itself in the axiomatic sense to the modern control design approach. As with SISO systems, bounded-input/bounded output best describes the ultimate criterion for stability. Ensuring that all eigenvalues of a multivariable system are all located in the left half s -plane is a sufficient stability test and a necessary condition for stability for the linear system. Unfortunately, the graphical tool sets developed for the simpler classical problems are not as practical in the world of optimization.

Aleksandr Mikhailovich Lyapunov (aka Liapunov), was a late nineteenth century Russian mathematician known for his work in stability evaluation of differential equations. He subsequently contributed several analytical methods that found a major role in modern controls design stability evaluation. Liapunov's 'Second Method' of stability is a powerful, more generalized approach applicable to higher order systems that may either be forced or unforced, linear or non-linear, or, deterministic or stochastic^[77]. An attractive feature of the method is that the solution of the system differential equation is not required. However, it does require the

identification of a scalar function $V(\mathbf{x})$ that, as implied, is a function of the system state variables \mathbf{x} . If properly selected, the function can be used to indicate stability of the system. $V(\mathbf{x})$ often takes the form of an expression of system energy, the sum of kinetic and potential energies for example. For a given energy expression, the rate of change of this energy along any phase plane trajectory can be found by differentiating $V(\mathbf{x})$. For a multivariable system,

$$\frac{dV(\mathbf{x})}{dt} = \dot{V}(\mathbf{x}) = \sum_{i=1}^n \frac{\partial V(\mathbf{x})}{\partial x_i} \frac{dx_i}{dt} = [\text{gradient } V(\mathbf{x})]^T \dot{\mathbf{x}}$$

Liapunov offers two sets of criterion, one for asymptotical stability in the vicinity of an equilibrium point; the second for global asymptotic stability. His 2nd Theorem states that for global asymptotic stability,

- $V(\mathbf{x})$ is continuous and has continuous first partial derivatives in the entire state space
- $V(\mathbf{x}) > 0$ for $\mathbf{x} \neq \mathbf{0}$
- $V(\mathbf{0}) = 0$
- $V(\mathbf{x}) \rightarrow \infty$ as $\|\mathbf{x}\| \rightarrow \infty$
- $\dot{V}(\mathbf{x}) \leq 0$
- Either $\dot{V}(\mathbf{x}) \neq 0$ except at $\mathbf{x} = \mathbf{0}$ or any locus in the state space where $\dot{V}(\mathbf{x}) = 0$ is not a trajectory of the system.

The Liapunov 2nd Method is powerful. A valid Liapunov function $V(\mathbf{x})$ is sufficient to indicate stability, however any particular Liapunov function is not unique. The failure of a proposed function to meet stability criteria does not mean that a valid function does not exist. The Liapunov function has been proven to be valuable to stability assessment of modern control designs. Mathematicians and controls engineers have determined how to incorporate its structure directly into the solution logic of optimal control problems.

Optimal control is based upon minimizing or maximizing an identified performance index. The Linear Quadratic Regulator performance index was shown in Section 2.3.1.3 to be

$$J = \int_0^{\infty} (\mathbf{x}^T \times \mathbf{Q} \times \mathbf{x} + \mathbf{u}^T \times \mathbf{R} \times \mathbf{u}) dt \quad (2.22)$$

The index itself is treated as a Liapunov function $V(\mathbf{x})$ in the derivation of the optimal control input, \mathbf{u} . The time derivative of the index is used to identify constraints established by Liapunov's 2nd Theorem. When folded back into J , the Algebraic Riccati Equation can be formulated and solved.

The significance of this approach is two-fold. The control input is optimized for the given criterion. Equally importantly, the system response is guaranteed stable.

2.3.4.3 Stability in the Non-Linear Design Case

Stability assessment of non-linear systems is a less 'formalized' since the notion of pole location does not apply. Neither Fuzzy Logic nor Neural Network control configurations can be distilled down to crisp mathematical models that can be used to check for stability. There is in fact, no generally accepted solution for such controllers [78]. Evaluating state trajectory behavior in the phase plane is a graphical method that can be used to demonstrate stability[79]. As with linear systems, bounded-output given bounded-input is again the evaluation criterion. Trajectories are examined to see if they tend to equilibrium points. Stable nodes, unstable nodes, and limit cycles or oscillatory behavior can often be determined in the phase plane. Care must be taken because stability in the local sense is not sufficient to establish stability in the global sense.

2.4 Modal Control and Inter-Modal Energy Transfer

Wang and Huang investigated an active technique based upon independent modal space control (IMSC)^[80]. A flexible cantilever structure was discretized. Vibration modes were estimated and assumed observable and able to be de-coupled. Modes were treated as independently controllable. Observation and control spillover was addressed. Discrete-time variable structure control was adapted. The IMSC approach was found to successfully attenuate vibration and be almost insensitive to parametric uncertainties and external disturbances.

Review of current literature revealed little research dealing with modal energy transfer intended for structural dynamics control. P. Molatkar and A. Nayfeh^[81] documented the results of their experimental and theoretical study investigating natural, unforced energy transfer from the third mode to the fundamental vibration mode of a simple cantilever structure. Continuous systems as simple as the cantilever exhibit non-linear behavior often overlooked in linear models. These non-linearities are believed to form coupling mechanisms that bridge linear uncoupled vibration modes leading to modal interactions that result in unsuspecting energy transfer.

Molatkar suggested that non-linear coupling mechanisms fall into two categories, resonant and non-resonant. A parametric combination resonant mechanism was described as a coupling when linear natural frequencies of the modes are commensurate, that is there exist nonzero integers k_i such that $k_1\omega_1 + \dots + k_n\omega_n = 0$. This particular study examined non-resonant mechanisms where the main requirement is that the modes be widely spaced, $\omega_i \gg \omega_j$. Interaction is believed to occur through asymmetric sidebands around the high-frequency component in the response spectrum.

A vertically mounted, slender cantilever beam was clamped to a shaker to investigate the energy transfer phenomenon. Excitation frequency was swept downward from above the third modal frequency. As the forcing frequency approached and excited the third mode, a growing component of the fundamental mode was observed. The effect can be likened to sideband generation during amplitude modulation. Sideband spacing is referred to as the Hopf bifurcation frequency.

Molatkrare found that it was evident that “energy transfer from low-amplitude, high frequency excitation to a high-amplitude, low-frequency response can occur in a structure irrespective of its stiffness, configuration, and inherent non-linearities” given much lower natural mode frequencies than the mode being excited. However, he could find no evidence or documented results of structurally inherent mechanisms facilitating energy transfer from low to high frequency modes.

Also noted, was that this phenomenon may be a concern to space based structures that tend to have many modes with low natural frequencies.

L. Caracoglia and N. Jones conducted an evaluation of a loose chain impact damper fastened inside an aluminum luminaire pole for the Illinois Department of Transportation. An unexpected perceived advantage was noted in addition to the assessment of impact damper performance. Nonlinear behavior of the chain damper resulted in energy transfer from the fundamental mode to higher order modes^[82]. In fact, this is not totally unexpected. The momentum transfer caused by the impact is analogous to an impulse function acting upon the pole. Controls engineers learn early in their education, that a linear system subjected to an impulse function results in the excitation of all natural or characteristic responses. In the case of the pole, an impulse excitation would theoretically result in a response composed of the fundamental mode and all higher order modes. Resulting amplitudes of the discrete modes would be

dependent on the physical nature/design of the pole itself and the placement of the excitation.

CHAPTER III

MODAL DAMPING... AN ALTERNATIVE CONTROL STRATEGY

This chapter discusses the theoretical framework leading to the conceptual simulation and concept demonstration of the Modal Damping concept. The literature research findings that initially motivated the approach are introduced. Modal analysis and characterization, modal energy distribution, modal excitation, and mode shape conversion with regard to the subject structures are discussed. The strategic elements and the selected implementation of Modal Damping are described.

3.1 Modal Damping Basis

Chapter II of this document reviews a variety of structural damping control strategies that range from simple passive to complex active augmentations. The findings suggest that the geometry of the light, slender and simple structure severely limits the number of practical damping augmentation options. The optimal augmentation system should not be overly complicated, require significant specialized maintenance, or impose significant costs. One of the few simple approaches currently implemented to help dampen vibrations of the luminaire support, and similar type structures, is the impact damper. The impact damper discussed in Section 2.2.3.4 is a passive mass that is hung down the center of the pole. The impact damper has been shown to provide measureable damping improvements. Its robustness is somewhat limited however, particularly in the face of severe vibration magnitudes. Although an improvement over

the non-augmented behavior, the need for alternate options and improvements still exists.

When warranted, more aggressive approaches using technologies described in Chapter II can be utilized; however they come with associated complexities and costs. This effort investigated a different, yet relatively simple damping enhancement strategy that may offer an alternative option for this select group of structures. Modal Damping attempts to exploit a flexible structure's own variable impedance to its natural vibration modes. A valuable feature of this approach is its non-reliance on external control energy and will be discussed and demonstrated. The structural type that might best lend itself to a Modal Damping approach can be summarized as follows:

- The height-to-width ratios for the structures of interest are assumed large. The baseline aluminum cantilever pole used in this study for example, has a height-to-width ratio that approached 70. The stress versus strain relationship was assumed to remain elastic. Elastic deformations are consequentially of the flexural type. Shear deformations are assumed negligible.
- The structure geometries are relatively simple. The structures are flexible.
- Most of the external excitation energy couples into the fundamental mode.
- Within the limitations of the noted assumptions, the physical properties were assumed time invariant. Inherent damping properties are small.
- The structure topology investigated was constrained to be terrestrial in nature. The topology was assumed to have a moment resisting connection at its base, and was un-supported at its opposite end which was free to translate and rotate. An alternate topology, also a long flexible structure, is fully un-supported. The FREE-FREE end topology is one that describes a space-based structure. The initial design of the International Space Station is an example of a structure with unsupported ends ^[83].

Its structural configuration was initially proposed to be formed around a 300 foot longitudinal truss which acted as the main structural spar as drawn in Figure 3-1. It is reasonable to assume that the modal vibration analysis performed herein and the damping control design can be applied to terrestrial, space-based and other light and flexible structural topologies of interest.

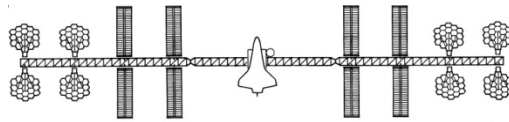


Figure 3-1 Space-Based Flexible Topology

3.1.1 Motivation and Objective

The Modal Damping augmentation approach was conceived during the literature investigation that was initially tailored to study general structural damping. The findings indicated that inherent structural damping mechanisms tend to become more efficient at higher order modes. The targeted inherent damping mechanisms of interest included frictional, environmental, and material. Frictional damping occurs within joints and cracks found in the structure. Even the simple cantilever pole experiences frictional damping at its interface with the transformer/break away base. Environmental energy dissipation occurs due to aerodynamic drag and interactions at the soil interface. Material damping is generally associated with recoverable, small strain deformations. Each of these mechanisms was believed to offer additional damping potential to capitalize upon, and be brought to bear on the structural settling problem. Evidence was found throughout the early investigation to support this premise:

- Measured data of actual damping exhibited by real structures was collected and compiled by Satake ^[17] (see Figures 2-4 and 2-5) and clearly indicated greater damping ratios naturally occur with higher order modes.
- Rheological models developed to capture anelastic stress-strain relationships indicate visco-elastic behavior, e.g. N.E. Dowling's rheological model schematically shown in Figure 2-6. Figure 3-2 illustrates the general model's normalized magnitude/phase/frequency (Bode plot) dependence of the impedance modulus.

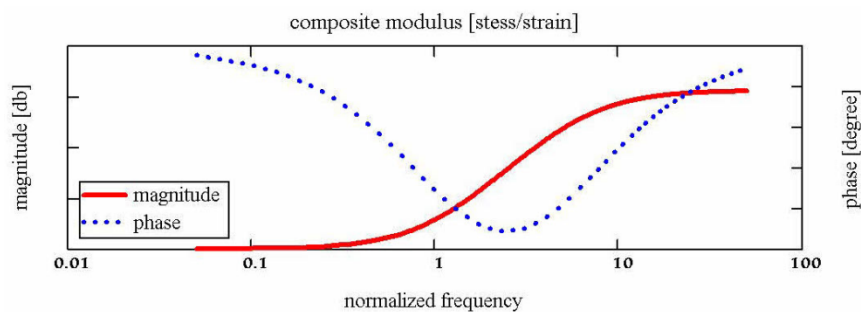


Figure 3-2 Typical Vibration Impedance Modulus for the Anelastic Rheological Model

- Two linear predictive mathematical models were prevalent in the literature that attempted to express structural damping behavior in terms of a simple relationship between the distinct modal parameters: the Rayleigh and the Kareem models. Both predictive models suggest the same modal behavior as that of Dowling's rheological model.

3.1.1.1 Rayleigh Predictive Model

The Rayleigh, or Proportional Damping model asserts that modal damping properties are proportional to the mass and stiffness associated with that particular mode. For a multi-degree-of-freedom linear system model, the Rayleigh damping model takes the generalized form

$$\mathbf{C} = \mathbf{C}_M + \mathbf{C}_K = \alpha_m \mathbf{M} + \alpha_k \mathbf{K} \quad (3.1)$$

For highly flexible structures such as the cantilever, where translational modes dominate, the mass matrix is diagonal while the stiffness matrix and the damping matrix are likewise symmetric and generally highly populated. The matrices can be diagonalized (de-coupled) using the systems modal matrix (discussed in more detail in Section 3.1.3 and expressed in Equation (3.20)). This leads to decoupled damping coefficient expressions for the n modes that will be shown to be analytically useful. The i^{th} decoupled damping coefficient becomes...

$$c_i = \alpha_m m_i + \alpha_k k_i$$

Since $\omega_i = \sqrt{\frac{k_i}{m_i}}$, the damping ratio for each mode can be expressed as,

$$\zeta_i = \frac{c_i}{2\sqrt{m_i \cdot k_i}} = \frac{\alpha_0}{2\omega_i} + \frac{\alpha_1 \cdot \omega_i}{2} \quad (3.2)$$

Equation (3.2) contains two unknowns, α_0 and α_1 , that can be derived for the system if the damping behavior of two modes are known or can be reasonably estimated. Charney ^[84] developed a 5 degree-of-freedom model for a five story framed building to investigate the viability of using the Rayleigh model to predict elastic damping. The damping curves shown in Figure 3-3 are similar to those of Charney's model, but were developed using the measured data from the Anelastic Damping Parameter Assessment Experiment described in Section 5.1. Although the curves are continuous functions of frequency, the predictions are only valid for the modal frequencies.

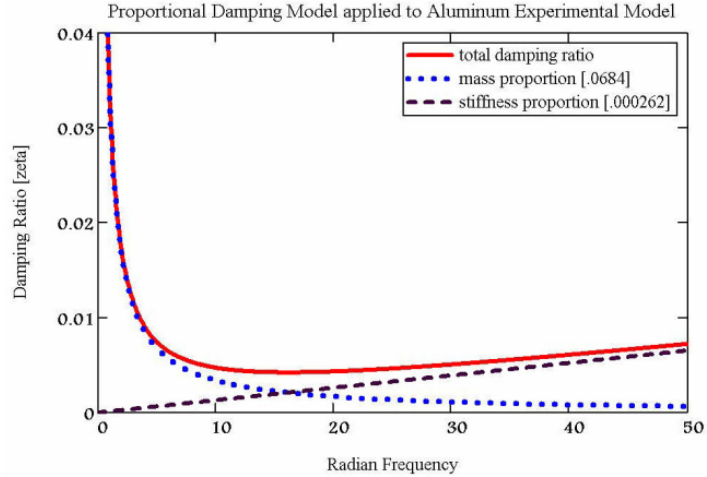


Figure 3-3 Sample Proportional Damping Curves

Charney’s model, like that of Figure 3-3, illustrates the direct relationship between damping ratio and vibration frequency. The model predicts increased damping ratio with increased vibration frequency. He noted that the Rayleigh model has the potential to introduce artificial damping if the structures response includes measurable non-linear components such as yielding. Yielding was not a consideration for the tall flexible structures of interest. Charney did investigate the consequences of using the Rayleigh model under such conditions with suggestions to mitigate or control errors.

3.1.1.2 Kareem Predictive Model

Kareem ^[85] suggests that the relationship of damping ratios among vibration modes can be modeled as follows:

$$\frac{\zeta_n}{\zeta_1} = 1 + C \cdot \left(\frac{f_n}{f_1} - 1 \right) \quad (3.3)$$

Kareem’s model was developed to predict damping characteristics for tall under-damped steel structures, and like the Rayleigh model, predicts ‘progressively higher damping ratios for progressively higher modes’. The coefficient ‘C’ is a constant that

must be determined empirically. Kareem determined that a value of $C = 0.38$ adequately represents the behavior of tall steel structures.

3.1.1.3 Modal Energy Environmental Coupling

Y. L. Xu, offered an additional motivating argument for the proposed Modal Damping approach [86]. Xu performed a parametric study of active mass dampers to evaluate their effectiveness to reduce wind excited motion of tall buildings. Xu's findings assert that the majority of dynamic vibration energy was found in the fundamental mode; the wind-induced response of tall buildings is primarily attributed to the two orthogonal fundamental sway modes and sometimes the fundamental torsional mode of vibration. The results of the dynamic modeling and evaluation of the aluminum luminaire cantilever is discussed in Section 4.3 of this document and were found to corroborates Xu's premise. As will be discussed... Modal Damping was specifically designed to capitalize upon this condition of abundant fundamental mode vibration energy.

3.1.1.4 Modal Damping Objectives

Intuitively then... if dynamic energy from lower vibration modes (where most of the energy is found to reside for tall cantilever type configurations) could be transferred to higher modes (that have been characterized as demonstrating higher vibrational impedance) increased natural damping due to inherent structure mechanisms could be achieved improving mitigation of the vibration energy. Consequently, a unique, semi-active feedback control scheme was developed and is presented herein as a candidate approach to enhance the damping performance of

tall/long flexible structures. Specifically, the technical objectives of this research were established as:

1. TRANSFER FUNDAMENTAL MODE DYNAMIC ENERGY TO THE 2ND VIBRATION MODE TO INCREASE THE OVERALL EFFECTIVE SYSTEM DAMPING (INTER-MODAL ENERGY TRANSFER).
2. HARVEST AND CONVERT THE KINETIC ENERGY OF THE VIBRATING STRUCTURE ITSELF TO SELF GENERATE THE NECESSARY CONTROL FORCES THAT ACTUATE INTER-MODAL ENERGY TRANSFER (SELF-POWERED).

These two elements, taken together define Modal Damping.

The review of documented research revealed no specific effort involving modal energy transfer for the purpose of structural vibration control. Modal energy exchange was investigated by P. Malatakar and A. Nayfeh ^[87]. However they experimentally determined that there is a natural tendency for energy to migrate or drift from higher order modes to lower order vibration modes. There was no evidence given that indicated that vibration energy flowed naturally from lower modes to higher order modes.

3.1.2 Mode Shape Fundamentals

The proposed damping control approach required specific knowledge of the structure's vibration behavior. Modal frequencies and spatial mode shape functions of the fundamental mode and higher order modes of interest needed to be formulated. An exact closed-form mathematical expression of mode shape characteristics is nearly impossible to analytically develop for all except the simplest of structures. Consider the simple cantilever structure diagrammed in Figure 3-4.

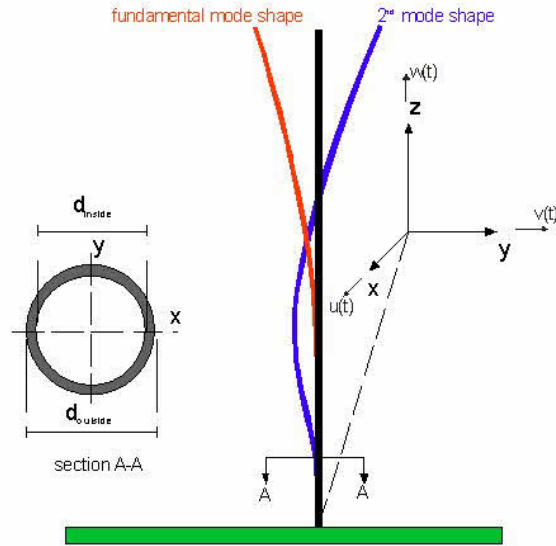


Figure 3-4 Cantilever Vibration Mode Shapes 1&2

A homogeneous and uniform cross-section was assumed. Its boundary conditions have been well defined. Given these (over)simplified constraints the vibration modes can be analytically predicted by using an Euler-Bernoulli beam model (appropriated for tall slender structures). Modal analysis begins by examining a small differential slice of the structural section located at some distance ‘z’ along its length as depicted in the schematics of Figure 3-5. Equilibrium equations for the differential slice lead to the following un-forced governing differential equation,

$$\frac{E \cdot I}{\rho \cdot A} \frac{\partial^4 v(z,t)}{\partial z^4} + \frac{\partial^2 v(z,t)}{\partial z^2} = 0 \quad (3.4)$$

where, E , I , ρ , A are sectional and material parameters, and $v(z,t)$ is the time varying displacement function.

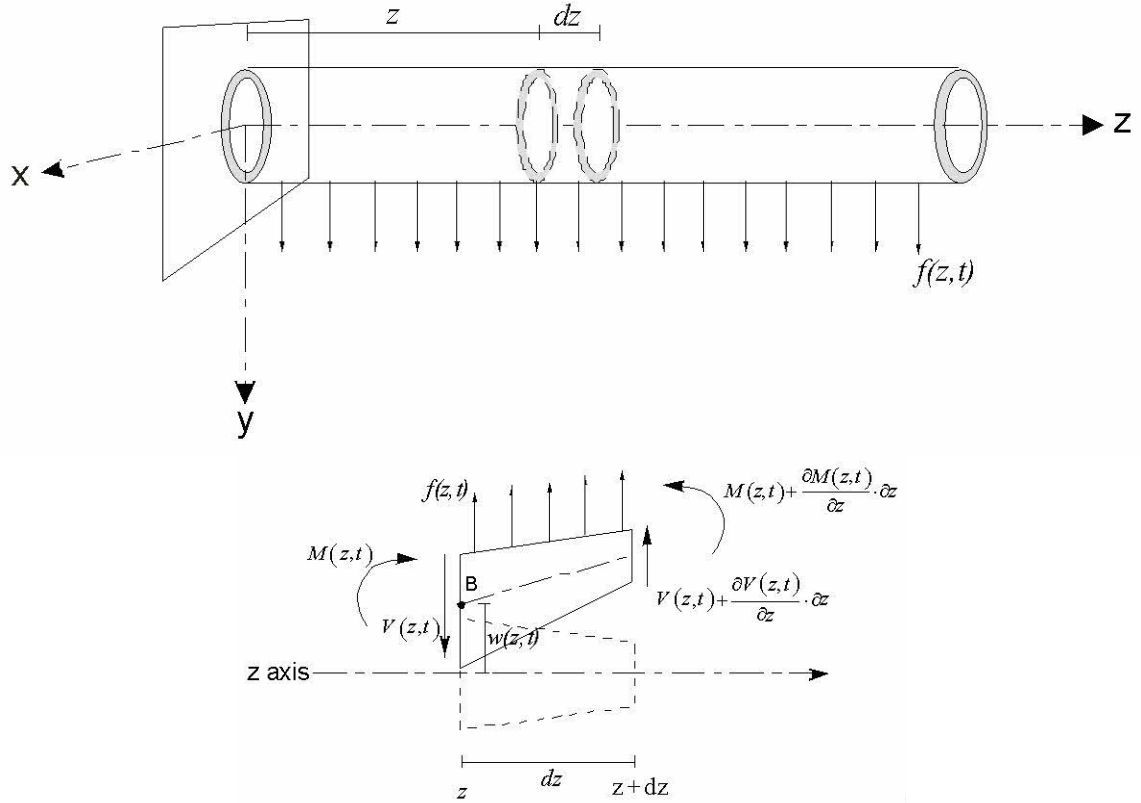


Figure 3-5 Free Body Diagram for the Simplified Vibrating Cantilever

Given that the sectional and material parameters are constant, a multivariable solution composed of a temporal and spatial component of the form $v(z,t) = Z(z)T(t)$ can be found [88]. In fact, the solution is composed of an infinite number of components,

$$v(z,t) = \sum_{i=1}^{\infty} [Z_i'(z) T_i'(t)], \text{ where}$$

$$\begin{aligned} T_i'(t) &= \alpha_i \cdot \sin(\omega_i t) + \beta_i \cdot \cos(\omega_i t) = \sqrt{\alpha_i^2 + \beta_i^2} \sin(\omega_i t - \phi) \\ &= \sqrt{\alpha_i^2 + \beta_i^2} T_i(t) \end{aligned} \quad (3.5)$$

$$\begin{aligned} Z_i'(z) &= a_i \left\{ \frac{\cosh(\beta_i \cdot L) + \cos(\beta_i \cdot L)}{\sinh(\beta_i \cdot L) + \sin(\beta_i \cdot L)} \cdot [\sin(\beta_i \cdot z) - \sinh(\beta_i \cdot z)] + \cosh(\beta_i \cdot z) - \cos(\beta_i \cdot z) \right\} \\ &= a_i Z_i \end{aligned} \quad (3.6)$$

$$\beta_i = \sqrt[4]{\omega_i^2 \cdot \frac{\rho \cdot A}{E \cdot I}}$$

The scalar coefficients from both the temporal and spatial components could be combined to yield one scalar or amplitude coefficient, $v_i = a_i \sqrt{\alpha_i^2 + \beta_i^2}$ so that

$$v(z, t) = \sum_{i=1}^{\infty} [v_i Z_i(z) T_i(t)].$$

If now, any of the assumed sectional or material parameters of Equation (3.4) are not constant, that is the structure has non-uniform cross-sections and/or mass distributions, the solution becomes significantly more difficult and likely impossible to derive in closed form. Of course the uniformity assumption for real-world structures is almost always inaccurate. Even the simple aluminum luminaire pole used as the baseline structure for Modal Damping development had variable cross-sectional geometry. Fortunately, mathematicians are able to offer alternate techniques. Linear Modal Analysis (LMA) is a powerful tool given such cases. LMA offers a straightforward approach to modeling the baseline system for dynamic simulation and mathematically predicting the structures modal properties.

3.1.3 Linear Modal Analysis (LMA)

Understanding a given structures modal properties is key to predicting expected vibration properties. LMA offers a methodical approach to determining modal properties. It is often times referred to as eigenvalue/eigenvector analysis. For equation sets representing the dynamic behavior of mechanical systems, the eigenvalues, or singularities, represent the system's modal frequencies, and eigenvectors its vibration mode shapes. LMA requires that the continuous system be discretized or modeled as having a finite number degrees-of-freedom. In general, vibrations for the structures of interest can be decoupled into two orthogonal transverse vibration components and one torsional vibration component. For convenience or simplicity, the modal components

are often evaluated separately and the component solutions superimposed to construct the net structural response. The inherent power of LMA allows for the composite solution to be developed simultaneously whether the modes are independent or coupled. The nodes represented lumped masses at designated spatial coordinates.

A single planar transverse mode (the y-z plane, refer to Figure 3-4) was selected for the analysis and development of the proposed Modal Damping control. Torsional vibrations modes were not expected given the external disturbances and the fact that the structure's cross-section was basically symmetric about its center of gravity. Modal decomposition of the transverse vibrational component began with the n nodal equilibrium equations expressed in matrix form:

$$\mathbf{M} \times \ddot{\mathbf{y}}(\mathbf{t}) + \mathbf{C} \times \dot{\mathbf{y}}(\mathbf{t}) + \mathbf{K} \times \mathbf{y}(\mathbf{t}) = \mathbf{f}(t) \quad (3.7)$$

The solution can proceed in a variety of ways. Casting the problem as a symmetric eigenvalue problem had several advantages of which real-valued, orthogonal eigenvalue and eigenvector were strategic [89]. Given the cantilever structure and its single transverse mode, the resulting mass matrix \mathbf{M} , the damping matrix \mathbf{C} , and the stiffness matrix \mathbf{K} were symmetric. It will be shown to be advantageous to retain symmetric properties as the analysis develops. However simple transformations can destroy symmetry, e.g. $\mathbf{M}^{-1} \times \mathbf{K}$ is not necessarily symmetric although each individual matrix is symmetric. With foresight of forthcoming transformations, symmetry can be retained when the following variable substitution is made,

$$\mathbf{y} = \mathbf{M}^{\frac{1}{2}} \times \tilde{\mathbf{y}}$$

Both variables \mathbf{y} and $\tilde{\mathbf{y}}$ are functions of time, but their dependency will be implied and not explicitly shown henceforth for simplicity. Substituting for \mathbf{y} and pre-multiplied by $\mathbf{M}^{-\frac{1}{2}}$ yields

$$\mathbf{M}^{-\frac{1}{2}} \times \mathbf{M} \times \mathbf{M}^{-\frac{1}{2}} \times \ddot{\tilde{\mathbf{y}}} + \mathbf{M}^{-\frac{1}{2}} \times \mathbf{C} \times \mathbf{M}^{-\frac{1}{2}} \times \dot{\tilde{\mathbf{y}}} + \mathbf{M}^{-\frac{1}{2}} \times \mathbf{K} \times \mathbf{M}^{-\frac{1}{2}} \times \tilde{\mathbf{y}} = \mathbf{M}^{-\frac{1}{2}} \times \mathbf{f}$$

Simplifying,

$$\ddot{\tilde{\mathbf{y}}} + \tilde{\mathbf{C}} \dot{\tilde{\mathbf{y}}} + \tilde{\mathbf{K}} \tilde{\mathbf{y}} = \tilde{\mathbf{f}} \quad (3.8)$$

where the resulting mass normalized matrices and vectors become

$$\begin{aligned} \tilde{\mathbf{K}} &= \mathbf{M}^{-\frac{1}{2}} \times \mathbf{K} \times \mathbf{M}^{-\frac{1}{2}} \\ \tilde{\mathbf{C}} &= \mathbf{M}^{-\frac{1}{2}} \times \mathbf{C} \times \mathbf{M}^{-\frac{1}{2}} \\ \tilde{\mathbf{f}} &= \mathbf{M}^{-\frac{1}{2}} \times \mathbf{f} \end{aligned}$$

ensure a symmetric geometry.

Modal analysis unveils the characteristic, or homogeneous, response behavior of the system. The characteristic response is independent of any possible forcing function that the system might be subjected. The analysis is straightforward and lends itself to various approaches. Two common techniques are: 1.) state-space analysis, and 2.) ODE decomposition. Determining the systems modal frequencies and mode shapes is the objective for each approach.

3.1.3.1 Modal Decomposition: State-Space Model

Equation (3.8) represents a set of n coupled 2nd order differential equations. Variable substitution converts this set of n 2nd order equations to $2n$ 1st order equations. The conversion takes advantage of the mathematical elegance associated with linear state-space analysis by letting

$$\mathbf{x} = \begin{bmatrix} \mathbf{x}_1 \\ \mathbf{x}_2 \end{bmatrix} = \begin{bmatrix} \tilde{\mathbf{y}} \\ \dot{\tilde{\mathbf{y}}} \end{bmatrix}, \quad \tilde{\mathbf{y}} = \begin{bmatrix} \tilde{y}_1 \\ \tilde{y}_2 \\ \vdots \\ \tilde{y}_n \end{bmatrix}, \quad \mathbf{x}_2 = \dot{\mathbf{x}}_1 \quad (3.9)$$

Rearranging Equation (3.8) and substituting yields,

$$\ddot{\tilde{\mathbf{y}}} = -(\tilde{\mathbf{C}} \dot{\tilde{\mathbf{y}}} + \tilde{\mathbf{K}} \tilde{\mathbf{y}}) \Rightarrow \dot{\mathbf{x}}_2 = -(\tilde{\mathbf{C}} \mathbf{x}_2 + \tilde{\mathbf{K}} \mathbf{x}_1) \quad (3.10)$$

Equations (3.9) and (3.10) form a set of $2n$ coupled 1st order differential equations,

$$\begin{aligned} \dot{\mathbf{x}}_1 &= \mathbf{x}_2 \\ \dot{\mathbf{x}}_2 &= -(\tilde{\mathbf{C}} \mathbf{x}_2 + \tilde{\mathbf{K}} \mathbf{x}_1) \end{aligned}$$

which can be further re-arranged and simplified in matrix form as,

$$\dot{\mathbf{x}} = \mathbf{A} \mathbf{x}, \quad \mathbf{A} = \begin{bmatrix} \mathbf{0} & \mathbf{I} \\ -\tilde{\mathbf{K}} & -\tilde{\mathbf{C}} \end{bmatrix} \quad (3.11)$$

Equation (3.11) forms the model for a state-space representation and analysis.

$\tilde{\mathbf{K}}$ and $\tilde{\mathbf{C}}$ are each $n \times n$ matrices and that \mathbf{I} is an $n \times n$ identity matrix. $\tilde{\mathbf{K}}$ and $\tilde{\mathbf{C}}$ are sub-matrices of the time-invariant coefficient matrix \mathbf{A} whose dimension is $2n \times 2n$.

\mathbf{x} and $\dot{\mathbf{x}}$ of Equation (3.11) are $2n \times 1$ column vectors. A solution for this set of coupled equations exists when \mathbf{x} and $\dot{\mathbf{x}}$ have the same direction in their state-space but differ only in magnitude by some proportionality factor $\dot{\mathbf{x}} = \Omega \mathbf{x}$ ^[90], yielding:

$$\Omega \mathbf{x} = \mathbf{A} \mathbf{x} \Rightarrow (\Omega \mathbf{I} - \mathbf{A}) \mathbf{x} = \mathbf{0} \quad (3.12)$$

Equation (3.12) is the classical statement of the algebraic eigenvalue problem and is used to determine both eigenvalues and eigenvectors. The solution is non-trivial when $\mathbf{x} \neq \mathbf{0}$, and can be found by letting

$$|\Omega \mathbf{I} - \mathbf{A}| = 0 \quad (3.13)$$

The determinant results in a $2n^{\text{th}}$ order polynomial representing the characteristic equation of the system. Equation (3.11) clearly shows that \mathbf{A} is not symmetric. Consequently, its roots will be complex. But since this model represents a real world mechanical system, the coefficients of the characteristic equation will be real, and its roots will exist as complex conjugate pairs. The $2n$ roots $\Omega_1 \cdots \Omega_{2n}$ conveniently combine to represent n modes of the structure. The imaginary component of the conjugate pairs identifies the harmonic property of the mode, while the real component reveals the inherent damping behavior of that same mode. The factored form of the characteristic equation takes the form:

$$|\Omega \mathbf{I} - \mathbf{A}| = (\Omega + (\sigma_1 + j\varpi_1))(\Omega + (\sigma_1 - j\varpi_1)) \cdots (\Omega + (\sigma_n + j\varpi_n))(\Omega + (\sigma_n - j\varpi_n)) = 0 \quad (3.14)$$

3.1.3.2 Modal Decomposition: Un-damped Ordinary Differential Equations (ODE)

Working directly with the ODE is often the preferred analytical approach when simplifying assumptions are made. Again, the eigenvalue analysis begins with the set of differential equation set given in Equation (3.8). When the damping components of the equations are ignored, a purely un-damped harmonic response is assumed. The assumption is reasonable because in this case, the system is severely underdamped and the small damping parameters can be argued as having nearly negligible effect on the eigenvalues location in the complex plane. This assumption yields,

$$\ddot{\tilde{\mathbf{y}}} + \tilde{\mathbf{K}} \times \tilde{\mathbf{y}} = \mathbf{0} \quad (3.15)$$

The solutions to 2^{nd} order equations of this form are well understood; since the elements of $\tilde{\mathbf{K}}$ are real, the equation set yields a generalized response of the form,

$$\tilde{\mathbf{y}} = \begin{bmatrix} v_1 e^{ot} & v_2 e^{ot} & \cdots & v_n e^{ot} \end{bmatrix}^T$$

Substituting the generalized solution into Equation (3.15) and rearranging yields,

$$\begin{aligned} (\lambda \mathbf{I} - \tilde{\mathbf{K}}) \times \tilde{\mathbf{v}} &= \mathbf{0} \\ \tilde{\mathbf{v}} &= [v_1 \quad \cdots \quad v_n]^T, \quad \lambda = \omega^2 \end{aligned} \quad (3.16)$$

For a non-trivial solution, $\mathbf{v} \neq \mathbf{0}$, so that

$$|\lambda \mathbf{I} - \tilde{\mathbf{K}}| = 0 \quad (3.17)$$

The solution for the ODE (degree n) approach results in an n^{th} order polynomial (characteristic equation) yielding n eigenvalues. $\tilde{\mathbf{K}}$ of Equation (3.17) is symmetric and the resulting matrix within the determinant is symmetric. The roots of the characteristic equation formed by its algebraic eigenvalue equation are therefore real. The characteristic equation has the factored form:

$$|\lambda \mathbf{I} - \tilde{\mathbf{K}}| = (\lambda + \lambda_1)(\lambda + \lambda_2) \cdots (\lambda_n + \lambda) = 0 \quad (3.18)$$

Each discrete root, $-\lambda_1, -\lambda_2, \dots, -\lambda_n$, of Equation (3.18) is real, yet the responses were assumed undamped and oscillatory; hence the system eigenvalues are expected to lie on the $j\omega$ -axis. Since $\lambda_i = \omega_i^2 \rightarrow \omega_{i,i+1} = \pm j\sqrt{\lambda_i}$, the factored form of the characteristic equation becomes a $2n^{\text{th}}$ order polynomial of the form:

$$\begin{aligned} |\lambda \mathbf{I} - \tilde{\mathbf{K}}| &= (\omega - j\sqrt{\lambda_1})(\omega + j\sqrt{\lambda_1})(\omega - j\sqrt{\lambda_2})(\omega + j\sqrt{\lambda_2}) \cdots (\omega - j\sqrt{\lambda_n})(\omega + j\sqrt{\lambda_n}) \\ &= (\omega - j\omega_1)(\omega + j\omega_1)(\omega - j\omega_2)(\omega + j\omega_2) \cdots (\omega - j\omega_n)(\omega + j\omega_n) = 0 \end{aligned}$$

Yielding the homogeneous solutions,

$$\tilde{\mathbf{y}}(t) = \alpha_1 \sin(\omega_1 t + \phi_1) \tilde{\mathbf{v}}_1 + \alpha_2 \sin(\omega_2 t + \phi_2) \tilde{\mathbf{v}}_2 + \dots + \alpha_n \sin(\omega_n t + \phi_n) \tilde{\mathbf{v}}_n$$

The system model was of degree n so both the state-space and ODE approaches must yield n possible solutions and were shown to do so. In both cases, the eigenvalues

identify the unique frequencies of the various vibration modes of the structure. The eigenvalues derived from Equation (3.18) identify the un-damped natural frequencies. Eigenvalues derived from the full state-space model of Equation (3.14) identify the damped natural frequencies of the vibration modes. Equation (3.14) should be more precise. Their eigenvalue solution set of the two approaches are not equal but they will be relatively close in value because the damping factors are small, so $\omega_i \approx \varpi_i$.

3.1.3.3 Eigenvector Evaluation

The distinct eigenvalues ($\Omega_1, \Omega_2, \dots, \Omega_{2n}$ or $\lambda_1, \lambda_2, \dots, \lambda_n$) when individually substituted back into Equations (3.12) for the state-space solution or (3.16) for the ODE solution enable the derivation of the independent eigenvectors,

$$\tilde{\mathbf{A}} = [\tilde{\mathbf{v}}_1 \quad \tilde{\mathbf{v}}_2 \quad \dots \quad \tilde{\mathbf{v}}_{\alpha n}], \quad \alpha = \begin{cases} 1 & (ODE) \\ 2 & (state - space) \end{cases}$$

Eigenvectors will be shown to provide an arbitrarily scaled but more commonly normalized spatial component to the modal solution. The eigenvalue substitution yields,

$$\begin{aligned} \text{State-Space: } & (\Omega_i \mathbf{I} - \mathbf{A}) \cdot \tilde{\mathbf{v}}_i = 0, \quad i = 1 \rightarrow 2n \\ \text{ODE: } & (\lambda_i \mathbf{I} - \tilde{\mathbf{K}}) \cdot \tilde{\mathbf{v}}_i = 0, \quad i = 1 \rightarrow n \end{aligned}$$

The eigenvalues for the ODE solution are real. The derived eigenvectors will likewise be real with the following syntax...

$$\tilde{\mathbf{v}}_i = [\tilde{v}_{i,1} \quad \tilde{v}_{i,2} \quad \dots \quad \tilde{v}_{i,n}]^T$$

where $\tilde{v}_{i,k}$ represents the k^{th} element, or nodal mode shape component of the i^{th} vibration mode. The eigenvalues for the state-space model are complex yielding a complex eigenvector set. Being a real world system, the complex eigenvectors, like the eigenvalues, will exist in conjugate pairs and have the following syntax...

$$\tilde{\mathbf{v}}_i = \begin{bmatrix} \tilde{v}_{i,1} \\ \tilde{v}_{i,2} \\ \vdots \\ \tilde{v}_{i,2n} \end{bmatrix} = \begin{bmatrix} a_{i,1} + j b_{i,1} \\ a_{i,2} + j b_{i,2} \\ \vdots \\ a_{i,2n} + j b_{i,2n} \end{bmatrix}, \quad \tilde{\mathbf{v}}_{i+n+1} = \tilde{\mathbf{v}}_i^* = \begin{bmatrix} \tilde{v}_{i,1}^* \\ \tilde{v}_{i,2}^* \\ \vdots \\ \tilde{v}_{i,2n}^* \end{bmatrix} = \begin{bmatrix} a_{i,1} - j b_{i,1} \\ a_{i,2} - j b_{i,2} \\ \vdots \\ a_{i,2n} - j b_{i,2n} \end{bmatrix} \quad (3.19)$$

The eigenvalue sets from both the ODE and state-space approaches were shown to yield near equivalent results. The eigenvector sets should likewise be expected to be equivalent. But, unlike the real eigenvector set derived using the ODE approach, the state-space results yield $2n$ complex eigenvectors that appear to have no ‘real world’ correlation. In fact, it is generally recommended to not attempt to visualize a vector whose components are complex numbers. Complex mode shapes allow for a general variation in phase between elements of the eigenvectors as opposed to simple in-phase or 180 degree out-of-phase proclamations of the eigenvectors found for the undamped systems^[91]. Never the less, the complex eigenvectors embody the spatial information of the modal solution.

The state-space vector is composed of both position and velocity states. It is of dimension $2n$ while there are only n degrees of freedom in the structural model. The elements of the eigenvectors that correspond to the position states of the state vector contain the mode shape information. These elements as shown in Equation (3.19) are in rectangular form (*real + j · complex*). MATLAB, for example, displays eigenvalue results in rectangular form. Given the rectangular representation, the free vibration component of the i^{th} vibration mode for the corresponding complex eigenvalue and eigenvector becomes^[92]:

$$\tilde{\mathbf{v}}_i(t) = (\mathbf{a}_i \cos(\omega_i t) + \mathbf{b}_i \sin(\omega_i t)) e^{-\sigma_i t}$$

$$\mathbf{a}_i = [a_{i,1} \quad a_{i,2} \quad \cdots \quad a_{i,n}]^T, \quad \mathbf{b}_i = [b_{i,1} \quad b_{i,2} \quad \cdots \quad b_{i,n}]^T$$

Rectangular notation can easily be converted to polar form (Euler's Formula) where magnitude and phase content are expressed explicitly. Note that ω_i and ϕ_i are constant along the structure.

$$a_{i,k} + j b_{i,k} = r_{i,k} e^{j\phi_i}$$

$$r_i = \sqrt{a_{i,k}^2 + b_{i,k}^2}, \quad \phi_i = \tan^{-1} \left(\frac{b_{i,k}}{a_{i,k}} \right)$$

yielding,

$$\tilde{\mathbf{v}}_i(t) = \mathbf{r}_i e^{-\sigma_i t} \cos(\omega_i t + \phi_i)$$

Of course the mode shapes derived using LMA are in fact approximations because the model was discretized based on mass, stiffness, and damping distribution assumptions. Spatial displacements between nodes require interpolation. The eigenvector sets, when taken together, form the discretized spatial basis of the dynamic response of the structure. In other words, all possible spatial responses of the system can be formed through some linear combination of the eigenvectors (mode shapes). So, at any instant in time

$$\tilde{\mathbf{y}}(t_1) = \alpha_1 \tilde{\mathbf{v}}_1(t_1) + \alpha_2 \tilde{\mathbf{v}}_2(t_1) + \dots + \alpha_n \tilde{\mathbf{v}}_n(t_1)$$

The n eigenvector norms, when arranged in matrix form establish the modal matrix ^[93] which can be used to diagonalized the system coefficient matrix, decoupling the system modes. The modal matrix takes the general form,

$$\tilde{\mathbf{T}} = \begin{bmatrix} \frac{\tilde{\mathbf{v}}_1}{\|\tilde{\mathbf{v}}_1\|} & \frac{\tilde{\mathbf{v}}_2}{\|\tilde{\mathbf{v}}_2\|} & \dots & \frac{\tilde{\mathbf{v}}_n}{\|\tilde{\mathbf{v}}_n\|} \end{bmatrix} \quad (3.20)$$

An earlier linear transformation was made to maintain symmetric geometry of the normalized stiffness matrix $\tilde{\mathbf{K}}$ and must be revisited when evaluating the results.

Linear transformations such as $\tilde{\mathbf{y}} = \mathbf{M}^{-\frac{1}{2}} \times \mathbf{y}$ do not effect system eigenvalues, but do effect eigenvectors [94]. This can be easily verified using the form of the assumed solution for $\tilde{\mathbf{y}}$ used earlier to determine the eigenvalues of the symmetric system.

$$\tilde{\mathbf{y}} = \tilde{\mathbf{v}} \cdot e^{j\omega t}$$

Now, reverse transform $\tilde{\mathbf{y}}$ in the assumed transformed solution...

$$\tilde{\mathbf{y}} = \mathbf{M}^{-\frac{1}{2}} \times \mathbf{y} \Rightarrow \mathbf{y} = \mathbf{M}^{\frac{1}{2}} \times \tilde{\mathbf{v}} \cdot e^{j\omega t}$$

Substituting into Equation (3.15), letting $\lambda = \omega^2$ and rearranging yields,

$$\left(\lambda \mathbf{I} - \tilde{\mathbf{K}}\right) \times \mathbf{M}^{\frac{1}{2}} \times \tilde{\mathbf{v}} = \left(\lambda \mathbf{I} - \tilde{\mathbf{K}}\right) \times \mathbf{v} = 0$$

As before, for a non-trivial solution, the eigenvalues of both the original and the transformed system are the scalar solutions of the same characteristic equation defined by the determinant,

$$|\lambda \mathbf{I} - \tilde{\mathbf{K}}| = 0$$

demonstrating that ‘linear transformations of the system basis do not affect the eigenvalues’ of that system.

The same cannot be said of the eigenvectors. In most cases eigenvectors of a linearly transformed system form a different basis for the solution set. Although the transformation used in the proceeding example did not affect the eigenvalues, it did affect the eigenvalue set since clearly for any given eigenvalue λ_i ,

$$\tilde{\mathbf{v}}_i \neq \mathbf{M}^{\frac{1}{2}} \times \tilde{\mathbf{v}}_i = \mathbf{v}_i$$

demonstrating that ‘linear transformations of the system basis do affect the eigenvectors’ of the system.

In summary, the computed eigenvector set of the mass normalized symmetric system of Equation (3.20) generalizes the idea of a mode shape basis or set for the given system. As derived however $\tilde{\mathbf{v}}_{i=1 \rightarrow n}$ represents the orthogonal mode shape basis of the transformed system (transformed from the basis of the variable \mathbf{y} to that of the variable $\tilde{\mathbf{y}}$, where $\tilde{\mathbf{y}} = \mathbf{M}^{\frac{1}{2}} \times \mathbf{y}$). The basis for the variable \mathbf{y} represents the ‘real world’ coordinates. The basis for the variable $\tilde{\mathbf{y}}$ represents the preferred ‘analytical’ world. The modal matrix can be transformed back to real world coordinates by the transformation:

$$\mathbf{v}_i = \mathbf{M}^{\frac{1}{2}} \times \tilde{\mathbf{v}}_i, \quad \mathbf{T} = \mathbf{M}^{\frac{1}{2}} \times \tilde{\mathbf{T}} = \mathbf{M}^{\frac{1}{2}} \times \begin{bmatrix} \frac{\tilde{\mathbf{v}}_1}{\|\tilde{\mathbf{v}}_1\|} & \frac{\tilde{\mathbf{v}}_2}{\|\tilde{\mathbf{v}}_2\|} & \dots & \frac{\tilde{\mathbf{v}}_n}{\|\tilde{\mathbf{v}}_n\|} \end{bmatrix}$$

3.1.3.4 Linear Modal Analysis for the baseline Aluminum Luminaire Support

The mode shape analysis for the 5-node, 5-DOF dynamic system model of the baselined cantilever was conducted using LMA methods. The mass distribution procedure for the cantilever model is described in Section 4.1.1.1. It included the top mounted luminaire. The model was found to take the following form:

$$\mathbf{M} = \begin{bmatrix} 2.67 & 0 & 0 & 0 & 0 \\ 0 & 2.12 & 0 & 0 & 0 \\ 0 & 0 & 1.45 & 0 & 0 \\ 0 & 0 & 0 & .92 & 0 \\ 0 & 0 & 0 & 0 & 2.12 \end{bmatrix} lbm$$

The associated stiffness matrix of the pole was computed to be (its formulation description is given in Section 4.1.1.3):

$$\mathbf{K} = \begin{bmatrix} 35039 & -27205 & 14521 & -4515 & 1729 \\ -27205 & 47707 & -45733 & 25490 & -9763 \\ 14521 & -45733 & 70841 & -72771 & 36773 \\ -4515 & 25490 & -72771 & 132610 & -81942 \\ 1729 & -9763 & 36773 & -81942 & 53635 \end{bmatrix} \frac{lbf}{ft}$$

The mass normalized stiffness matrix became,

$$\tilde{\mathbf{K}} = \mathbf{M}^{-\frac{1}{2}} \times \mathbf{K} \times \mathbf{M}^{-\frac{1}{2}}$$

$$\tilde{\mathbf{K}} = \begin{bmatrix} 13115 & -11439 & 7366 & -2878 & 726 \\ -11439 & 22536 & -26063 & 18254 & -4606 \\ 7366 & -26063 & 48708 & -62872 & 20928 \\ -2878 & 18254 & -62872 & 143960 & -58599 \\ 726 & -4606 & 20928 & -58599 & 25266 \end{bmatrix} \frac{1}{\text{sec}^2}$$

The vector of eigenvalues was computed to be,

$$\lambda = \begin{bmatrix} 32.37 \\ 1325 \\ 10172 \\ 40037 \\ 202020 \end{bmatrix} \left(\frac{\text{rad}}{\text{sec}} \right)^2$$

The modal matrix, computed eigenvectors, and mode shapes of the HAPCO-like baselined cantilever with the top mounted luminaire are each given here in matrix form:

$$\tilde{\mathbf{T}} = \begin{bmatrix} -0.040 & -0.381 & 0.813 & 0.426 & 0.097 \\ 0.156 & 0.651 & -0.077 & 0.675 & 0.300 \\ -0.415 & -0.527 & -0.509 & 0.371 & 0.392 \\ 0.833 & -0.306 & -0.101 & -0.104 & 0.438 \\ -0.330 & 0.245 & 0.252 & -0.462 & 0.745 \end{bmatrix}$$

$$\mathbf{T} = \mathbf{M}^{\frac{1}{2}} \times \tilde{\mathbf{T}} = [\mathbf{v}_1 \quad \mathbf{v}_2 \quad \mathbf{v}_3 \quad \mathbf{v}_4 \quad \mathbf{v}_5] = \begin{bmatrix} -0.024 & -0.233 & 0.498 & 0.261 & 0.059 \\ 0.107 & 0.447 & -0.053 & 0.464 & 0.206 \\ -0.344 & -0.437 & -0.422 & 0.308 & 0.325 \\ 0.868 & -0.319 & -0.105 & -0.108 & 0.457 \\ -0.266 & 0.168 & 0.173 & -0.317 & 0.511 \end{bmatrix}$$

Normalized mode shapes for modes one through three of the baselined cantilever with and without the luminaire mounted are diagrammed in Figure 3-6. The additional mass of the top mounted luminaire noticeably affects the location and magnitudes of nodes and anti-nodes of the 2nd and 3rd mode shapes.

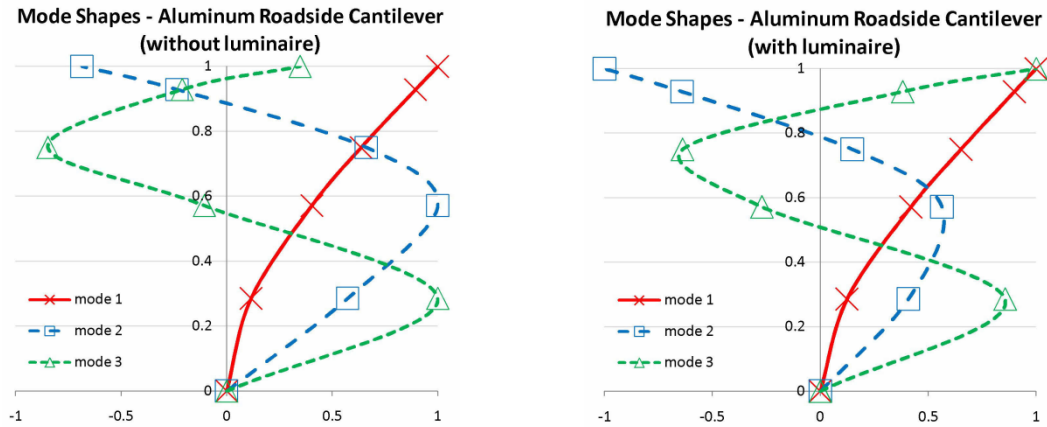


Figure 3-6 Baseline Aluminum Pole Mode Shape Functions [Linear Modal Analysis]

3.1.4 Exciting Targeted Vibration Modes

The fundamental question that needed to be addressed in order to invoke a Modal Damping control scheme was whether it was possible to excite a single, specific vibration mode with a limited input set?

The continuous analysis of the simplified vibrating structure showed that each vibration mode was in fact a standing wave that was shown to be expressed mathematically as a spatial deformation function with a harmonically time-varying magnitude. These continuous displacement functions were developed using a simplified structure having a homogeneous and prismatic geometry. The resultant continuous mode shape functions are similar but not necessarily identical to those of the discretized system model developed using Linear Modal Analysis. In both cases however, the set of all vibration modes form the ‘spatial basis’ for the dynamic response of the system (given linear elastic deformation) for the chosen model fidelity. Any system dynamic response can be found to be a weighted sum of these modes that define its spatial basis. For the discretized system,

$$\mathbf{v}(t) = \sum_n a_n \sin(\omega_n \cdot t + \phi_n) \cdot \mathbf{v}_n \quad (3.21)$$

where $\mathbf{v}(t)$ is a vector of length n representing instantaneous nodal displacements, ω_i and \mathbf{v}_i ($i = 1 \dots n$) represent the n vibration frequencies and associated mode shape vectors, and a_n, ϕ_n are constants associated with modal frequencies that are functions of nodal initial conditions $\mathbf{v}(0)$ and $\dot{\mathbf{v}}(0)$. When Equation (3.21) is expanded in series form,

$$\mathbf{v}(t) = a_1 \sin(\omega_1 t + \phi_1) \cdot \mathbf{v}_1 + a_2 \sin(\omega_2 t + \phi_2) \cdot \mathbf{v}_2 + \dots + a_n \sin(\omega_n t + \phi_n) \cdot \mathbf{v}_n \quad (3.22)$$

it takes the appearance of a Discrete Fourier Series function and again highlights the fact that instantaneous nodal displacements can be decomposed into a weighted sum of system natural vibration modes. The question at hand is whether or not any one particular component in the series can be uniquely excited; and if so, how? Equation (3.22) can further be expanded to the form,

$$\begin{aligned} \mathbf{v}(t) = & \alpha_1 \sin(\omega_1 t) \cdot \mathbf{v}_1 + \alpha_2 \sin(\omega_2 t) \cdot \mathbf{v}_2 + \cdots + \alpha_n \sin(\omega_n t) \cdot \mathbf{v}_n + \\ & + \beta_1 \cos(\omega_1 t) \cdot \mathbf{v}_1 + \beta_2 \cos(\omega_2 t) \cdot \mathbf{v}_2 + \cdots + \beta_n \cos(\omega_n t) \cdot \mathbf{v}_n \end{aligned} \quad (3.23)$$

where $a_i = \sqrt{\alpha^2 + \beta^2}$, $\phi_i = \tan^{-1}\left(\frac{\beta}{\alpha}\right)$. Let the initial nodal displacement and velocity conditions be defined as follows,

$$\begin{aligned} \mathbf{v}(0) &= [v_{0_1} \quad \cdots \quad v_{0_n}]^T \\ \dot{\mathbf{v}}(0) &= \mathbf{0} \end{aligned}$$

Equation (3.23) can be evaluated at $t = 0$ yielding

$$\mathbf{v}(0) = \beta_1 \cdot \mathbf{v}_1 + \beta_2 \cdot \mathbf{v}_2 + \cdots + \beta_i \cdot \mathbf{v}_i + \cdots + \beta_n \cdot \mathbf{v}_n \quad (3.24)$$

Taking the derivative of Equation (3.23) and evaluating at $t = 0$ yields

$$\dot{\mathbf{v}}(0) = \mathbf{0} = \alpha_1 \cdot \mathbf{v}_1 + \alpha_2 \cdot \mathbf{v}_2 + \cdots + \alpha_n \cdot \mathbf{v}_n \quad (3.25)$$

Since \mathbf{v}_i are each vectors representing distinct mode shapes of the vibrating structure, they are linearly independent and for non-trivial solutions, $\mathbf{v}_i \neq 0$ ($i = 1 \cdots n$). For Equation (3.25) to be true, $\alpha_i = 0$ ($i = 1 \cdots n$). Equation (3.24) can also be rearranged to form,

$$\mathbf{v}(0) = \mathbf{T} \times \mathbf{r}_0, \quad \mathbf{r}_0 = \begin{bmatrix} \beta_1 \\ \vdots \\ \beta_n \end{bmatrix}$$

where \mathbf{T} was previously defined as the modal matrix $\mathbf{T} = [\mathbf{v}_1 \quad \mathbf{v}_2 \quad \cdots \quad \mathbf{v}_n]$.

If now, the initial conditions are further constrained such that,

$$\begin{aligned} \beta_i &\neq 0 \quad (i = j) \\ \beta_i &= 0 \quad (i \neq j) \end{aligned}$$

$$\mathbf{v}(0) = \mathbf{T} \times \mathbf{r}_0 = [\mathbf{v}_1 \quad \mathbf{v}_2 \quad \cdots \quad \mathbf{v}_n] \times \begin{bmatrix} 0 \\ \vdots \\ \beta_j \\ \vdots \\ 0 \end{bmatrix} = \beta_j \mathbf{v}_j \quad (3.26)$$

And, for $t > 0$ given the initial conditions specified in Equation (3.26), the nodal displacement function becomes

$$\mathbf{v}(t) = \beta_j \cos(\omega_j t) \mathbf{v}_j \quad (3.27)$$

Equation (3.27) may appear to be trivial. However, this expression along with the journey taken to get to it revealed a strategy on how to couple energy into the 2nd vibration mode. It suggested that an individual vibration mode could be excited by forcing specific ‘initial’ conditions $\mathbf{v}(t_0)$ and $\dot{\mathbf{v}}(t_0)$. In other words, if the structure can be ‘re-shaped’ to approximate the desired mode shape and released, it will free-vibrate with those particular vibration mode properties.

A simplified demonstrated using the 5-DOF analytical model of the baselined cantilever can be illustrated. In accordance with the discussion above, the initial nodal displacement conditions were set to match the deformed shape of the 2nd vibration mode. The mode shapes were given earlier and formed the modal matrix \mathbf{T} . The mode shapes were also diagrammed in Figure 3-6. The normalized 2nd mode shape vector as given in \mathbf{T} , is $\mathbf{v}_2 = [.266 \quad .464 \quad .307 \quad -0.109 \quad -0.318]^T$. The resulting nodal responses for nodes 2 and 5 given the assigned initial conditions $\mathbf{v}(t_0) = \mathbf{v}_2$ are shown in Figure 3-7.

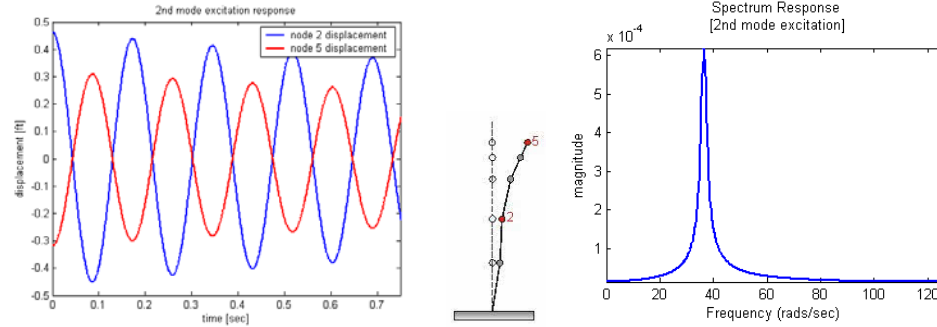


Figure 3-7 2nd Vibration Modal Excitation Test Response

The spectral response at node 1 is also shown and verifies the spectral content to contain ‘only’ the 2nd harmonic radial frequency, 36.4 rad/sec. The spectral spread behavior centered at the 2nd harmonic frequency can be verified through the Fourier transform of the waveform. Let,

$$f_i(t) = e^{-\sigma_i t} \sin(\omega_i t) u_{-1}(t)$$

where, $u_{-1}(t)$ represents a unit step function at $t = 0$. Its Fourier transform becomes^[95],

$$F_i(\omega) = \frac{\omega_i}{(\sigma + j\omega)^2 + \omega_i^2} \tag{3.28}$$

3.1.5 Modal Deformation Energy

Modal Damping approach is based upon modal energy transfer. It is important to establish the internal accord of the system energy when distributed among the possible vibration modes. The deformation of long, flexible structural types was assumed to be elastic and to follow Hooke’s Law. Under these conditions, deformation can be assumed to be purely bending; shear deformation was assumed negligible. During the vibration cycle, energy transitions between the potential and kinetic states.

Consider the maximum potential energy state where the degree of deformation can be expressed in terms of stored strain energy defined as.

$$PE_{total} = \iiint \frac{\sigma \cdot \varepsilon}{2} dV = \iiint \frac{\sigma^2}{2 \cdot E} dV \quad (3.29)$$

Referring to Figure 3-4, the cross-section is assumed uniform and the bending occurs in the y - z plane about the x -axis. The stress distribution becomes a function of y and z , and is independent of x . A constant I_{xx} along the structure was assumed. At any point within the structure,

$$\sigma(x, y, z) = -\frac{M(z) \cdot y}{I_{xx}}$$

Substituting and rearranging, the total strain energy within the structure can be expressed as

$$PE_{total} = \int \frac{M(z)^2}{2 \cdot E \cdot I_{xx}^2} \left(\iint y^2 dx dy \right) dz = \int \frac{M(z)^2}{2 \cdot E \cdot I_{xx}} dz \quad (3.30)$$

The moment/deflection curve^[96] relationship along the z -axis and about the x -axis is,

$$M(z) = E \cdot I_{xx} \cdot \frac{d^2 v(z)}{dz^2}$$

and noting that in the case of the vibrating pole, the spatially related deformation was found to be $v(z) = \sum_n Z_n(z)$ where $Z_n(z)$ represents the n vibration mode shapes given

by Equation (3.6). Substituting into Equation (3.30) yields,

$$PE_{total} = \int \left[\frac{E \cdot I_{xx} \cdot \frac{d^2 \left(\sum_n Z_n(z) \right)}{dz^2}}{2 \cdot E \cdot I_{xx}} \right]^2 dz$$

Simplifying, the total potential energy of the vibrating pole can now be expressed as,

$$PE_{total} = \frac{E \cdot I_{xx}}{2} \cdot \int \left(\sum_n \frac{d^2 Z_n(z)}{dz^2} \right)^2 dz \quad (3.31)$$

The non-linear square function embedded in Equation (3.31) appears to couple the deformation of the multiple modes shapes. It appears to indicate that total strain energy is not simply the linear sum of strain energies of the independent vibration modes. If true, directing energy from one specified mode to any given mode becomes what seems an ominous task. Investigating further, Equation (3.31) can be expanded to yield,

$$PE_{total} = \frac{E \cdot I_{xx}}{2} \cdot \int \left(\sum_i^n \sum_j^n \frac{d^2 Z_i(z)}{dz^2} \cdot \frac{d^2 Z_j(z)}{dz^2} \right) dz$$

Rearranging (the integral of a sum of series is equal to the sum of a series of integrals),

$$PE_{total} = \frac{E \cdot I_{xx}}{2} \cdot \sum_i^n \sum_j^n \int \left(\frac{d^2 Z_i(z)}{dz^2} \cdot \frac{d^2 Z_j(z)}{dz^2} \right) dz \quad (3.32)$$

At this point, Equation (3.32) is still menacing in appearance particularly when the complete expressions for $Z_i(z)$ from Equation (3.6) are substituted. The desired conclusion is not apparent. As noted earlier, the modes shapes when taken together form the ‘basis’ for the solution-space of the structure’s dynamic response... the ‘base’ components in Euclidean space are orthogonal. Orthogonality tests are straightforward and can be easily illustrated using the calculated modal matrix of the baseline aluminum pole,

$$\mathbf{T} = [\mathbf{v}_1 \quad \mathbf{v}_2 \quad \mathbf{v}_3 \quad \mathbf{v}_4 \quad \mathbf{v}_5] \Rightarrow \mathbf{T}^T \times \mathbf{T} \rightarrow \mathbf{I}_{5 \times 5}$$

A vanishing dot product can be used as an orthogonality test for the vector base components. The elements off diagonal represent

$\mathbf{v}_i^T \cdot \mathbf{v}_j = 0$, ($i=1 \rightarrow n$, $j=1 \rightarrow n$, $i \neq j$) and hence denote orthogonality. Each base component is orthogonal with every other base component as expected. The elements on the main diagonal represent dot products $\mathbf{v}_i^T \cdot \mathbf{v}_i = 1$, ($i=1 \rightarrow n$). The unit values on the main diagonal confirm that each component is parallel to itself.

If now the mode shape functions are continuous as is the case with Equation (3.32), an inner product can be used as an orthogonality test ^[97],

$$\langle Z_i(z), Z_j(z) \rangle = \int Z_i(z) Z_j(z) dz \begin{cases} 1, & i = j \\ 0, & i \neq j \end{cases}$$

The spatial mode shape functions for the cantilever structure with homogeneous cross-sectional properties was shown to be of the form

$$Z(z) \propto \alpha_n \cdot [\sin(\beta_n \cdot z) - \sinh(\beta_n \cdot z)] + \cosh(\beta_n \cdot z) - \cos(\beta_n \cdot z) \quad (3.33)$$

with α_n and β_n constant for the specified n^{th} mode. The orthogonality for between mode shapes for functions of this form can be shown. Taking the second derivative of Equation (3.33) yields,

$$\frac{\partial^2 Z(z)}{\partial u^2} \propto \beta_n^2 \left\{ \alpha_n \cdot [\sin(\beta_n \cdot z) - \sinh(\beta_n \cdot z)] + \cosh(\beta_n \cdot z) - \cos(\beta_n \cdot z) \right\} \quad (3.34)$$

Equations (3.33) and (3.34) have the same structural syntax, hence both demonstrate identical orthogonality behavior. Consequently, the inner product operation reduces Equation (3.32) to,

$$PE_{total} = \frac{E \cdot I_{xx}}{2} \sum_n \left(\int \left(\frac{d^2 Z_n(z)}{dz^2} \right)^2 dz \right) \quad (3.35)$$

The solution to this expression may not be available in closed form for all but the simplest of structural configurations. Equation (3.35) clarifies and ratifies in a

fundamental sense the damping control strategy. In the absence of non-linear mechanisms, the ‘total deformation energy associated with modal vibrations is simply the linear sum of deformation energies associated with each individual mode of the net response’. From a control standpoint, it implies that the energy associated with any given mode can be transferred to a target mode with minimal (negligible) effects to non-target modes; there is no undesired coupling.

3.1.6 Modal Energy Redistribution Risks

“You don’t get something for nothing”, or so the saying goes. The claim herein is that Modal Damping offers more expedient energy dissipation potential. What then are the risks, or costs to the system when those benefits are exercised? The modal spatial deflection equations (mode shape functions) enable the system effects to be evaluated from both a spatial and an energy perspective. The equations offer a means to compare the relative ‘dynamic threat’ on a structure given modal energy transfer. The baseline aluminum cantilever pole was the case subject for the following discussion.

Table 3-1 summarizes the required system energy that would be necessary to develop a 1-foot displacement of the structure at the ‘node’ of the specified mode shape for each of the first four modes.

Table 3-1 Modal Strain Energies Given Equivalent Deflections [1 ft]

Mode [n]	β_n $\left[\frac{\text{radians}}{\text{ft}} \right]$	$\frac{1}{\beta_n}$ $\left[\frac{\text{ft}}{\text{cycle}} \right]$	Strain Energy [U _n] [lb-ft]	$\frac{U_n}{U_1}$
1	.045	140.7	221	1
2	.112	56.2	8690	39.5
3	.187	33.6	68200	309.1
4	.262	24	262000	1189.1

The table emphasizes the non-linearity associated with generating equivalent displacements among the modes. A mode-2 1-foot displacement requires nearly 40 times the energy compared to a fundamental mode 1 foot displacement; and mode-4 requires nearly 1200 times the energy. β_n , derived in Equation (3.6), is a characterizing parameter of the structures spatial shape. It specifies the spatial frequency (radians/foot) for the n^{th} mode. Its inverse represents the spatial wavelength of that vibration mode and exposes how much of that standing wave is present in the structure. These analytical parameters are dependent on both physical properties and boundary conditions of the vibrating structure.

Next, the spatial displacement that equivalent energy would produce among the different modes was examined. Table 3-2 summarizes the displacement-energy relationship for the first three modes. The table indicates that given equivalent strain energy, mode-2 produces $\frac{1}{6}$ the deflection of the fundamental mode, while mode-3 produces only $\frac{1}{17}$ the deflection.

Table 3-2 Modal Deflections Given Equivalent Energies

Mode [n]	Strain Energy [lb-ft]	Maximum Deflection [ft]	$\frac{v_1}{v_n}$
1	55	1	1
2	55	0.16	6.25
3	55	0.057	17.5

Table 3-1 and Table 3-2 lead to the following observations. Transferring energy from the fundamental mode to some higher order mode can clearly produce significantly lower lateral sway displacements along the structure. The accompanying

velocities and accelerations that are time-derivative functions of the non-linearly related displacements may or may not be greater at any given location within the structure. The system simulation developed for the baseline system was utilized to further investigate the impact of energy transfer on nodal dynamics. The results are given in Section 4.3 and generally demonstrate dynamic improvements in the upper region of the structure but increased dynamics lower within the structure.

Another point to consider when assessing structural impact based on spatial dynamics is that nodes and anti-nodes of deformation caused by energy transfer will be relocated to different axial locations within the structure, possibly lending themselves to more practical control options.

An alternate assessment perspective of modal energy transfer examines the degree of deformation the structure itself incurs and the effect the deformation has on the subsequent redistribution of damped energy. The primary internal damping mechanism associated with the baseline cantilever structure was the anelastic mechanism. Its rheological model was given in Figure 2-6 and is repeated here for convenience.

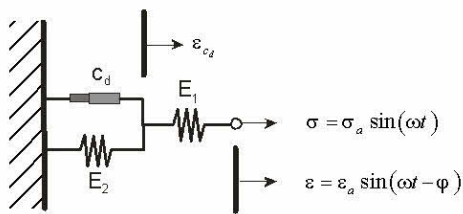


Figure 3-8 Material Damping Rheological Model

Based on this model, the mechanism's frequency dependent behavior (typical) is diagrammed in the normalized magnitude/phase Bode Plot of Figure 3-2 (shown again below) where E_1 is taken to be greater than E_2 .

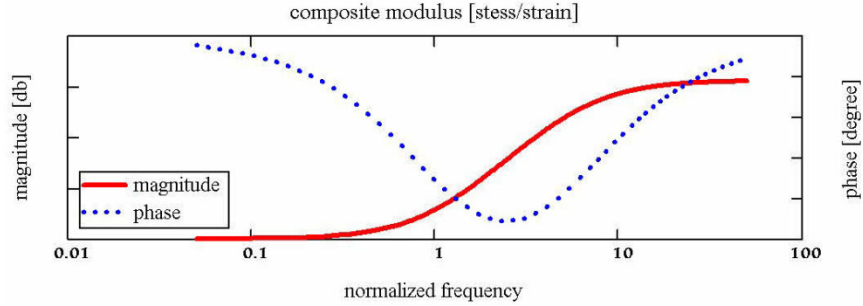


Figure 3-9 Typical Vibration Impedance Modulus for the Anelastic Rheological Model

The parallel/series spring and damper configuration diagrammed above is characterized by associated frequency breakpoints that form regions of distinct dynamical behavior:

1. Deformation behaves elastically at frequencies below the lower breakpoint.
2. Deformation behaves elastically at frequencies above the higher breakpoint.
3. Deformation behaves viscously at intermediate frequencies between the breakpoints characterized by a expected phase difference between stress and strain. It is within this range where energy dissipation related to anelastic deformation primarily occurs.

Equation (3.6), derived earlier, is the mode shape displacement function. It assumes that deformation is elastic. It follows that deflections relating to mode shapes produce small curvatures. Curvature is defined as

$$\kappa = \frac{1}{\nu} \cong \frac{d\theta}{dz} \quad (3.36)$$

where, κ is defined as the curvature of the longitudinal axis, ν is the radius of curvature, and θ is the angle of rotation between the deformed and the un-deformed longitudinal axis of the structure. The slope of the deformed longitudinal is related to

the axial rotation, $\tan \theta(z, t) = \frac{dv(z, t)}{dz}$. If θ is small, then

$$\theta(z, t) \cong \frac{dv(z, t)}{dz} \quad (3.37)$$

Generally, θ is assumed to be small. Given the flexible nature of the structure however, the assumption should be verified. This can be accomplished knowing the structure's specific geometry and material properties. Assuming a large deflection at the top of the baselined cantilever equal to 10% of the cantilever height the slope to rotation ratio for the fundamental mode at t equal to the maximum deformation was computed to be $\frac{\theta(h)}{\tan \theta(h)} \cong .994$. The approximation made in Equation (3.37) is therefore reasonable.

Substituting Equation (3.37) into Equation (3.36) yields (with units shown in square brackets),

$$\kappa(z, t) \cong \frac{d^2 v(z, t)}{dz^2}, \quad \left[\frac{1}{in} \right] \quad (3.38)$$

The curvature expression can now be used to determine strain across the section at any point along the structure. Deformation across the section is assumed to be elastic. The cross section is assumed to remain plane; shear deformation is assumed negligible. No longitudinal strain occurs at the neutral axis of the section. Longitudinal strain at some height along the z-axis of the structure, at some distance y from the neutral axis does exist and can be shown to be,

$$\varepsilon(z, t) = -y \cdot \kappa(z, t) = -y \frac{d^2 v(z, t)}{dz^2}, \quad \left[\frac{in}{in} \right] \quad (3.39)$$

Harmonic deformation along the z-axis of the structure due to lateral vibration develops elemental elastic and viscous stresses as diagrammed in Figure 3-10. The viscous stress component associated with the anelastic mechanism can be expressed as,

$$\sigma_{viscous}(z,t) \propto c_d \cdot \dot{\varepsilon}(z,t), \quad \left[\frac{lbf}{in^2} \right] \quad (3.40)$$

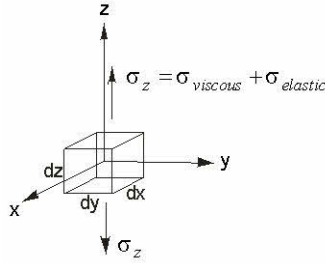


Figure 3-10 Stress Components During Elastic Harmonic Deformation

The units of the damping density constant can be inferred from the stress-strain rate relationship given in Equation (3.40) ...

$$c_d = \frac{lbf}{in^2} \cdot \left(\frac{in}{in} \right)^{-1}, \quad \left[\frac{lbf/in}{in/sec} \rightarrow \frac{lbf \cdot sec}{in^2} \right]$$

The fundamental relationships defined above can now be applied to develop a mathematical expression that describes the distribution of dissipated energy along the structure. Free-vibration behavior is assumed; system energy within the structure oscillates between kinetic and potential states. The deflection response is harmonic in nature with its time-varying equations of motion given by Equation (3.5). Subsequent deformation behavior is likewise harmonic and along the direction of z-axis. Shear deformation is assumed negligible. Time-varying viscous deformation spawns unrecoverable work. The damping mechanism dissipates this unrecoverable energy as heat. The differential *unrecoverable work* for the described deformation that is lost within some infinitesimally small viscous-like element over some interval of time can be expressed as,

$$dW_{viscous}(x, y, z) = \left(\int_{t_1}^{t_2} c_d \dot{\epsilon}(z, t) \dot{\epsilon}(z, t) dt \right) dx dy dz, \quad [lbf \cdot in] \quad (3.41)$$

Work is a scalar parameter and in this application, has spatial and temporal dependencies. Total work however provides little insight into internal dissipation and distribution behavior. Equation (3.41) can be manipulated and re-formed to be more insightful.

Power is the rate at which work is done, $p_v(t) = \frac{dW_v}{dt}$, and provides some insight to instantaneous damping effectiveness. Rearranging Equation (3.41) and using the 2nd Fundamental Theorem of Calculus [98] yields the differential power damped within the element,

$$dp_v(x, y, z, t) = \frac{\partial dW_v(x, y, z)}{\partial t} = c_d \cdot \dot{\epsilon}(z, t) \cdot \dot{\epsilon}(z, t) \cdot dx dy dz = c_d \cdot \dot{\epsilon}^2(z, t) \cdot dx dy dz \quad (3.42)$$

Substituting for strain from Equation (3.39),

$$dp_v(x, y, z, t) = c_d \left(\frac{d \left(-y \frac{d^2 v(z, t)}{dz^2} \right)}{dt} \right)^2 dx dy dz, \quad \left[\frac{\left(\frac{lbf \cdot in}{in} \right)}{sec} \right] \quad (3.43)$$

Integrating over the cross sectional area yields an expression for *differential damped power* within the cross-section at longitudinal position 'z' whose thickness is dz ,

$$dp_v(z, t) = c_d \iint_{section\ area} y^2 \cdot \left(\frac{d^3 v(z, t)}{dt dz^2} \right)^2 dx dy dz = c_d I_{xx} \left(\frac{d^3 v(z, t)}{dt dz^2} \right)^2 dz \quad (3.44)$$

Let $p(z, t) = \frac{dp_v(z, t)}{dz}$ be defined as the damped power density due to the viscous

behavior of the anelastic damping mechanism for the structure.

$$p(z,t) = c_d I_{xx} \left(\frac{d^3 v(z,t)}{dt dz^2} \right)^2, \left[\frac{\left(\frac{lbf \cdot in}{in} \right)}{sec} \right] \quad (3.45)$$

The structural cantilever dynamic spatial-temporal equation was found earlier to be the weighted sum of n standing waves, one for each of the n vibration modes:

$v(z,t) = \sum_{i=1}^{\infty} [v_i Z_i(z) T_i(t)]$. The *damped power density* resulting from the i^{th} vibration mode can be expressed as,

$$p_i(z,t) = c_{d_i} \cdot I_{xx} \cdot \left(\frac{d^3 (v_i Z_i(z) T_i(t))}{dt dz^2} \right)^2 \quad (3.46)$$

Note that the damping coefficient c_d shown in the generalized power density expression of Equation (3.45) has been replaced by a modal specific damping coefficient c_{d_i} . The modal specific coefficient captures the damper's frequency dependent effectiveness implied in the rheological model of Figure 3-2. The temporal and spatial dependent components can be factored yielding,

$$p_i(z,t) = c_{d_i} I_{xx} v_i^2 \left(\frac{d(T_i(t))}{dt} \right)^2 \left(\frac{d^2(Z_i(z))}{dz^2} \right)^2 \quad (3.47)$$

Since curvature is defined as $\kappa = \frac{d^2(Z_i(z))}{dz^2}$, the power density function can be expressed,

$$p_i(z,t) = c_{d_i} I_{xx} v_i^2 \kappa_i^2(z) \left(\frac{d(T_i(t))}{dt} \right)^2 \quad (3.48)$$

Based on the time dependent component derived and given in Equation (3.5),

$$\begin{aligned} \left(\frac{d(T_i(t))}{dt} \right)^2 &= (\omega_i \cos(\omega_i t - \phi))^2 = \omega_i^2 \cos^2(\omega_i t - \phi) \\ &= \frac{\omega_i^2}{2} \cdot (1 + \cos(2\omega_i t - 2\phi)) \end{aligned} \quad (3.49)$$

Equation (3.49) indicates that the modulating time component is clearly periodic with a frequency twice that of the sway frequency. One complete dissipation period occurs during each half cycle of sway. It is continuously positive and is shown diagrammed in Figure 3-11 relative to the sway of the structure. Its positive nature verifies that the damped power ‘flows’ in one direction; the power is unrecoverable as it is dissipated over time as heat caused by the deforming structure.

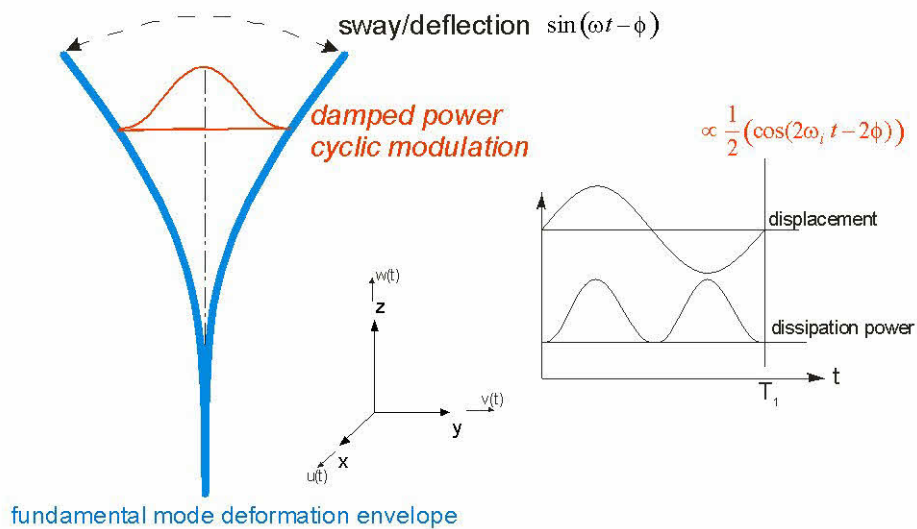


Figure 3-11 Damped Power Temporal Modulation Function

Substituting the temporal modulating component, the generalized *modal damped power density* function becomes,

$$p_i(z, t) = c_{d_i} I_{xx} v_i^2 \kappa_i^2(z) \frac{\omega_i^2}{2} (1 + \cos(2\omega_i t - 2\phi)) \quad (3.50)$$

Maximum, or *peak modal damped power* for a given mode occurs when

$$t = \frac{n\pi + \phi}{\omega_i} \quad n=0,1,2,\dots \quad \text{where } \cos(2\omega_i t - 2\phi) = 1. \text{ Therefore,}$$

$$p_{peak_i}(z, t = t_{peak}) = c_{d_i} I_{xx} v_i^2 \omega_i^2 \kappa_i^2(z) \quad (3.51)$$

The total *damped power density* can be computed as,

$$p(z, t) = \sum_n \left[c_{d_i} I_{xx} v_i^2 \kappa_i^2(z) \frac{\omega_i^2}{2} (1 + \cos(2\omega_i t - 2\phi)) \right] \quad (3.52)$$

The *damped energy density*, or the dissipated energy per unit length at a section along the longitudinal axis, can be determined by the time integral of the total damped power density. Consider the *damped energy density* during an interval equal to one complete sway cycle of the fundamental mode:

$$\begin{aligned} W(z) &= \sum_n \left(\int_{T_1} p_i(z, t) dt, \left(T_1 = \frac{1}{f_1} = \frac{2\pi}{\omega_1} \right) \right) \\ &= I_{xx} \sum_n \left(c_{d_i} v_i^2 \kappa_i^2(z) \frac{\omega_i^2}{2} \int_t^{t+T_1} (1 + \cos(2\omega_i t - 2\phi)) dt \right) \end{aligned} \quad (3.53)$$

The damped energy density dissipated by the fundamental mode over one complete sway cycle is,

$$W_1(z) = 2\pi\omega_1 c_{d_1} I_{xx} v_1^2 \kappa_1^2(z)$$

Finally, the *total damped energy* can be found from the time and space integral of Equation (3.50) for all modes,

$$W_{total} = \sum_n \iint p_i(z, t) dt dz$$

The ‘damped power’ and ‘energy density’ functions can now be applied to the baseline 42 foot cantilever aluminum luminaire pole, the analytical baseline flexible

structure, in order to investigate energy re-distribution effects and risks of the modal energy transfer mechanism. The strategic approach taken compares damped energy densities ‘immediately before’ the transfer with those ‘immediately after’ the transfer. The transfer scenario dynamics, as utilized herein, are reconstructed utilizing MATLAB/SIMULINK simulation results. The simulation revealed that approximately 75% of the dynamic energy in the fundamental mode is transferred to the 2nd vibration mode during the controlled Modal Damping transfer event. The energy transfer mechanism does not, or more precisely cannot transfer 100% of the energy because the 3-point tendon control device cannot fully replicate the shape of the 2nd vibration mode. A worst case risk condition with 99% energy transfer from fundamental to 2nd mode is assumed, even though not truly attainable in order to amplify critical energy dissipation densities. A real world Modal Damping energy transfer event would further result in energy transfer from the fundamental mode to not only the 2nd mode, but also to higher order modes. This would be due to the 3-point tendon 2nd mode shape approximation. Simulation results indicated that compared to the 2nd mode, the higher order modes receive negligible amounts of energy due to the transfer event.

The transfer scenario assumes initial fundamental mode dynamic energy resulting from a high deformation condition defined by a deflection at the top of the structure equal to 10% of its height. Figure 3-12 diagrams the deflection functions before and after the transfer event. It contains the deflection function of the fundamental mode prior to the event and the deflection functions of the fundamental mode and 2nd mode immediately after the transfer event. Notice that although 99% of the strain energy is transferred, there is still a visible fundamental mode component after the transfer.

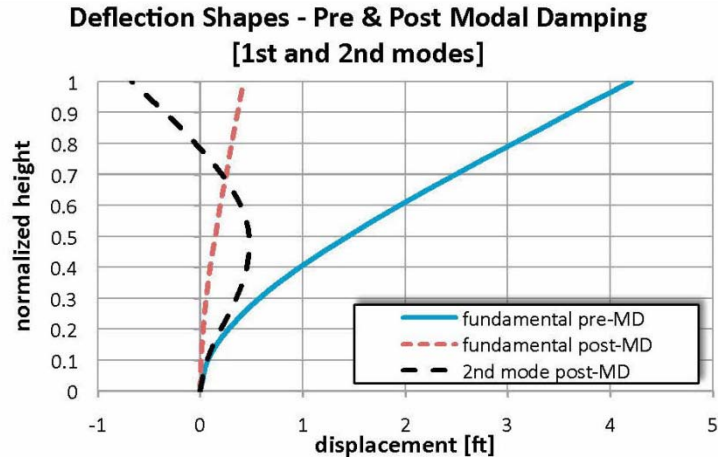


Figure 3-12 Modal Deflection Functions [Before & After Energy Transfer Event]

Figure 3-13 diagrams ‘Peak Damped Power Density’ along the longitudinal length of the vibrating cantilever given the deflections shapes of Figure 3-12. The before and after-transfer ‘Peak Damped Power Densities’ are included in the diagram. The functional values represent ‘Damped Power Per Unit Length’, or a longitudinal ‘Damped Power Density’ with units: $\frac{ft \cdot lbf}{ft} / sec$. Negligible damped power is developed by the fundamental mode after the transfer event since 99% of its energy was assumed transferred to the 2nd vibrational mode.

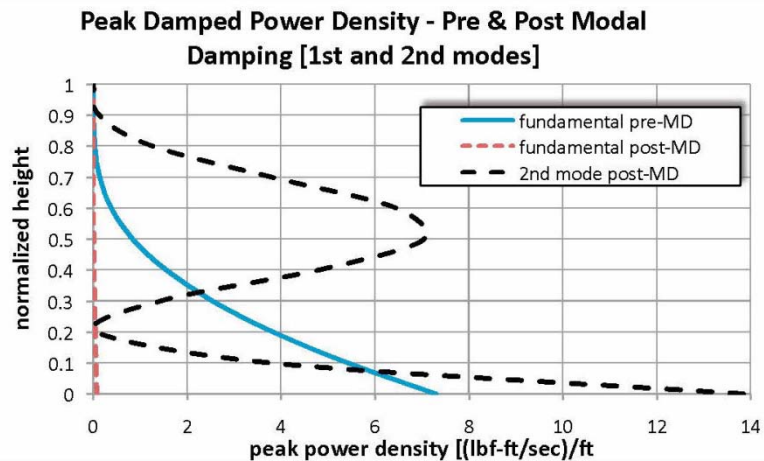


Figure 3-13 Peak Damped Power Density Function

For a given mode, the ratio of energy density to peak power density is a simple scalar, and derived as,

$$\begin{aligned} \frac{W_i(z)}{P_{peak_i}(z, t = t_{peak})} &= \frac{c_{d_i} I_{xx} v_i^2 \kappa_i^2(z) \frac{\omega_i^2}{2} \int_t^{t+\Delta t} (1 + \cos(2\omega_i t - 2\phi)) dt}{c_{d_i} I_{xx} v_i^2 \omega_i^2 \kappa_i^2(z)} \\ &= \frac{1}{2} \int_t^{t+\Delta t} (1 + \cos(2\omega_i t - 2\phi)) dt \\ &= \eta_i \text{ sec} \end{aligned} \tag{3.55}$$

Figure 3-14 diagrams the ‘Damped Energy Densities’ during an interval of time equal to the vibration period of the fundamental mode, $\Delta t = .867 \text{ sec}$. Again, the before and after-transfer ‘Damped Energy Densities’ are diagrammed. As expected, the functions of Figure 3-14 are proportional to those of Figure 3-13. The ‘Damped Energy Densities’ units are $\frac{ft \cdot lbf}{ft}$. The respective modal functions are related by the scalar $\eta_i \text{ sec}$ as given in Equation (3.55) that are determined by the time interval of interest Δt . For $\Delta t = .867 \text{ sec}$, $\eta_1 = .433$, $\eta_2 = .432$.

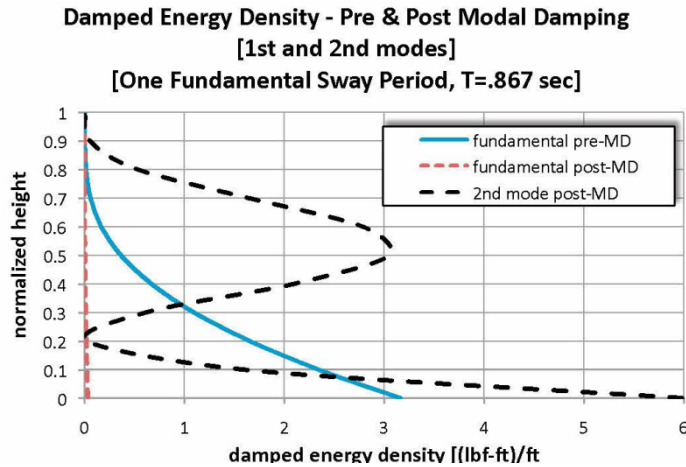


Figure 3-14 Energy Dissipation Density Function

The ‘Damped Energy Densities’ reveal two important aspects of the energy transfer event:

- The 2nd mode utilizes different regions of the structure to dissipate its energy.
- And, the energy densities developed by the 2nd mode immediately within the base region of the structure are nearly twice those of the fundamental mode.

Figure 3-15 attempts to provide a visualization of ‘Damping Efficiency by Location’ within the structure. It offers one means to generalize where energy dissipation occurs. The functions represent the integral of the ‘Damped Energy Density’ functions shown above. The integral is taken along the longitudinal axis of the structure beginning at the structural base. The functions reveal the following:

- Nearly the same energy is dissipated in the lower 50% of the structure whether the vibration energy resides in the fundamental (pre-xfer) or 2nd mode (post-xfer).
- The Modal Damping technique exploits the third quadrant of the structure (50 → 75% of the structure height) to dissipate additional energy.
- For the assumed worst case scenario in which 99% of fundamental energy was transferred to the 2nd vibration mode, an additional of approximately 82% overall energy dissipation occurred during this time interval... a sizeable efficiency improvement.

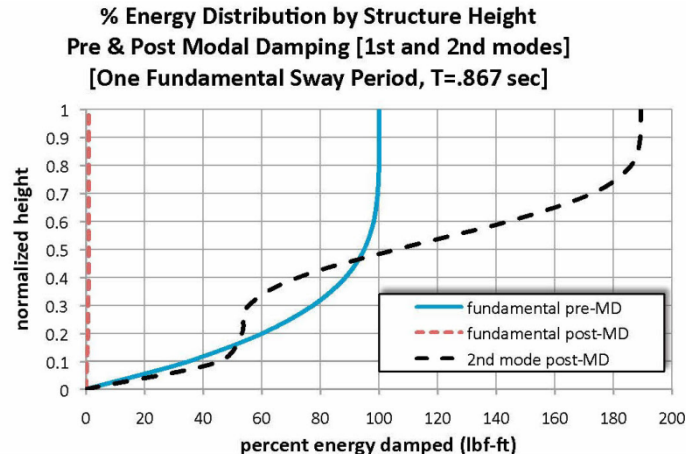


Figure 3-15 % Energy Dissipation versus Structural Height

99% energy transfer efficiency was assumed for the Modal Damping assessment conducted above although not realistically attainable with the 3-point tendon control device. The effect of reduced energy transfer efficiency on ‘Damped Energy Densities’ was investigated and is summarized below. Energy transfer efficiency conditions ranging from 0→99% were examined. Surface plots were generated that provide ‘Damped Energy Density’ behavior as a function of transfer efficiency. The initial conditions for the transfer scenarios were similar to that used above:

- All vibration energy initially resides in the fundamental mode.
- The initial fundamental mode dynamic energy results from a high deformation condition defined by a deflection at the top of the structure equal to 10% of its height.

Figure 3-16 is a contour plot of the post-transfer ‘Damped Energy Density’ that includes both resultant vibration modes. As expected, 2nd mode dissipation increases as transfer efficiency increases. In all instances, the greatest dissipation per unit length occurs near the base. As the transfer efficiency increases, dissipation increases in the third quarter (50-75%) of the structure’s height.

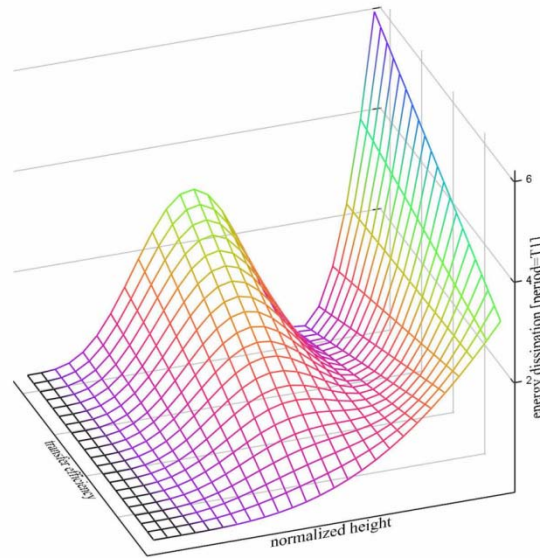


Figure 3-16 Energy Dissipation Density Contour [0→99% energy transfer]

In summary, ‘Damped Power Density’ and ‘Damped Energy Density’ functions were developed for a tall, flexible cantilever structure characterized by the typical roadside aluminum luminaire pole. The structure was taken to be prismatic and homogeneous. The functions were developed to investigate energy dissipation behavior of the ‘anelastic’ damping mechanism. Since the vibration modes are orthogonal, distribution functions of the discrete modes can be superimposed. The anelastic dissipation models were used to evaluate energy redistribution risks associated with the Modal Damping vibration control concept. The transfer scenario utilized in this evaluation involved energy transfer from the fundamental to the 2nd mode. Given equivalent dynamic energy in each of the fundamental and the 2nd vibration modes of the structure:

- The energy densities developed by the 2nd mode immediately within the base region of the structure are nearly twice those of the fundamental mode.
- Both the fundamental and the 2nd modes dissipate approximately the same energy over the lower 50% of the structures height.

- The 2nd mode utilizes the third quadrant of the structure’s height (50→75%) to dissipate nearly 50% additional energy than the fundamental mode given realistic transfer efficiencies. The utilization of the third quadrant makes the 2nd mode significantly more efficient than the fundamental mode in terms of dissipating dynamic energy.

3.1.7 Control Forces

Section 3.1.4 describes how a particular vibration mode could be excited by first elastically deforming the structure to match the profile, or shape of the desired mode, releasing it, and allowing the structure to free vibrate. The required deformation would only occur in the real world if the structure were subjected to the correct force distribution along its longitudinal axis. The relationship between lateral force distribution and spatial deflection can be determined beginning with Figure 3-5. In this case, equilibrium in the static sense yields,

$$EI \frac{d^4 v(z)}{dz^4} = f_i(z)$$

The mode shape function $v_i(z)$ is known by way of mode shape analysis. The modal deformations are given in Equation (3.6) for a prismatic, homogeneous cantilever. Deforming the ‘real world’ structure to identically match a complicated function may not be practical, or even possible given limited control input into the structure. So, how might a reasonable approximation of the force distribution be achieved in a practical manner?

A controllable tendon, or set of tendons, provides one possible means to deform the flexible structure and was selected for this analytic investigation. Figure 3-17

diagrams the generalized, single 3 point tendon configuration connected to the cantilever pole.

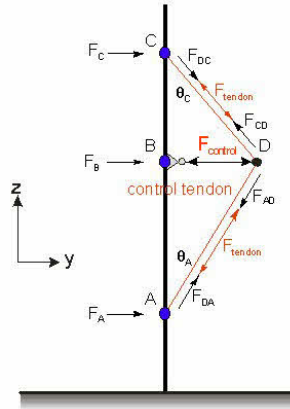


Figure 3-17 Generalized Cantilever/Tendon Configuration

Let the control input be defined as a single force generated from the structure at node- B, to the tendon at some location between the tendon's endpoints, node-D. When this single control force, $F_{control}$ is introduced between nodes B and D, three forces are subsequently distributed upon the structure at nodes A, B, and C. The induced structural forces are related to the control force and geometry of the cantilever/tendon configuration. When the structural deformation is small, the distributed forces have the following approximate values,

$$\begin{aligned}
 F_A &\approx \frac{b}{a+b} F_{control} \\
 F_B &\approx -F_{Control} \quad , \quad F_{control} \rightarrow small \\
 F_C &\approx \frac{a}{a+b} F_{control}
 \end{aligned}
 \tag{3.57}$$

Now consider Figure 3-18 where a 3-point single tendon device is connected to the cantilever pole for the purpose of forcing an approximated 2nd mode shape deformation. The diagram shows the pole, the deflection shape of the fundamental mode, and the deflection shape of the 2nd mode shape. The 2nd mode shape shown is

approximated from the computed modal matrix derived for the baseline aluminum pole, whose first three mode shapes were diagrammed in Figure 3-6. The single 3-point control tendon is overlaid on the diagram and scaled to induce its forces at key points of the 2nd mode shape. Specifically, nodes and anti-nodes (peak deflections and zero crossings) of the mode shape were selected as points to effect the control forces generated by the tendon. Different arrangements can be investigated to optimize the mode shape approximation but are not within the scope of this investigation.

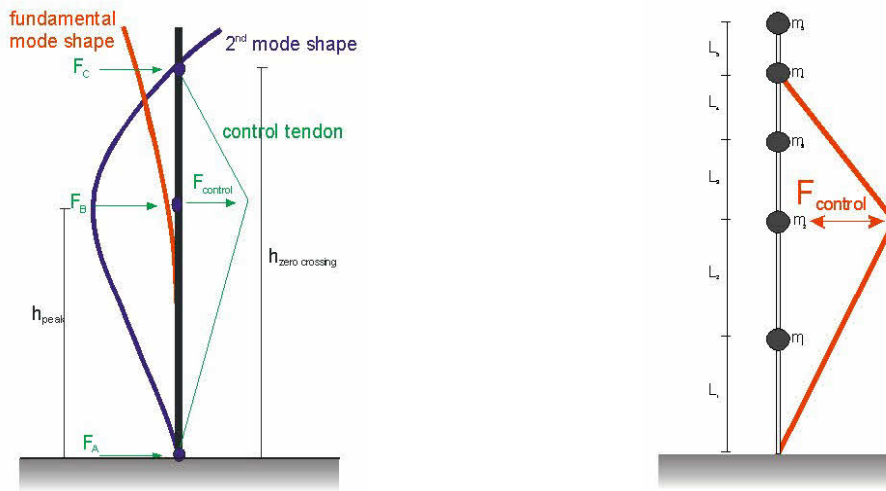


Figure 3-18 Control Tendon Geometry and Projection to Lumped Mass Model

The connection geometry and the control force polarities seem reasonable with regard to approximating the 2nd mode deflection shape. From Equation (3.57), the distributed force components for the diagrammed 3-point tendon geometry can more precisely be approximated as,

$$\begin{aligned}
 F_A &= \frac{(h_{zero\ cross} - h_{peak})}{h_{peak} + h_{zero\ cross}} F_{control} \\
 F_B &= -F_{Control} \\
 F_C &= \frac{h_{peak}}{h_{peak} + h_{zero\ cross}} F_{control}
 \end{aligned}
 , \quad F_{control} \rightarrow small \quad (3.58)$$

Figure 3-18 also illustrates how the 3-point tendon was ‘connected’ to the 5 node, 5-DOF lumped mass model of the cantilever pole used in the dynamic simulation. The normalized 2nd mode shape vector for the model, \mathbf{v}_2 (developed earlier and repeated here for convenience) was used to determine the 3-point tendon control force distribution scheme.

$$\mathbf{v}_2 = [.266 \quad .464 \quad .307 \quad -0.109 \quad -0.318]^T$$

The specific nodal forces required to develop the 2nd vibration mode nodal displacements specified by \mathbf{v}_2 can easily be determined using the elastic relationship

$$\mathbf{f} = \mathbf{K} \times \mathbf{v}_2$$

where \mathbf{K} is the stiffness matrix of the structure. As an example, the required input force vector needed to produce \mathbf{v}_2 was calculated to be

$$\mathbf{f} = f [.710 \quad 1 \quad .455 \quad -.102 \quad -.687]^T \text{ lbf} \quad (3.59)$$

Clearly the single 3-point control tendon cannot generate the necessary force vector \mathbf{f} to produce the exact mode shape for the reduced DOF model since the tendon can only effect control forces at three distinct points. Nevertheless, if the simple tendon connection configuration can induce vibration with measureable 2nd mode content, the approximation would have considerable potential. In fact, although the 2nd mode is the targeted mode, if fundamental energy is transferred to any higher order mode the approach would demonstrate value added as far as meeting control objectives.

The cantilever pole model was configured with a finite number of spatial nodes for simulation purposes, with each node representing lumped masses. The node location design defines the spatial resolution of the model. Control forces must be directed into one or more of the defined nodes in order to be compatible with the

cantilever/tendon implementation. The distribution profile of the desired force vector \mathbf{f} given in Equation (3.59) indicates that the peak displacement occurs at approximately node 2. And, the zero crossing occurs between nodes 3 and 4, but closer to node 4. This lead to the resultant control tendon/cantilever connection configuration diagrammed in Figure 3-18.

Given now the force component equations for the three point tendon, Equation (3.58), and the peak and zero-crossing node locations, the approximation for the 3-point tendon control force distribution vector for small deformation becomes,

$$\mathbf{u} = F_{control} [0 \quad 1 \quad 0 \quad -.381 \quad 0]^T$$

This control force distribution was evaluated with the cantilever model using an impulse as the control force; Figure 3-19 displays the resulting displacement response and the associated DFT.

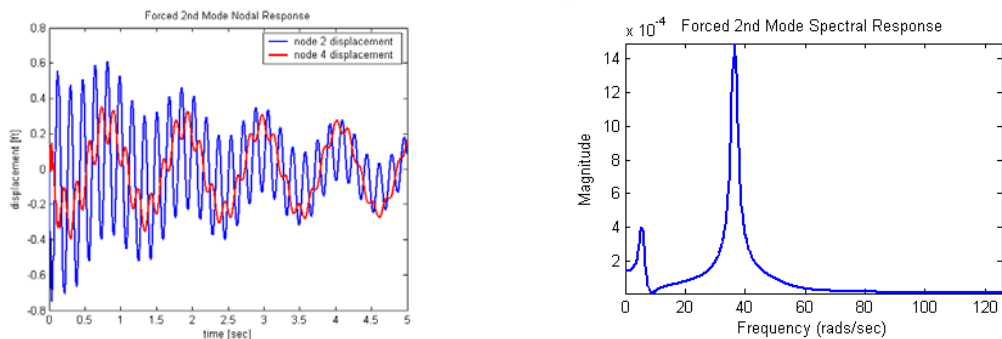


Figure 3-19 3-Point Tendon Configuration Effectiveness [Impulse Control Force]

The DFT was taken at node 2 of the model. The simulation responses indicated that the control force distribution scheme of the simple 3-point control tendon can in fact excite a 2nd mode response. And, although a fundamental mode component is also visible, significant vibration energy was coupled into the 2nd vibration mode. Furthermore, the tendon connection geometry can be reasonably approximated given a reasonable understanding of the structures mass and stiffness distributions.

3.2 Automated Control Implementation Strategy

At this point, the primary Modal Damping augmentation objective and its motivation were discussed and was stated earlier to be:

1. TRANSFER FUNDAMENTAL MODE DYNAMIC ENERGY TO THE 2ND VIBRATION MODE TO INCREASE THE OVERALL EFFECTIVE SYSTEM DAMPING (INTER-MODAL ENERGY TRANSFER).

Modal vibration impedance was discussed. The mathematical soundness of modal energy orthogonality was shown. And the feasibility of select mode excitation using a simple controllable actuation device was analytically demonstrated. The WHAT and the WHY have been discussed. The next step in the engineering process is the HOW.

The targeted structures of interest were tall and flexible and assumed relatively simple by design. The basic, economical 3-point controllable tendon was selected as the candidate actuator device to effect energy transfer. The final ‘strategic’ question addressed was how the actuator (tendon) was to be energized? Depending on external energy was counter to the overall objective: removing energy from the system at minimum cost. An alternate approach was conceived: to draw upon existing internal vibration energy to self-power the control forces. This lead to the second element of the Modal Damping objective:

2. HARVEST AND CONVERT THE KINETIC ENERGY OF THE VIBRATING STRUCTURE ITSELF TO SELF GENERATE THE NECESSARY CONTROL FORCES THAT ACTUATE INTER-MODAL ENERGY TRANSFER (SELF-POWERED).

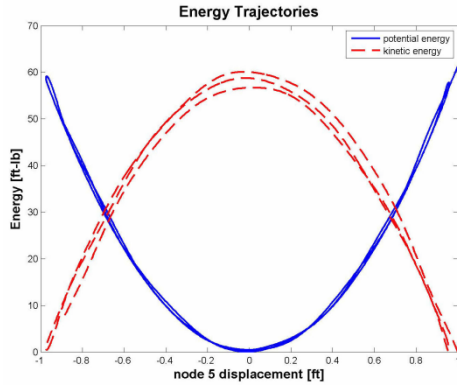
Specifically, the Modal Damping approach was required to utilize the dynamic energy of the fundamental vibration mode to self-transfer energy and excite 2nd mode vibrations via the 3-point tendon.

3.2.1 Control Logic

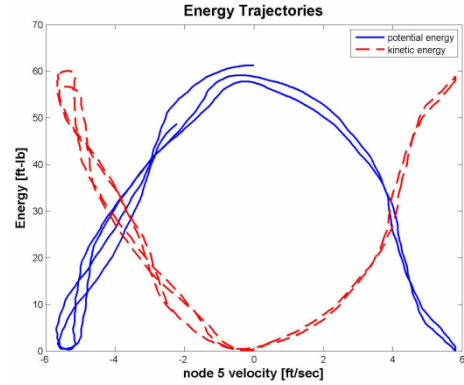
The detailed control logic design began by examining behavior associated with the fundamental mode from an energy perspective. Kinetic energy and potential energy complement themselves in 2nd order systems. Given that the system is underdamped, energy oscillates between the two energy states as the system responds to some input. This can be seen in the potential and kinetic energy trajectories of Figure 3-20 associated with the free vibrating simulated baseline structure, where

$$KE = \frac{\dot{\mathbf{x}}^T \times \mathbf{M} \times \dot{\mathbf{x}}}{2}, \quad PE = \frac{\mathbf{x}^T \times \mathbf{K} \times \mathbf{x}}{2}$$

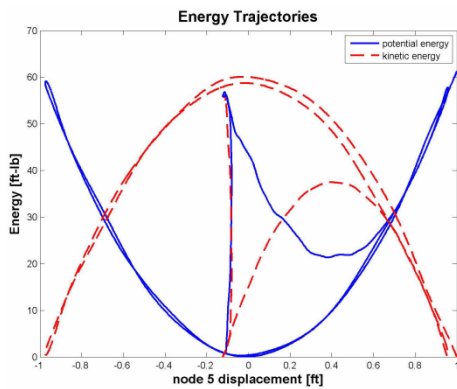
The trajectories shown were derived by plotting system energy as a function of displacement of the top node. Vibration was primarily fundamental mode as would be the case for these structural types. The queues that were determined necessary for the control logic to execute the modal energy conversion were determined from the behavior of these trajectories.



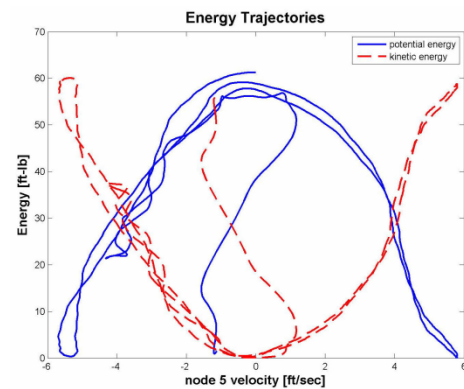
(a) Energy versus displacement
[without Modal Damping]



(b) Energy versus velocity
[without Modal Damping]



(c) Energy versus displacement
[with Modal Damping]



(d) Energy versus velocity
[with Modal Damping]

Figure 3-20 Vibration Energy Trajectories

The modal energy transfer procedure should ideally begin at the peak potential energy (minimal kinetic energy) point in the sway cycle of the fundamental mode component. This occurs when the structure is maximally deformed in the fundamental mode shape. The energy trajectories of Figure 3-20a & b show that peak potential energy coincides with node-5 velocity being minimized and its displacement maximized. Figure 3-20c & d were included to show the effects of Modal Damping on system energy trajectories once exercised. Note that once Modal Damping was implemented, the maximum Node-5 displacement and velocity visibly reduce. This behavior is discussed in more detail in Chapter 4. Trajectories were generated by the dynamic simulation after the control

modeling was completed and integrated. Once the Modal Damping transfer decision is made, the fundamental mode kinetic energy is redistributed through the 3-point tendon to reform the structure to approximate the 2nd mode shape during the following half-way cycle. Clearly control timing is important. The kinetic energy trajectory is used to make this assessment and synchronize the conversion. Modal energy transfer occurs throughout the kinetic energy phase of the fundamental mode cycle, the Modal Damping transfer is completed at the end of the kinetic phase of the cycle.

Admittedly, the conversion narrative to this point may not by itself provide an adequate visualization of the process. The following control sequence description is intended to offer a visual image of the mechanics of the energy transfer process.

3.2.2 Control Sequence

The sequence of control events for the 3-point tendon is summarized in the diagram of Figure 3-21. The sequence contains four still frame schematics of the cantilever-tendon as they sway.

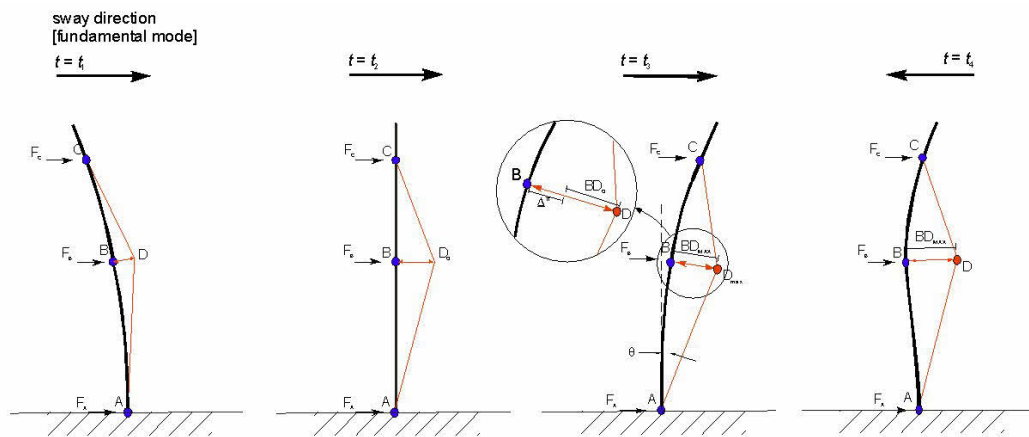


Figure 3-21 Tendon Control Sequence

The first three frames capture the cantilever at different positions as it sways from left to right. The snapshot of the last frame captures the cantilever-tendon in the “LOCK”

mode as the couple begin their sway back to the left. The simulation control device is shown in the drawings as element BD. The control variable was defined as the length of BD. It was assumed that element BD has the ability to vary its length and to 'LOCK/UNLOCK' at a commanded position.

Frame #1: The first frame captured the cantilever at the beginning of a sway cycle (for the purpose of this discussion). It is deformed (leaning) to the left, nodal velocities are zero, potential energy of the system is at a maximum. The control element BD is at its shortest length.

Frame #2: The cantilever is swaying from left to right; the frame captures the cantilever as it passes through its zero deformation state. Nodal velocities and system kinetic energy are at maximum. The element BD is at its static length.

Frame #3: This frame captures the state of the cantilever-tendon pair at the instant the sway of the fundamental mode has completed its travel to the right. Its nodal velocities are again zero and potential energy is again at its maximum. The cantilever is about to continue the cycle and transition its direction to the left. At this instant, the length of element BD is at its greatest. The control logic shall recognize this state and 'LOCKS' the length of the control element BD.

Frame #4: The strain energy stored in the deformed structure described in frame #3 forces the cantilever to sway left. However, as it begins to sway left, the 'LOCKED' control element temporarily forms a semi-rigid structure defined by the quadrangle ABCD. This rigid body within the structure rotates about Node-A as the cantilever sways left. It maintains its quadrangular shape. The control logic continues to monitor key nodal velocity states associated with the fundamental mode during this phase of the sway cycle. As the end of the left-sway is detected, the cantilever is maximally deformed by the rigid body

connections created by the ‘LOCKED’ tendon. The kinetic energy of the fundamental mode was harnessed and re-shaped the cantilever. At this point, the control logic releases the ‘LOCKED’ state of element BD, and the strain energy of the reshaped cantilever excites higher vibration modes that were shown to be functions of the re-shaped condition.

3.2.3 Simulation Specifications for the Cantilever-Tendon Geometry

The following basic geometric specifications were established to ‘baseline’ the mechanization of the cantilever-tendon pair Modal Damping energy transfer sequence. The established geometric specifications facilitated the simulation of the cantilever-tendon pair dynamics. It is important to note that although these specifications controlled the simulation design, they do not necessarily reflect a real-world design implementation per se. The concept demonstration design discussed in Section 5.2 leveraged off of the simulated design, but its mechanization was more pragmatic. For purposes of simulation, the design specifications with respect to Modal Damping mechanization were as follows:

- The length of the tendon (ADC) remained constant, and was considered to be constructed using a single flexible cable. The tendon element ratio $\frac{AD}{CD}$ remained constant.
- The control member (BD) was pinned-connected to the pole at node B so that it rotated freely. No moments were generated at the connection node B. The connection of the control element to the cable at point D was also a pin type connection. The connection was non-sliding at D, but enabled rotation.

- The length of the control element (BD) varied as the pole vibrated; its length was controllable and was used as a control input during the closed loop design.
- Analysis of the pole/tendon geometry indicated that the length of the control element (BD) was expressible as a function of nodal displacement

3.2.3.1 Sensor Requirements

Accelerometers were selected to measure nodal state behavior. Accelerometers were simulated at selected nodes. For the cantilever structure, they were placed at nodes 2 and 4. These signals were used by the control logic to determine sway cycle states and tendon control timing.

CHAPTER IV

MODAL DAMPING SIMULATION AND ANALYSIS

This section describes the dynamic modeling details and simulation approach. The simulation results of the Modal Damping Concept as applied to the baseline cantilever structure are presented and evaluated.

4.1 Dynamic Modeling of the Baseline Flexible Cantilever Structure

In nearly all cases, the design and evaluation effort of closed-loop feedback control occurs as an analytical process. Simulation offers a methodical and powerful, yet economical design approach. In keeping with this philosophy, the MATLAB/SIMULINK (Version 2007a) environment was selected to host the simulation. The optimal level of model fidelity is generally found to be a trade-off between algorithm complexity and its computational demands versus accurate dynamical behavior. A reduced order model is typically implemented, sometimes by design, often by circumstance since higher order physics of complex systems are not always completely understood. The system of interest was a simple cantilevered structure whose dynamics have been studied at infinitum. It posed no unusual modeling challenges. However, the phenomenological model of the tendon interaction was more compelling.

An aluminum luminaire support typical of roadside application (reference discussion in Chapter I) was selected as the representative plant. The poles stand 42 feet

in height above the transformer base. The cross section of the pole varies along its length. The base diameter is 8 inches with .25 inch wall thickness. It maintains the 8 inch diameter for the first 24 feet, followed by a 15 foot tapered section. The final 3 feet is again uniform with a diameter of 6 inches. Figure 4-1a is a simple schematic drawing of the pole.

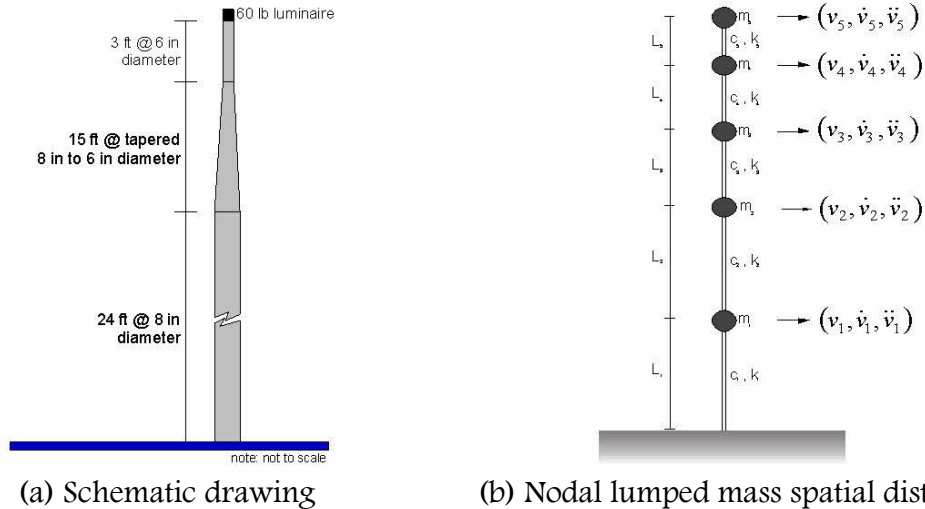


Figure 4-1 Baseline Cantilever Pole and Lumped Mass Model

Basic dynamic requirements for the cantilever included the following:

- Highly underdamped harmonic behavior. Damping properties were initially determined using test measurements of actual roadside poles combined with the Kareem linear predictive model (Section 3.1.1.2). Damping parameters were later adjusted using the results of the Anelastic Damping Parameter Assessment results (Section 5.1) once available.
- Elastic deformation caused only by flexural forces. The cantilever cross-section was assumed to remain planar throughout the vibration sway cycle.
- Negligible axial deformation.

- The fundamental mode and a small set of higher order modes were of interest. This study was specifically concerned with the fundamental and 2nd vibration modes. The continuous system was discretized accordingly. A five degree-of-freedom (DOF) dynamic model was designed and implemented to capture the necessary dynamics.

4.1.1 Model Formulation

Nodal locations were selected to:

- 1.) Differentiate physical cross-sectional properties of the pole.
- 2.) Capture the necessary vibration mode dynamics of the first three modes.
- 3.) Provide sufficient resolution for coupling control forces.

The equations of motion for each of the identified nodal points were formulated to satisfy general nodal force equilibrium constraints.

$$m_i \ddot{y}_i(t) + c_i \dot{y}_i(t) + k_i y_i(t) = f_i(t) \quad (4.1)$$

where, $\ddot{y}_i(t)$, $\dot{y}_i(t)$, and $y_i(t)$ represent the i^{th} nodal acceleration, velocity, and displacement at time t . $f_i(t)$ represents external excitation forces introduced at the i^{th} node.

4.1.1.1 Mass Distribution

Lumped masses were associated with each of the distributed nodes. Assigning tributary regions to nodes is a common approach to distributing loads for structural analysis. General rules of thumb were used; nodal masses were set equal to one-half the sum of the actual mass of the segments above and below the nodes location,

$m_i = \frac{mass_{L_i} + mass_{L_{i+1}}}{2}$. The top lumped mass was set equal to one-half the actual mass of the upper segment and also included the mass of a 60 pound luminaire for full system simulation. The general lumped mass schematic of the flexible cantilever model is shown in Figure 4-1b. There was no expected mass coupling in this geometry; torsional vibration was negligible for the baseline cantilever. The mass matrix was formed by inspection, becoming a simple diagonal matrix.

$$\mathbf{M} = \begin{bmatrix} m_1 & 0 & \cdots & 0 \\ 0 & m_2 & & \\ \vdots & & \ddots & \\ 0 & & & m_n \end{bmatrix}$$

4.1.1.2 Gravity Influence Matrix

Because the structure was flexible by definition, significant deformation was expected to occur. The effect of gravity on nodal lateral forces was considered and consequently included in the linear model. Figure 4-2 diagrams the linearized gravity component.

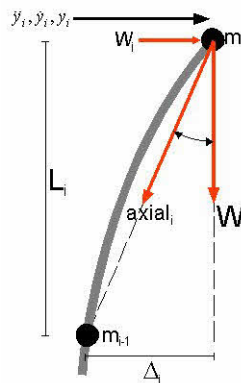


Figure 4-2 Gravity Force Contribution

The weight of the nodal mass during high deformation states projects an additional lateral force component and was modeled as a function of the nodal displacement:

$$w_i = W_i \tan(\theta) = W_i \left(\frac{\Delta_i}{L_i} \right) = m_i g \left(\frac{y_i - y_{i-1}}{L_i} \right)$$

When the effects of gravity are included, Equation (4.1) becomes,

$$m_i \ddot{y}_i(t) + c_i \dot{y}_i(t) + k_i y_i(t) = f_i(t) + w_i(t)$$

Substituting the linear definition for the weight component $w_i(t)$ yields,

$$m_i \ddot{y}_i(t) + c_i \dot{y}_i(t) + \left(k_i - \frac{g m_i}{L_i} \right) y_i(t) + \frac{g m_i}{L_i} y_{i-1}(t) = f_i(t) \quad (4.2)$$

This general form of the equation of motion is used for each nodal equation. When taken together, the equations form a set of coupled differential equations that must be solved simultaneously. The equation set that includes the gravity influence can be expressed in matrix form,

$$\mathbf{M} \times \ddot{\mathbf{y}}(\mathbf{t}) + \mathbf{C} \times \dot{\mathbf{y}}(\mathbf{t}) + (\mathbf{K} + \mathbf{G}) \times \mathbf{y}(\mathbf{t}) = \mathbf{f}(\mathbf{t}) \quad (4.3)$$

where $\mathbf{y}(\mathbf{t})$ is the nodal displacement vector, \mathbf{M} , \mathbf{C} , and \mathbf{K} are the mass, damping, and stiffness matrices respectively. \mathbf{G} is defined as the gravity influence matrix. From Equation (4.2) above, the lateral nodal weight force component can be defined as

$$g_i(t) = \frac{g m_i}{L_i} \cdot [y_i(t) - y_{i-1}(t)]$$

Generalized in matrix form,

$$\mathbf{G}(t) = \mathbf{G} \times \mathbf{y}(t) = g \cdot \begin{bmatrix} \frac{m_1}{L_1} & 0 & 0 & \cdots & 0 \\ -\frac{m_2}{L_2} & \frac{m_2}{L_2} & 0 & \cdots & 0 \\ \vdots & & \ddots & & \vdots \\ 0 & \cdots & -\frac{m_{n-1}}{L_{n-1}} & \frac{m_{n-1}}{L_{n-1}} & 0 \\ 0 & 0 & \cdots & -\frac{m_n}{L_n} & \frac{m_n}{L_n} \end{bmatrix} \cdot \begin{bmatrix} y_1(t) \\ y_2(t) \\ \vdots \\ y_{n-1}(t) \\ y_n(t) \end{bmatrix} \quad (4.4)$$

For programming purposes, the gravity influence matrix can be re-arranged as,

$$\mathbf{G} = g \cdot \begin{bmatrix} \frac{m_1}{L_1} & 0 & 0 & \cdots & 0 \\ 0 & \frac{m_2}{L_2} & 0 & \ddots & 0 \\ 0 & 0 & \ddots & & \vdots \\ \vdots & & & \frac{m_{n-1}}{L_{n-1}} & 0 \\ 0 & 0 & \cdots & 0 & \frac{m_n}{L_n} \end{bmatrix} \cdot \begin{bmatrix} 1 & 0 & 0 & \cdots & 0 \\ -1 & 1 & 0 & & 0 \\ 0 & -1 & 1 & & 0 \\ \vdots & & \ddots & \ddots & \vdots \\ 0 & 0 & \cdots & -1 & 1 \end{bmatrix} \quad (4.5)$$

4.1.1.3 Stiffness Distribution

Except for the simplest of structures, the stiffness matrix \mathbf{K} is not readily known or directly measurable but can generally be computed. Computation is straightforward for the cantilever. If necessary, Bernal ^[99] discusses how a flexibility matrix can be extracted at sensor coordinates from collected data for a realized minimum order state-space model. \mathbf{K} for the baseline cantilever can be computed using one of several methods. Regardless of the particular approach, the equilibrium equations are generally used in an inverse manner; \mathbf{K} is computed from forced and measured deformations. If the system has been discretized a set of algebraic equations can be developed and used

to solve for \mathbf{K} , where $\mathbf{K} \times \mathbf{y}(\mathbf{t}) = \mathbf{f}(\mathbf{t})$. \mathbf{K} was assumed to be constant and time-invariant. Static loading can be used when feasible, harmonic loading can alternatively be used. Realistically, there may be technical and practical limitations to experimentally determining stiffness properties of full scale structures. Furthermore, many force sets and many measurements may be necessary to satisfy the fidelity of the model desired.

Analytical solutions offer practical advantages when compared to their experimental counterparts. Two fundamentally different approaches are considered herein. The first approach is based on a dynamic loading scenario. J. J. Conner ^[100] suggests that stiffness parameters can be selected so that the fundamental mode shape of the structure is satisfied. The underlying assumption is that the fundamental mode shape is independent of damping. This is reasonable for highly underdamped structures.

The second approach determines stiffness parameters based on static loading profiles. There are a number of variations. In general, the structure is first decomposed into beam elements. Virtual work or slope-deflection methods can then be used to compute the stiffness coefficients directly or, indirectly after first computing the flexibility matrix ^[101]. The different approaches were each considered and are briefly described and compared below.

Consider Conner's approach. He showed that if the fundamental vibration mode dynamics are known via measurement, observation, or some other means, the stiffness factors of the discrete beam elements can be computed.

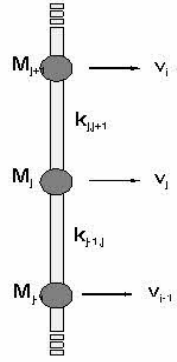


Figure 4-3 Discretized Mass Model

For a discretized, multiple-degree-of-freedom un-damped system schematically depicted in Figure 4-3, the nodal equilibrium equations can be expressed in matrix form as

$$\mathbf{M} \times \ddot{\mathbf{y}}(t) + \mathbf{K} \times \mathbf{y}(t) = \mathbf{f}(t) \quad (4.6)$$

\mathbf{M} is the known diagonalized mass matrix, $\mathbf{f}(t)$ represents the set of external forces that for this discussion is set to $\mathbf{0}$ because the system is assumed to be in a state of free vibration. \mathbf{K} is the unknown stiffness matrix. $\mathbf{y}(t)$ is the time varying displacement vector. Here it is defined to represent the specialized case

$$\mathbf{y}(t) = \mathbf{v}_{\text{model}} \cos(\omega_1 t + \delta) \quad (4.7)$$

where $\mathbf{v}_{\text{model}}$ is the n -dimension fundamental mode shape vector of the form:

$$\mathbf{v}_{\text{model}} = \begin{bmatrix} v_1 \\ v_2 \\ \vdots \\ v_n \end{bmatrix}$$

The elements of $\mathbf{v}_{\text{model}}$ each represent fundamental mode shape displacements at their respective nodal location in structure.

Substituting the definition for $\mathbf{y}(t)$ into Equation (4.6) yields:

$$\mathbf{K} \times \mathbf{v}_{\text{model}} = \omega_1^2 \cdot \mathbf{M} \times \mathbf{v}_{\text{model}} \quad (4.8)$$

At this point, Connor suggests that the un-damped equilibrium expression for any given node can be treated as if it were a statically loaded. Referencing the general discrete model diagrammed in Figure 4-3, nodal equilibrium can be approximated as:

$$f_j = (y_j - y_{j-1})k_j + (y_j - y_{j+1})k_{j+1} \quad (4.9)$$

Which, when all equations are taken together form

$$\tilde{\mathbf{V}} \times \mathbf{k} = \mathbf{f}$$

Assuming now that $\mathbf{f} \rightarrow \omega_1^2 \cdot \mathbf{M} \times \mathbf{v}_{\text{model}}$, and $\tilde{\mathbf{V}}$ is a Relative Displacement Matrix:

$$\tilde{\mathbf{V}} = \begin{pmatrix} v_1 & v_1 - v_2 & \cdots & 0 \\ 0 & v_2 - v_1 & v_2 - v_3 \cdots & 0 \\ 0 & 0 & \ddots & 0 \\ 0 & 0 & 0 & v_n - v_{n-1} \end{pmatrix}$$

where each individual element $\tilde{\mathbf{V}}_{i,j}$ represents the relative displacement between nodes i and j for the fundamental mode shape. The stiffness vector \mathbf{k} for that particular mode can now be determined.

$$\mathbf{k}_i = \tilde{\mathbf{V}}_i^{-1} \times \mathbf{f} = \omega_i^2 (\tilde{\mathbf{V}}_i^{-1} \times \mathbf{M} \times \mathbf{v}_i) \quad (4.10)$$

Conner's approach yields the stiffness matrix necessary to dynamically model the subject cantilever. However, what is required to utilize this approach is the mode shape vector \mathbf{v}_i and the modal vibration frequency ω . This approach is valuable when deriving the stiffness distribution for existing structures using measured vibration data.

An alternate analytical approach offers mathematical elegance when the structural geometry is known and analytical as was the baseline cantilever where the

equilibrium expressions for internal stresses and strains were able to be expressed in continuous form. Geometric and material properties were required, but known. Flexural deformation was assumed for the tall flexible structure, but this approach is equally apropos for more complicated deformations. Stiffness factors were computed using the principle of Complimentary Virtual Work (CVW) by establishing static force-deformation relationships that enable the construction of the system flexibility matrix \mathbf{S} .

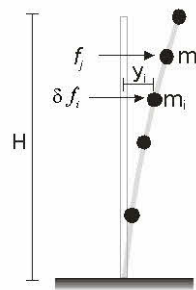


Figure 4-4 Complimentary Virtual Work Schematic

The elements of \mathbf{S} are the flexibility influence coefficients that quantify the elastic relationship between nodal forces and displacements: s_{ij} represents the deflection influence factor of node i to a force introduced at node j . The composite static relationship is expressed as,

$$\begin{bmatrix} y_1 \\ y_2 \\ \vdots \\ y_n \end{bmatrix} = \begin{bmatrix} s_{11} & s_{12} & \cdots & s_{1n} \\ s_{21} & s_{22} & \cdots & s_{2n} \\ \vdots & \vdots & \ddots & \vdots \\ s_{n1} & s_{n2} & \cdots & s_{nn} \end{bmatrix} \cdot \begin{bmatrix} f_1 \\ f_2 \\ \vdots \\ f_n \end{bmatrix}$$

The element solution set for \mathbf{S} is obtained through the relationship

$$s_{ij} = \frac{y_i}{f_j}, \quad f_{n \neq j} = 0$$

f_j is a ‘real’ external force introduced at node j . Subsequent nodal deflections at each node $i = 1 \rightarrow n$ are required and must be computed. A compatible ‘virtual’ force system is developed to facilitate the calculation. In this case, the virtual force was chosen to be a simple lateral force δf_i alternately introduced at each nodal location.

Equating internal and external work yields the flexibility coefficients,

$$s_{ij} = \frac{\int_0^H \delta M_i(z) \cdot \frac{m_j(z)}{E \cdot I} dz}{\frac{\delta f_i}{f_j}}$$

where: $\delta M_i(z)$ is the ‘virtual force system’ force distribution function (virtual force at node- i), $\frac{m_j(z)}{E \cdot I}$ is the ‘real deformation system’ curvature function (unit force at node- j), δf_i is the node- i ‘virtual force’, f_j is the ‘real force system’ nodal force (unit force at node- j) generating the deformation system. The stiffness matrix was subsequently found by inverting the flexibility matrix. The stiffness matrix, like the flexibility matrix, is fully populated and symmetric, a reflection of Maxwell’s law of reciprocal deflections^[102].

$$\mathbf{f} = \mathbf{S}^{-1} \times \mathbf{y} = \mathbf{K} \times \mathbf{y} = \begin{bmatrix} k_{11} & k_{12} & \cdots & k_{1n} \\ k_{21} & k_{22} & \cdots & k_{2n} \\ \vdots & \vdots & \ddots & \vdots \\ k_{n1} & k_{n2} & \cdots & k_{nn} \end{bmatrix} \cdot \begin{bmatrix} y_1 \\ y_2 \\ \vdots \\ y_n \end{bmatrix}$$

4.1.1.4 Damping Distribution

Unlike mass and stiffness properties, the level of damping of a structure is not easily measurable or calculable. Although damping can be associated with physical

mechanisms, phenomenological relationships do not exist at the macro level to simply compute the damping values associated with a given structure. Two different damping parameter sets were developed and utilized during the course of the simulation effort. Both data sets were based on deflection decay envelopes that were measured during free vibration tests. The initial parameter set was based upon results taken from characterization tests conducted on full roadside aluminum luminaire supports^[4,35]. The full scale testing provided the damping ratio associated with the fundamental mode. Higher order damping parameters were then extrapolated using the Kareem linear predictive model ^[103] (Section 3.1.1.2). Damping parameters were later adjusted using the results of the Anelastic Damping Parameter Assessment tests (Section 5.1) once available. A modified Logarithmic Decrement Algorithm (Section 5.1.2.1) was applied to determine modal damping coefficients,

$$\sigma = -\frac{\ln\left(\frac{y_0 \cdot e^{-\sigma(t+nT)} \sin(\omega_d(t+nT)+\phi)}{y_0 \cdot e^{-\sigma t} \sin(\omega_d t + \phi)}\right)}{nT}$$

from which, damping ratios were determined for the Kareem model,

$$\zeta_i = \frac{c_i}{2\sqrt{k_i m_i}} = \frac{c_i}{2m_i \omega_i} = \frac{\sigma_i}{\omega_i} \quad (4.11)$$

For the continuous cantilever pole there are an infinite number of vibration modes, each mode characterized by its own damping ratio ζ_i , shown above to be a function of the mode effective mass, damping and stiffness properties.

Once the necessary damping ratios ($\zeta_i, i = 1 \rightarrow n$) were estimated, the detailed system damping coefficient matrix \mathbf{C} was constructed. Constructing \mathbf{C} began with the de-coupled n differential nodal equations of the undamped system. The undamped n decoupled equations were individually completed with the damping properties given by

the damping ratios estimated by the Kareem model using Equation (4.11). The procedure is described in detail below.

The system equations were decoupled by casting the problem as a symmetric eigenvalue problem ^[104] as discussed in Section 3.1.3. Symmetric system coefficient matrices offer real valued eigenvalues and eigenvectors. The construction of the damping matrix \mathbf{C} began with transformation of the system equations to the symmetric eigenvalue form. The mass normalized stiffness matrix was determined to be $\tilde{\mathbf{K}} = \mathbf{M}^{-\frac{1}{2}} \times (\mathbf{K} + \mathbf{G}) \times \mathbf{M}^{\frac{1}{2}}$. The algebraic eigenvalue problem was then formed as $(\lambda \mathbf{I} - \tilde{\mathbf{K}}) \times \mathbf{v} = 0$ from which the eigenvalues and eigenvectors were derived enabling the formation of the normalized modal matrix ^[105],

$$\mathbf{T} = \begin{bmatrix} \frac{v_1}{\|v_1\|} & \frac{v_2}{\|v_2\|} & \dots & \frac{v_n}{\|v_n\|} \end{bmatrix}$$

The modal matrix represents the orthonormal basis for the structural dynamic response. By way of a linear transformation of state variables the modal matrix decouples the mass normalized stiffness matrix to form a diagonalized eigenvalue matrix Λ ,

$$\Lambda = \mathbf{T} \tilde{\mathbf{K}} \mathbf{T} = \begin{bmatrix} \lambda_1 & 0 & \dots & 0 \\ 0 & \lambda_2 & & \\ \vdots & & \ddots & \\ 0 & 0 & & \lambda_n \end{bmatrix}$$

Letting $\mathbf{y}(t) = \mathbf{M}^{-\frac{1}{2}} \times \mathbf{T} \times \tilde{\mathbf{y}}(t)$, substituting into the system of un-forced, damped equations of motion, and pre-multiplying by $\mathbf{T}^{-1} \times \mathbf{M}^{\frac{1}{2}}$, yields:

$$(\mathbf{T}^{-1} \times \mathbf{T}) \ddot{\tilde{\mathbf{y}}}(t) + \left(\mathbf{T}^{-1} \times \mathbf{M}^{-\frac{1}{2}} \times \mathbf{C} \times \mathbf{M}^{\frac{1}{2}} \times \mathbf{T} \right) \dot{\tilde{\mathbf{y}}}(t) + \left(\mathbf{T}^{-1} \times \mathbf{M}^{-\frac{1}{2}} \times (\mathbf{K} + \mathbf{G}) \times \mathbf{M}^{\frac{1}{2}} \times \mathbf{T} \right) \tilde{\mathbf{y}}(t) = 0$$

Simplifying,

$$\ddot{\tilde{\mathbf{y}}}(t) + \Lambda_c \dot{\tilde{\mathbf{y}}}(t) + \Lambda_k \tilde{\mathbf{y}}(t) = 0 \quad (4.12)$$

The coefficient matrix Λ_c represents the diagonalized modal damping matrix [106],

$$\Lambda_c = \begin{bmatrix} \chi_1 & 0 & \cdots & 0 \\ 0 & \chi_2 & & \\ \vdots & & \ddots & \\ 0 & 0 & & \chi_n \end{bmatrix}$$

The diagonal elements of Λ_c represent decoupled, modal damping factors that can now be computed using Equation (4.11) above.

$$\zeta_i = \frac{\chi_i}{2 \cdot \sqrt{\lambda_i m_i}}$$

Once the diagonal modal damping factors are determined, the damping matrix \mathbf{C} can finally be back-calculated as

$$\mathbf{C} = \mathbf{M}^{-\frac{1}{2}} \times \Lambda_c \times \mathbf{T} \times \mathbf{M}^{\frac{1}{2}}$$

4.1.2 MATLAB/SIMULINK Implementation

The generalized cantilever model described above was implemented in SIMULINK [107], a powerful block diagram based environment. A state-space model convention was utilized.

$$\begin{aligned} \dot{\mathbf{x}} &= \mathbf{A} \times \mathbf{x} + \mathbf{B} \times \mathbf{u} \\ \mathbf{y}_{out} &= \mathbf{C}_{out} \times \mathbf{x} + \mathbf{D} \times \mathbf{u} \end{aligned}$$

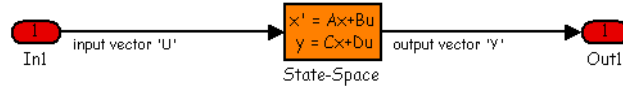


Figure 4-5 SIMULINK State Space Function Block

where \mathbf{x} is the vector of state variables and \mathbf{u} is the vector of input excitation forces. \mathbf{y}_{out} , the observed output vector of the state space model, is not to be confused with \mathbf{y} used above in the system differential equations. This state space convention was easily implemented in SIMULINK using a simple, built-in toolbox functional block shown in Figure 4-5.

From Equation (4.3), the mass normalized system equations became,

$$\ddot{\tilde{\mathbf{y}}}(t) + \mathbf{M}^{-\frac{1}{2}} \times \mathbf{C} \times \mathbf{M}^{-\frac{1}{2}} \times \dot{\tilde{\mathbf{y}}}(t) + \mathbf{M}^{-\frac{1}{2}} \times (\mathbf{K} + \mathbf{G}) \times \mathbf{M}^{-\frac{1}{2}} \times \tilde{\mathbf{y}}(t) = \mathbf{M}^{-\frac{1}{2}} \times \mathbf{f}(t)$$

$$\mathbf{y}(t) = \mathbf{M}^{-\frac{1}{2}} \cdot \tilde{\mathbf{y}}(t)$$

The state space structure yields $2n$ state variables for the n -DOF system; the n 2nd order differential equations were converted to $2n$ 1st order differential equations. The state variable vector took the following form:

$$\mathbf{x} = [x_1 \quad x_2 \quad \cdots \quad x_n \quad x_{n+1} \quad x_{n+2} \quad \cdots \quad x_{2n}]^T$$

$$= [\dot{\tilde{y}}_1(t) \quad \dot{\tilde{y}}_2(t) \quad \cdots \quad \dot{\tilde{y}}_n(t) \quad \tilde{y}_1(t) \quad \tilde{y}_2(t) \quad \cdots \quad \tilde{y}_n(t)]^T$$

The system coefficient matrix \mathbf{A} was easily constructed from the parametric matrices developed earlier: \mathbf{M} , \mathbf{C} , \mathbf{K} , and \mathbf{G} .

$$\mathbf{A} = \begin{bmatrix} -\mathbf{M}^{-\frac{1}{2}} \times \mathbf{C} \times \mathbf{M}^{-\frac{1}{2}} & -\mathbf{M}^{-\frac{1}{2}} \times (\mathbf{K} + \mathbf{G}) \times \mathbf{M}^{-\frac{1}{2}} \\ \mathbf{I}_{5 \times 5} & \mathbf{0} \end{bmatrix}$$

The gravity influence matrix was incorporated directly into the \mathbf{A} matrix using the modified stiffness matrix $(\mathbf{K} + \mathbf{G})$. An alternative approach would have been to incorporate \mathbf{G} outside the state space block as a feedback loop configured to form an

additional input, a gravity influence input, $\mathbf{u}_G = [\mathbf{0} \quad \mathbf{G}] \times \mathbf{x}$. The external feedback loop implementation offered immediate visualization of the gravity effects, however it was decided to assimilate \mathbf{G} directly into the \mathbf{A} matrix. In doing so the gravity effects were included in the synthesis of the system eigenvalues and eigenvectors.

The coefficient matrix \mathbf{B} helped map external excitation forces to analytical nodes of the structural model. \mathbf{B} was constructed as follows...

$$\mathbf{u}_{external} \Delta \mathbf{u} = f(t)_{test} = f(t) [\Delta u_1 \quad \cdots \quad \Delta u_n]^T$$

$$\therefore \mathbf{B} = \begin{bmatrix} \mathbf{M}^{-\frac{1}{2}} & \mathbf{0} \end{bmatrix}^T \rightarrow \dot{\mathbf{x}} = \mathbf{A} \times \mathbf{x} + \mathbf{B} \times \mathbf{u}_{external}$$

\mathbf{B} was designed as $2n \times n$ in dimension. $\mathbf{u}_{external}$ represented the distributed physical nodal forces for some given test scenario. The distribution vector $\Delta \mathbf{u}_{test}$ was tailored for the specific test, e.g. impulse, pluck, etc. In addition, a unique distribution vector was constructed to accommodate feedback forces for closed loop tendon operation.

\mathbf{C}_{out} and \mathbf{D} transform \mathbf{y}_{out} to observable or measurable system states. In forming the mass normalized equations, the following variable transformation was made, $\mathbf{y} = \mathbf{M}^{-\frac{1}{2}} \times \tilde{\mathbf{y}}$. A reverse transformation was required in order to observe real-world variables,

$$\mathbf{C}_{out} = \begin{bmatrix} \mathbf{M}^{-\frac{1}{2}} & \mathbf{0} \\ \mathbf{0} & \mathbf{M}^{-\frac{1}{2}} \end{bmatrix}$$

4.1.3 Model Validation

Once designed and implemented, basic analytic testing was conducted to provide some credence to the homogeneous behavior of the model. The simulated

cantilever was subjected to a virtual unit impulse forcing function to excite its characteristic response. If properly simulated, the impulse response is valuable as it excites all inherent vibration modes of the n-DOF distributed mass model. Although difficult to emulate in the real-world, the simulation world can easily accommodate the impulse function. The model is linear; the Laplace transfer of the impulse is

$$Laplace[u_{-1}(t)] = \int_0^{\infty} \delta(t) \cdot e^{-st} dt = 1 \quad \text{and the output becomes } \mathbf{X}(s) = (s\mathbf{I} - \mathbf{A})^{-1} \times \mathbf{B}.$$

The impulse was assumed to act on the cantilever in whole. The impulse force was distributed among the lumped masses based on simple cross-sectional area of the discretized sections. The mapping matrix \mathbf{B} was used to distribute the impulse force accordingly. The simulation results were evaluated against field test results of the modeled aluminum luminaire pole [108].

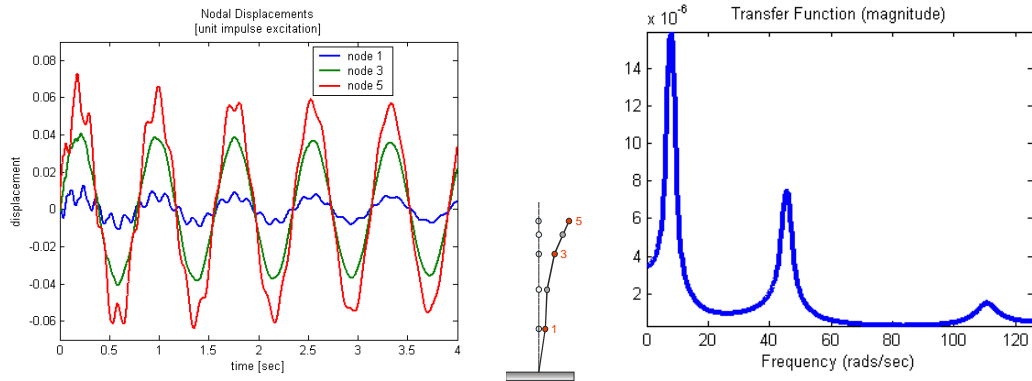
4.1.4 Impulse Test Results

Table 4-1 summarizes the resulting modal frequencies of the pole model with and without the top mounted luminaire. These analytically values were derived using the eigenvalues of the system state-space coefficient matrix \mathbf{A} . The added mass due of the top mounted luminaire introduced at the upper node of the model lowered frequencies of all modes as expected.

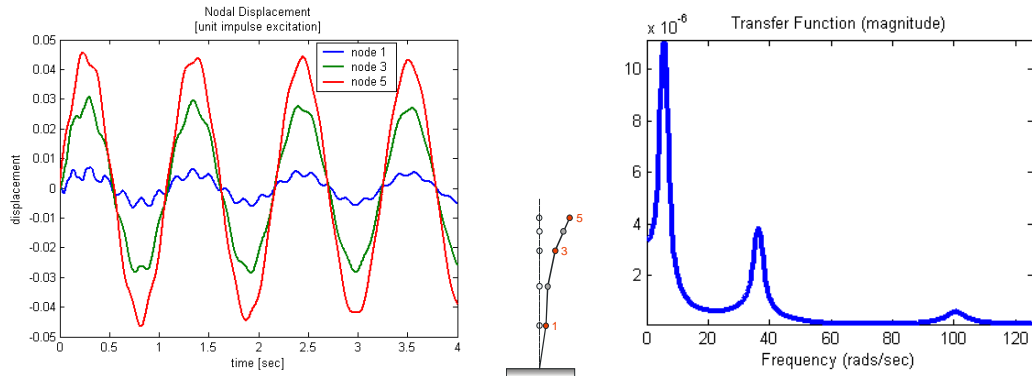
Table 4-1 Predicted Baseline Luminaire Cantilever Modal Frequencies

Pole Model [without luminaire]	Rad/sec	Hz
Fundamental Mode	7.9	1.26
Second Mode	45.6	7.3
Third Mode	110.8	17.6
Pole Model [with luminaire]		
Fundamental Mode	5.7	.91
Second Mode	36.4	5.8
Third Mode	100.9	16.1

Nodal displacements responses from a simulated unit impulse response and the associated Fast Fourier Transforms (FFT) for the pole model are shown in the Figure 4-6. The spectral content shown in the FFT corroborates the expected eigenvalue results providing a sense of satisfactory implementation in the SIMULINK environment. Displacement responses for nodes 1, 3, and 5 are shown in the figure, node-5 being at the top of the cantilever. The traces of the nodal displacement reveal the superimposed higher order modal components. The FFT was performed on the response computed for Node-1. The addition of the top mounted luminaire produces a minor, but visible impact on the dynamic behavior of the cantilever pole. The relative magnitudes between the modal components (with versus without the luminaire) illustrated in the FFT indicate that the inclusion of the luminaire mass resulted in more vibration energy being coupled into the fundamental mode (compare $\frac{1^{st} \text{ mode}}{2^{nd} \text{ mode}}$ ratio) given the same force distribution. However, the increased inertia of the luminaire resulted in the modal sway displacements being reduced.



(a) Nodal displacements and FFT [without top mounted luminaire]



(b) Nodal displacements and FFT [with top mounted luminaire]

Figure 4-6 Unit Impulse Test Simulation Results

4.2 Coupled Tendon/Cantilever Phenomenological Model Design

A 3-point tendon was selected as the control mechanism to distribute control forces along the cantilever structure. As discussed in Section 3.1.7, the 3-point tendon when properly connected was shown to distribute control forces that deformed the cantilever structure in such a way that it approximated the shape of the 2nd vibration mode. The generalized cantilever/tendon configuration was given in Figure 3-17 and is repeated below. The element BD in the configuration was defined as the controlling element of the 3-point tendon.

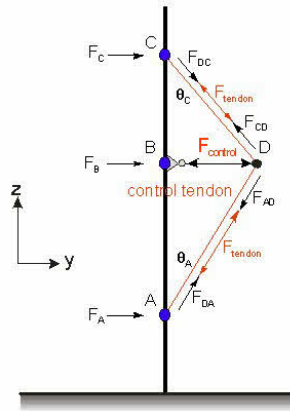


Figure 4-7 Generalized Cantilever/Tendon Configuration (repeated)

During tendon activation, compression control forces are generated along the axis of BD. The tendon distributes the control force to Nodes A and C. As was discussed, a major feature/benefit of this particular approach is that the control force driving the tendon is self-harvested from the kinetic forces of the motion of the cantilever itself. No external energy is required to reshape the cantilever.

The established geometric specifications of the integrated tendon configuration that affected its modeling approach were introduced in Section 3.2.3 and are summarized below:

1. The length of the tendon (ADC) was required to remain constant, and was assumed to act as a single cable.
2. The tendon section ratio $\left(\frac{AD}{CD}\right)$ was required to remain constant.
3. The control element (BD) was required to be a rigid member able to resist compressive forces.
4. The control element (BD) was required to be pinned-connected to the pole at Node B resulting in zero-moment rotation. The connection of the control element to the

- cable at Node D was required to be a non-sliding, pin type connection enabling zero-moment rotation.
5. The control element (BD) was required to be variable in length.
 6. The instantaneous length of the control member, $|BD(t)|$, was a function of pole sway. Analysis of the pole/tendon geometry showed that $|BD(t)|$ was a function of nodal displacement, $BD(t) = f(x_A(t), x_B(t), x_C(t))$. Its instantaneous length was required as a control variable.

4.2.1 Cantilever/Tendon Pair Dynamic Model... The Philosophical Approach

Philosophically, establishing the simulation topology was simple process; it emerged from an engineering background somewhat biased by control theory. The control tendon when coupled to the cantilever pole was considered to form a closed loop feedback system as diagrammed in Figure 4-8. The simulation design and implementation proceeded accordingly. When commanded at the appropriate phase in the vibration cycle, the tendon 'LOCKED' into a rigid configuration using the control member BD, redistributing kinetic energy along the cantilever as forces. The distributed forces were believed to act, and were modeled as feedback forces that were inputted into the dynamic model of the cantilever as shown diagrammed in Figure 4-8. The feedback forces were assumed to act on the cantilever in the same manner as any external forcing function. The cantilever was assumed to be, and was modeled as behaving linearly for the dynamical environment of interest. As a linear device, the cantilever 'doesn't care' where, when, or how its excitation forces are generated. It superimposes the forced response due to the feedback with those of other forces acting upon it.

Also shown diagrammed in Figure 4-8 is a second feedback loop... an outer loop. This outer loop establishes the logic path of the Modal Damping control law that generates the 'LOCK' command at the appropriate time in the vibration cycle. The Modal Damping control law is of course, the major component to the proper operation of the system in both the virtual world as well as the real world.

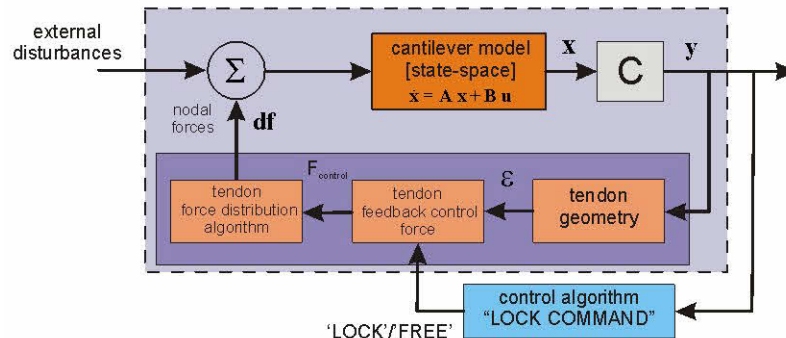


Figure 4-8 Closed-Loop Cantilever/Tendon Block Diagram

The configuration of Figure 4-8 represents the implemented design scheme. The scheme maintains the mathematical distinctiveness of the cantilever and adds the distinctiveness of the tendon as a separate stand-alone entity. This stand-alone approach required that each of the diagrammed functional blocks be mathematically detailed with input/output variable sets and the transfer relationships between the sets.

An alternate approach would have been to model the cantilever/tendon pair as an integrated system... a black box approach with some unified set of equations of motion defined for the coupled pair. This approach was thought to be viable and could have been accomplished by assuming that the coupled pair in fact formed a single structure with:

- The same approximate mass distribution as the cantilever alone (the tendon elements add little mass, but nevertheless can be accounted for and distributed).
- A new stiffness distribution.

- The same approximate damping distribution as the cantilever alone (negligible damping is expected to occur within the tendon elements since negligible deformation would occur).

The segregated cantilever/tendon or stand-alone approach was selected and implemented as part of this investigation. It offered the advantage of increased visibility into the physical parameters of the coupled pair. Instantaneous forces within the tendon elements were easily accessible for example. The preferred approach also lacked the transition problems that the alternative unified approach was thought to experience when switching from a NOT 'LOCKED' state to a 'LOCKED' state, and vice-versa.

The stand-alone algorithms (functional blocks) that were required to be developed to capture the cantilever/tendon physics followed from Figure 4-8, they were:

- A dynamic model of the cantilever structure (described in Section 4.1).
- A spatial geometry algorithm for the tendon.
- A feedback force distribution algorithm for the coupled pair.
- A Modal Damping control law contained in the outer feedback loop.

The algorithms for functions 2, 3 and 4 are described in the following sections.

4.2.2 Tendon Geometric Algorithm

The instantaneous length of element BD (See Figure 4-9), hereafter referred to as BD_length , is a required parameter for accurate simulation. It was primarily used to determine feedback force distribution once the element is commanded 'LOCKED'. In the real or physical world, force distribution occurs naturally given the instantaneous geometry of the tendon/cantilever pair and their dynamical states. In the simulation,

or virtual world, the geometry must be determined analytically at a rate required by the simulation. Furthermore, force distribution does not occur naturally in the virtual world. It will be shown to be a function of the instantaneous geometry of the coupled pair.

The following geometric analysis was somewhat tedious, but not thought to be of an advanced nature. It is reviewed here for completeness. Figure 4-9 shows the relative geometry of interest for the generalized cantilever/tendon pair at some time during its vibration cycle.

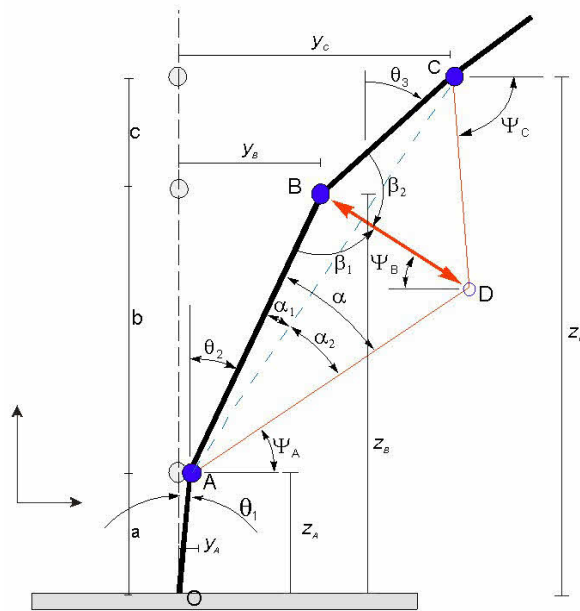


Figure 4-9 Generalized Cantilever/Tendon Geometric Parameters

Since the cantilever is modeled as a finite number of nodes, the model was visualized as a series of end-to-end connected column elements. The end connections have associated stiffness and damping properties. The particular parametric values were developed during the formulation of the cantilever dynamic model. Only the geometric parameters are of interest at this point.

The algorithm to determine BD_length is a relatively straightforward application of trigonometric relationships. Recall the cantilever/tendon geometric constraints documented above. The algorithm proceeded from the following observations:

- The known parameters are: $a, b, c, y_A, y_B, y_C, AD, CD$.
- Given no deformation, $\beta_1 = \beta_2 = \frac{\pi}{2}$, during deformation $\beta_1 = \beta_2$.
- Axial deformations of the cantilever are assumed negligible; therefore, $OA = a, AB = b, BC = c$
- The following variables can be computed directly from the known parameters:

$$\theta_1 = a \sin\left(\frac{y_A}{a}\right), \quad \theta_2 = a \sin\left(\frac{y_B - y_A}{b}\right), \quad a \sin\left(\frac{y_C - y_A - y_B}{c}\right)$$

$$AC = \sqrt{(z_C - z_A)^2 + (y_C - y_A)^2}$$

$$\alpha_1 = a \cos\left(\frac{AB^2 + AC^2 - BC^2}{2 \cdot AB \cdot AC}\right), \quad \alpha_2 = a \cos\left(\frac{AD^2 + AC^2 - CD^2}{2 \cdot AD \cdot AC}\right)$$

Noting that

$$\text{if } \theta_2 \leq \theta_3, \quad \alpha = \alpha_1 + \alpha_2$$

$$\text{if } \theta_2 > \theta_3, \quad \alpha = \alpha_1 - \alpha_2$$

Using the Law of Cosines...

$$BD(t_{sim}) = \sqrt{AB^2(t_{sim}) + AD^2(t_{sim}) - \cos(\alpha(t_{sim}))(2 \cdot AB(t_{sim}) \cdot AD(t_{sim}))} \quad (4.13)$$

The generalized control tendon was a 3-point device; the cantilever model was a 5 node, 5-DOF cantilever representation. Figure 4-9 illustrates the generalized configuration of the tendon/cantilever couple. Figure 4-10 illustrates the specific geometric relationships between the 3-point tendon and the 5-DOF cantilever model.

Basic computations enabled the transformation of BD_length from the generalized to the specific configuration.

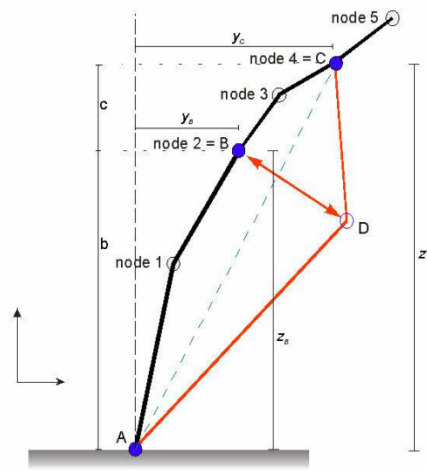


Figure 4-10 Specific 3-Pt Tendon/5-DOF Cantilever Connection Geometry

As discussed, BD_length , Ψ_A , Ψ_B , and Ψ_C were necessary in order to compute the tendon feedback force distribution thus requiring that the spatial coordinates of Node D (y_D, z_D) be known. Referring to Figure 4-9, the conversion relationships were developed by noting that,

$$\psi_A = \frac{\pi}{2} - (\theta_2 + \alpha) \quad \text{radians}$$

From which,

$$y_D = y_A + AD \cos(\psi_A)$$

$$z_D = z_A + AD \sin(\psi_A)$$

$$\psi_B = \text{atan} \left(\frac{z_B - z_D}{y_B - y_D} \right)$$

$$\psi_C = \text{atan} \left(\frac{z_C - z_D}{y_C - y_D} \right)$$

4.2.3 Tendon Feedback Force Algorithm

Ultimately, the tendon model must compute feedback forces that emulate the forces that would in the real world be generated by the tendon and would deform the cantilever as the LOCKED cantilever/tendon pair sways. Figure 4-11 diagrams the force set involved in the redistribution of kinetic energy within the cantilever.

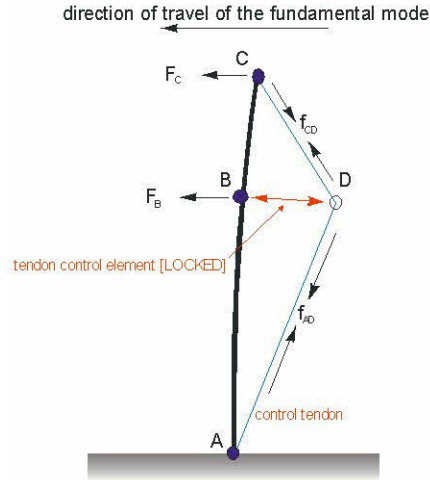


Figure 4-11 Control Tendon Force Set

The force set is self-developed by the motion of the structure itself due to the vibration energy contained within the system. The total system energy at any instant in time is the sum of the instantaneous inertial, or kinetic energy associated with nodal masses

$$\left(\frac{\dot{\mathbf{x}}^T \times \mathbf{M} \times \dot{\mathbf{x}}}{2} \right)$$

and the instantaneous strain, or potential energy of the deformed cantilever

$$\left(\frac{\mathbf{x}^T \times \mathbf{K} \times \mathbf{x}}{2} \right).$$

The feedback force set illustrated in Figure 4-11 occurs when the state of the system can be described as follows:

- The structure is vibrating.
- The fundamental mode is dominant.

- The structure is traversing from right to left in its sway cycle (dictated by the tendon connection geometry).
- The control element BD, is assumed 'LOCKED' in length.
- Tendon elements AD and CD are in tension, and the control element BD is in compression.

Given this state, Node B is being pushed, while Node C is being pulled with the goal to approximate the shape of the 2nd vibration mode.

The Feedback Force Algorithm was developed to compute the instantaneous force distribution set for the described dynamical state of the cantilever. Simulating the instantaneous force set required capturing the associated physics in mathematical expression and programming those formulas into the virtual environment, in this case the MATLAB/SIMULINK environment. The general approach of this process was shown to take the form of a closed loop control problem. Multiple physics-based algorithm candidates were identified and investigated to emulate the tendon feedback forces. In each case, selected states of the coupled cantilever/tendon pair were uniquely established as control variables based upon the prescribed governing physics identified. Control variables were evaluated via simulation to determine viability of the control algorithm. The algorithm computed feedback forces were coupled to the plant (closed loop) and control variable metrics were determined and evaluated. The detailed results are described below.

Algorithms that were considered were found to align themselves into one of two distinct categories:

- 1.) Geometry Control Techniques.
- 2.) Energy Control Techniques.

4.2.3.1 Geometric Based Tendon Control Algorithms

Each of the geometry control algorithms that were considered was based upon the premise that once the control element BD was commanded “LOCKED,” the structure defined by the triangular sections ABD and BCD formed a rigid body, essentially a 5 element vertical truss. As the cantilever/tendon pair continued to sway, or rotated left, the temporary truss ABCD rotated as a rigid body about the base support, Node A. This notion is captured in Figure 4-12 where the ‘rigid body’ ABCD is overlaid on the continuous and the lumped mass cantilever/tendon models.

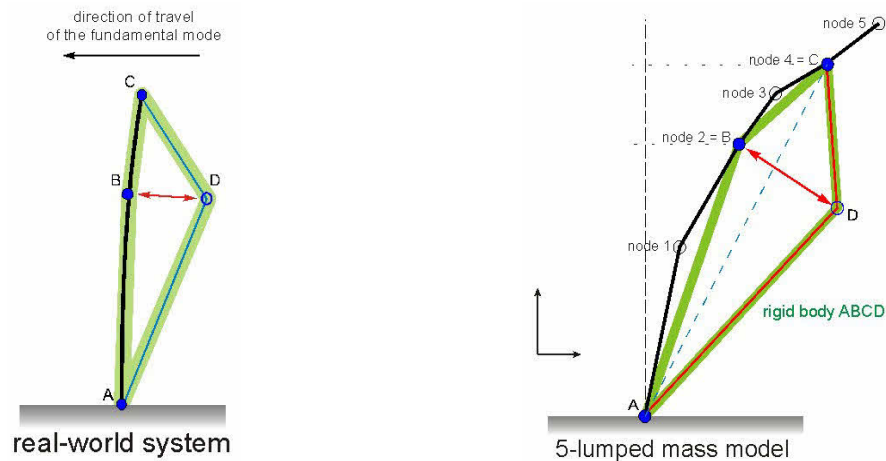


Figure 4-12 Cantilever/Tendon Rigid Body Truss Model

This rigid body can be characterized by a number of geometric parameters that can serve as control variables and can be monitored and evaluated to assess whether ABCD remains rigid while rotating. The logic embodied in each of the geometric control algorithms was straightforward. Each was based upon a different characterizing parameter, or control variable, that establishes ABCD as a rigid body. Each individual algorithm computed an error signal associated with the control variable that indicated undesired deformation to this rigid body ABCD. The error signal was transformed (linearly or non-linearly as required by the algorithm) to compensating nodal forces in an attempt to correct detected rigid body deformations,

thereby satisfying the given geometric constraint. Each variable had associated sensitivities and stability considerations. A variable that had significant variation for small deformation of ABCD was desired; unfortunately, such sensitivities are not always apparent. Several approaches were considered and evaluated.

In summary, the geometric control strategies were developed under the following assumptions:

- The control tendon is 'LOCKED' as the cantilever/tendon pair traverses right to left.
- The cantilever/tendon section ABCD rotates rigidly about Node A when 'LOCKED'.
- The cantilever/tendon pair can be modeled as a closed loop feedback system as depicted in the block diagram of Figure 4-8.
- A single feedback force, or control force, can be computed and introduced between Nodes B and D and distributed to the cantilever/tendon connections at Nodes B and C to emulate the effects of the tendon.

Four versions of geometric control algorithms were designed, implemented and evaluated in the MATLAB/SIMULINK environment coupled to the 5-DOF cantilever model of the aluminum cantilever pole.

Version 1: Angle Rate Feedback Control

Because the control element BD is 'LOCKED' radials from Node A to each node of the rigid body ABCD rotate left about the base support (Node A) with equal angular velocity. The angle rate $\dot{\theta}_2$ of radial AB must equal the angle rate $\dot{\phi}$ of the radial AC (reference Figure 4-13).

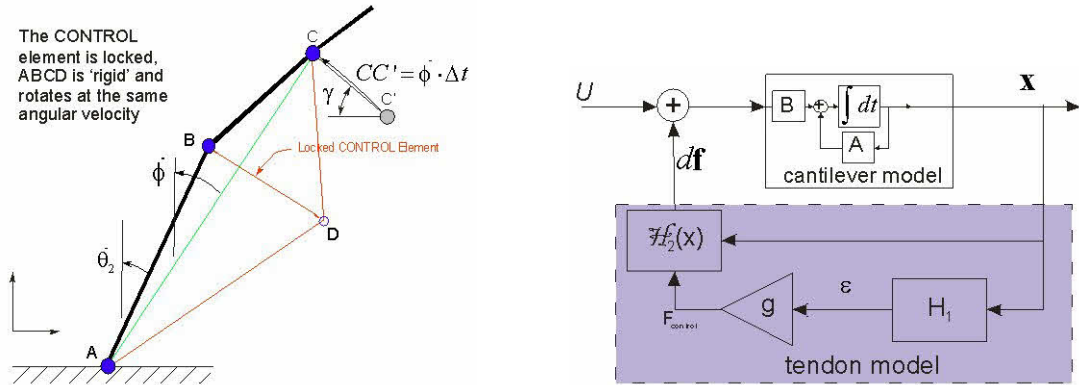


Figure 4-13 Angle Rate Feedback [Geometric Version 1] Block Diagram

Since radial AC diagonally spans ABCD, $\dot{\phi}$ would appear to be a reasonable reference; it would be sensitive to any deformation of ABCD when compared to the radial rates of either AB or AD which lie on the perimeter of ABCD. By making this comparison, an error signal can be formulated by which to control the rigid shape of ABCD:

$$\varepsilon = \dot{\phi} - \dot{\theta}_2 \quad (4.14)$$

When $\varepsilon > 0$, a compressive control force is required between Nodes B and D in order to maintain the rigid shape of ABCD. When $\varepsilon \leq 0$ the control force must be removed since compressive forces cannot be transmitted through the tendon elements AD and CD.

The length of each radial of interest (e.g. radial AC) is very long compared to the length of the arc swept by the end node during one simulation time increment. Therefore, the cord of the arc can be assumed to approximate the length of the arc (see Figure 4-13).

$$CC'_{arc} \approx CC'_{cord}$$

Furthermore, the arc-lengths (cord-lengths) swept by the radial end Nodes B and C over some differential time element Δt are proportional to their distances from the base support Node A. For equal angular rates...

$$(\dot{\theta}_2 \Delta t) AB = BB'_{cord}, \quad (\dot{\phi} \Delta t) AC = CC'_{cord}$$

$$\frac{BB'_{cord}}{AB} = \frac{CC'_{cord}}{AC}$$

If the deformation of the cantilever is reasonably small such that the radials (AB and AC in this case) are near vertical, that is $\gamma \underset{vicinity}{\approx} 0$ (again reference the diagram of Figure 4-13 but note that the deformation is exaggerated for emphasis), then the angular rates can be approximated using the nodal velocities.

$$\begin{aligned} CC'_{arc} &= (\dot{\phi} \Delta t) AC \approx [x_c(t) - x_c(t - \Delta t)] \\ \dot{\phi} &\approx \frac{x_c(t) - x_c(t - \Delta t)}{\Delta t} \cdot \frac{1}{AC} = \frac{\dot{x}_c}{AC} \end{aligned} \quad (4.15)$$

Likewise,

$$\dot{\theta}_2 \approx \frac{x_B(t) - x_B(t - \Delta t)}{\Delta t} \cdot \frac{1}{AB} = \frac{\dot{x}_B}{AB} \quad (4.16)$$

It follows then from Equations (4.14), (4.15), and (4.16) that the control variable (error signal) becomes

$$\varepsilon = \frac{\dot{x}_B}{AB} - \frac{\dot{x}_C}{AC} \quad (4.17)$$

Since the cantilever deformation was assumed reasonably small, AB and AC can be estimated as:

$$\begin{aligned} AC &\approx \text{static node C height} = AC_0 \\ AB &\approx \text{static node B height} = AB_0 \end{aligned}$$

Equation (4.17) is attractive because AB_0, AC_0 are constants, and \dot{x}_B, \dot{x}_C are simply state outputs of the state space model. A linear feedback gain can be formulated from the error signal ε :

$$\begin{aligned}\varepsilon &= \mathbf{H}_1 \times \mathbf{x} \\ \mathbf{x} &= [x_1 \quad x_2 \quad x_3 \quad x_4 \quad x_5 \quad \dot{x}_1 \quad \dot{x}_2 \quad \dot{x}_3 \quad \dot{x}_4 \quad \dot{x}_5]^T \\ \mathbf{H}_1 &= \begin{bmatrix} 0 & 0 & 0 & 0 & 0 & 0 & \frac{1}{AB_0} & 0 & -\frac{1}{AC_0} & 0 \end{bmatrix}\end{aligned}$$

In this case, the feedback gain function is linear because it is formed directly from a linear combination of the cantilever state space output vector. This made analysis and implementation nicely straightforward. The feedback is used to compute forces that are to be directed to the discrete nodes. Unfortunately, the actual distribution function $\mathcal{H}_2(x)$ is non-linear. A zero-order approximation of the distribution function was investigated and derived using the static force distribution set (reference Figure 3-17 and Equation 3.57).

$$\frac{F_C}{F_{B \text{ (static, } \bar{x}=0)}} = -\frac{a}{a+b}$$

The linearized distribution function consequently becomes:

$$\mathcal{H}_2(x) \underset{\text{constant}}{\approx} \mathbf{H}_2 = \begin{bmatrix} 0 & \frac{a}{a+b} & 0 & -1 & 0 \end{bmatrix}^T$$

A scalar gain function g was used to amplify the error signal. In doing so, the overall response behavior of the feedback path could be adjusted. The net expression for the linearized feedback forces is derived by examining the feedback path shown in Figure 4-13:

$$d\mathbf{f} = (g \varepsilon) \mathbf{H}_2^T = (g (\mathbf{H}_1 \times \mathbf{x})) \mathbf{H}_2^T$$

Ultimately, the error signal ε should be driven to zero in a reasonable time. The proper selection of g accomplishes this goal. The dynamic behavior of ε can be investigated and tailored as a function of g . The transfer function of the closed-loop signal flow diagrammed in Figure 4-13 can be expressed using Laplace transform yielding:

$$\varepsilon(s) \left[1 - g H_1 C (s I - A)^{-1} B H_2^T \right] = 0$$

For non-trivial solutions, the bracketed expression is evaluated. The eigenvalues were examined and determined based on the scalar feedback gain, g .

In summary, for Angle Rate Feedback Control:

Control Objective:

$$\begin{aligned} \dot{\theta}_2 &= \dot{\phi} \quad (t \geq t_{LOCK}) \\ \varepsilon(t) &= \frac{\dot{x}_B}{AB} - \frac{\dot{x}_C}{AC} \rightarrow 0 \end{aligned}$$

Control Force:

$$F_{control} = \begin{cases} g [\dot{\theta}_2(t) - \dot{\phi}(t)] & \text{if } \varepsilon > 0 \\ 0 & \text{if } \varepsilon \leq 0 \end{cases}$$

Simulation results using the Angle Rate feedback algorithm, Version 1, are shown in Figure 4-14.

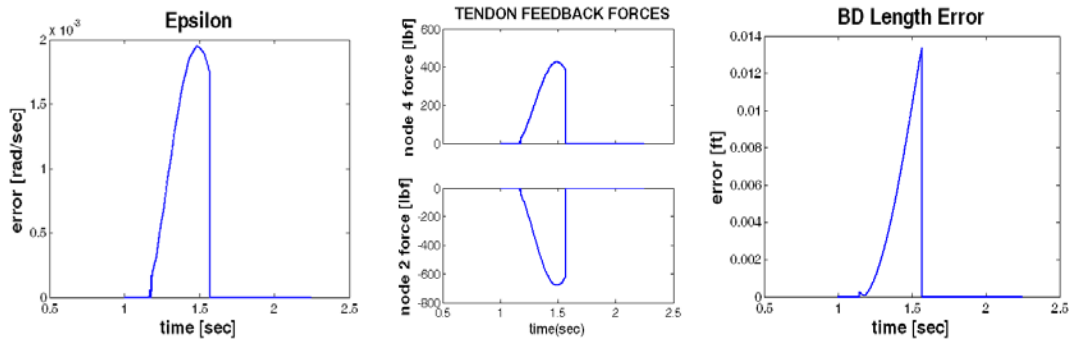


Figure 4-14 Tendon Model Performance [Geometric Version 1]

The control variable (error ε), the error in BD-Length and the tendon feedback forces are shown plotted during the BD ‘LOCK’ phase as the cantilever swung from right to left as diagrammed in Figure 4-11. BD-Length was used to measure the effectiveness of the control algorithm since it was the parameter that was being regulated. In this case,

the algorithm was extremely effective maintaining its virtual length to within $\sim 0.2\%$ of its 'LOCKED' value.

Version 2: Angle Rate Feedback Control #2

Geometric Control Algorithm Version 2 is similar in nature to that of Version 1. It also assumes that radials from Node A to each node of the rigid body ABCD rotates left about the base support (Node A) with equal angular velocity.

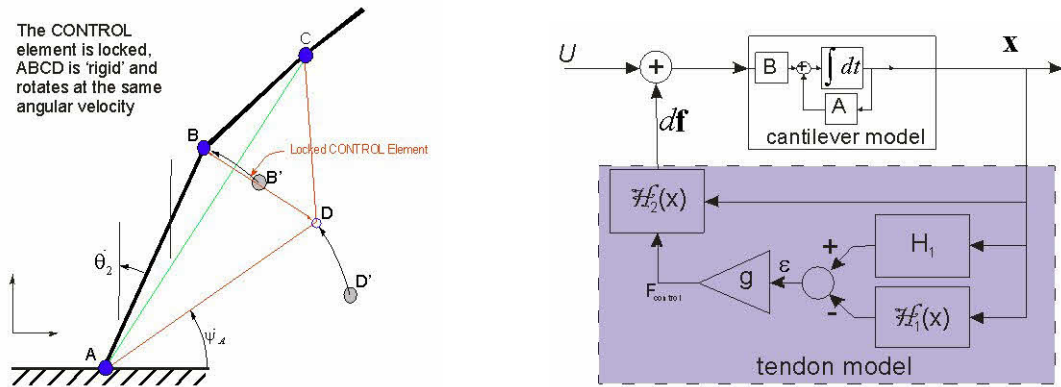


Figure 4-15 Angle Rate Feedback [Geometric Version 2] Block Diagram

In this approach, the angular rate of Node D (rather than that of Node C as used in Version 1) is compared to the angular rate of Node B (reference Figure 4-15). When ABCD rotates as a rigid body the angle rate $\dot{\theta}_2$ of cantilever element AB must equal the angle rate $\dot{\psi}_A$ of the tendon element AD. Again, an error signal can be formulated by which to control/adjust the rigid shape of ABCD:

$$\varepsilon = \dot{\theta}_2 - \dot{\psi}_A \quad (4.18)$$

When $\varepsilon > 0$ a compressive control force is required between BD resulting in tension forces in elements AD and CD; when $\varepsilon \leq 0$ the control force must be removed since compressive forces cannot be transmitted through the tendon elements AD and CD. As discussed for the geometric version 1 approach, the arc-lengths (cord lengths) swept by

the radial end Nodes B and D over some time Δt are proportional to their distances from the base support Node A so that

$$\frac{BB'_{cord}}{AB} = \frac{DD'_{cord}}{AD} \quad (4.19)$$

It was shown in Equation (4.16) that the angular rate $\dot{\theta}_2$ could be approximated as being proportional to the nodal velocity of Node B. This is not the case for $\dot{\psi}_A$ because the radial AD cannot be assumed to be nearly vertical as was the case with AB and AC. Because the simulation time increment is small and the radial AD is large, the cord of DD'_{arc} can again be used to approximate its arc length. \dot{x}_D can be used to compute $\dot{\psi}_A$, but the relationship cannot be immediately assumed linear, instead:

$$\dot{\psi}_A \approx \frac{\dot{DD}'_{arc}}{AD} \approx \frac{\dot{x}_D}{\cos\left(\frac{\pi}{2} - \psi_A\right)} \cdot \frac{1}{AD} \quad (4.20)$$

It follows from Equations (4.16), (4.18), and (4.20) that,

$$\varepsilon = \frac{\dot{x}_B}{AB} - \frac{\dot{x}_D}{\cos\left(\frac{\pi}{2} - \psi_A\right)} \cdot \frac{1}{AD} \quad (4.21)$$

Unlike Version 1, Equation (4.21) is not directly calculable since \dot{x}_D is not an outputted variable of the cantilever state space model. Instead, it must be continuously computed as a non-linear function of \mathbf{x} . Therefore, the functional block diagram of Figure 4-15 shows the feedback function $\mathcal{H}_1(x)$ as ‘scripted’ to emphasize its nonlinearity. The error signal becomes:

$$\varepsilon = \mathbf{H}_1 \times \mathbf{x} - \mathcal{H}_1(x)$$

$$\mathbf{x} = [x_1 \quad x_2 \quad x_3 \quad x_4 \quad x_5 \quad \dot{x}_1 \quad \dot{x}_2 \quad \dot{x}_3 \quad \dot{x}_4 \quad \dot{x}_5]^T$$

$$\mathbf{H}_1 = \begin{bmatrix} 0 & 0 & 0 & 0 & 0 & 0 & \frac{1}{AB_0} & 0 & 0 & 0 \end{bmatrix}$$

$\mathcal{H}_1(x)$ represents a series of non-linear functions that follow from Section 4.2.2 and the geometric relationships identified above in the Tendon Geometric Algorithm description that were used to derive \dot{x}_D .

In summary, for Angle Rate Feedback Version 2 Control:

Control Objective:

$$\dot{\theta}_2 = \dot{\psi}_A \quad (t \geq t_{LOCK})$$

$$\varepsilon = \frac{\dot{x}_B}{AB} - \frac{\dot{x}_D}{\cos\left(\frac{\pi}{2} - \psi_A\right)} \cdot \frac{1}{AD} \rightarrow 0$$

Control Force:

$$F_{control} = \begin{cases} g[\dot{\theta}_2(t) - \dot{\psi}_A(t)] & \text{if } \varepsilon > 0 \\ 0 & \text{if } \varepsilon \leq 0 \end{cases}$$

Simulation results using the Angle Rate feedback algorithm, Version 2, are shown in Figure 4-16.

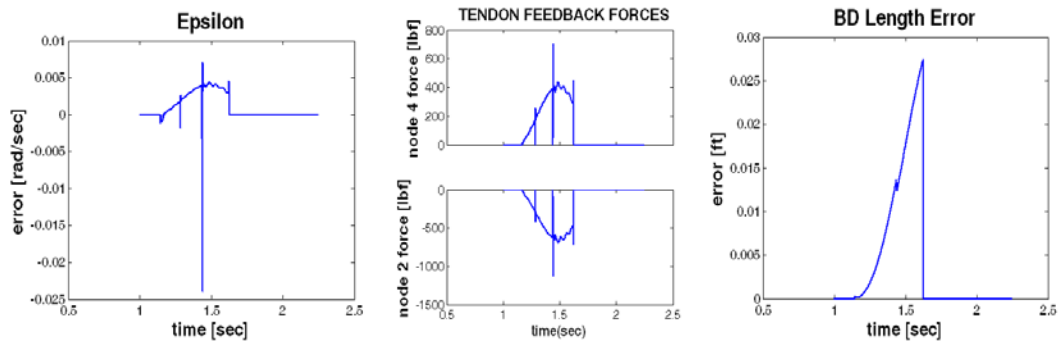


Figure 4-16 Tendon Model Performance [Geometric Version 2]

The spikes observed in the signals were the result of differentiating the variable x_D which itself is a non-linear function containing piecewise segments. The results plotted occurred during the BD ‘LOCK’ phase as the cantilever traversed from right to left as diagrammed in Figure 4-11. BD-Length was used to measure the effectiveness of the control algorithm since it was the parameter that was being regulated. In this case, the algorithm maintained the virtual length to within $\sim 0.55\%$ of its ‘LOCKED’ value.

Version 3: Angle Feedback Control

Geometric Control Algorithm Version 3 at first appears to duplicate the logic of Version 2. The SIMULINK implementation strategy is different, however. The control strategy of Version 2 attempts to eliminate the angle rate differential between radials AB and AD as ABCD rotates about Node A. If designed and implemented properly, the angle ($\angle\alpha$) between AB and AD as diagrammed in Figure 4-17 remains constant. The control strategy of Version 3 regulates $\angle\alpha$ directly. $\angle\alpha$ is a non-linear function of the cantilever state variables \mathbf{x} .

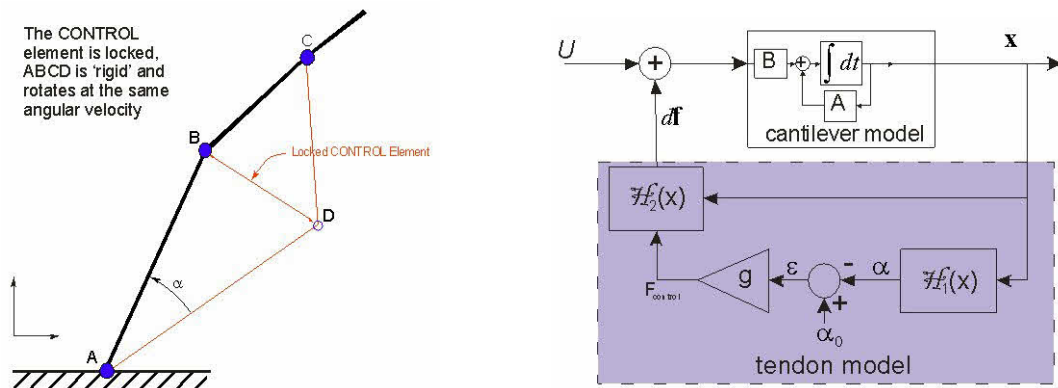


Figure 4-17 Angle Feedback [Geometric Version 3] Block Diagram

At the instant the control element BD is ‘LOCKED’ $\angle\alpha_0$ is computed and used as the control reference. As the cantilever/tendon pair swing left, the instantaneous value

of $\angle\alpha$ is computed and compared to the reference, $\angle\alpha_0$. An error signal is derived and used to compute the necessary tendon control force required to maintain the rigid body geometry.

$$\varepsilon = \angle\alpha - \angle\alpha_0$$

When $\varepsilon > 0$, a compressive control force is required between Nodes B and D, when $\varepsilon \leq 0$ the control force must be removed.

In summary, for Angle Feedback Control:

Control Objective:

$$\alpha(t) = \text{constant} = \alpha_0 = \alpha(t_{LOCK}) \quad (t \geq t_{LOCK})$$

Control Force:

$$F_{control} = \begin{cases} g[\alpha(t) - \alpha_0] & \text{if } \varepsilon > 0 \\ 0 & \text{if } \varepsilon \leq 0 \end{cases}$$

Simulation results using the Angle feedback algorithm, Version 3, are shown in Figure 4-18.

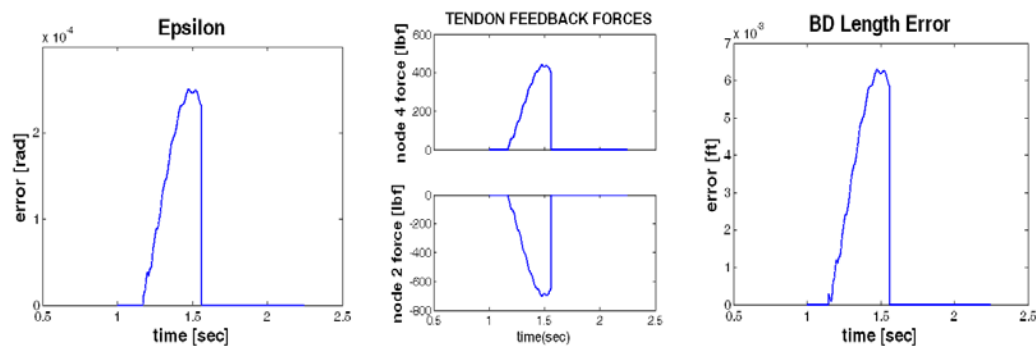


Figure 4-18 Tendon Model Performance [Geometric Version 3]

The control variable (error ε), the error in BD-Length, and the tendon feedback forces are shown plotted; they occurred during the BD ‘LOCK’ phase as the cantilever swings from right to left as diagrammed in Figure 4-11. Once again, BD-Length was used to

measure the effectiveness of the control algorithm because it was the parameter that was being regulated. In this case, the algorithm was very effective maintaining its virtual length to within $\sim 0.154\%$ of its 'LOCKED' value.

Version 4: Length Feedback Control

Geometric Control Algorithm Version 4 is represented in Figure 4-19. It is a simple algorithm developed to generate the tendon control force $F_{control}$ to be a scalar gain function of length error associated with the control element BD itself.

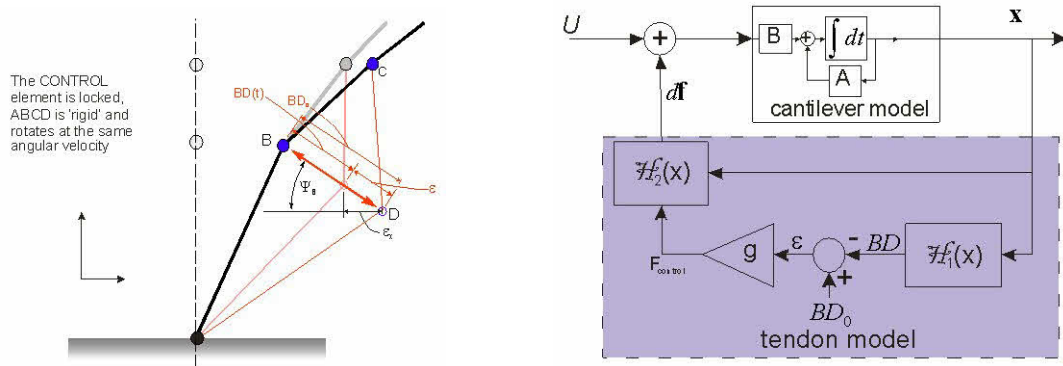


Figure 4-19 Length Feedback Control [Geometric Version 4] Block Diagram

At the instant the control element BD is 'LOCKED' the length BD_0 is computed and used as the control reference. As the cantilever/tendon pair swing left, the instantaneous value of BD is computed and compared to BD_0 . The non-linear algorithm used to compute the length of BD is described in an earlier section. The differential control error becomes:

$$\varepsilon = BD_0 - BD(t)$$

When $\varepsilon > 0$, a compressive control force is required between Nodes B and D, when $\varepsilon \leq 0$ the control force must be removed.

Control Objective:

$$BD(t) = \text{constant} = BD_0 = BD(t_{LOCK}) \quad (t \geq t_{LOCK})$$

Control Force:

$$F_{control} = \begin{cases} \kappa [BD(t) - BD_0] & \text{if } \varepsilon > 0 \\ 0 & \text{if } \varepsilon \leq 0 \end{cases}$$

The scalar gain ‘ κ ’ was determined empirically. Two criteria were considered; the magnitude of ε and the convergence behavior of ε . Alternatively, ‘ κ ’ could be determined analytically given the linearization of \mathcal{H}_1 and \mathcal{H}_2

Simulation results using the length control feedback algorithm of Version 4 are shown in Figure 4-20. The control variable (error ε) in this version was the BD-Length error and is shown plotted with the tendon feedback forces during the BD ‘LOCK’ phase as the cantilever swings from right to left as diagrammed in Figure 4-11. In previous versions, the BD-Length error was used to measure the effectiveness of the control algorithm. Once again, it was used as the measure of effectiveness, however in this case it was also the control variable, high performance was therefore expected.

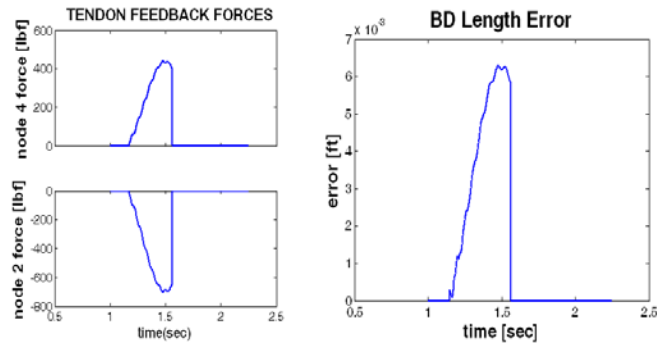


Figure 4-20 Tendon Model Performance [Geometric Version 4]

The simulation results indicated that the algorithm maintained the element BD virtual length to within $\sim 0.15\%$ of its 'LOCKED' value. Version 4 demonstrated the best regulation performance of BD length among the geometric algorithms.

4.2.3.2 Force Distribution Algorithm – $\mathcal{H}_2(x)$

The force distribution algorithm computed the instantaneous nodal force set given the computed feedback control force ($F_{control}$) generated by the 'LOCKED' tendon. The geometric algorithms determine one feedback force, $F_{control}$ that is introduced between Nodes B and D. The tendon distributes $F_{control}$ to cantilever Nodes B and C as tendon feedback forces. The force distribution function for the static, un-deformed cantilever was computed earlier which when rearranged for the 5-DOF dynamic model becomes,

$$d\mathbf{f} = \begin{bmatrix} df_1 \\ df_2 \\ df_3 \\ df_4 \\ df_5 \end{bmatrix} = \begin{bmatrix} 0 \\ -1 \\ 0 \\ \frac{a}{a+b} \\ 0 \end{bmatrix} \cdot F_{control} \quad (4.22)$$

where, df_i represents the differential feedback force for node- i . Recall that the lower tendon connection, Node A, is made at the cantilever base support so is not represented in the differential force vector. Equation (4.22) is valid only at the un-deformed state. The force distribution in fact varies as a function of the cantilever nodal displacement, as illustrated in Figure 4-21.

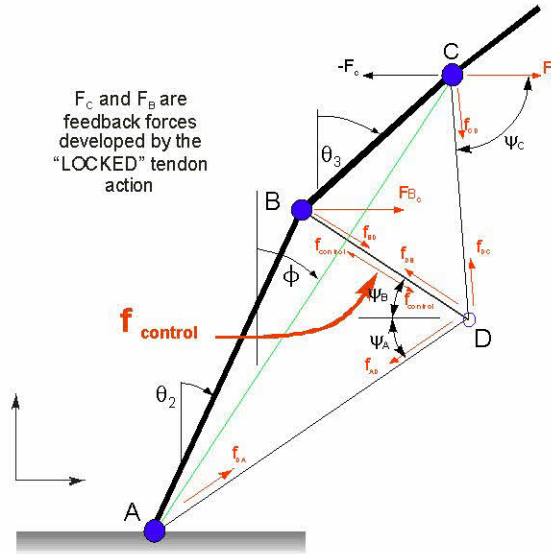


Figure 4-21 Deformed Cantilever/Tendon Geometric Parameters

The equilibrium equations for Node D

$$\sum_{horizontal} f_D = 0$$

$$\sum_{vertical} f_D = 0$$

lead to the ensuing control force distribution functions...

$$\begin{bmatrix} F_B \\ F_C \end{bmatrix} = F_{control} \cdot \begin{bmatrix} -\cos(\psi_B) \\ \cos(\psi_C) \cdot \frac{\sin(\psi_A) \cdot \cos(\psi_B) + \cos(\psi_A) \cdot \sin(\psi_B)}{\cos(\psi_C) \cdot \sin(\psi_A) + \cos(\psi_A) \sin(\psi_C)} \end{bmatrix} \quad (4.23)$$

Equation (4.23) forms the basis for the 5-DOF distributed feedback force distribution function for the deformed cantilever/tendon pair,

$$\begin{bmatrix} df_1 \\ df_2 \\ df_3 \\ df_4 \\ df_5 \end{bmatrix} = \begin{bmatrix} 0 \\ -\cos(\psi_B) \\ 0 \\ \cos(\psi_C) \cdot \frac{\sin(\psi_A) \cdot \cos(\psi_B) + \cos(\psi_A) \cdot \sin(\psi_B)}{\cos(\psi_C) \cdot \sin(\psi_A) + \cos(\psi_A) \sin(\psi_C)} \\ 0 \end{bmatrix} \cdot F_{control} \quad (4.24)$$

As expected, Equation (4.24) \rightarrow Equation (4.22) as the structural pair approaches the static, un-deformed state.

4.2.3.3 Energy Based Tendon Control Algorithm

Energy based control algorithms offer an alternative approach to determining the effects of the ‘LOCKED’ tendon on the vibrating cantilever. As with the geometry based control algorithms, energy control algorithms determine feedback forces that actuate the cantilever deformation effects of the ‘LOCKED’ tendon. The differential force vector $d\mathbf{f} = [df_1 \ df_2 \ df_3 \ df_4 \ df_5]^T$ (reference Figure 4-8) was determined in such a way so as to satisfy two criteria:

1. Like each geometry based algorithm, the energy algorithm must determine tendon feedback forces that maintain a constant BD-length, more specifically, eliminate BD length discrepancies computed each simulation iteration.
2. In addition to the geometric criterion, the particular global energy constraint must be met each simulation time iteration.

Variations of energy based algorithms can be envisioned: total system energy, conservation of momentum, and work for example. The total system energy conservation approach has been investigated and is described in the following section.

Version 5: Total Energy Conservation Control

The tendon feedback force set delivered to the cantilever must neither add to nor subtract from the net energy of the system when emulating tendon behavior; total energy after the simulation increment (tendon force correction event) must equal the total energy before the increment. The signal flow diagram shown in Figure 4-22 appears similar to those of the geometric approach, particularly Version 4 where the

control element BD is regulated in length. In this case however, the control force $F_{control}$ is determined by the non-linear energy-based algorithm designated $\mathcal{H}_3(x)$.

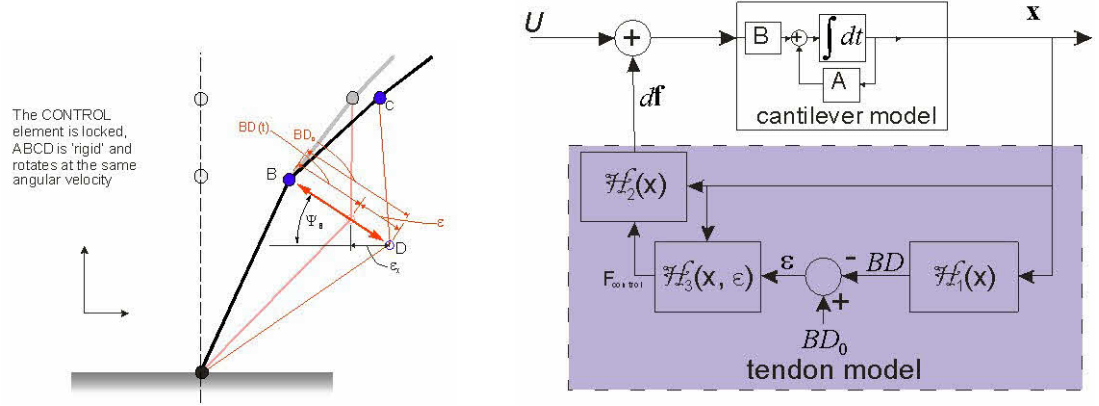


Figure 4-22 Energy Conservation Control [Version 5] Block Diagram

The fundamental and the governing energy constraint can be stated as:

$$U_{total}(t) = U_{total}(t+) \quad (4.25)$$

$$U_{total}(t) = U_{kinetic}(t) + U_{potential}(t) = \left(\frac{\dot{\mathbf{x}}^T \times \mathbf{M} \times \dot{\mathbf{x}}}{2} \right) + \left(\frac{\mathbf{x}^T \times \mathbf{K} \times \mathbf{x}}{2} \right) \quad (4.26)$$

$$U_{total}(t+) = \left(\frac{(\dot{\mathbf{x}} + d\dot{\mathbf{x}})^T \times \mathbf{M} \times (\dot{\mathbf{x}} + d\dot{\mathbf{x}})}{2} \right) + \left(\frac{(\mathbf{x} + d\mathbf{x})^T \times \mathbf{K} \times (\mathbf{x} + d\mathbf{x})}{2} \right)$$

From Equations (4.25) and (4.26),

$$\left(\frac{\dot{\mathbf{x}}^T \times \mathbf{M} \times \dot{\mathbf{x}}}{2} \right) + \left(\frac{\mathbf{x}^T \times \mathbf{K} \times \mathbf{x}}{2} \right) = \left(\frac{(\dot{\mathbf{x}} + d\dot{\mathbf{x}})^T \times \mathbf{M} \times (\dot{\mathbf{x}} + d\dot{\mathbf{x}})}{2} \right) + \left(\frac{(\mathbf{x} + d\mathbf{x})^T \times \mathbf{K} \times (\mathbf{x} + d\mathbf{x})}{2} \right) \quad (4.27)$$

Expanding Equation (4.27) yields

$$\begin{aligned} & \left[\left(\frac{\dot{\mathbf{x}}^T \times \mathbf{M} \times \dot{\mathbf{x}}}{2} \right) + \left(\frac{\mathbf{x}^T \times \mathbf{K} \times \mathbf{x}}{2} \right) \right]_{t_1} = \left[\left(\frac{\dot{\mathbf{x}}^T \times \mathbf{M} \times \dot{\mathbf{x}}}{2} \right) + \left(\frac{\mathbf{x}^T \times \mathbf{K} \times \mathbf{x}}{2} \right) + \dots \right. \\ & \dots + \left(\frac{(d\dot{\mathbf{x}})^T \times \mathbf{M} \times (\dot{\mathbf{x}})}{2} \right) + \left(\frac{(\dot{\mathbf{x}})^T \times \mathbf{M} \times (d\dot{\mathbf{x}})}{2} \right) + \left(\frac{(d\dot{\mathbf{x}})^T \times \mathbf{M} \times (d\dot{\mathbf{x}})}{2} \right) + \dots \\ & \left. \dots + \left(\frac{(d\mathbf{x})^T \times \mathbf{K} \times (\mathbf{x})}{2} \right) + \left(\frac{(\mathbf{x})^T \times \mathbf{K} \times (d\mathbf{x})}{2} \right) + \left(\frac{(d\mathbf{x})^T \times \mathbf{K} \times (d\mathbf{x})}{2} \right) \right]_{t_2} \end{aligned}$$

For a non-trivial solution,

$$\begin{aligned} & \left(\frac{(d\dot{\mathbf{x}})^T \times \mathbf{M} \times (\dot{\mathbf{x}})}{2} \right) + \left(\frac{(\dot{\mathbf{x}})^T \times \mathbf{M} \times (d\dot{\mathbf{x}})}{2} \right) + \left(\frac{(d\dot{\mathbf{x}})^T \times \mathbf{M} \times (d\dot{\mathbf{x}})}{2} \right) + \dots \\ & \dots + \left(\frac{(d\mathbf{x})^T \times \mathbf{K} \times (\mathbf{x})}{2} \right) + \left(\frac{(\mathbf{x})^T \times \mathbf{K} \times (d\mathbf{x})}{2} \right) + \left(\frac{(d\mathbf{x})^T \times \mathbf{K} \times (d\mathbf{x})}{2} \right) = 0 \end{aligned} \quad (4.28)$$

Equation (4.28) must be satisfied as the cantilever is deformed during the vibration cycle to emulate the effects of the ‘LOCKED’ tendon regardless of the fact that the ultimate control objective is to maintain a constant length for the ‘LOCKED’ control element BD. Equation (4.28) implies that state position and state velocity must both be ‘considered’ when developing the solution to satisfy the geometric objective; both contribute to ensure conservation of energy.

Recall that the unforced linear state space model of the cantilever was established as $\dot{\mathbf{x}} = \mathbf{A} \mathbf{x}$. Since the behavior is assumed linear,

$$\frac{d(\mathbf{x} + d\mathbf{x})}{dt} \rightarrow \dot{\mathbf{x}} + d\dot{\mathbf{x}} = \mathbf{A} \mathbf{x} + \mathbf{A} d\mathbf{x} \rightarrow d\dot{\mathbf{x}} = \mathbf{A} d\mathbf{x}$$

Substituting these relationships into Equation (4.28) yields,

$$\begin{aligned} & \left((d\mathbf{x})^T \times (\mathbf{K} + \mathbf{A}^T \times \mathbf{M} \times \mathbf{A}) \times (\mathbf{x}) \right) + \left((\mathbf{x})^T \times (\mathbf{K} + \mathbf{A}^T \times \mathbf{M} \times \mathbf{A}) \times (d\mathbf{x}) \right) + \dots \\ & \dots + \left((d\mathbf{x})^T \times (\mathbf{K} + \mathbf{A}^T \times \mathbf{M} \times \mathbf{A}) \times (d\mathbf{x}) \right) = 0 \end{aligned} \quad (4.29)$$

Equation (4.29) is now only a function of state position.

Let, $\mathbf{KK} = \mathbf{K} + \mathbf{A}^T \times \mathbf{M} \times \mathbf{A}$ so that

$$\left((d\mathbf{x})^T \times \mathbf{KK} \times (\mathbf{x}) \right) + \left((\mathbf{x})^T \times \mathbf{KK} \times (d\mathbf{x}) \right) + \left((d\mathbf{x})^T \times \mathbf{KK} \times (d\mathbf{x}) \right) = 0 \quad (4.30)$$

The energy constraint expressed in Equation (4.28) has been rearranged to form the expression given in Equation (4.30), but it still represents the energy constraint for the feedback forces. Upon examination, Equation (4.30) is now potential energy like in form, which infers that \mathbf{KK} is an equivalent stiffness matrix. As such, and given that the deformation is assumed elastic so that

$$\mathbf{df} = \mathbf{KK} \times d\mathbf{x} \quad (4.31)$$

The cantilever model is a 5-noded 5 degree-of-freedom model. The tendon is connected a two of these nodes in addition to the base (reference Figure 4-10). Therefore, the feedback force vector takes the following form,

$$\mathbf{df} = [0 \quad df_2 \quad 0 \quad df_4 \quad 0]^T \quad (4.32)$$

From Equation (4.32).

$$d\mathbf{x} = \mathbf{KK}^{-1} \times \mathbf{df} = \mathbf{SS} \times \mathbf{df} \quad (4.33)$$

\mathbf{SS} becomes the equivalent flexibility matrix, where $\mathbf{SS} \times \mathbf{KK} = \mathbf{I}$. For the 5-DOF cantilever model, \mathbf{KK} and \mathbf{SS} take the following form,

$$\mathbf{KK} = \begin{bmatrix} kk_{11} & kk_{12} & \dots & kk_{15} \\ kk_{21} & kk_{22} & \dots & kk_{25} \\ \vdots & & \ddots & \\ kk_{51} & kk_{52} & \dots & kk_{55} \end{bmatrix}, \quad \mathbf{SS} = \begin{bmatrix} ss_{11} & ss_{12} & \dots & ss_{15} \\ ss_{21} & ss_{22} & \dots & ss_{25} \\ \vdots & & \ddots & \\ ss_{51} & ss_{52} & \dots & ss_{55} \end{bmatrix}$$

KK and **SS** are both fully populated and symmetric.

Substituting Equations (4.32) and (4.33) into Equation (4.30) and rearranging yields,

$$df_2^2 \cdot ss_{22} + df_2 \cdot df_4 \cdot ss_{24} + df_2 \cdot df_4 \cdot ss_{42} + df_4^2 \cdot ss_{44} + 2(x_2 \cdot df_2 + x_4 \cdot df_4) = 0 \quad (4.34)$$

Equation (4.34) becomes the resultant energy constraint for the force vector **df**.

At this point, the second constraint for the energy conservation algorithm can be folded into the analysis. The horizontal geometric error signal can be expressed as

$$\varepsilon_y(t) = (BD_0 - BD(t)) \cos(\psi_B(t)) \quad (4.35)$$

The geometric error is the BD length discrepancy and is shown in Figure 4-23.

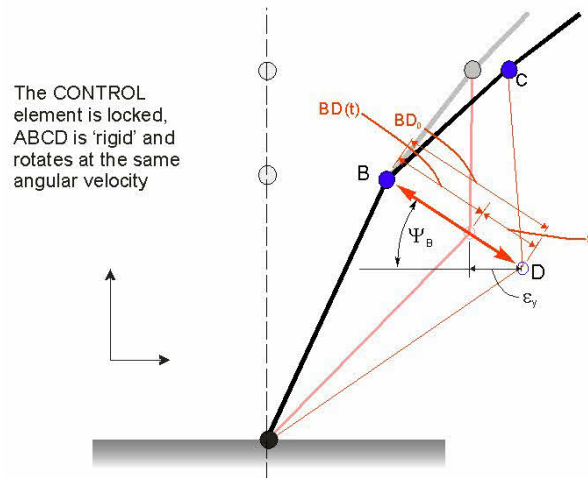


Figure 4-23 Cantilever/Tendon Geometric Parameters

Once the 'LOCK' command is given, the length of BD should remain constant. This criterion is identical to the design constraint for the geometric control algorithm of Version 4. However, in energy conservation approach, this error signal will not be converted directly to a differential force vector. The error signal of Equation (4.35) can be shown to be a function of a differential position, or correction vector,

$$\varepsilon_y = f(dx) = dx_4 - dx_2 \quad (4.36)$$

Utilizing Equation (4.31), Equation (4.36) can be expressed as,

$$\varepsilon_y = df_2 \cdot ss_{42} + df_4 \cdot ss_{44} - (df_2 \cdot ss_{22} + df_4 \cdot ss_{24}) \quad (4.37)$$

Rearranging yields a relationship between the two nodal feedback forces...

$$df_2 = \frac{df_4 (ss_{24} - ss_{44}) + \varepsilon_y}{ss_{22} - ss_{42}} \quad (4.38)$$

Equation (4.38) can now be substituted into the force vector energy constraint expressed in Equation (4.34) yielding,

$$a \cdot df_4^2 + b \cdot df_4 + c = 0 \quad (4.39)$$

Where,

$$\begin{aligned} a &= \frac{(ss_{22} \cdot ss_{44} - ss_{24} \cdot ss_{42}) \cdot (ss_{22} - ss_{24} - ss_{42} + ss_{44})}{(ss_{22} - ss_{42})^2} \\ b &= x_2 \frac{2(ss_{22} - ss_{42}) \cdot (ss_{24} - ss_{44})}{(ss_{22} - ss_{42})^2} + 2x_4 + \varepsilon_y \frac{(ss_{42}^2 + s_{22} \cdot s_{24} - s_{22} \cdot s_{42} - 2s_{22} \cdot s_{44} + s_{24} \cdot s_{42})}{(ss_{22} - ss_{42})^2} \\ c &= \varepsilon_y^2 \frac{s_{22}}{(ss_{22} - ss_{42})^2} - x_2 \frac{2\varepsilon_y}{(ss_{22} - ss_{42})} \end{aligned} \quad (4.40)$$

The quadratic equation of Equation (4.39) yields two possible solutions for df_4 ,

$$df_4 = \begin{bmatrix} \frac{-b + \sqrt{b^2 - 4ac}}{2a} \\ \frac{-b - \sqrt{b^2 - 4ac}}{2a} \end{bmatrix} \quad (4.41)$$

Consequently, from Equation (4.38),

$$df_2 = - \left[\frac{(ss_{24} - ss_{44}) \left(\frac{-b + \sqrt{b^2 - 4ac}}{2a} \right) + \varepsilon_y}{2a(ss_{22} - ss_{42})} \right. \\ \left. \frac{(ss_{24} - ss_{44}) \left(\frac{-b - \sqrt{b^2 - 4ac}}{2a} \right) + \varepsilon_y}{2a(ss_{22} - ss_{42})} \right] \quad (4.42)$$

The derivation yields two sets of solutions. Only one is correct. The correct solution can be determined by investigation the following conditions:

1. The direction of df_2 must be in the direction of \dot{x}_2 (fundamental component).
2. The correct solution set will perform the minimum work since energy conservation is ideally expected. Each solution set will perform some work (due to approximations made) on the cantilever which can be determined by,

$$W = \mathbf{df}^T \times \mathbf{S} \times \mathbf{df}$$

By nature, the system will take the path of least resistance; that is the path that requires the least work to traverse.

4.2.4 Damping Control Law

The Damping Control Law (DCL) is represented by the outermost control loop in the functional block diagram of Figure 4-8. The DCL manages the overall system behavior during activation, and is ultimately responsible for effecting the transfer of dynamic energy from the fundamental vibration mode to a higher order mode, in this case, vibration Mode 2. The DCL control logic is detailed in Section 3.2.2. The DCL implementation utilized to complete the concept Demonstration is detailed in Section 5.2.7.

4.3 Simulation and Analytical Results

This section summarizes the results of the dynamic simulation effort established to develop the Modal Damping conceptual mechanization and demonstrate its feasibility to enhance natural vibration energy dissipation. The MATLAB/SIMULINK environment was selected to host the simulation. Detailed descriptions of the cantilever

and tendon phenomenological modeling approach were given in Sections 4.1 and 4.2 respectively.

It is important to note that THE ONLY DAMPING MECHANISM INCLUDED IN THE SIMULATION MODEL IS THE ANELASTIC MECHANISM this is modeled to be viscous-like. This was thought to offer a worst-case test of the Modal Damping concept as it provided but one damping mechanism to exploit. The Concept Demonstration experiment on the other hand, (describe in Section 5.2) included drag and frictional mechanisms.

Two simulation scenarios were identified for evaluating the augmented damping behavior of the structure: 1.) The Pluck Test, and 2.) The Wind Gust Test. The Pluck Test is an analytical emulation of actual experimentation performed under laboratory conditions on actual cantilever specimens by the manufacturer. The wind gust test was developed to emulate an extreme real-world event that the cantilever system might be expected to endure. The pluck test can be thought of as a dynamic characterization test, while the wind gust test represents a stress test.

4.3.1 Pluck Test Description and Analytical Test Results

Unit impulse forces are valuable analytical devices, but difficult to realize in the real world. The characteristic feature of the impulse input is that it introduces energy across the entire spectrum. This is not always a prerequisite for real world testing. The pluck test is an alternative approach tailored for emulating real-world excitation events of flexible cantilever structures. As the name implies, it somewhat imitates a plucking action similar to plucking a guitar string. Analysis will show that it tends to primarily excite fundamental mode vibrations. This feature makes the pluck test a valuable

system test condition and the reason it was employed as the primary condition to demonstrate the Modal Damping Concept.

4.3.1.1 The Pluck Test Mathematical Model

The classical analytical input forcing functions include the impulse, the step, the ramp, etc. Their respective cause and effect relationships are well understood. By comparison, the ‘pluck’ function rarely shows up in classroom lectures. It no doubt evolved as a laboratory innovation motivated by the constraints of the physical world. Mathematically, the pluck test can be shown to be related to the simple step input test.

The step is commonly used to investigate transient behavior. It excites characteristic components of the system like the impulse function. Unlike the impulse, the system response to a step also includes a steady state forced component. Consider

the n^{th} order cantilever state space model: $\dot{\mathbf{x}} = \mathbf{A} \times \mathbf{x} + \mathbf{B} \times \mathbf{u}$, $\mathbf{x} = \begin{pmatrix} \mathbf{y}(t) \\ \dot{\mathbf{y}}(t) \end{pmatrix}$. The system was considered time-invariant. \mathbf{A} and \mathbf{B} were constant coefficient matrices.

Consider the system response to the step input. Let the step function occurring at $t = \tau$ be expressed as $r(t) = u_{-1}(\tau)$. Assuming zero initial conditions the Laplace transform of the system response becomes:

$$\mathbf{X}(s) = (s \mathbf{I} - \mathbf{A})^{-1} \times \mathbf{B} \times \mathbf{U}(s)$$

Noting that $\mathbf{U}(s) = \mathcal{L}_{aplace} [f_{step} u_{-1}(0)] = \frac{f_{step}}{s}$, where f_{step} is its scalar magnitude,

$$\mathbf{X}(s) = (s \mathbf{I} - \mathbf{A})^{-1} \times \mathbf{B} \cdot \frac{f_{step}}{s} = \frac{f_{step}}{[(s \mathbf{I} - \mathbf{A})] \cdot s} \text{Adjoint}(s \mathbf{I} - \mathbf{A}) \times \mathbf{B}$$

The determinant $|(s\mathbf{I}-\mathbf{A})|$ represents the system characteristic equation and is a $2n^{\text{th}}$ order polynomial of function 's' that can be factored into n pairs of complex conjugate factors,

$$|(s\mathbf{I}-\mathbf{A})| = (s+(\sigma_1+j\omega_1))(s+(\sigma_1-j\omega_1))(s+(\sigma_2+j\omega_2))(s+(\sigma_2-j\omega_2))\cdots(s+(\sigma_n+j\omega_n))(s+(\sigma_n-j\omega_n))$$

The adjoint matrix of $(s\mathbf{I}-\mathbf{A})$ is the transpose of the cofactor matrix

$$\text{adj}(s\mathbf{I}-\mathbf{A}) = \begin{pmatrix} \Delta_{1,1} & \cdots & \Delta_{1,2n} \\ \vdots & \ddots & \\ \Delta_{2n,1} & \cdots & \Delta_{2n,2n} \end{pmatrix}^T$$

Each cofactor is $\leq (2n-1)^{\text{th}}$ order polynomial of 's'.

The plucking action is assumed introduced at the top node of the cantilever hence for this model \mathbf{B} would take the form $\mathbf{B} = (0 \ 0 \ \cdots \ 1)^T$, and the step response becomes,

$$\mathbf{X}(s) = \frac{f_{step}}{|(s\mathbf{I}-\mathbf{A})| \cdot s} \begin{pmatrix} \Delta_{2n,1} \\ \Delta_{2n,2} \\ \vdots \\ \Delta_{2n,2n} \end{pmatrix}.$$

When the cofactors are expanded, the response takes the general form,

$$\mathbf{X}(s) = \frac{f_{step}}{|(s\mathbf{I}-\mathbf{A})| \cdot s} \begin{pmatrix} \sum_{m_1} a_{m_1} s^{m_1} \\ \vdots \\ \sum_{m_n} a_{m_n} s^{m_n} \\ s \sum_{m_{n+1}} a_{m_{n+1}} s^{m_{n+1}} \\ \vdots \\ s \sum_{m_{2n}} a_{m_{2n}} s^{m_{2n}} \end{pmatrix}, \quad m_i \leq (2n-1)$$

Note that all cofactors associated with nodal velocities $\dot{\mathbf{Y}}(s)$ have the additional factor ‘s’ in their expanded form. With the use of the Heavyside Expansion Theorem ^[109] the response can be factored to identify individual components:

$$\mathbf{X}(s) = f_{step} \begin{pmatrix} \frac{N_{1,1}(s)}{(s+(\sigma_1+j\omega_1))(s+(\sigma_1-j\omega_1))} + \dots + \frac{N_{1,n}(s)}{(s+(\sigma_n+j\omega_n))(s+(\sigma_n-j\omega_n))} + \frac{c_1}{s} \\ \vdots \\ \frac{N_{n,1}(s)}{(s+(\sigma_1+j\omega_1))(s+(\sigma_1-j\omega_1))} + \dots + \frac{N_{n,n}(s)}{(s+(\sigma_n+j\omega_n))(s+(\sigma_n-j\omega_n))} + \frac{c_n}{s} \\ \frac{N_{n+1,1}(s)}{(s+(\sigma_1+j\omega_1))(s+(\sigma_1-j\omega_1))} + \dots + \frac{N_{n+1,n}(s)}{(s+(\sigma_n+j\omega_n))(s+(\sigma_n-j\omega_n))} \\ \vdots \\ \frac{N_{2n,1}(s)}{(s+(\sigma_1+j\omega_1))(s+(\sigma_1-j\omega_1))} + \dots + \frac{N_{2n,n}(s)}{(s+(\sigma_n+j\omega_n))(s+(\sigma_n-j\omega_n))} \end{pmatrix} = f_{step} \begin{pmatrix} \mathbf{Y}(s) \\ \dot{\mathbf{Y}}(s) \end{pmatrix}$$

$\mathbf{Y}(s)$ of $\mathbf{X}(s)$ contains both natural and forced response components. $\dot{\mathbf{Y}}(s)$ contains only natural components. The state final values can be computed as

$$\lim_{t \rightarrow \infty} \mathbf{x}(t) = \lim_{s \rightarrow 0} (s \mathbf{X}(s)) = f_{step} (c_1 \quad \dots \quad c_n \quad 0 \quad \dots \quad 0)^T \quad (4.43)$$

The state vector was defined above as $\mathbf{x}(t) = \begin{pmatrix} \mathbf{y}(t) \\ \dot{\mathbf{y}}(t) \end{pmatrix}$. The computed final value

indicates that the system is at rest; nodal velocities decay to zero. The final value vector can therefore be simplified to

$$\mathbf{x}(\infty) = \begin{pmatrix} \mathbf{y}(\infty) \\ \mathbf{0} \end{pmatrix} = f_{step} (c_1 \quad \dots \quad c_n \quad 0 \quad \dots \quad 0)^T \quad (4.44)$$

The step input response can be applied to evaluate the nature of the Pluck input, which again is a laboratory innovation. Mathematically, the Pluck Test can be modeled as taking the form of the step input... more precisely, two step inputs. The first step deforms the structure to some specified initial conditions. It ‘pre-positions’ the structure to the desired initial condition set. The second step input is equal but opposite the first

step so that the sum of the two force sets equate to a zero force set for $t \geq 0$. It acts to release the structure emulating the ‘pluck’ action.

As shown above however, the step input produces transient and forced components. If the pre-positioning step is assumed to have occurred at $t = -\infty$, then the only remaining component of its forced response is the final value shown in Equation (4.44). The transient component can be expected to have decayed, and can therefore be assumed to be negligible.

The composite Pluck Test forcing function can be expressed as,

$$r_{pluck}(t) = f_{step} (-u_{-1}(-\infty) + u_{-1}(0)) = \begin{cases} -f_{step}, & t < 0 \\ 0, & t \geq 0 \end{cases}$$

$r_{pluck}(t)$ is clearly a two sided function; it is defined over the range $-\infty \leq t \leq \infty$.

However, the analysis can be converted to one-sided ($t \geq 0$) given the following conditions are met:

1. The transient component of the pre-positioning step is negligible.
2. The net force set on the system the instant after the pluck is the zero set.
3. The steady state component resulting from the pre-positioning step is treated as initial position conditions for the pluck-step.

Given these conditions, $\mathbf{r}_{pluck}(0^+) = \mathbf{0}$; $\mathbf{x}(0^+) = f_{step} \begin{pmatrix} c_1 \\ \vdots \\ c_n \\ \mathbf{0} \end{pmatrix}$. The Laplace transform of the

system response now becomes:

$$\mathbf{X}(s) = (s \mathbf{I} - \mathbf{A})^{-1} \times (\mathbf{B} \times \mathbf{U}(s) + \mathbf{x}(0^+))$$

where, $\mathbf{x}(0^+) = \begin{pmatrix} \mathbf{y}(0^+) \\ \mathbf{0} \end{pmatrix}$.

Following the same analytical steps as above,

$$\mathbf{X}(s) = \frac{f_{step}}{|(s \mathbf{I} - \mathbf{A})|} \text{Adjoint}(s \mathbf{I} - \mathbf{A}) \begin{pmatrix} c_1 \\ \vdots \\ c_n \\ \mathbf{0} \end{pmatrix}$$

$$\mathbf{X}(s) = \begin{pmatrix} \frac{c_1 \Delta_{1,1} + c_2 \Delta_{1,2} + \dots + c_n \Delta_{1,n}}{|(s \mathbf{I} - \mathbf{A})|} \\ \vdots \\ \frac{c_n \Delta_{n,1} + c_2 \Delta_{n,2} + \dots + c_n \Delta_{n,n}}{|(s \mathbf{I} - \mathbf{A})|} \end{pmatrix} \quad (4.45)$$

All components of the response $\mathbf{X}(s)$ are transient in nature. The final value of the Pluck Test is,

$$\lim_{t \rightarrow \infty} \mathbf{x}_{pluck}(t) = \lim_{s \rightarrow 0} (s \mathbf{X}_{pluck}(s)) = \mathbf{0}$$

as expected.

The transient response $\mathbf{X}(s)$, Equation (4.45), is shown to be a function of all the initial nodal displacements $\mathbf{y}(0^+) = (y_1(0^+) \ y_2(0^+) \ \dots \ y_n(0^+))^T$. The actual initial conditions for the concept demonstration test were predetermined to be $\mathbf{y}(0^+) = (.8 \ 2.85 \ 4.56 \ 6.43 \ 7.2)^T$ inch. This displacement set was driven by desiring a 10% height, or 7.2 inch displacement at the top node of the model. The associated force set required to achieve these initial conditions was computed to be $\mathbf{f} = (0 \ 0 \ 0 \ 0 \ 7 \ .)^T$ lbf.

The mode shapes for the experimental model were computed by Linear Modal Analysis. These modes shapes were utilized to decompose the displaced shape caused by the initial conditions into a weighted sum of modal components.

$$\mathbf{y}(0^+) = \mathbf{T} \times \mathbf{w}$$

where \mathbf{T} is the modal matrix and $\mathbf{w} = \mathbf{T}^{-1} \times \mathbf{y}(0^+)$ is the weighting vector. For the conditions given,

$$\mathbf{w} = (w_1 \quad w_2 \quad \cdots \quad w_5)^T = (1.0 \quad -.018 \quad .0018 \quad -.0002 \quad -.0003)^T \quad (4.46)$$

The weighting vector clearly indicates that the primary modal component associated with the Pluck test is the fundamental mode. This is precisely what was desired for Modal Damping testing. Because it became the targeted test for concept demonstration, it was one of the primary developmental and evaluation tests during the simulation activity.

Test setup involved determining nodal displacements that become the initial conditions for the simulation. Initial displacement at the top node of the cantilever was selected as the governing parameter and was pre-specified for simulation testing to be one foot. The force set necessary to deform the cantilever to meet the displacement criteria was easily determined from the elastic behavior of the cantilever,

$$\begin{aligned} \mathbf{f}_0 &= \mathbf{K} \times \mathbf{x}_0 \quad \rightarrow \quad \mathbf{x}_0 = \mathbf{K}^{-1} \times \mathbf{f}_0 \\ \mathbf{x}_0 &= [1 \quad x_2 \quad x_3 \quad x_4 \quad x_5]^T \\ \mathbf{f}_0 &= [f_1 \quad 0 \quad 0 \quad 0 \quad 0]^T \\ \mathbf{K} &= \begin{bmatrix} k_{11} & \cdots & k_{15} \\ \vdots & \ddots & \vdots \\ k_{51} & \cdots & k_{55} \end{bmatrix}, \quad \mathbf{K}^{-1} = \mathbf{S} = \begin{bmatrix} s_{11} & \cdots & s_{15} \\ \vdots & \ddots & \vdots \\ s_{51} & \cdots & s_{55} \end{bmatrix} \end{aligned}$$

From which,

$$\mathbf{f}_0 = \begin{bmatrix} 1 \\ s_{11} \\ 0 \\ 0 \\ 0 \\ 0 \end{bmatrix}^T$$

The initial displacement vector became

$$\mathbf{x}_0 = \mathbf{S} \times \mathbf{f}_0 = \begin{bmatrix} 1 & s_{21} & s_{31} & s_{41} & s_{51} \\ s_{11} & s_{11} & s_{11} & s_{11} & s_{11} \end{bmatrix}^T$$

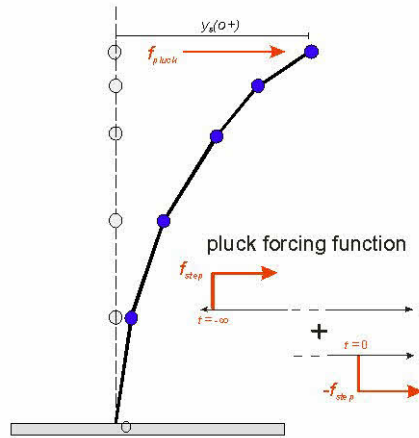


Figure 4-24 Pluck Test Initial Conditions

4.3.1.2 Pluck Test Response of the Aluminum Cantilever Structure (NO Augmentation)

Figure 4-25 diagrams the nodal position and velocity responses for the cantilever with no augmentation. These responses represent the ‘natural’ or characteristic responses of the system and are not very event filled. The responses represent a sum of orthogonal vibration modes of the cantilever structure with relative magnitudes related to the weighting function given in Equation (4.46). The Pluck Test response is primarily 1st mode as is evident by the simulation responses. Never the less, nodal position and velocity responses reveal some higher order component(s) content; the 2nd vibration mode is certainly visible at nodes 1 and 2 where the nodal axial locations correspond to the peak displacement location of the 2nd vibration mode shape.

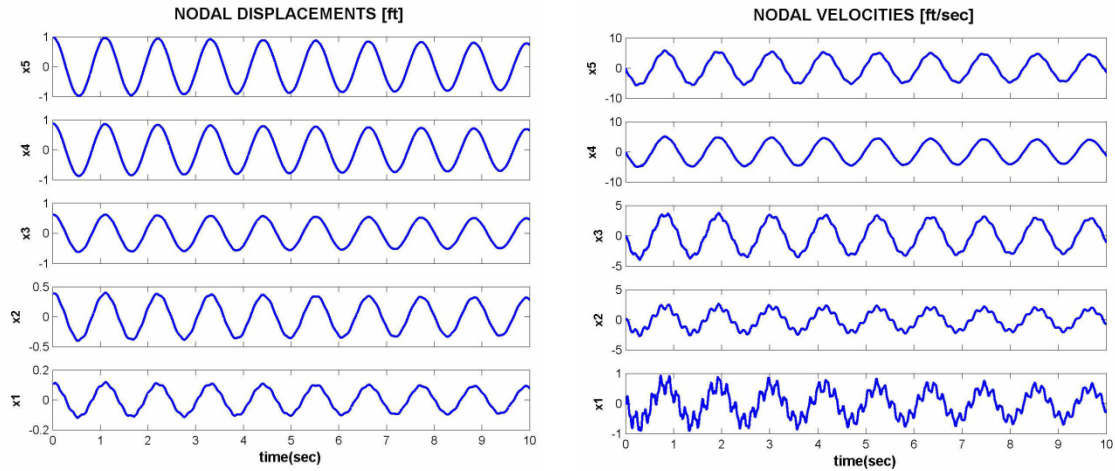


Figure 4-25 Pluck Test Nodal Responses [NO Augmentation]

The Discrete Fourier Transform and the Power Spectrum of the Node-1 position response are given in Figure 4-26. The diagrams confirm that the response is basically composed of the fundamental vibration mode of approximately .9 HZ. The data window for the analysis was 0 → 5 seconds.

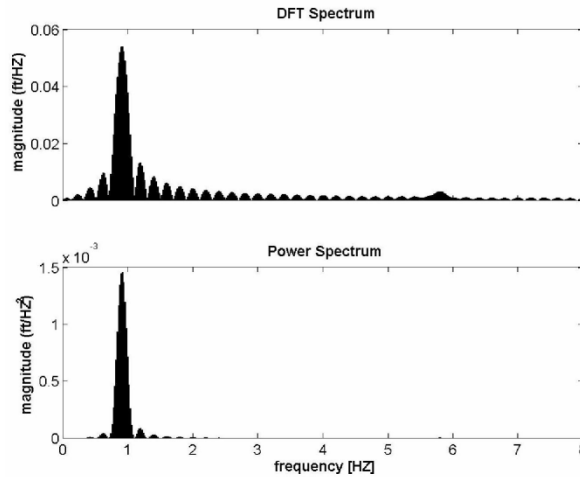


Figure 4-26 Pluck Test DFT [Node-1 Displacement/NO Augmentation]

4.3.1.3 Pluck Response of Cantilever/Tendon Pair [Modal Damping Augmentation]

Initial conditions for the augmentation test were identical to those described above for the natural response with no augmentation. However, the tendon control was

activated for this test. The simulation was designed to initiate one energy transfer (Modal Damping) event:

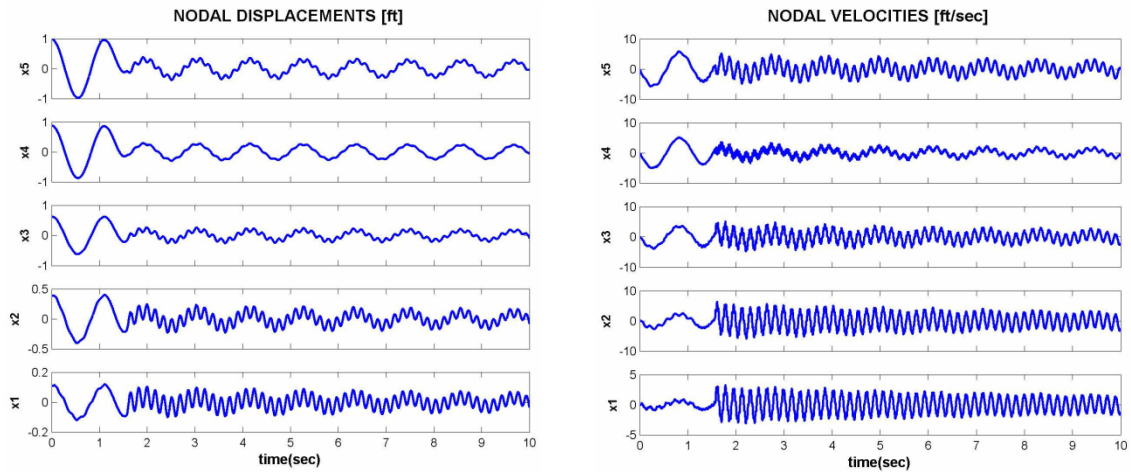


Figure 4-27 Pluck Test Nodal Responses [With Augmentation]

The control action can clearly be seen within both the position and velocity responses displayed in Figure 4-27. The tendon was ‘LOCKED’ during the 2nd vibration cycle at the 1.147 second mark. The ‘LOCKED’ cantilever/tendon pair redistributed the system kinetic energy to deform the shape of the cantilever. Tendon ‘LOCK’ was released at approximately the 1.57 second mark. The nodal responses reveal the generation of higher order vibrations caused by the re-distributed energy. The spectral analysis of the response of the Node 1 position response is diagrammed in Figure 4-28. The DFT window was adjusted, it was performed on the response after tendon ‘LOCK’ was released, at about the 1.57 second mark to the 5 second mark.

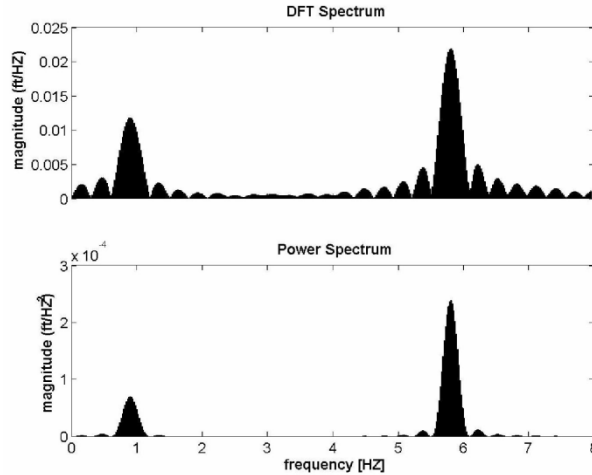


Figure 4-28 Pluck Test DFT [Node-1 Displacement/Augmentation]

The spectrum corroborates that significant energy was transferred to the 2nd vibration mode whose frequency was analytically predicted to be 5.8 HZ [Section 4.1.4].

In general, the position responses given in Figure 4-27 exhibit an overall reduction in peak-to-peak magnitude, particularly displacements of the upper nodes of the cantilever (Nodes 4 and 5). Peak-to-peak velocity magnitudes of the upper nodes have been somewhat reduced, while peak-to-peak magnitudes of the lower nodes show some amplification.

An alternative perspective of the augmentation effects can be found by plotting state-space trajectories of the cantilever/tendon pair dynamics during the energy transfer action. The state trajectory is an analysis technique often employed during the investigation of non-linear systems where classical linear analysis techniques are limited. State trajectories for Node 2 and for Node 4 were developed and are shown plotted in Figure 4-29. The trajectories formed by plotting nodal velocity as a function of nodal position reveal the effects of forcing energy into higher order modes. They visually illustrate the impact of energy redistribution within the structure.

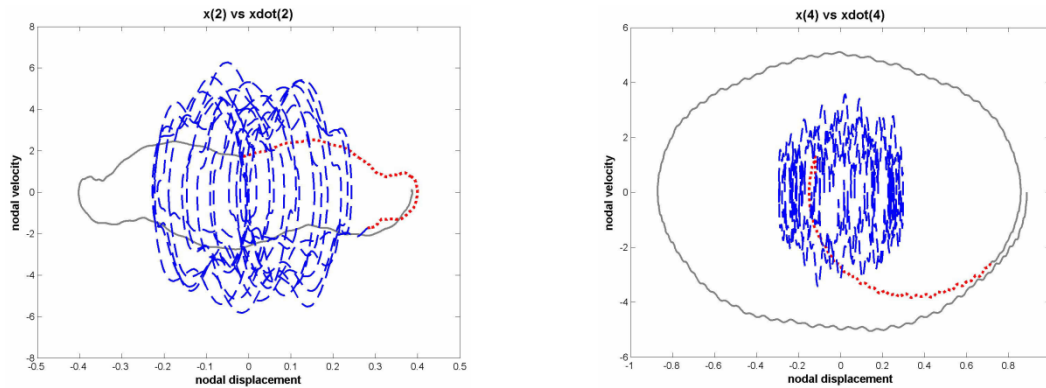


Figure 4-29 Nodes 2 & 4 State Trajectories [Pluck Test]

The trajectory has been plotted to distinguish three different phases:

1. Pre-'LOCK' phase (plotted as a solid dark grey line).
2. Transition or 'LOCKED' phase (plotted as a dotted red line).
3. Post-'LOCK' phase (plotted as a dashed blue line).

Consider first Node-2 which was located in the lower section of the cantilever. In general, the modal damping event exchanged nodal-displacement for nodal velocity. This was in fact, the fundamental objective, since the internal anelastic damping mechanism of the structure is directly related to the velocity of structural deformation ($f_{damping} \propto \dot{x}$). The trajectory also shows that the peak-to-peak displacement range decreased ($\pm .4 ft \rightarrow \pm .27 ft \sim 33\%$). The number of displacement cycles increased, but each cycle is smaller in magnitude.

The modal damping event significantly improved the dynamical behavior of Node-4. Both the nodal displacement range and the nodal velocity range were reduced. In fact, the trajectory of the Post-'LOCK' phase is shown to be completely enveloped by the trajectory of the Pre-'LOCK' phase. Node-4 was located within the upper section of the structure. The demonstrated dynamic improvement would be highly desirable given an inhabited structure. The trajectory does indicate that a residual fundamental

vibration component remained after the modal damping event, however it was significantly reduced in magnitude. There appeared to be appreciable higher order dynamics but the peak-to-peak magnitude was relatively small.

4.3.1.4 Simulation Animation

The simulation output of the Pluck Test was rendered into an animation graphically showing the dynamic behavior. Although the resolution is limited by the 5 DOF model, it is sufficient to reveal the modal energy conversion. A sequence of frames was taken from the animation and compiled in Figure 4-30 in an attempt to capture the essence of the animation. Note that the horizontal and vertical scales are not equal. The horizontal scale has been exaggerated in order to emphasize the cantilever deformation. The frames are shown grouped into the following three phases:

Pre-‘LOCK’ Phase — These frames capture the cantilever during free vibration from $t=0$ sec until the ‘LOCK’ command was executed. The cantilever initial conditions show it offset to the right by 1 foot measured at the top node. After the cantilever was released, it swayed toward the left, and then swayed to the right. It completed one sway cycle in approximately 1.1 seconds indicating a sway frequency of approximately .91 Hz.

‘LOCK’ Phase — When the fundamental mode potential energy was determined maximum, the tendon control element BD was ‘LOCKED’ in length. The cantilever began its sway to the left powered by the internal strain energy. The ‘LOCKED’ cantilever/tendon pair caused the cantilever to re-shape into the approximate 2nd mode shape. The connection forces are shown in the figures as bars located at the static positions of the connecting nodes. The scale is shown to be 500 lbf per unit grid element.

Post-‘LOCK’ Phase — Once the monitored kinetic energy of the fundamental mode during the ‘LOCKED’ the half cycle was determined depleted, the tendon control element BD was ‘UNLOCKED’. The cantilever began to free-vibrate once again. The 2nd mode shape can be seen in the animation frames. Also note that the magnitude of deflections from fundamental mode vibration decreased.

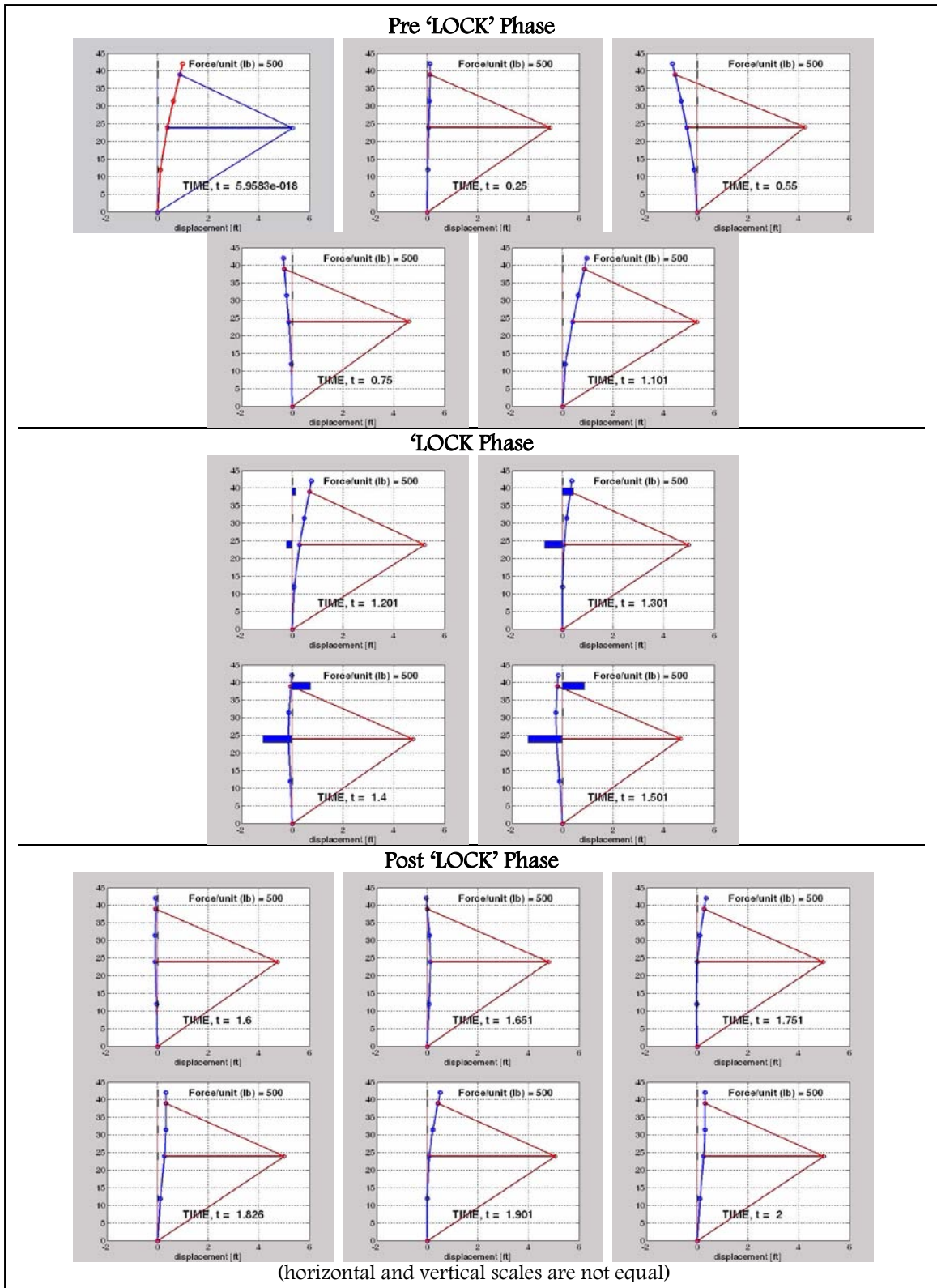


Figure 4-30 Animated Sequence of Pluck Test Simulation Results

4.3.2 Wind Gust Test Description and Results

The wind gust test was designed to emulate a pseudo real-world, extreme stress event. The gust was designed to produce a forcing function diagrammed in Figure 4-31. The event time was selected to be relatively short; the gust duration was only 1 second. The short time period of the event was of particular interest because its frequency components offered the potential of resonant coupling into the fundamental vibration frequency of the cantilever pole.

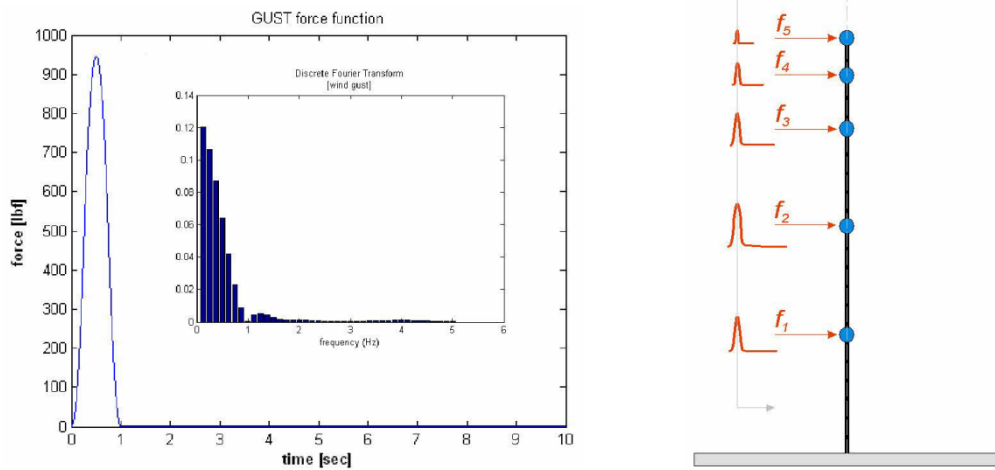


Figure 4-31 Wind Gust Forcing Function and Distribution

The peak magnitude of the gust function was modeled using data produced by “Wind Loads on Structures v1.6”^[110], a software application that computes wind loading on structures. An extreme wind condition was examined: a 120 MPH peak wind velocity. The total wind force inflicted on the pole was calculated to be 946.5 lbf.

The gust force function was distributed over the cantilever structure based upon sectional area in conjunction with ASCE/SEI 7-05^[111]. No local topography was assumed in the neighboring area to effect force distribution.

4.3.2.1 Wind Gust Response of Cantilever (No Augmentation)

Figure 4-32 diagrams the nodal time responses of the cantilever with no augmentation. The associated DFT for the node-2 displacement is diagrammed in Figure 4-33 for the time period $0 \rightarrow 5$ seconds.

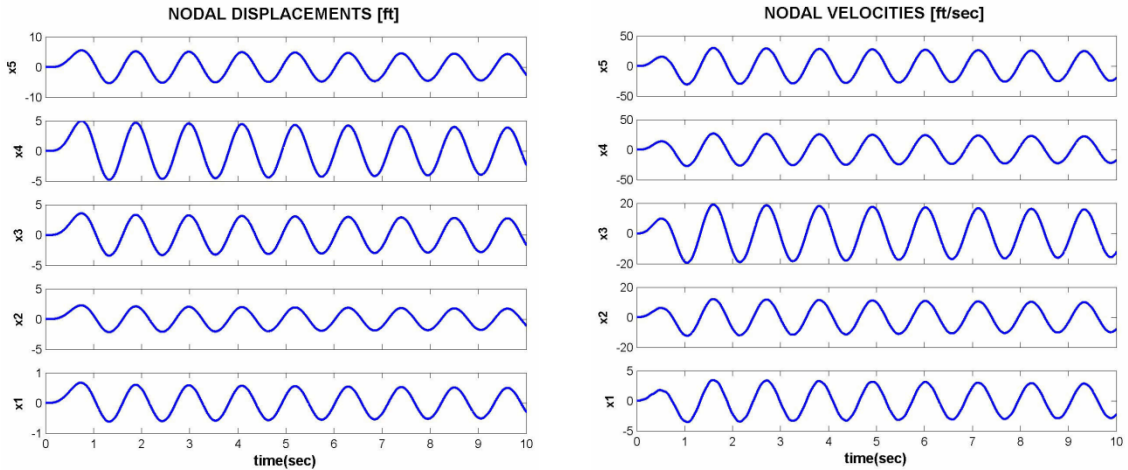


Figure 4-32 Wind Gust Test Nodal Responses [NO Augmentation]

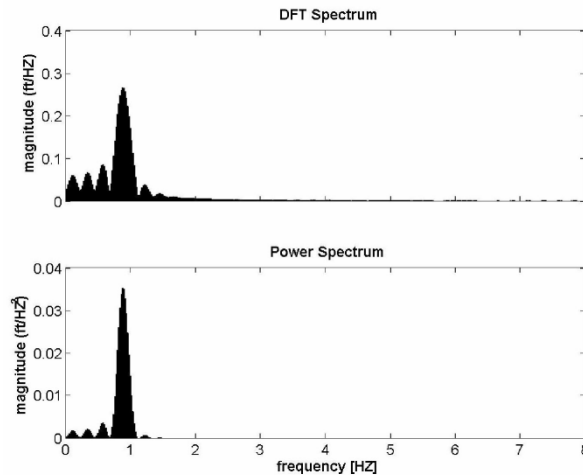


Figure 4-33 Wind Gust Test DFT [Node-1 Displacement/NO Augmentation]

The responses indicate that:

- The cantilever was at rest prior to being subjected to the gust forcing function; there were no initial displacements or velocities $\mathbf{x}(0) = \dot{\mathbf{x}}(0) = \mathbf{0}$.

- The displacement and velocity magnitudes for all nodes were significantly greater than those produced by the Pluck Test, a displacement of approximately 5.4 feet and a nodal velocity in excess of 32 feet per second at the top node.
- Unlike the responses produced by the Pluck Test, the responses produced by the Gust Test not only included natural or characteristic components of the structure, but also components related to the gust forcing function. The DFT displayed evidence of additional components due to the forcing function at and below the fundamental frequency of the system when compared to the Pluck Test.
- The response spectrum indicates that the fundamental mode is dominant for the gust forcing function in agreement with Y. L. Xu's findings^[86]. Very little higher order response was observed.

4.3.2.2 Wind Gust Response of Cantilever/Tendon Pair [Active Damping Augmentation]

Initial conditions were identical for this test to those described above for the Wind Gust Response (No Augmentation) simulation. However, the tendon control was activated for this test. The simulation was designed to initiate one energy transfer or Modal Damping event.

The control action can clearly be seen within both the displacement and velocity time responses displayed in Figure 4-34. The controller 'LOCKED' the tendon at the .81 second mark. The 'LOCKED' cantilever/tendon pair forced system dynamic energy to deform the shape of the cantilever. Tendon 'LOCK' was released at approximately the 1.23 second mark.

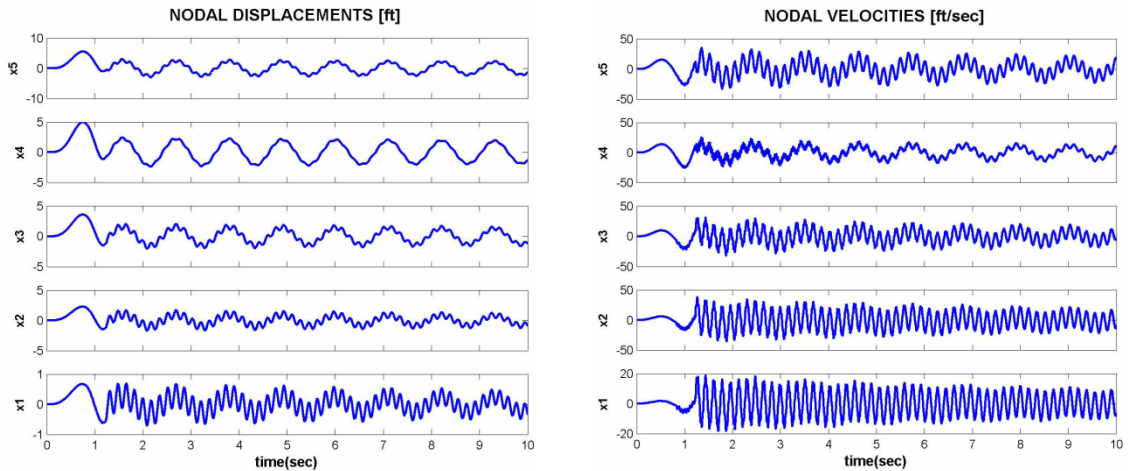


Figure 4-34 Wind Gust Test Nodal Responses [With Augmentation]

The nodal responses of Figure 4-34 clearly reveal the generation of higher order vibrations caused by the re-distributed kinetic energy. Figure 4-35 diagrams the spectral analysis of the Node-1 displacement response.

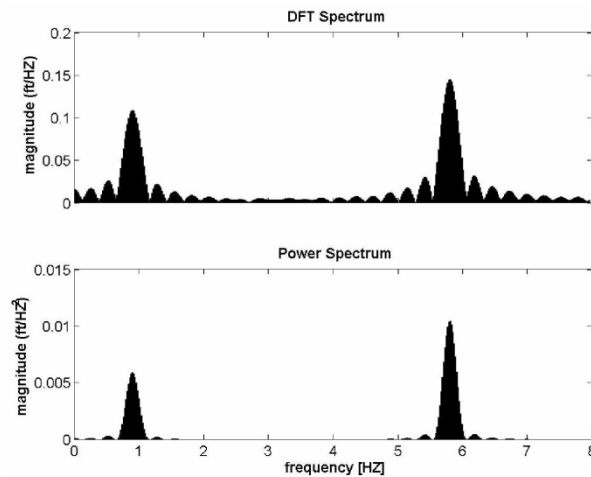


Figure 4-35 Wind Gust Test DFT [Node-1 Displacement/Augmentation]

The DFT was performed on the response after tendon ‘LOCK’ was released, beginning at the 1.23 second mark and continuing through the 5 sec mark. The spectrum verifies that significant energy was transferred to the 2nd vibration mode whose frequency was computed to be 5.8 Hz.

Nodal displacements of the augmented system were compared to those of the non-augmented system. In general, augmentation resulted in an overall reduction in nodal displacements of approximately 40-50% in the upper nodes of the cantilever (Nodes 4 and 5). Nodal velocity comparisons between augmented and un-augmented systems were more dramatic. Nodal velocities attributed to the fundamental mode were notably reduced in magnitude. All nodes showed an increase in velocity due to 2nd mode action. Lower nodes in particular show significant 2nd mode contributions. In fact, the resultant peak magnitude of velocity for the lower nodes was nearly all due to the augmentation action. The dominance of the nodal velocity contribution due to the 2nd vibration mode is diagrammed in the DFT Figure 4-36 of the node-1 velocity response for the period 1.23 sec → 5 sec.

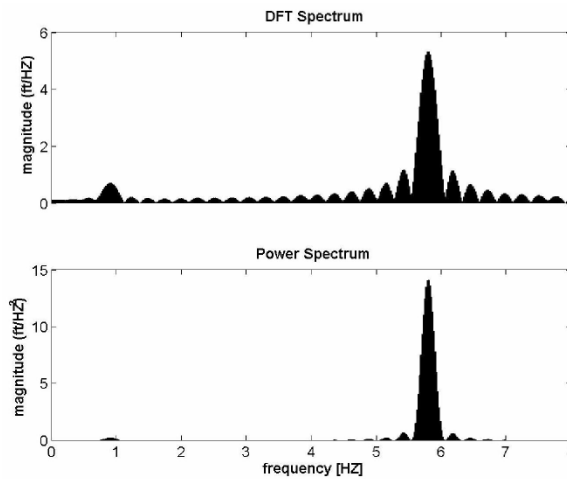


Figure 4-36 Wind Gust Test DFT [Node-1 Velocity/With Augmentation]

Again, the plot of the state space trajectory was developed to provide an alternative perspective of the augmentation effects. State trajectories for node-2 and for node-4 are shown plotted in Figure 4-37. The three different phases are distinguished in the trajectories: Pre-‘LOCK’ phase (plotted as a solid dark grey line), Transition or

‘LOCKED’ phase (plotted as a dotted red line), Post-‘LOCK’ phase (plotted as a dashed blue line).

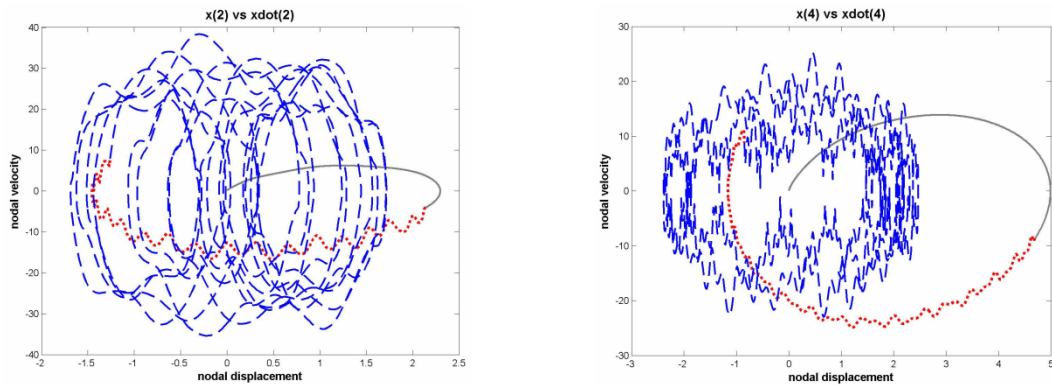


Figure 4-37 Nodes 2 & 4 State Trajectories [Wind Gust Test/Augmentation]

The trajectory of node-2, located in the lower section of the cantilever, visually illustrates the intense 2nd order vibrations. Again, this was expected and essentially demonstrates the execution of the fundamental objective of transferring energy to a higher vibration mode. The increased velocity behavior translated into increased damped energy. The trajectory also shows that displacement range decreased some ($\pm 2.0\text{ ft} \rightarrow \pm 1.75\text{ ft}$, $\sim 12\%$), but the peak-to-peak per vibration cycle was reduced.

Node-4 is located in the upper section of the cantilever. The state space trajectory indicates that the modal damping event did improve its dynamical behavior somewhat. Specifically, the nodal displacement range was reduced ($\pm 4.8\text{ ft} \rightarrow \pm 2.8\text{ ft}$, $\sim 42\%$) with minor 2nd order contribution. The nodal velocity range is approximately unchanged but shows 2nd order contribution.

4.3.3 Damping Augmentation — Summary Analysis of the Simulation Findings

The analytical damping model of the aluminum cantilever dynamic simulation was initially designed to incorporate the findings of Kareem^[85] who suggested that the

damping properties of inherent vibration modes for tall, underdamped flexible steel structures could be correlated by the following relationship:

$$\frac{\zeta_n}{\zeta_1} = 1 + C \left(\frac{f_n}{f_1} - 1 \right)$$

Increased vibration energy dissipation in the higher order modes is implied when $C > 0$ and $\frac{f_n}{f_1} > 1$ which was shown to be the case for the structures of interest. The initial damping model was enhanced with experimentally measured parameters taken during the Anelastic Damping Parameter Assessment (see Section 5.1). The measured data demonstrated similar damping trends among the vibration modes.

The simulation plan was designed to evaluate much more than the damping model. The investigation of the concept of transferring energy between orthogonal vibration modes, the control scheme to effect such energy transfer, the phenomenological modeling of the non-linear process exhibited by the control actuator, and the overall impact on the structure, all of which lead up to the utilization of the damping models that in the end indicated accelerated damping of vibration energy, were significant objectives of the exercise.

Figure 4-38 contains two energy damping trajectories generated from simulated Pluck Tests. Instantaneous system energy is computed as the sum of potential and kinetic energies of the nodal lumped masses.

$$U(t) = \frac{\mathbf{x}^T \times \mathbf{K} \times \mathbf{x}}{2} + \frac{\dot{\mathbf{x}}^T \times \mathbf{M} \times \dot{\mathbf{x}}}{2}$$

The leftmost trajectory represents that of the natural response, or un-augmented test. The other was generated with the Modal Damping augmentation active. Enhanced energy dissipation is illustrated. This is a testimony to: 1.) fundamental energy

transferred into the 2nd vibration mode, and 2.) more efficient vibration impedance within the 2nd vibration mode. Anelastic energy dissipation is generally considered to be, and was experimentally observed to be exponential in nature. The exponential decay rate increased in the trajectory after the Modal Damping event. The smaller time constants associated with this roll-off was due to the anelastic damping nature of the 2nd vibration mode.

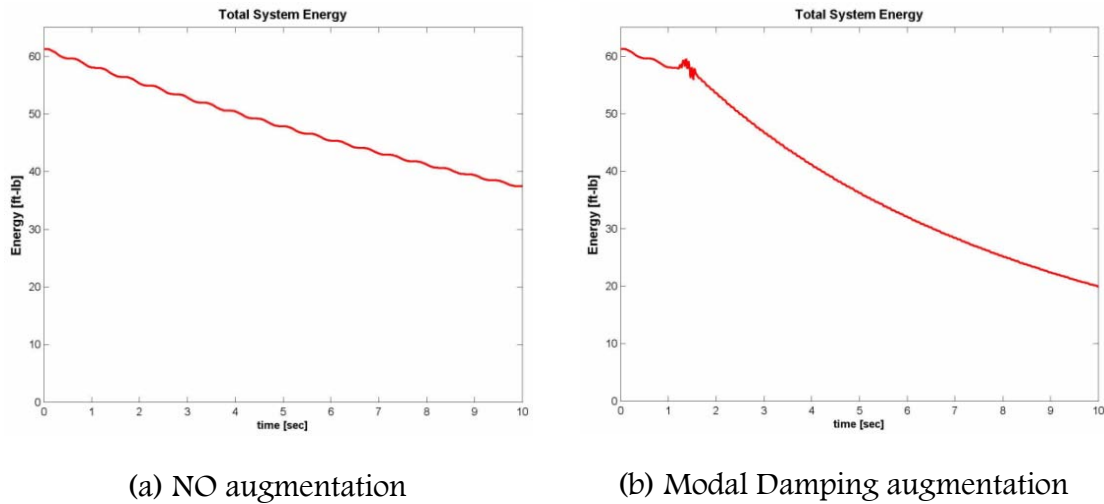
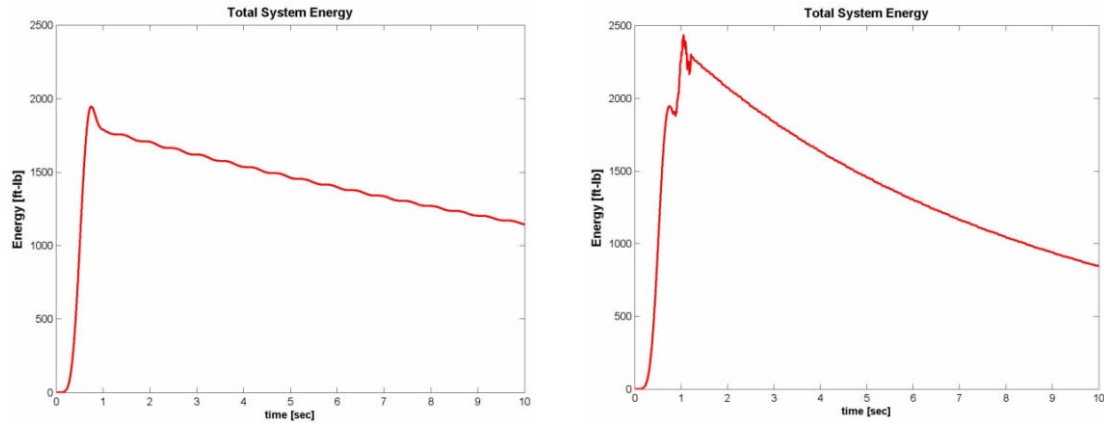


Figure 4-38 Energy Dissipation Trajectories - Pluck Test

Energy dissipation trajectories were similarly determined for the simulated Wind Gust Tests. The resulting trajectories are shown in Figure 4-39. Again, improved energy dissipation roll-off is shown occurring after the Modal Damping augmentation event. The Wind Gust Test did reveal a weakness to the Modal Damping logic as implemented. When compared, the energy dissipation trajectories given in Figure 4-39 indicate that more energy was introduced into the system when using Modal Damping. First thoughts were that the tendon model was the cause of the perturbation; the emulated control force was not distributed accurately resulting in work being done on the system consequently adding energy.



(a) NO augmentation

(b) Modal Damping augmentation

Figure 4-39 Energy Dissipation Trajectories – Wind Gust Test

Further analysis indicated that the tendon model did in fact respond correctly, but the timing of the Modal Damping event taken in conjunction with the wind gust event resulted in more wind energy coupled into the structure. The results of the Wind Gust Test points out the need to enhance the logic of the Control Law to account for the behavior of the excitation function in order to prevent a positive-feedback like condition. The addition coupled energy was never the less dissipated quickly after the Modal Damping event. At the 5 second mark, the total system energy after Modal Damping had dipped below that of the naturally damped system.

A simple benchmark can be made between the naturally damped and the Modal Damping augmented system using the energy trajectories by comparing the state of the system energy at some mark in time. The 10 second mark was selected and the comparison is summarized in Table 4-2. The *Dissipation Ratio* specified in the table, quantifies the damping improvement using the Modal Damping Augmentation.

Table 4-2 Simulation Damping Performance Summary (10 sec mark)

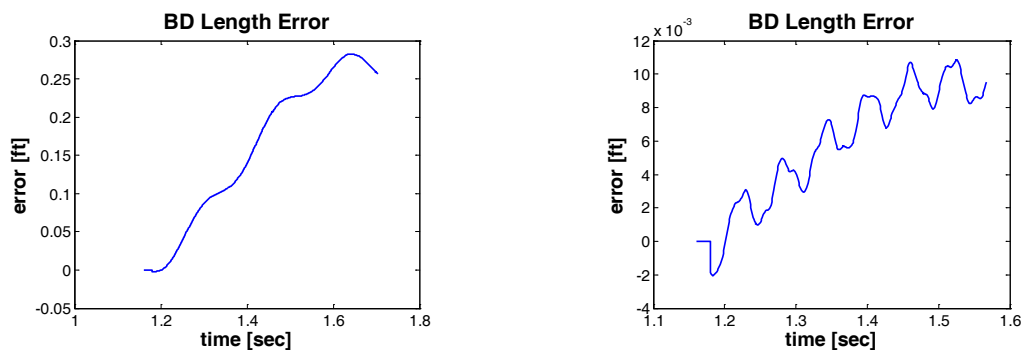
	Natural Damping [% damped]	Modal Damping [% damped]	Improved Dissipation Ratio
Pluck Test	38.8%	67.5%	1.74
Wind Gust Test	41.2%	56.5%	1.37

$$\% \text{ damped} = \left[1 - \frac{\text{Energy}(t = 10 \text{ sec})}{\text{Energy}_{\text{natural damping}}(t_{\text{peak}})} \right] \times 100\% \quad \text{Energy} = \frac{x^T \cdot K \cdot x}{2} + \frac{\dot{x}^T \cdot M \cdot \dot{x}}{2}$$

4.3.3.1 Tendon Model Evaluation

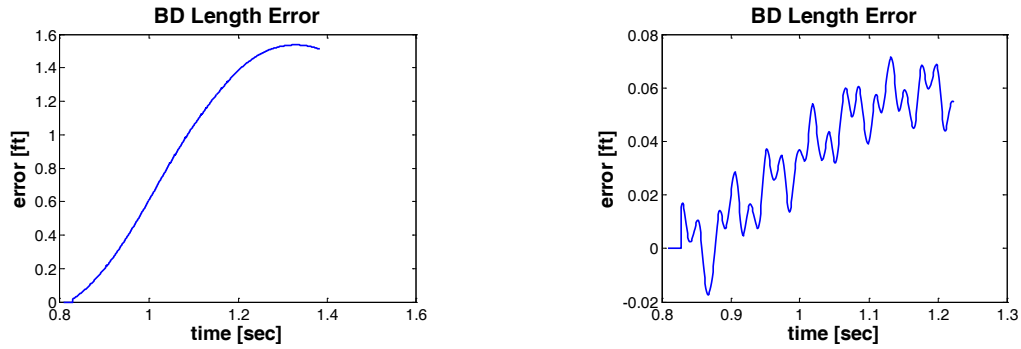
Multiple versions of potential tendon physical based models were discussed and evaluated in Section 4.2. Each modeling approach had predictable errors associated with simplifying assumptions or linearizations. The selected tendon phenomenological model was designed to regulate the length of the control element (BD) during the energy transfer event. Post-test evaluation involved comparing simulated results to the control objectives.

Control variable performance of the Tendon Feedback Force algorithm for both the Pluck Test and the Wind Gust Test conditions are illustrated in Figure 4-40 and Figure 4-41.



(a) BD variation without feedback control (b) BD variation with feedback control

Figure 4-40 BD Errors - Pluck Test



(a) BD variation without feedback control (b) BD variation with feedback control

Figure 4-41 BD Errors – Wind Gust Test

Ideally, the tendon model would precisely regulate the length of BD and drive the BD length error to zero (in some finite time). Although the error magnitudes were small, the results indicate that the responses were not truly ideal. The proportional gain regulator reduced BD length error by a factor of approximately 4 in the Pluck Test case, and a factor of approximately 20 in the Wind Gust Test case. The regulator design did not drive the error to zero nor did the error trajectory appear to tend to zero. However, length errors were reduced to fractions of an inch where there would otherwise have been length errors of multiple inches (Pluck Test) to feet (Wind Gust Test). And the sensitivity of the regulator design resulted in error magnitudes for the regulated variable that were in the approximate range $-0.02 \rightarrow 0.09 \text{ ft}$ for both tests, despite the different test conditions.

The resulting regulator performance was in fact predictable. Steady-state error of the closed loop system is related to plant type and feedback design. The system itself exhibited 2nd order dynamics while the feedback associated with tendon behavior was designed to be proportional. Consider any one node in the system; it has a basic minimum phase characteristic transfer function that takes the form,

$$G(s) = \frac{Y(s)}{U(s)} = \frac{K_G}{s^2 + a_1s + a_2}$$

When a closed loop linear feedback configuration is formed in order to regulate the output, the error signal to some disturbance becomes,

$$E(s) = \frac{G(s) \cdot H(s)}{1 + G(s) \cdot H(s)} \delta(s)$$

The disturbance (δ) manifested by the tendon 'LOCK' command, as shown as the second plots of Figure 4-40 and Figure 4-41, is 'ramp like'. Given a proportional control gain,

$$H(s) = K_H$$

The final value error, $e(\infty)$, can then be found,

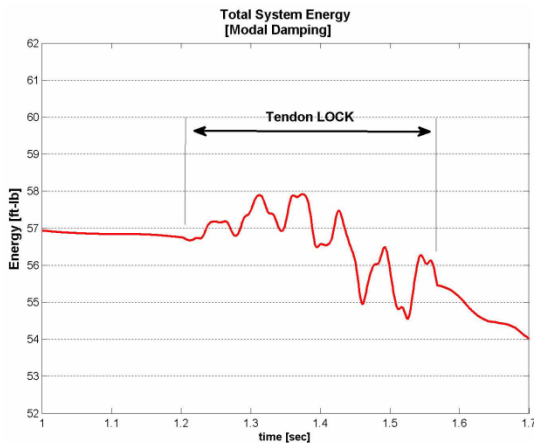
$$E(s) = \frac{K_G \cdot K_H}{(s^2 + a_1s + a_2) + K_G \cdot K_H} \cdot \frac{\delta}{s^2}$$

$$e(\infty) = s \cdot E(s)_{s \rightarrow 0} = \infty$$

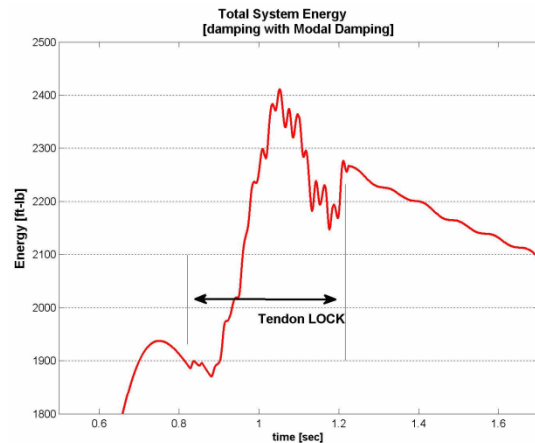
The disturbance is ramp like', but if decomposed, it would contain higher order functions as well as a ramp component. The discussion above is still valid in that it explains the nature of the steady state error. The disturbance actually embodies nonlinearities that are the result of the varying geometric configuration. Therefore, the regulator design with its proportional feedback gain will never completely eliminate length error when emulating the 'LOCKED' tendon. However, its performance was nonetheless determined reasonable and acceptable. The disturbance time is relatively short and the error over this time was shown to be small. There are further advantages to the proportional gain design as it reduced model implementation complexity and simulation run-time requirements. Finally, and most importantly, the emulation

demonstrated the ability of the 3-point tendon to transfer energy from the fundamental vibration mode to that of the second mode... the ultimate objective.

Although proven to be more than adequate in the Concept Demonstration testing, the non-perfect representation of the tendon physics caused small perturbations in the energy dissipation trajectories recorded during the Modal Damping augmentation simulation runs (Figure 4-38 and Figure 4-39). Both trajectories should ideally be monotonically decreasing since no energy was added to the system by the ‘LOCKED’ tendon. Examine first the results of the Pluck Test. The trajectory segment during the ‘LOCK’ phase (~1.2 sec → 1.57 sec) is shown in Figure 4-42a. The trajectory indicates that a small amount of energy appeared to be added. This transient is caused by the dynamics of the closed-loop cantilever/tendon model that includes the approximations and assumptions previously described.



(a) Pluck test



(b) Wind gust test

Figure 4-42 Energy Trajectory Discrepancies

The same trajectory segment captured during the ‘LOCK’ phase of the Wind Gust Test (.81 sec → 1.23 sec) is shown in Figure 4-42b. At first glance, the added energy in this case appears to be significant for this scenario, over 500 lb-ft of work

when compared to the un-augmented case. After closer examination, the added energy was determined to be the result of two contributors. The major contributor was the wind gust itself, which continued to subject the cantilever to forces beyond the 1 second mark. The Modal Damping action served to couple additional energy into the system during the time that the wind gust overlapped the Modal Damping event. The ‘LOCKED’ tendon caused the upper portion of the cantilever to reverse acceleration direction, synchronizing it with the direction of the wind gust. While synchronized, the gust amplified the effect of the tendon, causing additional wind energy to be captured by the cantilever. The tendon related energy contributions are difficult to distill from the composite response. They are more clearly visible during the 2nd half of the ‘LOCK’ phase (~1 sec → 1.23 sec). The tendon effects appear to be similar in proportion to those illustrated in the Pluck Test.

4.3.3.2 Base Support Forces

Another merit considered during the Modal Damping evaluation is the effect on forces at the base support of the cantilever. The resultant base moment force for the Pluck Test and the Wind Gust Test are plotted in Figure 4-43 and Figure 4-44 respectively. Each figure shows the un-augmented versus the Modal Damping augmented resultant base force response. The resultant base moment was computed to be,

$$M_{base} = \mathbf{h}^T \cdot (\mathbf{K} \times \mathbf{x}) \quad (4.47)$$

where, \mathbf{K} is the system stiffness matrix, \mathbf{x} is the nodal displacement vector, and \mathbf{h} is the nodal height vector that represents the distance between the base and the axial position of the lumped nodal mass..

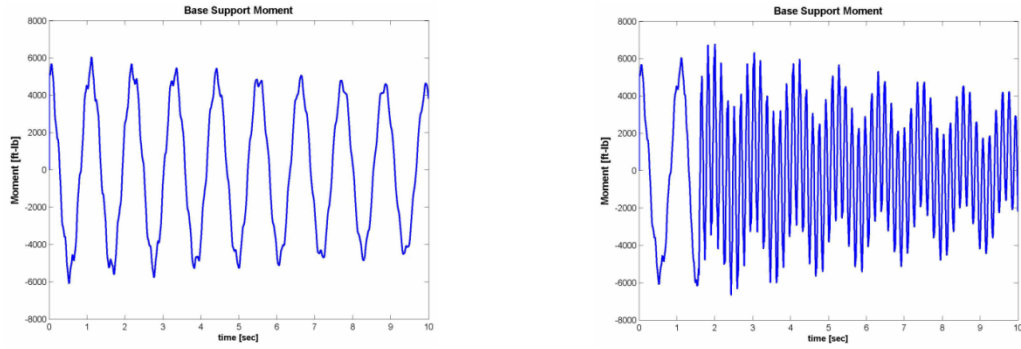


Figure 4-43 Base Moment [Pluck Test][NO Augmentation vs. Augmentation]

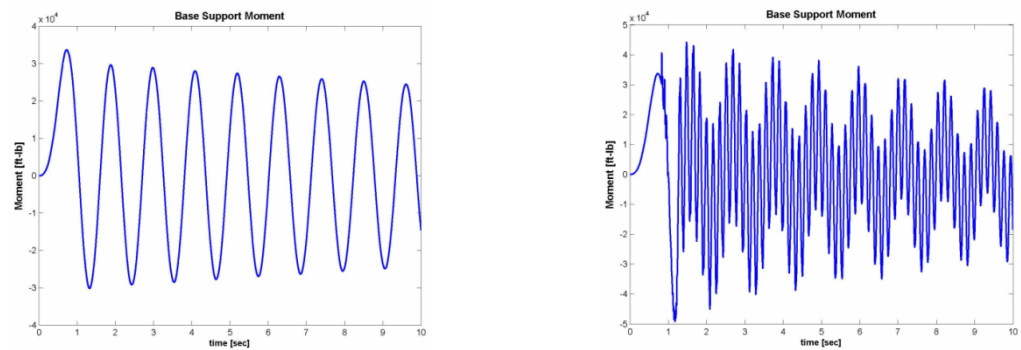


Figure 4-44 Base Moment [Wind Gust Test][NO Augmentation vs. Augmentation]

Damping augmentation had no appreciable effect on the worst case magnitude of moment during the Pluck Test response. When decomposed into modal components, the results indicated that:

- The forced 2nd mode vibration introduced more stress cycles over the period of time plotted, however the peak-to-peak magnitude of each cycle was noticeably less than the un-augmented stress cycle.
- The stress cycles associated with the fundamental mode noticeably decreased due to transferred energy facilitated by the Modal Damping event.

In general, the base force computed during the Wind Gust test was found to behave similarly to that computed during the Pluck Test. There was some noticeable increase in absolute moment magnitudes immediately after tendon ‘LOCK’ was first activated. This

was due to the added energy coupled into the system from the wind gust caused by the 'LOCKED' action of the cantilever/tendon pair. This larger base force was damped quickly however and the subsequent stress cycles were at or significantly below that of the un-augmented response.

4.3.3.3 Summary

The analytical results of the MATLAB/SIMULINK simulation of the Modal Damping Augmentation lead to the following findings:

1. Vibration energy can be transferred between the fundamental mode and the 2nd order mode using a relatively simple 3-point controllable tendon.
2. Modal Damping Augmentation improved the overall dynamic energy dissipation behavior of the subject structure. Improvements in the range of 30% to 70% were shown for the test scenarios investigated.
3. In general, nodal displacements were improved across the structure after the Modal Damping event, in some locations up to 40%. Nodal velocities lower in structure experienced an increase in magnitude up to 100%. The increased velocities coincided with increased structural deformation rates leading to increased energy dissipation by the anelastic mechanism.
4. The Modal Damping control law could be enhanced allowing the amount of energy transferred to be adjustable. In doing so, an optimal condition could be found that would result in a compromise between modal energy transferred and the resulting structural dynamics. Improved energy dissipation could still be achieved yet maximum nodal velocities could be constrained.

CHAPTER V
EXPERIMENTAL TESTING

Two separate experimental test activities were conducted to support the Modal Damping study:

1. The Anelastic Damping Parameter Assessment investigated the anelastic damping behavior of both structural aluminum and steel.
2. The Modal Damping Concept Demonstration was a closed-loop system proof-of-concept and qualitative evaluation.

5.1 Anelastic Damping Parameter Assessment

The objective of the parametric assessment was to investigate the material/anelastic damping behavior of two common structural materials: 6061 aluminum and a common carbon alloy steel. Simple cantilever structures, each with prescribed dynamics were designed and fabricated using the structural materials. Specific test objectives were:

1. Conduct the necessary dynamic tests to determine the damping coefficients for a sufficient number of vibration modes ($\sigma_{i=1 \rightarrow 4}$).
2. Investigate the modal damping relationships.
3. Compared the measured damping behavior to that predicted using the Rayleigh (proportional) damping model, and the Kareem damping model.

4. Investigate the linearity of the damping behavior as a function of deformation magnitude within the elastic range of the material.
5. Develop a reasonable anelastic damping model for integration into the dynamic simulation.

This experimentation activity was accomplished as a supporting investigation as opposed to an in-depth research program. Although a methodical approach was developed and adhered to, it could be argued that there was neither a sufficient amount, nor range of testing conducted. The objective was to develop a believable damping model that could be used to develop the Modal Damping concept. The intended objective was believed to be met. However, it could again be reasonably argued that the results should be considered more qualitative than quantitative.

5.1.1 Technical Discussion

The Rayleigh and the Kareem formulations are linear predictive models developed to estimate general structural vibration damping parameters. Each was introduced in Section 3.1.1. The Rayleigh model assumes that damping properties can be modeled as being proportional to the system mass and stiffness associated with the particular mode of interest,

$$c = c_m + c_k = \alpha_m m + \alpha_k k \quad (5.1)$$

Equation (5.1) can be rearranged to yield,

$$\sigma_i = \omega_i \zeta_i = \omega_i \left(\frac{\alpha_m}{2 \omega_i} + \frac{\alpha_k \cdot \omega_i}{2} \right) \quad (5.2)$$

where σ_i represents the coefficient of the exponential damping component as shown in the simple characteristic decaying modal response given as $y(t) = y_0 e^{-\sigma_i t} \sin(\omega_i t + \phi)$.

The formulation of Equation (5.2) was found to have more utility when correlating experimentally measured behavior. Equation (5.2) contains two unknown coefficients: α_m and α_k that were computed using a least squares fit to measured experimental data. The predictive model formed by Equation (5.2) yields ζ and σ as continuous functions of ω , however the damping parameters are assumed valid at only the structure's distinct natural modes.

The Kareem model assumes that general damping properties can be expressed as a function of the system fundamental mode behavior,

$$\zeta_i = \zeta_1 \left[1 + C \cdot \left(\frac{\omega_i}{\omega_1} - 1 \right) \right]$$

The parameter C is a constant that must be computed. Once computed, it is applicable for a given class of structures. Kareem determined that .38 adequately represents the behavior of tall steel structures. Once again, substituting $\zeta_i = \frac{\sigma_i}{\omega_i}$ yields the Kareem relationship as a function of the damping coefficient, σ_i .

$$\sigma_i = \sigma_1 \left[C \left(\frac{f_i}{f_1} \right)^2 + (1 - C) \left(\frac{f_i}{f_1} \right) \right]$$

5.1.1.1 Geometric Design

The design process was identical for both the aluminum damping parameter (ADP) and steel damping parameter (SDP) specimens. Simple cantilever structures were constructed to represent the flexible underdamped structures of interest. Vibrations were desired in only one lateral direction; therefore the structures were designed to be flexible along one lateral axis and stiff along its orthogonal axis. A cross-sectional

geometry was chosen so that one axis dominated in terms of moment of inertia. A simple flat plate structure where the width to depth ratio was much greater than unity satisfied these requirements.

Both material properties and geometry (height, width and depth of the cantilever plate) factor into the specimens dynamic behavior. Material properties were established by the specimen type; the specimen's dimensions became the independent design variables. Modal behavior governing the system response was controlled by the appropriate height (h_c), width (w_c), and thickness (t_c) definition. Specimen dimensions were chosen to achieve approximate deformation rates of the baseline HAPCO-like aluminum cantilever luminaire support. As was discussed, anelastic damping is generally considered and modeled as a viscous-like mechanism. The parameter test results will in fact be shown to support this assumption. Linear viscous damping mechanisms have velocity dependent behavior, and since deformation rates are proportional to modal frequencies, the test specimen geometry was chosen to develop vibration modes comparable to that of the baseline structure whose fundamental frequency was found to be approximately 1 Hz. Consequently the specimen's fundamental modal frequency was used as the primary 'design-to' specification. Figure 5-1 schematically diagrams the simple experimental model showing the required design parameters h_c , t_c , and w_c . The experimental models were positioned so that the longitudinal axes of the structures were aligned in a horizontal orientation to eliminate gravity affects on the dynamic responses. Figure 5-2 shows the fabricated steel and aluminum damping parameter experimental models with mounted sensors. Figure 5-3 shows the SDF model mounted in the cantilever support.

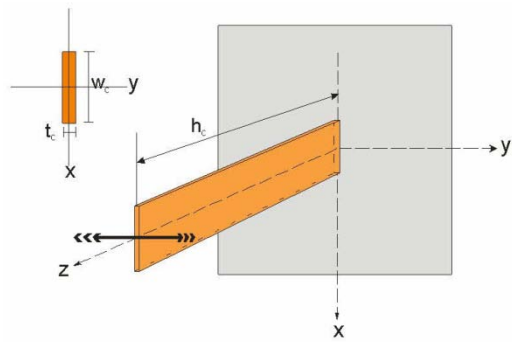


Figure 5-1 ADP Experimental Model Schematic and Design Parameters



Figure 5-2 ADP & SDP Test Specimens

Table 5-1 Parameter Test Specimen Design Specifications

	aluminum	steel
thickness	$\frac{1}{16} in$	$\frac{1}{16} in$
width	5 in	5 in
height	42 in	42 in
material	aluminum 6061	carbon alloy steel
total mass	1.28 lbm	3.73 lbm
f_1	$f_1 = 1.16 Hz$	$f_1 = 1.14 Hz$



Figure 5-3 Mounted Steel Damping Parameter (SDP) Experimental Specimen

5.1.1.2 Simulation Validation

5-DOF lumped-mass dynamic models of the damping parameter test specimens were developed in the MATLAB/SIMULINK environment. Simulated characterization test results validated equivalent HAPCO-like pole behavior. The results provided insight to the expected parameter ranges for sensor selection. The nodal acceleration time response for Node-5, the upper node, is plotted in Figure 5-4. The DFT spectrum of Figure 5-5 illustrates the existence of dynamic activity for the fundamental, 2nd, and 3rd vibration modes.

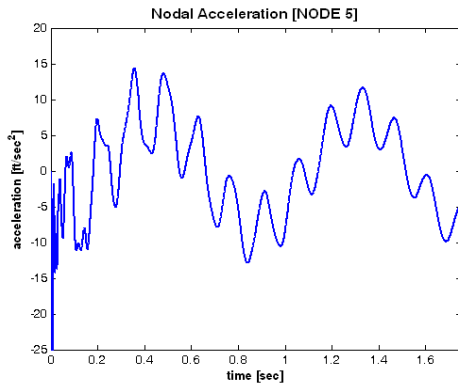


Figure 5-4 Node-5 Acceleration

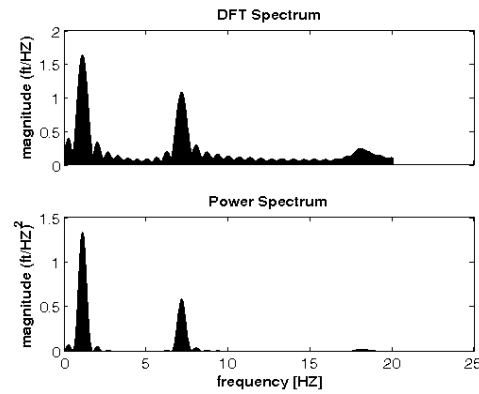


Figure 5-5 Node-5 Spectral Content

The simulation results confirm the expected modal activity at the nodes of interest and quantified the dynamic range requirements for the proposed accelerometers.

5.1.1.3 Sensor Requirements

Both crystal based accelerometers and general purpose strain gages were mounted on the test specimens to capture vibration dynamics. Responses of the first three vibration modes were desired as a minimum. Optimal sensor placement was determined primarily based on mode shape geometry determined from the linear modal

analysis. Sensors were mounted at strategic locations based on compromises between two geometric influences...

1. The mode shape peaks (nodes), or locations of maximum deflection.
2. Lumped mass locations of the simulated damping parameter test specimens.

Ideally, sensor placement would correlate precisely with modal peaks (nodes). However, the actual placement was determined by the lumped-mass locations modeled in the MATLAB/SIMULINK dynamic simulation. This maximized the simulation utility as an evaluation/trouble-shooting tool. Figure 5-6 diagrams the estimated mode shapes mapped to the experimental cantilever model. The mapping was used to aid in sensor placement. An optical position sensor was initially considered but not used.

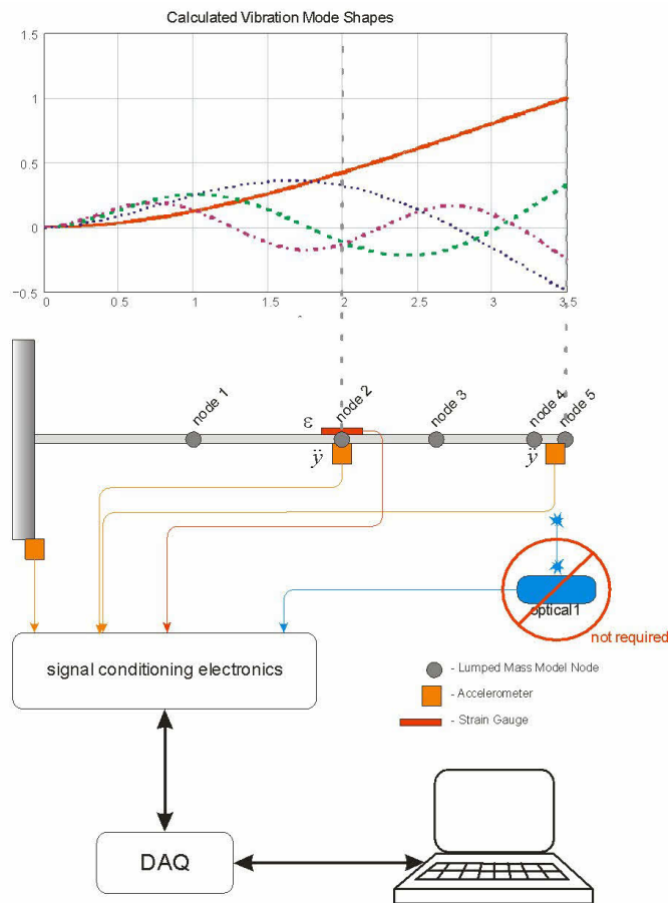


Figure 5-6 Damping Parameter Experimental Configuration Schematic

Also diagrammed in the figure are sensor placements. Table 5-2 specifies sensor location and the nearest calculated mode shape peak (node) for comparison. Distances are measured from the model's fixed base. Table 5-2 summarizes analytically predicted modal frequencies and specifies sampling rates for the ADP. These specifications were also utilized for the SDP model; comparable dynamics were predicted.

Table 5-2 Aluminum Damping Parameter (ADP) Data Sampling Specification

Vibration Mode	Predicted Modal Frequency [Hz]	Sensor Placement/ Mode Shape Peak (z) [in]	Min Sample rate [Hz]
Fundamental	1.14	42	20
2nd	7.13	24/20.4	50
3rd	18.1	24/32.4	200

The ADP specimen was prepared with two accelerometers. They were mounted one each at lumped mass model node locations 2 and 5 (reference Figure 5-6). Measurement Specialties Accelerometer ACH-01^[112] was selected for the ADP and SDP application. The ACH-01 has a wide frequency and acceleration dynamic range although it was operated at its lower range of specification. More importantly, was its mass of only 8 grams. One strain gage was mounted at lumped mass model node location 2. A Micro-Measurements general purpose gage was selected, CEA-XX-125UW-350^[113].

The SDP specimen was prepared with three accelerometers. They were mounted one at lumped mass model node locations 2 and two at lumped mass model node 5 (reference Figure 5-6). The two accelerometers at node 5 were mounted one each at opposite edges (at the same node height, (z)) to capture twisting dynamics that might occur during the test. None were discernable however. The Measurement Specialties Accelerometer ACH-01^[112] was utilized as it was for the ADP application. One strain

gage was mounted at lumped mass model node location 2. Again, a Micro-Measurement general purpose gage was selected, CEA-XX-125UW-350 [113].

5.1.1.4 Data Acquisition

National Instruments device NI USB DAQ-6009 [114] was selected to perform the necessary data acquisition. Specifications for the NI-6009 are summarized in Table 5-13. The DAQ was USB connected to an APPLE MacBook Pro. The data acquisition control and management was performed by a MATLAB/SIMULINK model.

5.1.2 Test Results

Three separate vibration tests were completed on both the ADP and SDP: an Impulse Test, a Pluck Test with a 6 inch initial offset, and a Pluck Test with a 2 inch initial offset. The two variations of Pluck Tests were intended to investigate the linearity of the anelastic damping behavior with respect to deformation magnitude. 30 seconds of free vibration was recorded from each sensor during each test to allow for sufficient evaluation of damping behavior. 30 seconds of data provided at least one exponential time constant of damping for the fundamental mode, and multiple time constants for the higher order modes.

Each sensor response was analyzed utilizing a MATLAB/SIMULINK coded algorithm designed to extract the exponential decay/damping coefficients. The raw data signal was first decomposed into modal components 1 through 4 using n^{th} -order ($n \geq 2$) Butterworth bandpass filters. The Butterworth filter ensured a maximally flat response in the bandpass, however an n^{th} -order filter introduced measurable transient noise. To demonstrate, Figure 5-7 illustrates the filter effect on an emulated 2nd mode component. The filter order is one of a number of filter variables that determine the

transient effect. The bandpass design variables also affect the filter transient. To compensate, damping analysis was delayed until after the transient subsided. Transient decay varied for each mode. High order filtering also introduced phase shift, however phase shift did not affect signal damping coefficients determination.

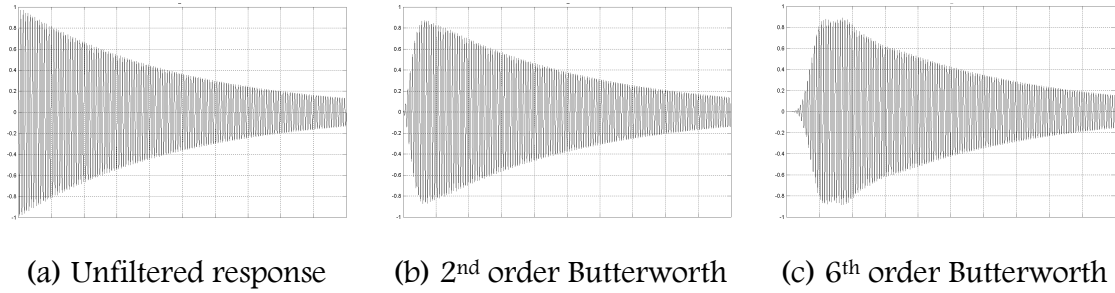


Figure 5-7 Butterworth Filter Transient Effect

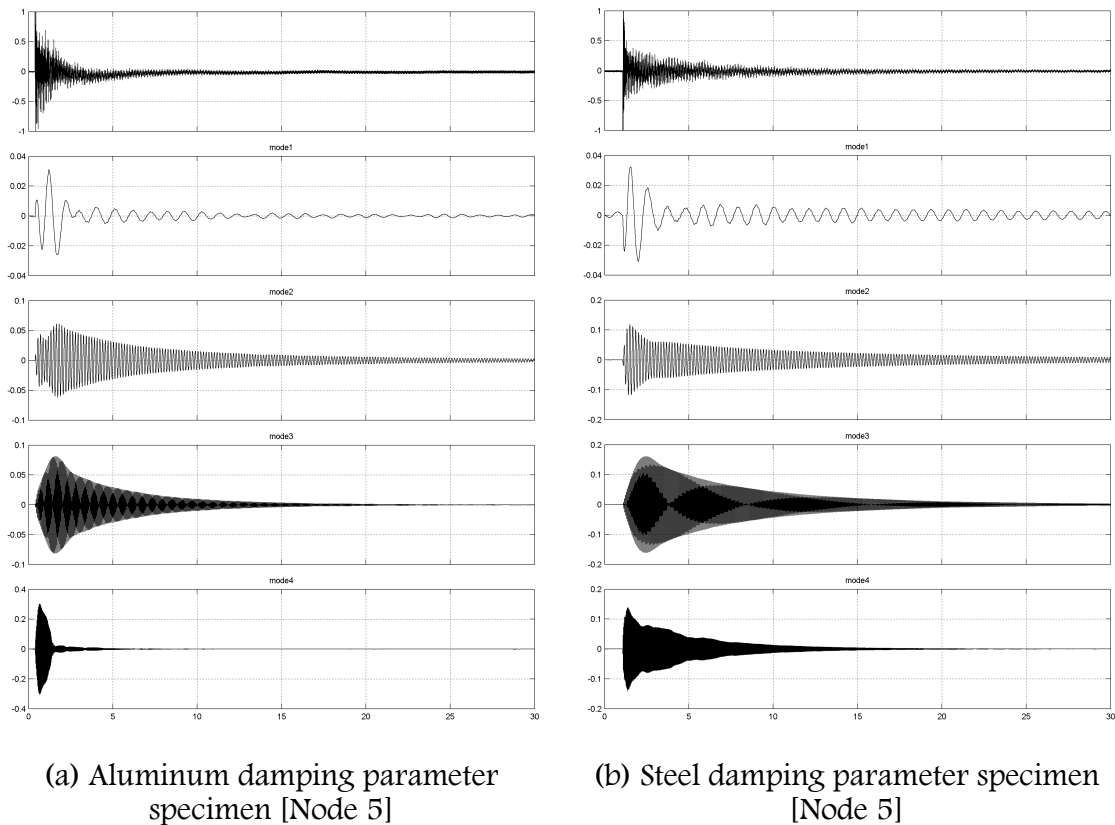


Figure 5-8 Accelerometer Modal Components [Emulated Impulse Test]

Figure 5-8a illustrates the filtered modal components of the sensed acceleration measured at the Node-5 location of the ADP. Figure 5-8b illustrates the same components at Node-5 for the SDP. Vibration modes 1 through 4 (traces 2 through 5 respectively) were filtered from the normalized sensor output shown in the figure as trace-1. The fact that the higher order vibration components dampen more quickly can be observed even before the coefficients were extracted.

5.1.2.1 Modified Logarithmic Decrement Algorithm

The next step of the analysis was designed to distill the damping coefficient σ_i , from each of the modal components. This was accomplished using a Modified Logarithmic Decrement Algorithm. The Logarithmic Decrement Algorithm is based upon comparing the response signal magnitude at two separated temporal points. The algorithm requires that samples be taken precisely one cycle time period apart, at the same phase mark within the sequential cycles; otherwise estimated damping would be corrupted. The algorithm was implemented using peak value detection because it was relatively straightforward to code in SIMULINK. The algorithm was modified to allow n -cycles between temporal samples rather than a single cycle in order to average out peak detection errors.

As previously noted, the modal response was assumed to take the form $y(t) = y_0 \cdot e^{-\sigma t} \sin(\omega_d t + \phi)$. Comparing magnitudes of two samples that were n -cycles separated yields the following ratio,

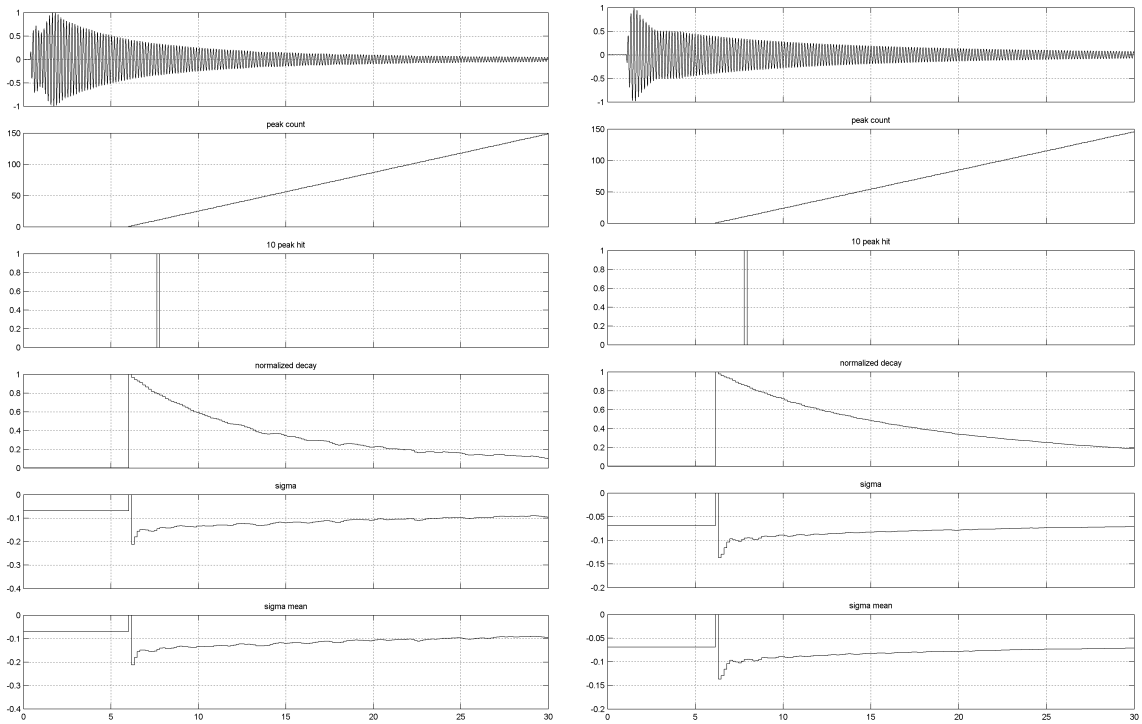
$$\eta(nT) = \frac{y(t+nT)}{y(t)} = \frac{y_0 \cdot e^{-\sigma(t+nT)} \sin(\omega_d(t+nT) + \phi)}{y_0 \cdot e^{-\sigma t} \sin(\omega_d t + \phi)} = e^{-\sigma(nT)}$$

This assumes that the sample was accomplished at peak value where $\omega_d (t+nT)+\phi = \frac{\pi}{2}$, $n=0 \rightarrow \infty$. The function $\eta(nT)$ is discrete, being defined at $t = nT$, $n=0 \rightarrow \infty$. It follows then that the damping coefficient σ is defined as,

$$\sigma = -\frac{\ln(\eta(nT))}{nT} \quad (5.3)$$

Applying this MATLAB/SIMULINK implemented algorithm to the third modal component shown in Figure 5-8 yields the output shown in Figure 5-9. The MATLAB/SIMULINK output contains the following:

- The mode 2 component is shown as trace-1.
- The second trace is a count of the peaks detected after the start of the damping algorithm. Trace 4 indicates that the analysis started at approximately the 6 second mark to allow the filter transient to decay.
- The third trace indicates the detection of the 11th peak. The frequency and time period of the vibration mode is determined during the first 10 cycles.
- The fourth trace is the normalized envelope of the decaying harmonic as determined by the magnitude of the detected peaks of each cycle. It has been normalized using the first peak magnitude.
- The fifth trace represents the instantaneous (discretized) damping coefficient estimate determined using the modified logarithmic decrement algorithm given in Equation (5.3).
- The sixth trace is a time averaged estimate of the damping coefficient using a sliding window.



(a) Aluminum damping parameter specimen

(b) Steel damping parameter specimen

Figure 5-9 Mode-2 Damping Coefficient Analysis [Emulated Impulse Test]

The following observations and conclusions were made after reviewing the analytical output:

- The decay behavior of the 2nd vibration mode component plotted in the first trace for both the ADP and SDP has the appearance of an exponential damped harmonic. The damping rate of the ADP (aluminum specimen) appears to be greater than that of the SDP (steel specimen).
- The instantaneous estimated damping coefficient shown in the fifth trace indicates that damping is not purely exponential however. If it were, the estimated coefficient would be a constant value with respect to time. Instead, the estimate demonstrates a slight time dependent variation, although it does appear to trend to some constant value in an asymptotic-like manner. This estimate variation is believed to be caused

by an additional mechanism contributing to the damping, that being drag. The additional contribution is more pronounced early in the response when the vibration magnitudes are greatest. The drag contribution during the response is illustrated in Figure 5-10. The estimated exponential damping envelop is overlaid on the actual modal response in both figures. The identical exponential damping model does not account for all of the decay initially. It is a much better representation later in the response where drag is less of a contributor.

- The damping coefficient estimated by the MATLAB/SIMULINK algorithm for the ADP specimen for the 2nd mode shown above was -.08. The damping coefficient estimated for the SDP specimen was .066. The qualitative observation suggesting a greater decay rate for the ADP specimen was found to be quantitatively correct.

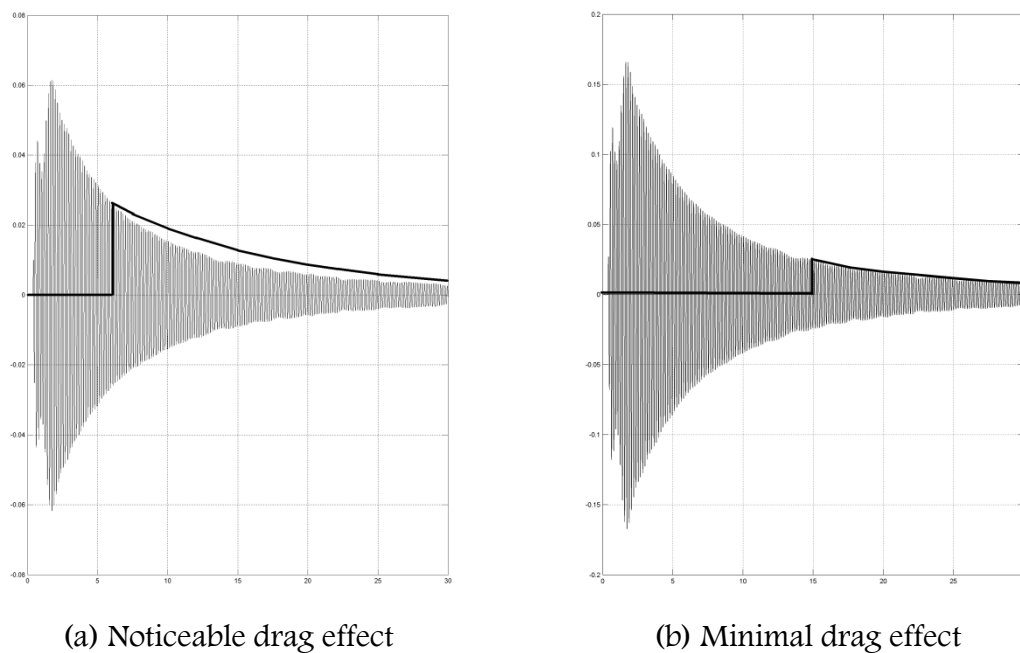


Figure 5-10 Exponential Decay Fit

ADP damping coefficient analysis was performed for each of the four modes, using each of the three sensor responses, for each of the three tests. This yielded nine damping coefficient estimates for each of the four ADP modal components. Similarly,

SDF damping coefficient analysis was performed for each of the four modes, using each of the four SDF sensor responses, for each of the three tests yielding twelve damping coefficient estimates for each of the four SDF modal components. The results from all tests were simply averaged to develop a composite estimate. The damping parameter estimates are summarized in Table 5-3 below for both the aluminum and steel specimens.

Table 5-3 Anelastic Damping Parameter Assessment Summary

Mode	Aluminum Damping Specimen		Steel Damping Specimen	
	Frequency (Hz)	Damping Coefficient ($-\sigma$)	Frequency (Hz)	Damping Coefficient ($-\sigma$)
fundamental	0.968	-0.048	0.960	-0.033
2nd mode	6.2	-0.082	6.1	-0.066
3rd mode	17.6	-0.173	17.3	-0.142
4th mode	34.5	-0.375	33.7	-0.246

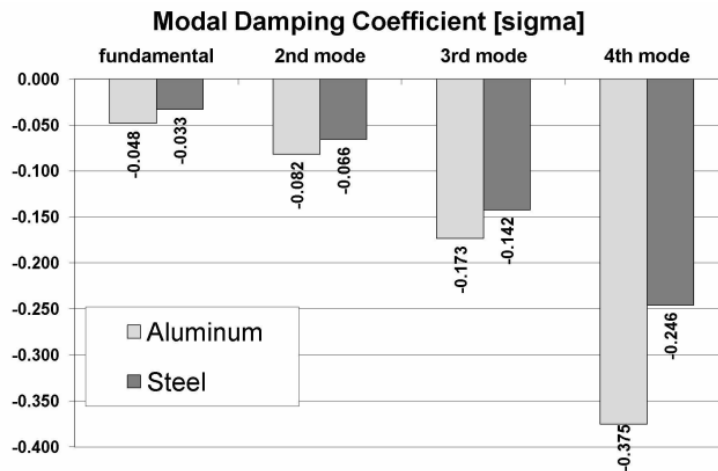


Figure 5-11 Measured Modal Damping Coefficient Summary [ADP/SDF]

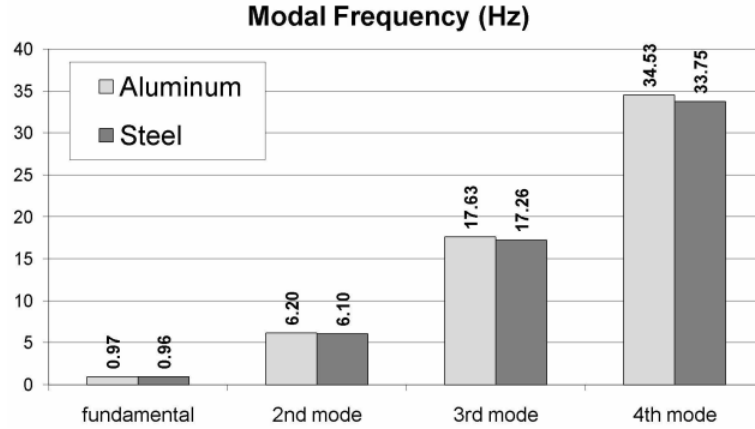


Figure 5-12 Measured Modal Frequency Summary [ADP/SDP]

5.1.3 Damping Coefficient Modeling

In general, the estimated damped envelopes matched the exponential decay behavior well. Consequently, the damping coefficient findings were used to investigate the viability of a Rayleigh and Kareem damping model fit. Both damping models are described in more detail in Section 5.1.1. A Least Square Fit was used to compute model coefficients.

5.1.3.1 Rayleigh (Proportional) Damping Model

The Rayleigh model takes the following form for the i th vibration mode:

$$c_i = \alpha_m m_i + \alpha_k k_i \Rightarrow \sigma_i = \frac{\alpha_m}{2} + \frac{\alpha_k \omega_i^2}{2} \quad (5.4)$$

Aluminum: $\alpha_m = .0684$, $\alpha_k = .000262$

Steel: $\alpha_m = .0581$, $\alpha_k = .000173$

5.1.3.2 Kareem Damping Model

The Kareem damping model takes the following form:

$$\zeta_i = \zeta_1 \left(1 + C \left(\frac{f_i}{f_1} - 1 \right) \right), \quad \zeta_i = \frac{\sigma_i}{\omega_i}$$

$$\sigma_i = \sigma_1 \frac{f_i}{f_1} \left(1 + C \left(\frac{f_i}{f_1} - 1 \right) \right) = \sigma_1 \left(C \left(\frac{f_i}{f_1} \right)^2 + (1 - C) \frac{f_i}{f_1} \right) \quad (5.5)$$

Aluminum: $C = -0.024$

Steel: $C = -0.024$

5.1.3.3 Modified Kareem Damping Model

The Kareem model was found to provide a poor fit so a modified version of the Kareem approach was developed that took the following form:

$$\sigma_i = \sigma_1 \left(C \left(\frac{f_i}{f_1} \right) + (1 - C) \right) \quad (5.6)$$

Aluminum: $C = 0.185$

Steel: $C = 0.120$

5.1.3.4 Damping Model Summary

Figure 5-13 and Figure 5-14 compare the actual measured damping coefficients with those predicted by the discussed models. Table 5-4 summarizes the RMS error associated with each of the models over the four measured modes.

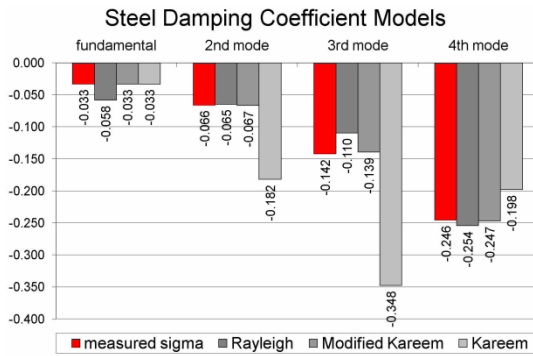


Figure 5-13 Steel Damping Coefficient Model Comparison

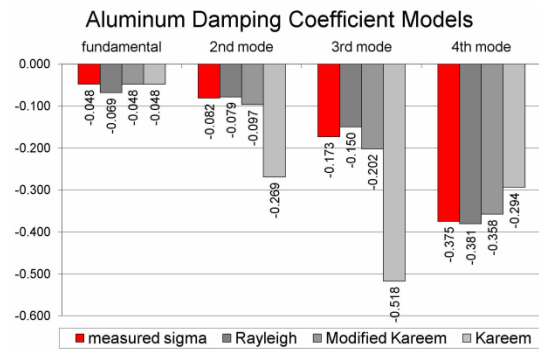


Figure 5-14 Aluminum Damping Coefficient Model Comparison

Table 5-4 Damping Model Prediction Accuracies [RMS]

	Steel Error [RMS]	Aluminum Error [RMS]
Rayleigh	0.021	0.016
Kareem	0.120	0.20
Modified Kareem	0.002	0.018

5.2 Modal Damping Concept Demonstration

The primary goal of the subject test was to ‘demonstrate’ the Modal Damping Vibration Control concept by way of a real-world experimental model. Demonstration generally implies a qualitative level validation. In this case, careful attention was given to the design and fabrication of the physical model in order to achieve repeatability and predictable behavior with the secondary goal to establish a basic level of quantization of concept effectiveness. Baseline dynamic requirements were established early in the simulation phase of this research. The HAPCO-like roadside cantilever was installed as the baseline structure of interest. The analytical model that followed, and was used to develop the Modal Damping concept, was designed to replicate the dynamic behavior of the baseline cantilever. Following suit, the experimental model was required to dynamically behave like the analytical model. Material properties and model geometries for the experimental model were determined accordingly.

The necessary control hardware for the three point tendon emulation was then designed and integrated with the experimental model. The Modal Damping control algorithm was designed, coded and compiled using Microsoft Visual Studio development environment. The Modal Damping executable file was ported and hosted on a generic laptop computer. The laptop computer interfaced with the experimental model/control tendon using a National Instruments bi-directional data acquisition system. The laptop computer served as the intelligent controller, and the data collection and storage vehicle.

Once the system integration was completed, the closed loop experimental system was subjected to controlled external excitation. The test scenario allowed the Modal Damping control law to transfer dynamic energy from the fundamental mode to the 2nd vibration mode. Key system states were measured and monitored as required. All collected data was stored for post test analysis.

Data reduction and evaluation was accomplished on over 100 separate tests. The data was evaluated and indicates on both a statistical and an individual test level that a net improvement in the dissipation of vibration energy resulting in a observable improvement in vibration settlement time.

5.2.1 Concept Demonstration Work Plan

The work breakdown structure given in Figure 5-15 was developed to guide the design and fabrication of the demonstration model. The plan included 4 major design tasks that bridged a variety of technologies:

1. Structural design and fabrication.
2. Electrical Interface design and fabrication.

3. Control software design and code.
4. Control algorithm design.

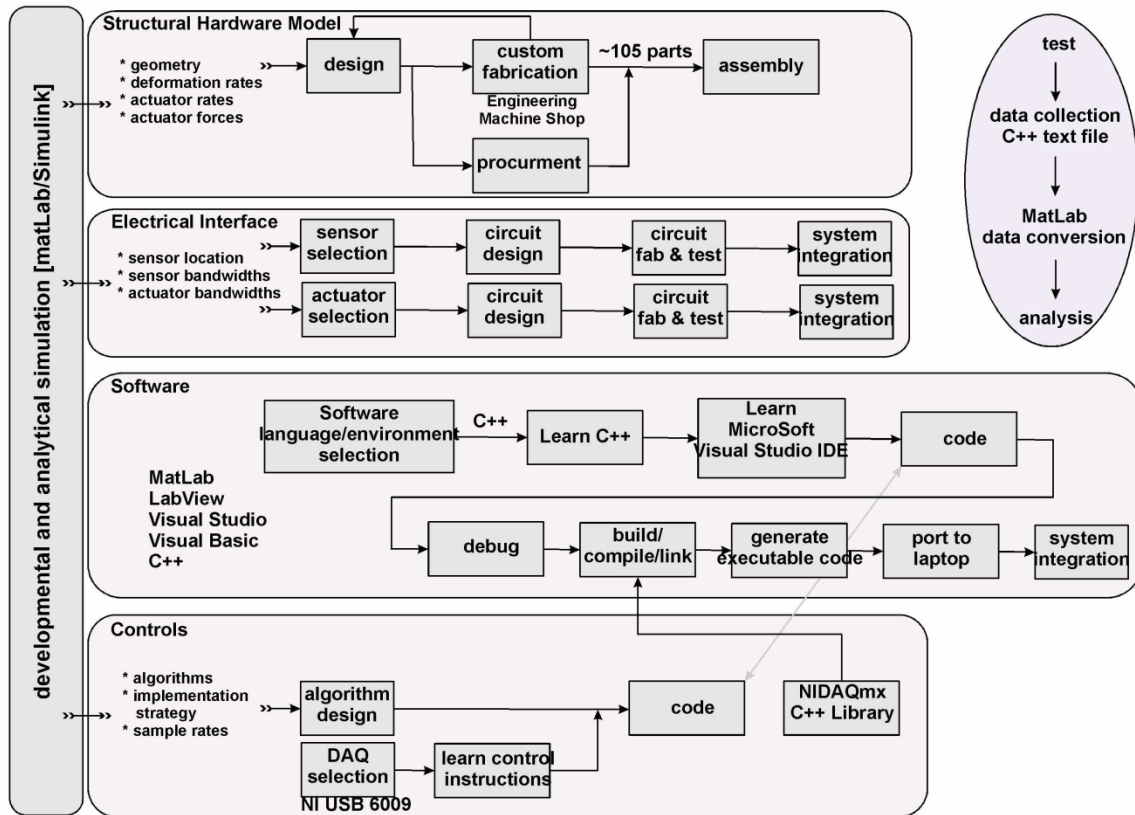


Figure 5-15 Concept Demonstration Developmental Work Plan

In addition, the plan identified the following test related elements:

1. Test plan development.
2. Test execution.
3. Post test data conversion.
4. Post test data analysis.

Each of these major work elements was directed/governed by findings of the modeling and simulation effort. Some of the simulation related design specifications are annotated on the WBS flowchart. Results from each of the major work elements are further discussed below.

5.2.2 Hardware Design and Fabrication

The dynamics of the experimental model were required to ‘reflect’ those of the analytical model, which in turn replicated those of the baseline aluminum cantilever pole... a tall, flexible and under-damped structure. The experimental model was required to demonstrate equivalent modal vibration frequencies and mode shapes shared by its analytical counterpart. In doing so, any Modal Damping benefits established and demonstrated by this research would automatically inherent a reasonable path to a potential real-world vibration control application.

During the modeling and simulation phase, the system was implemented as a simple cantilever structure with the 3-point tendon ‘awkwardly projecting’ from one side as was schematically diagrammed earlier and repeated below in Figure 5-16.

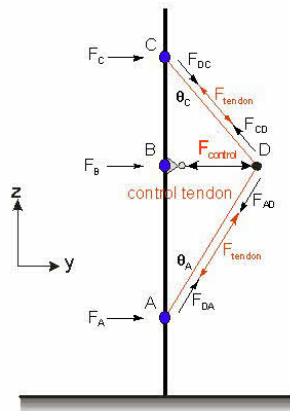


Figure 5-16 Generalized Cantilever/Tendon Configuration

As shown, the tendon configuration is admittedly, an unpractical implementation approach. However, the approach possesses some valuable attributes. The 3-point tendon represents one of the simplest forms of control mechanisms available to effect force distribution. Furthermore, the simple, albeit it awkward, arrangement made for a straightforward modeling and simulation activity; one whose function was more easily

communicated. The practicality of the 3-point tendon approach will become apparent as the system design is shown to evolve within the forthcoming discussion.

5.2.2.1 Dual Cantilever Approach

Realizing that the rudimentary configuration of the analytical representation shown above would be an impossible sell for any real-world application meant that practicality and aesthetics, as well as the technical aspects needed to be improved during the Concept-Demo detailed design activity. The technical requirements established during the analysis and simulation phases were:

- The concept demonstration model had to represent the tall flexible structure of interest: a simple cantilever type, with a fixed base support that resists angular rotation. Standing wave deformations of the model had to be equivalent to those of the baseline analytical model. The mode shapes for the baseline structure were diagrammed in Figure 3-6.
- The mass and stiffness distribution of the concept demonstration model had to be designed to achieve equivalent modal dynamic properties to the baseline analytical model. Specifically, the modal vibration frequencies had to be equivalent to those of the baseline analytical model determined during the simulation and summarized in Table 4-1.
- Damping distribution had to be typical of structural mechanisms associated with flexible cantilever structure, primarily the anelastic and drag mechanisms.
- Vibrations were desired in only one lateral axis direction. The concept demonstration experimental model had to be flexible along one lateral axis and stiff along its orthogonal axis. A simple flat plate design with cross-sectional geometry

having one axis dominate in terms of moment of inertia was the preferred design approach for the experimental model.

- The concept demonstration experimental model had to be fabricated using a structural aluminum alloy in order to retain the inherent anelastic damping properties associated with small strain energy dissipation.
- In general, the behavior of the concept demonstration experimental model had to emulate the dynamics of the analytical model which in turn, simulated the dynamics of the HAPCO-like roadside cantilever luminaire pole.
- The concept demonstration structure was scaled as required according to the constraints noted above. It had to be large enough to accommodate the 3-point modal damping actuation system, but affordable and realizable in a timely manner.

An alternative implementation of the 3-point tendon was required in order to make it practical (palatable). After investigating different approaches, a rather innovative idea was arrived at; the 3-point tendon could be ‘folded’ to fit inside a given structure by using additional connection points. And, although folded, analysis would show that the tendon would still retain the fundamental force distribution attributes of the simpler 3-point connection if the additional connections were roller/pulley-type. The folding of the tendon at each story level was found to generate extremely small residual lateral forces when the upper and lower story separations were not equal. Residual forces resulted because the tendon geometry (angles of incidence) was not perfectly anti-symmetric at ends of that given story. These residual forces were computed and determined negligible. Tests results showed that residual forces did not affect the effectiveness of the control tendon.

Folding was realized by way of a second cantilever as shown in Figure 5-17. The two cantilevers when connected with ‘story-like’ horizontal members took on a high-

rise look. Story connections to the vertical cantilevers were non-moment, hinge-type connections. The structure maintained its simple cantilever behavior as opposed to moment-resisting frame action.

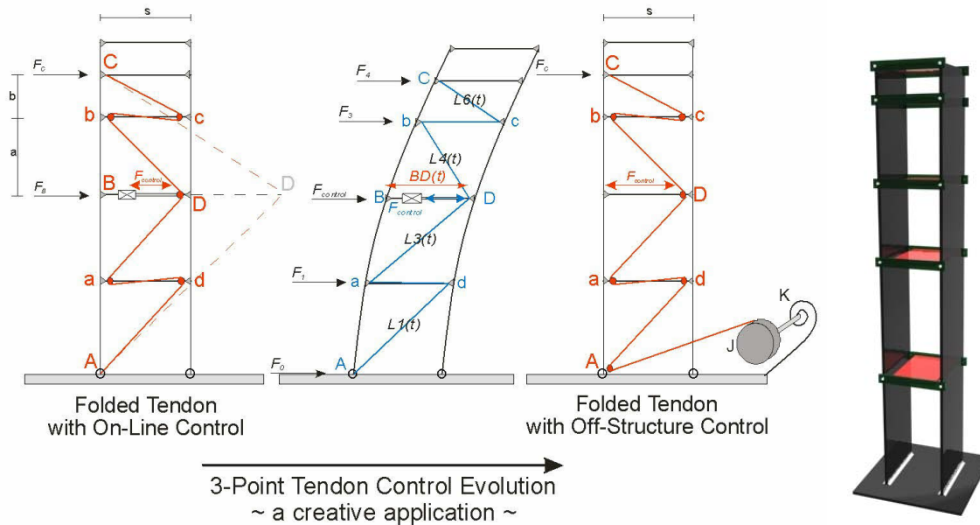


Figure 5-17 The Concept-Demo Model Design Evolution

As the detailed design phase progressed, it became evident that the modal damping actuator had to be moved off-structure. This design decision minimized dynamics associated with mass and motion of the actuation system from imposing themselves on the dynamics of the experimental model. This decision proved to be effective; however it meant that the control tendon required a control mechanization strategy different than its analytical counterpart. The simulation strategy assumed that the control tendon length ADC remained constant within the structure. The length of the control element BD was assumed controllable, and compensated for geometry variations during the cantilever sway cycle and thus eliminating tendon slack. Moving the control element off structure eliminated the requirement for a controllable element BD; the control tendon length ADC was allowed to vary during sway. To compensate, the off-structure actuation mechanism was designed to include a ‘wind-up’ function to eliminate slack yet maintain a minimum tension on the tendon throughout the sway

cycle. The strategy is schematically diagrammed in the evolution drawing of Figure 5-17, along with a rendering of the anticipated two-cantilever model approach. The resulting ‘folded’ tendon connection requirements are summarized in the Table 5-5.

Table 5-5 Cantilever/Tendon Connection Specifications

Node	Concept-Demo Realization
A	pulley
B	n/a
C	pin-connected
D	pulley
a	pulley
b	pulley
c	pulley
d	pulley

After taking into account the concept demonstration requirements itemized above, the major geometry specifications were determined to be:

Table 5-6 Concept Demonstration General Design Requirements

Specification	Design Requirement
overall height	$h_c = 72 \text{ in}$
cantilever width/depth	$w_c = 5 \text{ in}$
cantilever thickness	$t_c = \frac{1}{4} \text{ in}$
material	6061 structural aluminum
dual cantilever separation	$\Delta_y = 6 \text{ in}$

The analytically predicted vibration frequencies for the specified geometry and fabrication material were computed and are given in Table 5-7 and Figure 5-18. For comparison, the measured behavior is also provided.

Table 5-7 Concept Demonstration Modal Frequencies

Specification [mode]	Predicted	Measured
fundamental mode [single cantilever]	$f_1 = 1.49 \text{ Hz}$ [Mathcad]	$f_1 = 1.42 \text{ Hz}$
second mode [single cantilever]	$f_2 = 9.38 \text{ Hz}$ [Mathcad]	$f_2 = 9.25 \text{ Hz}$
fundamental mode [dual cantilever w/stories]	$f_1 = 1.10 \text{ Hz}$ [MATLAB]	$f_1 = 1.03 \text{ Hz}$
second mode [dual cantilever w/stories]	$f_2 = 7.35 \text{ Hz}$ [MATLAB]	$f_2 = 7.40 \text{ Hz}$

The difference in modal frequencies between the single and dual cantilever configurations given in Table 5-7 was due to the added masses of the story elements. Differences were accurately accounted for in the Concept Demonstration dynamic model. Modal frequencies of the dual cantilever design adequately represented those of the roadside cantilever frequencies given in Table 4-1. The control tendon had negligible effect on the modal frequencies. Figure 5-18 displays the mode shape differences between the aluminum roadside cantilever analytical model and the concept demonstration analytical model. Normalized fundamental mode shapes are nearly identical. The mass distribution deviations resulting from the additional stories of the concept demonstration model caused minor deviation of the 2nd mode shape.

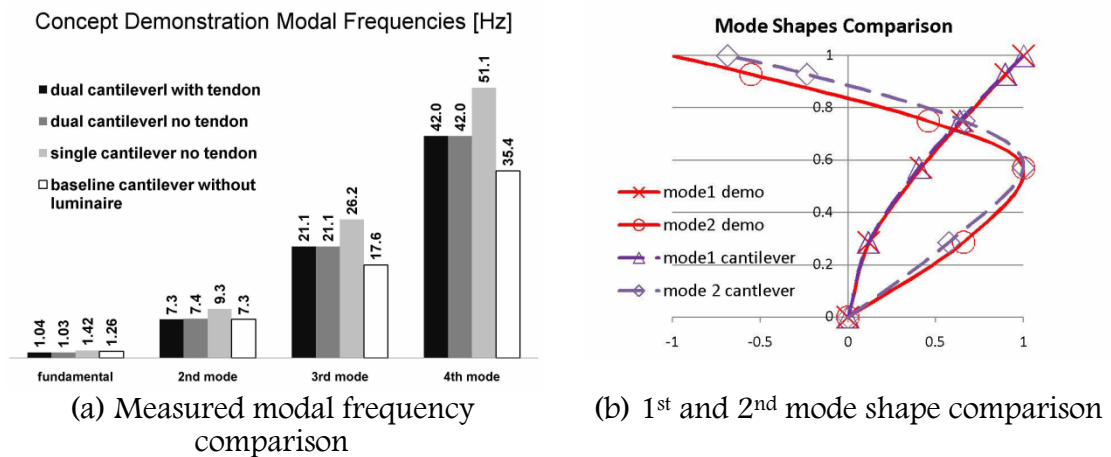


Figure 5-18 Dynamic Comparison of Concept Demo versus Baseline Cantilever

5.2.2.2 Control Tendon

The control tendon selection criteria were based upon dynamic simulation findings that are summarized in the following table:

Table 5-8 Concept Demonstration Control Tendon Selection Criteria

specification	design requirement
maximum tendon length variation during maximum sway	$\Delta L_{tendon} = \pm 1 \text{ in}$
maximum tendon length variation rate during maximum sway	$\Delta \dot{L}_{tendon} = \pm 30 \frac{\text{in}}{\text{sec}}$
maximum tendon tension	$f_{tendon_{max}} = 80 \text{ psi}$
allowable strain	$0.1 \Delta L_{tendon}$

The tendon length variation represents the change in the total intra-structure folded length of tendon that occurs during its sway cycle. It is computed as (reference Figure 5-17),

$$\Delta L(t) = L1_0 + L2_0 + L3_0 + L4_0 - (L1(t) + L2(t) + L3(t) + L4(t))$$

Length variation is directly related to modal content of the sway. The dynamic simulation (MATLAB/SIMULINK) was used to quantify the expected tendon behavior and its stress. The simulation results are given in Figure 5-19, Figure 5-20 and Figure 5-21 below. The following response is the tendon length variation generated during a simulated pluck test/energy transfer event (variation shown in inches).

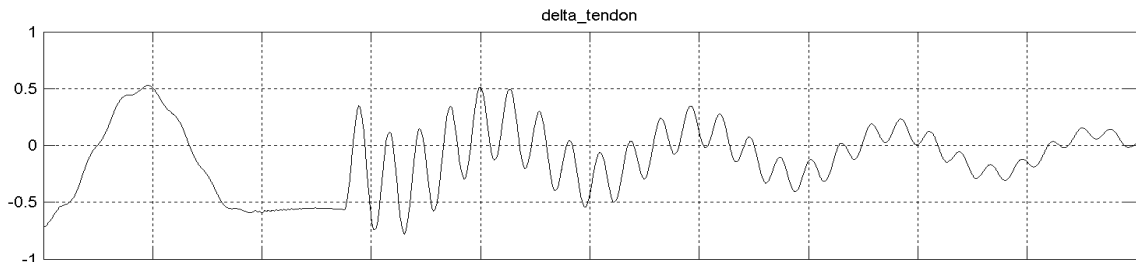


Figure 5-19 Tendon Length Variation [time 0→5 sec]

The following response is the tendon length variation rate generated during a simulated pluck test/energy transfer event (variation rate shown in inches per second).

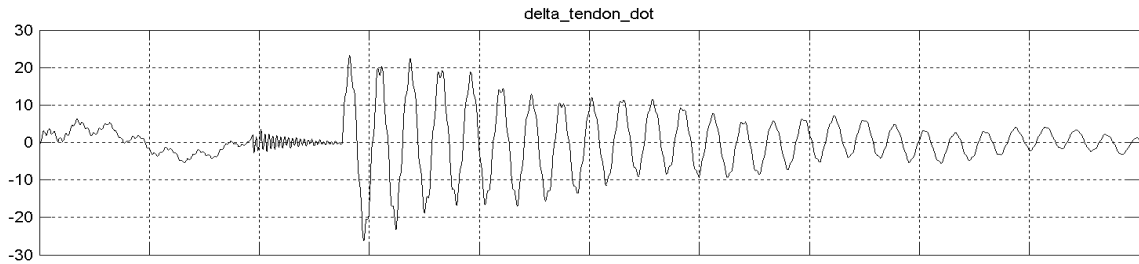


Figure 5-20 Tendon Length Variation Rate [time 0→5 sec]

The following response is the tendon tension likewise generated during a simulated pluck test/energy transfer event (force shown in lbf).

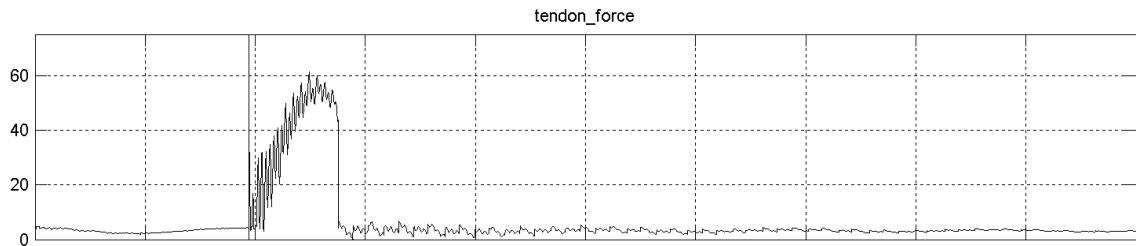
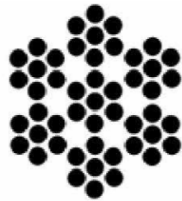


Figure 5-21 Tendon Tension Force [time 0→5 sec]

These tendon related simulation results were utilized to select a multi-strand stainless steel cable for the experimental model with the following specifications ^[115]:

Table 5-9 Concept Demonstration Control Tendon Design Specifications



Wire Rope Material	Stainless Steel
Stainless Steel Type	Type 304 Stainless Steel
Finish/Coating	Plain
Construction	7x7 Strand Core
Formation	Preformed and Lubricated
Diameter	3/64"
Available Lengths	25, 50, 100, 300, and 500 feet
Breaking Strength	270 lbs.
Specifications Met	Federal Specifications (FED), Military Specifications (MIL)
FED Specification	RR-W-410
MIL Specification	MIL-DTL-83420

5.2.2.3 Control Actuator

The control actuator evolved from an on-structure device to that of an off-structure device due to the state dynamics associated with the control tendon as revealed in Figure 5-19 and Figure 5-20 above. The anticipated inertial forces associated with a linear actuator response were estimated to be influential in the overall system behavior and was undesired.

The off-structure approach offered options of different actuation schemes. Instead of a linear ‘tracking’ device similar to what was emulated during simulation, a ‘wind-up’ device with a rotational ‘braking’ function similar to that of an automotive disc brake was investigated and selected. The new approach maintained the 3-point force distribution feature, but offered a more eloquent realization. An off-structure topology evolved the actuation device from a linear to a rotational implementation.

Significant time was spent attempting to minimize the complexity and dynamic effects of the braking device. An off the shelf electro-magnet/disc brake was ultimately decided upon. The specific braking device was selected utilizing the performance criteria established by the dynamic simulation. Performance requirements were related to tendon tension forces and rotation rates predicted using a simulated Pluck test scenario. Typical simulation results are shown in Figure 5-20 and Figure 5-21 above. The selected rotational brake is shown mounted to its bulkhead in Figure 5-22a and b below. This brake had a static braking capacity of $\tau_{brake} = 80 \text{ lbf} \cdot \text{in}$ which proved to be sufficient given the wind-up pulley geometry.

The rotational mechanics and dynamics of the actuation subsystem were investigated and quantified to ensure that they dovetailed with those of the primary vibrating structure. Mass, stiffness and damping of the rotating system were controlled to the extent possible in order to dictate and minimize subsystem dynamic effects. The

actuation subsystem was composed of the following key components and their respective mechanical properties:

Table 5-10 Concept Demonstration Actuation Subsystem Dynamic Properties

component	rotational inertia $J, \left(\frac{\text{in} \cdot \text{lb} \cdot \text{f}}{\text{rad} / \text{sec}^2} \right)$	stiffness $\tau, \left(\frac{\text{in} \cdot \text{lb} \cdot \text{f}}{\text{rad}} \right)$	damping
wind-up pulley [aluminum]	2.0×10^{-5}	—	—
wind-up spring [torsional]	—	2.143	—
axel [steel]	8.6×10^{-6}	—	—
axel bearings	—	—	note 1
rotating brake disc [steel]	81×10^{-5}	—	—
axel collar & misc.	8.6×10^{-6}	—	—

(note 1: Damping associated with the axel bearing assembly was expected to be frictional. Therefore, bearings were selected to minimize their size. No attempt to quantify the bearing frictional behavior was made.)

The actuation subsystem took on a 2nd order dynamic behavior. The natural frequency was easily computed based on the dynamic properties of Table 5-10 as,

$$\omega_{\text{subsystem}} = \sqrt{\frac{\tau}{J}} = 50.5 \frac{\text{rad}}{\text{sec}}$$

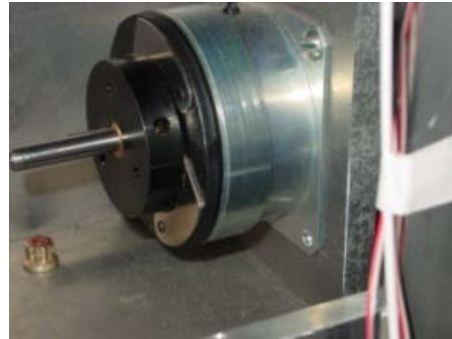
The subsystem components were carefully designed and selected with $\omega_{\text{subsystem}}$ in mind. A minimum subsystem responsiveness was necessary so that the dynamics associated with the fundamental and 2nd vibration modes of the primary system would dominate those of the subsystem wind-up mechanism. In other words, the windup subsystem was slaved to the experimental model's dynamics. Rotational inertia was a function of design geometry and material which could be controlled to some extent. The optimal rotational stiffness was empirically investigated. The subsystem was

required to ‘wind-up’ the tendon and eliminate slack but not produce excess tendon tension.

The actuation subsystem was schematically shown in the concept diagram of Figure 5-17. Fabricated and assembled components of the actuation system are pictured in Figure 5-22.



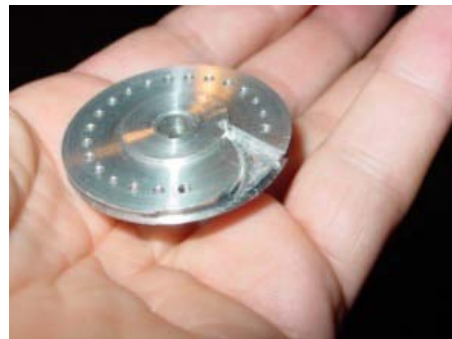
(a) Braking actuation system



(b) Electro-magnetic disc brake



(c) Mounted wind-up mechanism



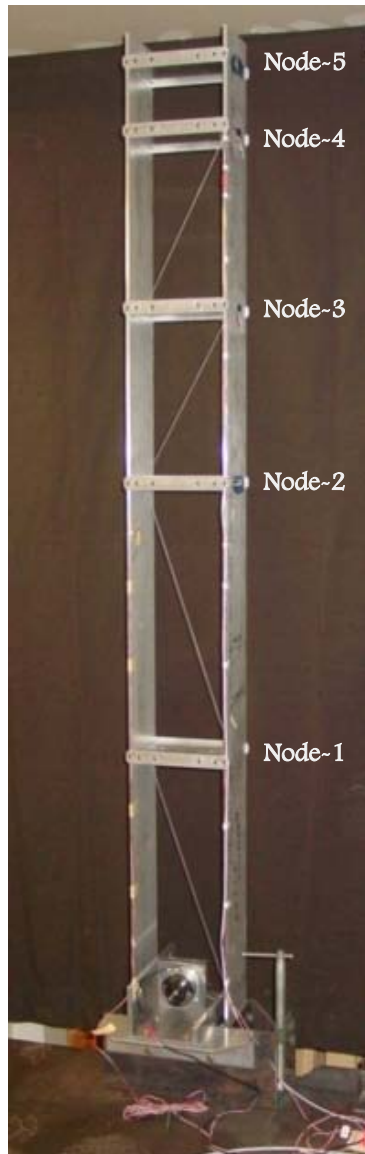
(d) Wind-up pulley

Figure 5-22 Control Tendon Actuation System

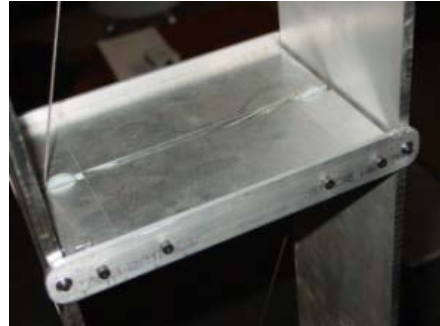
5.2.3 Fabrication and Assembly

The final assembly contained over 100 separate elements, many of which were custom designed and fabricated. Fabrication drawings were generated using AutoCad. Fabrication was accomplished with the help of Mr. Dale Ertley, Senior Engineering Technician of the Graduate Engineering Machine Shop, University of Akron.

The final assembled structure is pictured in Figure 5-23. The full length photo shows the dual cantilever structure with the off-structure actuation mechanism attached at the base.



(a) Final concept demonstration assembly



(b) Story 'Node' with hinge connection



(c) Multi-story design



(d) Story hinge (bearing) connection

Figure 5-23 Concept Demo Experimental Model

5.2.4 Electrical Interface Design and Fabrication

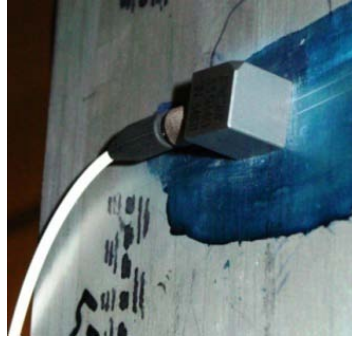
Three accelerometers were mounted on the structure to monitor nodal accelerations at stories 2, 3, and 4. The sensor set consisted of two separate accelerometer types shown in Figure 5-24 whose properties are summarized in Table 5-11.

Table 5-11 Concept Demonstration Accelerometer Performance Specifications

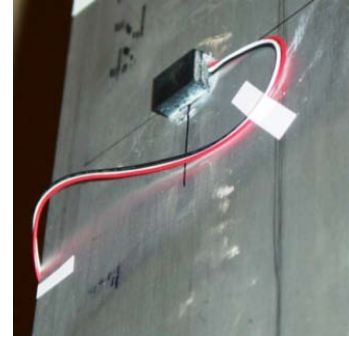
	PCB Piezotronics [333B50]	Measurement Specialties [ACH-01]
type	ceramic shear element	piezo-electric polymer film
frequency range	0.5Hz – 3kHz	2Hz – 20kHz
sensitivity (typical)	1000mV/g	9 mV/g
non-linearity (typical)	<1%	0.1%
dynamic range	± 5 g	± 150 g
weight	7.5 gm	8 gm
supply type	constant current	constant voltage
attachment	mechanical fastener	adhesive
cost	~ \$350.00	~ \$20.00

The ACH-01 low cost accelerometer was more than adequate, with sufficient sensitivity and frequency range for modes 1 through 4. The sensor output included noticeable drift probably due to its high impedance, charge-amplified design. The drift was easily filtered from the output response. The ACH-01 was mounted at nodes 3 and 4 in the structure.

The PCB accelerometer was selected because of its high sensitivity and low output impedance making it less susceptible to noise coupling. It was selected for use at Node 2 for accurate sensing of modes 1 and 2.



(a) PCB accelerometer



(b) ACH-01 accelerometer

Figure 5-24 Concept Demo Accelerometers

Two electromagnets were required. The first was a very simple electromagnet whose purpose was to ‘hold’ position of the structure in its required initial conditions. The electromagnet then served to initiate the test by releasing the structure by way of a controller commanded signal. The pre-positioning electromagnet is pictured in Figure 5-25.

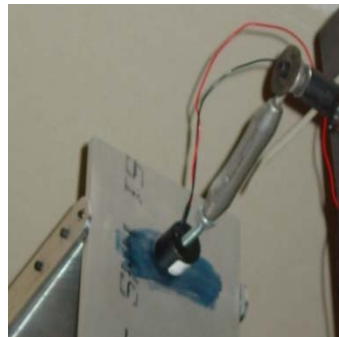


Figure 5-25 Pluck Test Positioning Actuator

The second device was more sophisticated in design and required more attention during its specification evaluation. It served as the control actuator braking device. Its dynamics and static behavior directly effected system performance and are described in more detail in Section 5.2.2.3 above. The actuator itself was pictured in Figure 5-22b. Basic design-to specifications for the two electromagnets are given in Table 5-12.

Table 5-12 Concept Demonstration Actuator Specifications

	Braking Actuator	Pluck Test Actuator
type	flange mount 2-5/8 in diameter	1 in diameter circular
rated power (watts)	9.5	3.2
holding force	80 lbf-in	15 lbf
engagement/disengagement time (msec)	15/35	—

5.2.5 Circuit Design

Four distinct circuits were required: one signal conditioning circuit each for the two sensors (schematically shown in Figure 5-26) and one actuation driving circuit for each of the two actuator devices (schematically shown in Figure 5-27). Circuit designs were essentially generalized application circuits albeit each was carefully tailored as required.

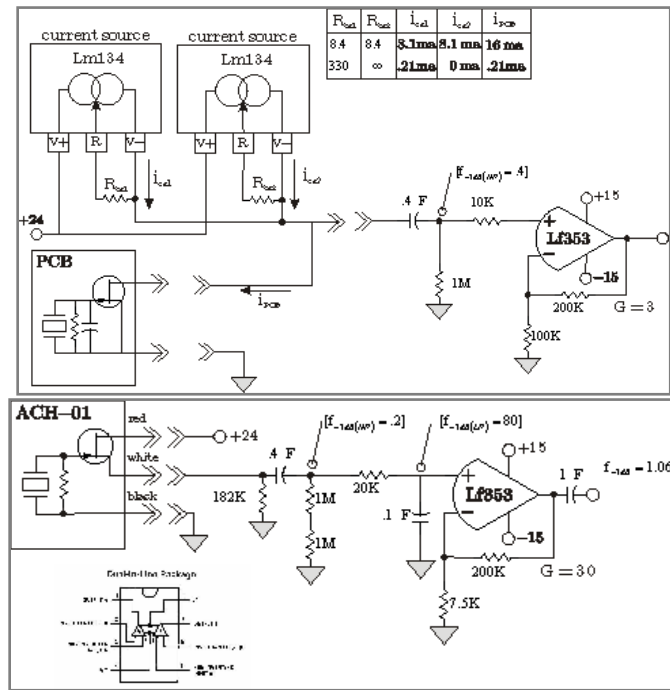


Figure 5-26 Sensor Conditioning Circuits [PCB and ACH-01]

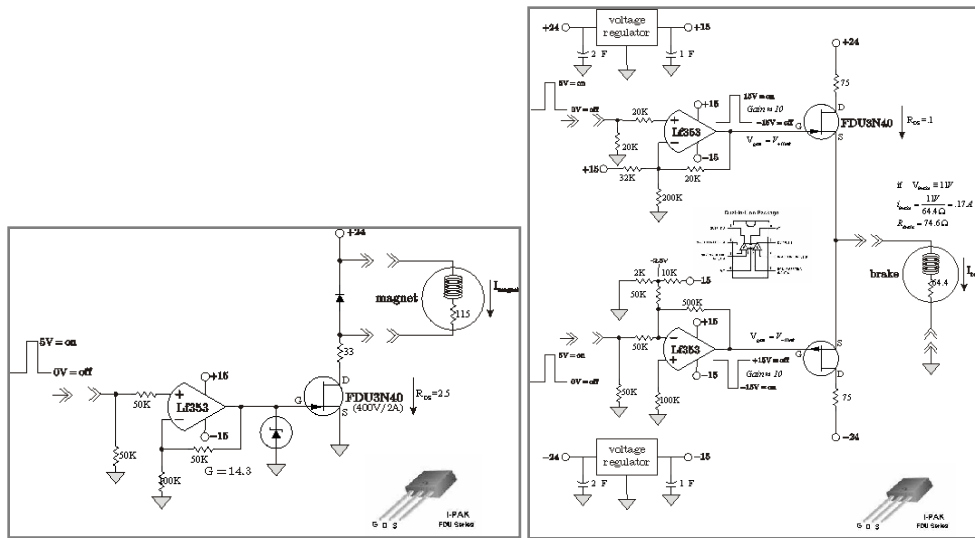


Figure 5-27 Actuator Driving Circuits [Pluck and Braking]

5.2.6 Control Algorithm Design

The control algorithm strategy evolved directly from the simulation developmental phase. The successful development of this system component, more than any, was highly dependent on the simulation activity. The goal of Modal Damping is to transfer energy from the fundamental mode to some higher order vibration mode for improved inherent dissipation; the concept demonstration's specific goal was to transfer energy to the 2nd vibration mode. The control algorithm represents the intelligence that oversees the transfer operation. Implementation of the Modal Damping concept is keyed to monitoring system energy status. System energy assessment was accomplished by monitoring nodal accelerations and performing the required numerical integration on the high priority node to compute nodal velocity. These sensed/computed states were then used to determine maximum system potential energy occurrences during the system sway cycle. These occurrences trigger the controlled energy transfer event by way of the actuation system. The basic energy transfer sequence was nearly identical to

what was used in the simulation; it was however, tailored for the selected actuation system. The sequence is diagrammed in Figure 5-28.

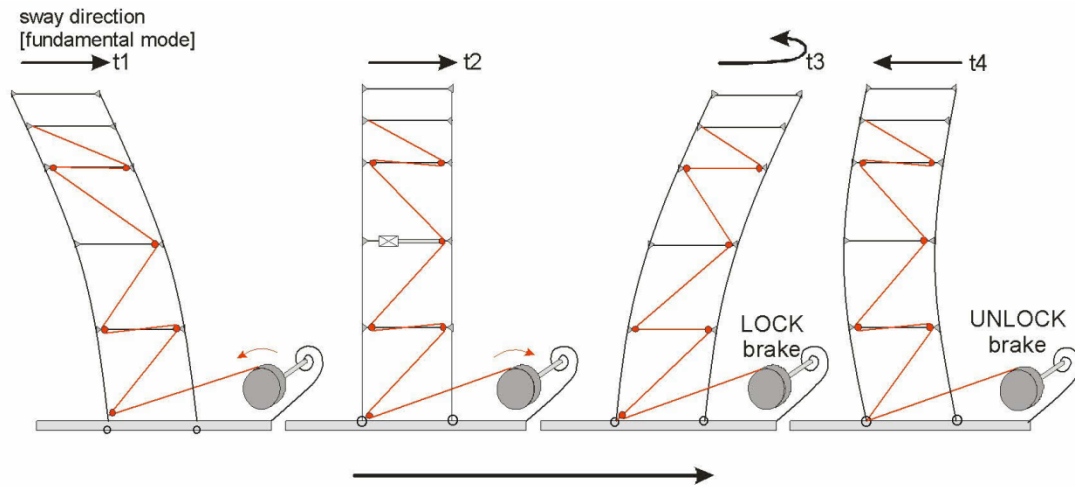


Figure 5-28 Modal Damping Control Sequence

- At time t_1 , the structure begins to sway to the right.
- At time t_2 , the structure has achieved maximum fundamental mode velocity. System kinetic energy (as associated with the fundamental) is maximum.
- At time t_3 , zero fundamental mode velocity is detected (at a designate spatial position). System potential energy is maximum. Modal Damping is initiated; the tendon control configuration is set to 'LOCK'. As the cantilever sway reverses, the 'LOCKED' tendon geometry redistributes forces generated by the developing kinetic energy, deforming the cantilever to an unnatural shape that approaches that of the second vibration mode.
- When the reverse cycle (sway to the left) is at the completion of the kinetic energy phase, the tendon control 'UNLOCKS' its configuration. The removal of the tendon related distributed forces causes the structure to free vibrate. The modal content of the free vibration is a function of the structural shape dictated by the distributed

tendon forces. The placement of the 3-point tendon was judiciously chosen to force 2nd mode vibration (reference discussion in Section 3.1.4).

The detailed function flow chart representing this control algorithm is given below in Section 5.2.7.

5.2.6.1 Data Acquisition

The Concept Demonstration control algorithm was a closed loop design and required a data input and output capability. The National Instrumentation NI USB 6009 DAQ was selected to perform this function. The relevant NI USB 6009 specifications are listed below in Table 5-13.

Table 5-13 Concept Demonstration Data Acquisition Specifications

Specification ^[116]	NI USB-6009
form factor	USB
measurement type	voltage
analog input channels	8 single-ended/4 differential
analog sample rate	48 KS/sec
analog timing	internal clock
digital channels	12 input/output
digital timing	software controlled

National Instruments makes available the necessary drivers and instruction sets to interface with the NI USB 6009^[117]. These utilities required time for familiarization and understanding, but dramatically reduced the software coding effort.

5.2.7 Software Design and Coding

The following software development and implementation options were investigated and considered:

1. MATLAB.

2. Labview.
3. Visual Basic.
4. Microsoft Visual Studio.

The selection criteria included:

1. Real Time Capability.
2. Development Environment.
3. Data Acquisition Interfacing.
4. Software Language.

Microsoft Visual Studio was determined to be the most time-effective and professional approach. The Visual Studio development environment offered multiple language options as well as powerful tools to develop the source code, compile, link, debug, and finally generate executable code with or without a debug capability. C++ was selected as the source code language. It is a widely utilized object-oriented language that imposes structured design and code. Many C++ routines can be readily found and accessed over the internet. Equally important, the internet offers many sites with support and problem solving ideas.

The NI USB 6009 DAQ was the enabling component to achieving real time operation. It contained a programmable internal clock that was configured to periodically sample the necessary system states at prescribed sample rates. In addition, it was configured to monitor operating system execution timing to ensure that software tasks were completed within prescribed limits; else system errors would be set. Control of, and communication with the NI USB 6009 DAQ was made possible using existing National Instrumentation NI-DAQmx driver software ^[117]. NI-DAQmx was specifically designed for text based programming language, and included C++. The driver software set is composed of a macro-instruction set of DAQ commands that can be inserted into

the C++ source code. National Instruments makes available the linkable library necessary for source code compiling of DAQ instructions.

All of the system intelligence resided in software. No intelligence was designed into the hardware interface. The overall high-level functional flow diagram is given in Figure 5-29.

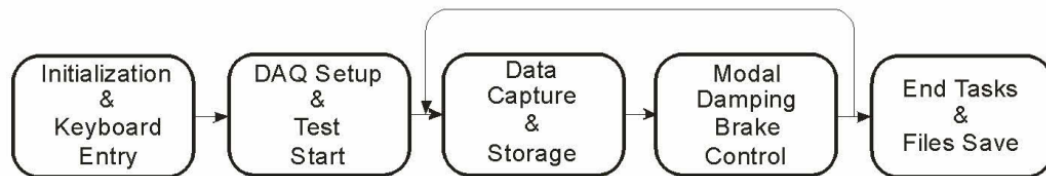


Figure 5-29 Software Functional Flow Diagram

Initialization involved variable declaration and definition. In addition to the many variables used within the program and subprograms, the brake command syntaxes were declared and defined. The file structure for the measured data was created. Time-stamped file names were created based on the on-board real-time clock. Unique test parameters were requested and entered by keyboard. The specific parameters are given and described in Section 5.2.11.

DAQmx setup involved the following steps:

1. Create a Task and Virtual Channels.
2. Configure the Timing Parameters.
3. Start the Task.
4. Perform a Read operation from the DAQ.
5. Perform a Write operation to the DAQ.
6. Stop and Clear the Task.

The sampled data were imported from the DAQ. The data vector was decomposed. The data were stored in the appropriate files.

The Modal Damping function implements the control law and takes the form of the multi-branch decision tree shown in Figure 5-30.

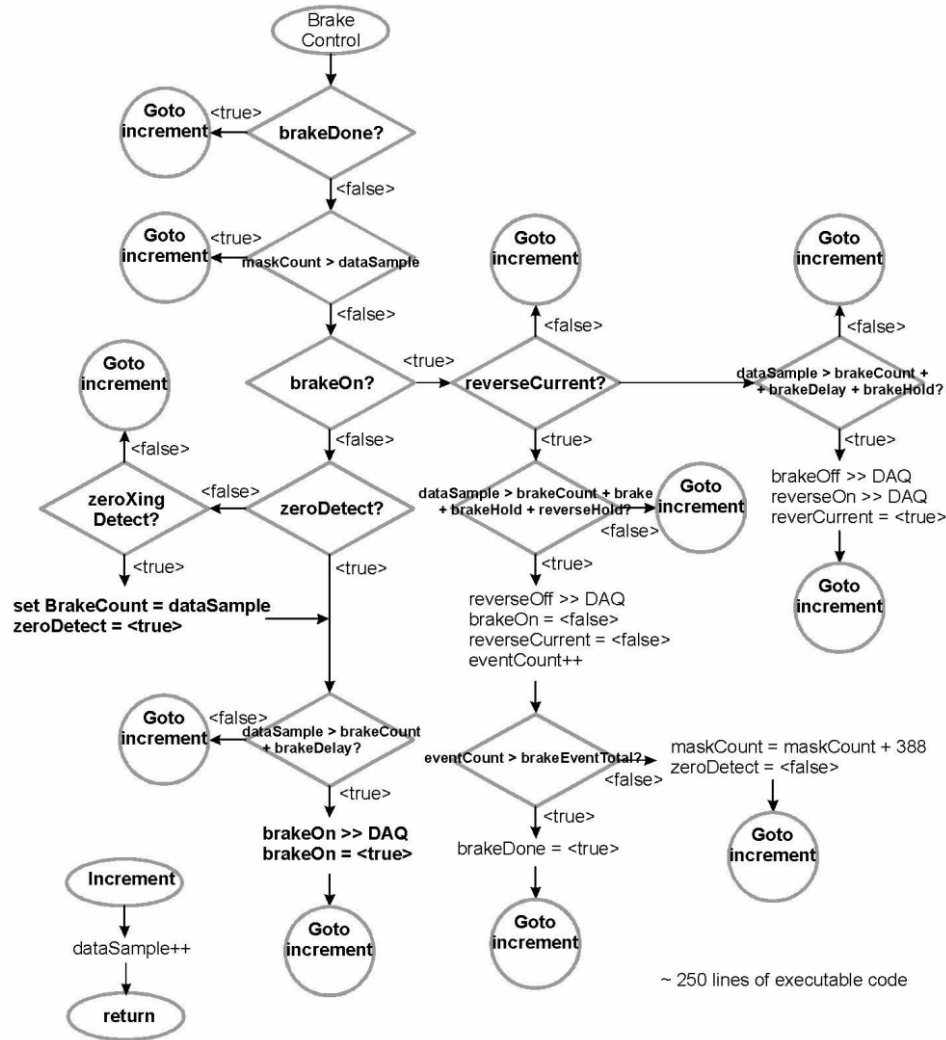


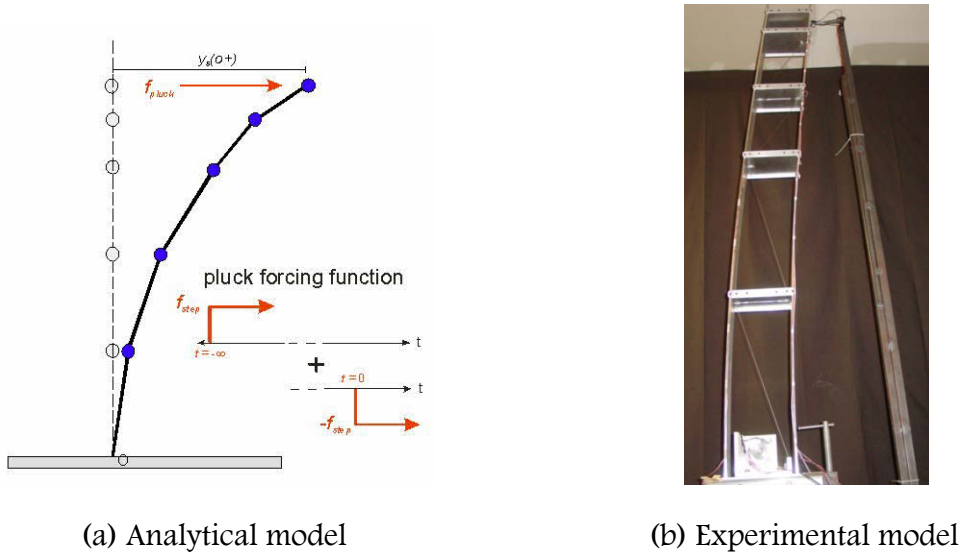
Figure 5-30 Modal Damping Actuator Control Logical Flow Diagram

A stand alone executable file was generated by Visual Studio. This file was able to be ported to a generic laptop computer running Microsoft XP. The code was run within the XP environment with no problems. Unnecessary XP and Windows application tasks and services were carefully shut down using the *msconfig* utility

before running the test code in order to free up the CPU as much as possible. No timing problems were encountered during any tests.

5.2.8 The Pluck Test

The ‘Pluck’ Test is the name given to the specific test conditions employed to demonstrate the Modal Damping Concept. The Pluck Test is described in detail in Section 4.3.1.1. A schematic drawing along with the actual concept demonstration Pluck Test set-up configuration is shown in Figure 5-31.



(a) Analytical model

(b) Experimental model

Figure 5-31 Pluck Test Implementation [Pre-Positioning]

5.2.9 Characterization Test

Once fabricated and assembled, the dynamic behavior of concept demonstration experimental model was characterized. Modal frequencies and damping properties were determined using the Pluck Test described above. The system was allowed to decay naturally during characterization testing. Three damping mechanisms were expected to be involved in the dissipation of vibration energy:

1. Anelastic (viscous).

2. Aerodynamic drag.
3. Friction (coulomb).

Each of the three mechanisms has characteristic decay behaviors as can be observed in their respective analytical model responses shown in Figure 5-32 as reference.

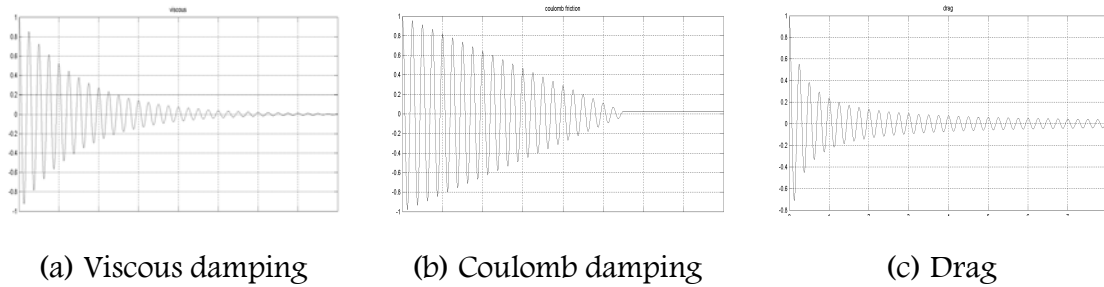


Figure 5-32 Damping Mechanisms of Interest

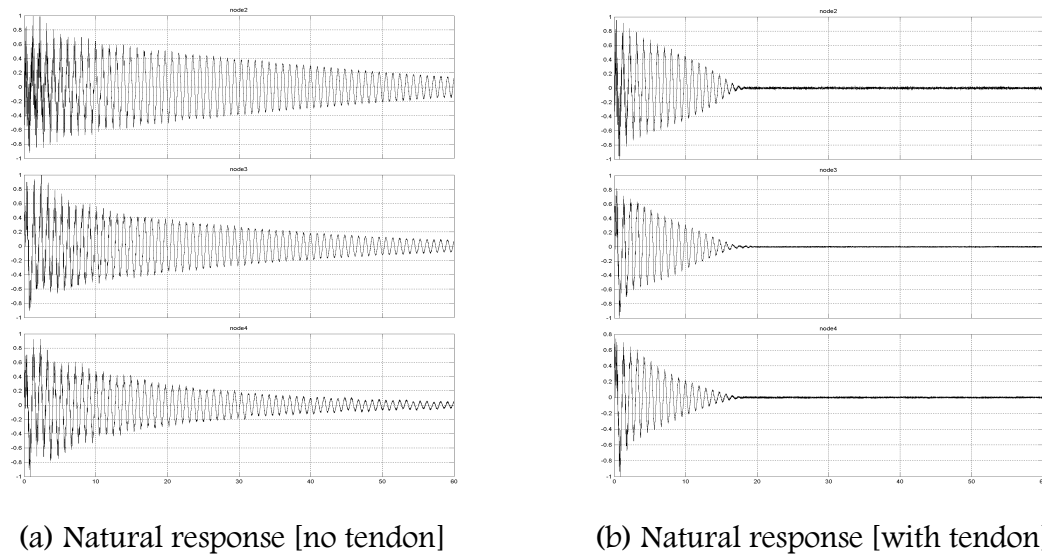


Figure 5-33 Natural System Response to Pluck Input

The natural response of the experimental model to the Pluck Test was measured without the control tendon (Figure 5-33.a) and with the control tendon integrated (Figure 5-33.b). When the response of Figure 5-33.b was compared to those of the expected mechanisms, it disclosed that the control subsystem added significant frictional damping to the system. The measured dominance of the friction mechanism

was not expected. The decay envelope was nearly identical to that of the linearly decaying coulomb dissipation function even though extreme care was taken in designing and selecting all subsystem components.

There were three possible components where frictional damping was expected to exist: the pulleys within the structure, the ball bearings in the off-structure actuator assembly, and within the multi-strand cable. Both the pulleys and the bearings were selected based on their relatively small size and construction geometry in order to minimize frictional effects. The cable was selected based on strength properties and flexibility. The cable, although only .050 inch in diameter, was composed of 49 separate strands of steel wire woven together. The surface to surface interactions between the individual strands as the cable deformed around the pulleys may have resulted in unexpected dissipation. The cable was advertised as being lightly lubricated. No additional lubrication was added. It is believed that the small scale of the experimental model resulted in the amplified effect of the damping control mechanism, even in its passive state.

The dominance of the coulomb damping mechanism was not predicted. Nevertheless, it does not have a significant impact on the conclusions established by the demonstration. The three damping mechanisms identified above are inherent to some degree, in all structures that fall into the tall/long and flexible category. Even the simple roadside cantilever will contain frictional damping. The typical mounting is on a transformer/break away base. The interaction and mounting would have some frictional damping properties. Impact dampers often hang inside the cantilever structure. The friction based interaction between the impact damper and the cantilever is vital to its effectiveness. Modal Damping is designed to exploit the increased damping

impedance of higher order modes regardless to what mechanism the damping might be attributed.

5.2.10 Formal Test Overview

One hundred twenty-nine (129) separate Pluck Tests were formally completed during the test phase. A formal test was defined as one conducted while meeting the following conditions:

- Test execution was initiated and controlled by automated scripted procedures taking the form of a compiled and linked executable code run on a generic laptop computer.
- Measured and computed structural states, and actuator control commands were collected, time-stamped, and stored by the controller.
- Data were reduced and analyzed offline.

Many more test runs were executed, or partially executed while integrating and validating subsystem components but were not considered or included in the formal system test database. No unexpected hardware related issues were encountered.

Ninety-two (92) of the 129 formal tests were specified as ‘Evaluation’ level tests and were book-kept in a performance database that was used for statistical analysis and system performance characterization. The remaining 40 tests, all completed early in the testing phase, were determined non-Evaluation level tests due to design weaknesses associated with either the braking actuator circuit and/or earlier builds of the control software executable code.

The 92 Evaluation Tests were further differentiated by varying test parameters assigned to their test execution scripts at test start. The five performance related parameters specified were:

1. Test duration.
2. Brake HOLD count.
3. Braking DELAY count.
4. Brake REVERSE CURRENT count.
5. Number of ENERGY TRANSFER EVENTS.

Most of these parameters were related to variable timing features programmed into the test script, and were utilized to determine pseudo-optimal actuator performance. Assignment of these parameters was accomplished by keyboard entry at scripted queuing. The test variables and associated system results for the 92 Evaluation Tests are tabularized and included as Attachment B.

5.2.11 Formal Test Results

The overall performance of the Modal Damping concept is summarized in the two distribution plots given in Figure 5-34. These distributions reflect the improved settling time of the vibrating structure as a result of modal energy transfer from the fundamental mode to higher order modes, primarily that of the 2nd mode. Each chart is a composite of four fitted Gaussian distributions. The four Gaussian distributions model the measured data for zero, one, two, and three Modal Damping energy transfer events respectively. The two charts are intended to provide a relative comparison of the settling time of the vibrating system when subjected to one or more Modal Damping events, to the same system simply allowed to dampen naturally. In all cases the system is excited by the same forcing function. The distribution of the set of settling times of the natural damped system is normalized to 100% and assumed the baseline. The Modal Damped distributions are scaled and positioned according to the baseline.

Figure 5-34a is a summary of the full Evaluation Set and includes the responses from the full range of variable performance parameters investigated. Figure 5-34b is a summary of 66 tests, a subset of the full 92 Evaluation Set of tests.

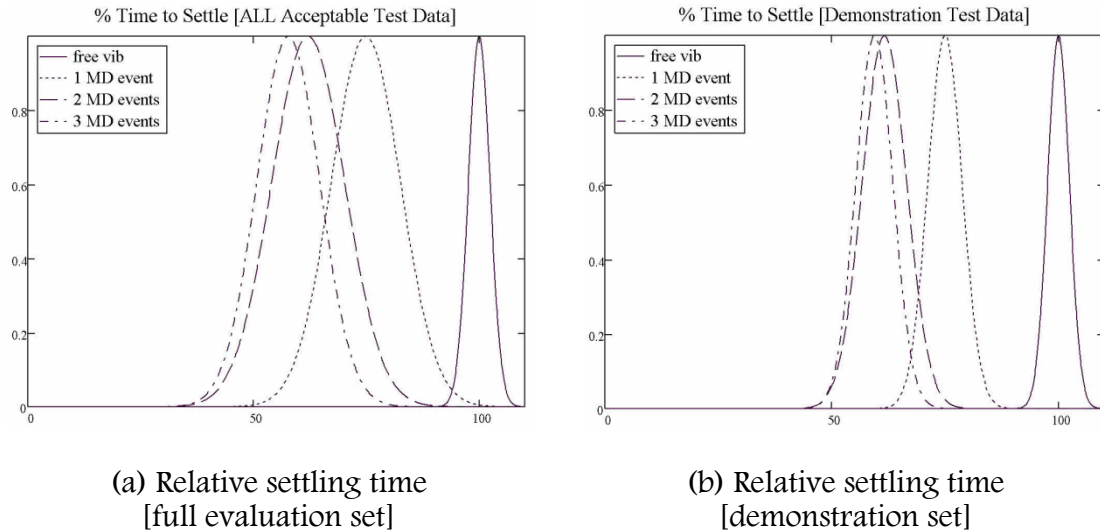


Figure 5-34 Modal Damping Performance Summary

The 66 tests represent tests performed using a reduced or pseudo-optimized range of parameter variations, and are considered to represent the ‘Demonstration Set’ for the Modal Damping Concept.

The data from the Demonstration Set used to create Figure 5-34b is also shown plotted as a scatter chart in Figure 5-35. The scatter chart provides a visual presentation of the settling-time distributions. The sample count is not necessarily large nor perfectly Gaussian, however the observed scatter demonstrates some Gaussian-like features. The model does not seem unreasonable for the charts of Figure 5-34. Table 5-14 provides a numerical summary of Modal Damping effectiveness.

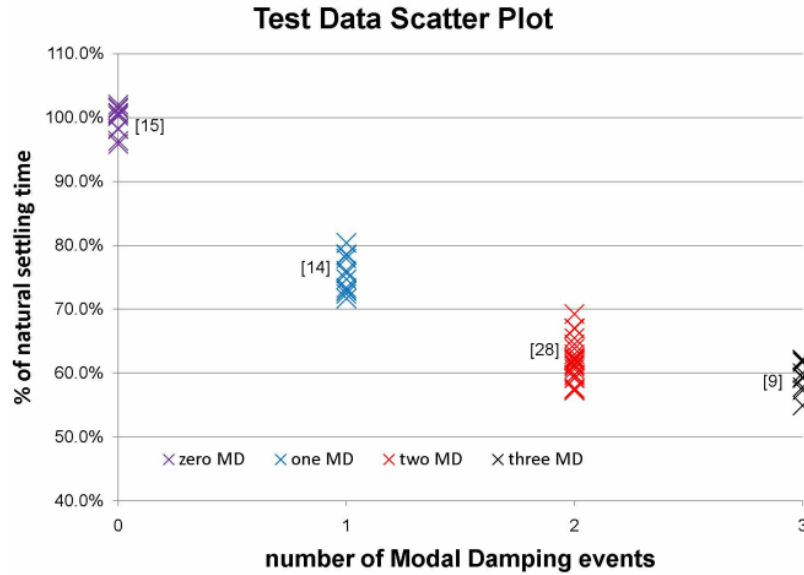
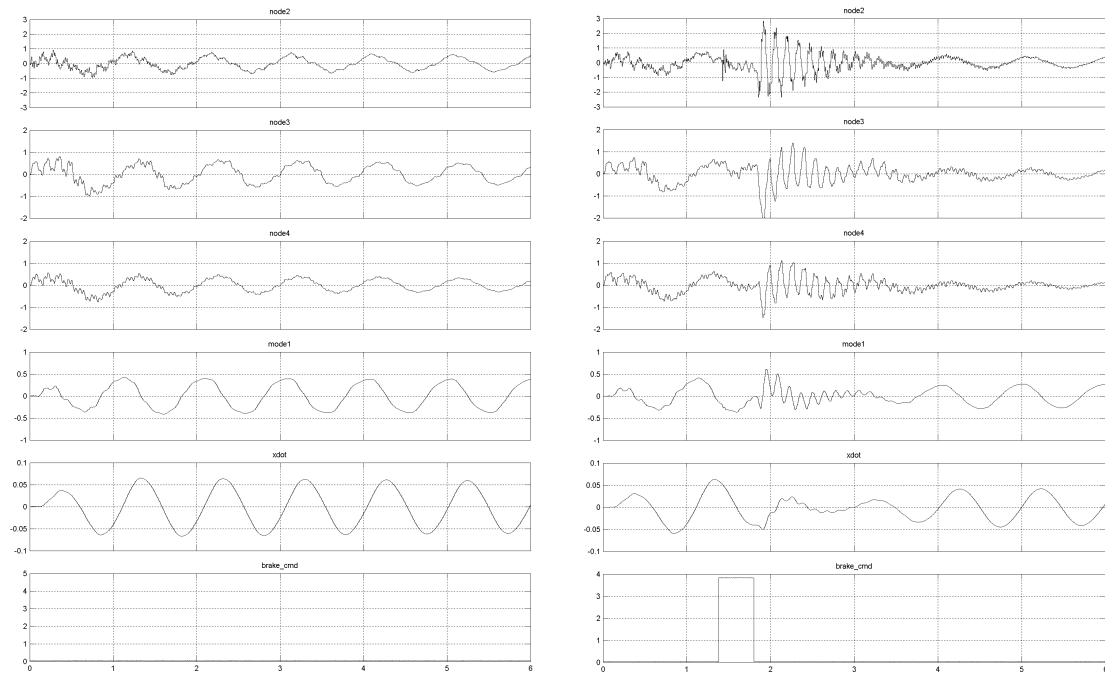


Figure 5-35 Demonstration Tests Scatter Chart

Table 5-14 Modal Damping Settling Time Summary

MD Events	Test Count [Evaluation Set]	Test Count [Demonstration Set]	Total Settling Time Improvement [%] [Demonstration Set]	Incremental Settling Time Improvement [%] [Demonstration Set]
0	15	15	—	—
1	21	14	24.3	24.3
2	37	28	38	18.1
3	17	9	40.3	3.6
4	1	0	—	—

The performance summaries given above were derived using the raw data captured in real-time, and stored by the controller. Accelerations were directly measured at nodes 2, 3, and 4 (see Figure 5-23). These nodal locations correspond to the peak deformations for the vibration modes of interest. Each individual test generated six text based data files. The collected text-based data files were converted to MATLAB compatible form for post test analysis.



(a) No MD events [test: feb04091516]

(b) One MD event [test: feb04091528]

Figure 5-36 Measured Test Data [Single MD Event]

Data compilations from two representative tests are shown in Figure 5-36. Figure 5-36a is the response-set of the system naturally damped, while Figure 5-36b is that of the system subjected to one Modal Damping event. Figure 5-37 points out the sequence of events that occurred during the Modal Damping energy transfer event.

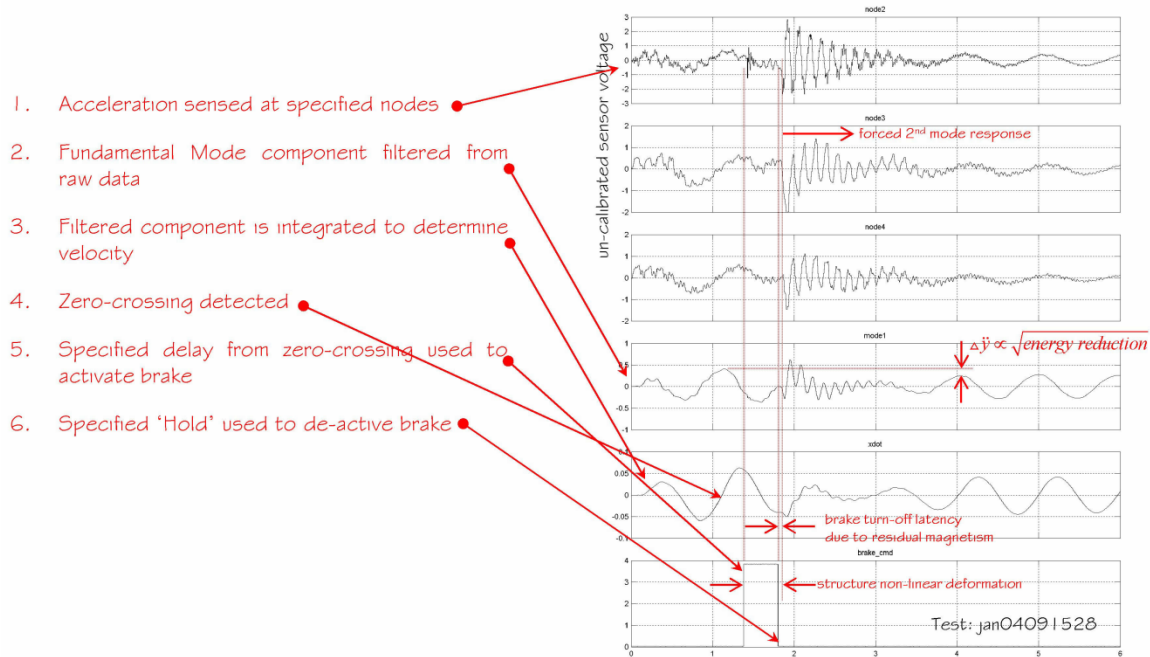


Figure 5-37 Modal Damping Control Sequence

The control logic sequence is coupled to the behavior of fundamental mode component. This component was filtered out of raw measured data, in this case from Node-2, using a basic first order filter designed to minimize phase shift error. The integrated, filtered component represents velocity and is used to determine structural position in the sway cycle. Structural position given by this signal combined with the keyed-in parameters provide the necessary timing to execute the energy transfer event using the control tendon device.

The measured data shown in Figure 5-36 illustrates that the 2nd vibration mode component is dominant at all nodal locations immediately after the Modal Damping event but decays rapidly as expected and desired. Comparing the before and after (Modal Damping) amplitudes of the fundamental mode acceleration component is an indicator of the amount of available energy transferred. Comparing the estimated peak mode-1 accelerations shown on Figure 5-36 yields,

$$\frac{U^+}{U^-} = \left(\frac{\ddot{y}_{peak}^+}{\ddot{y}_{peak}^-} \right)^2 \approx \left(\frac{.25}{.4} \right)^2 = .40$$

This indicates that approximately $(U^+ - U^-) \cdot 100\% = 60\%$ of the fundamental energy was transferred during the Modal Damping event. Figure 5-38 illustrates the improved settling time of the vibrating system that resulted from that single Modal Damping Event; as shown, almost 25% improvement was achieved.

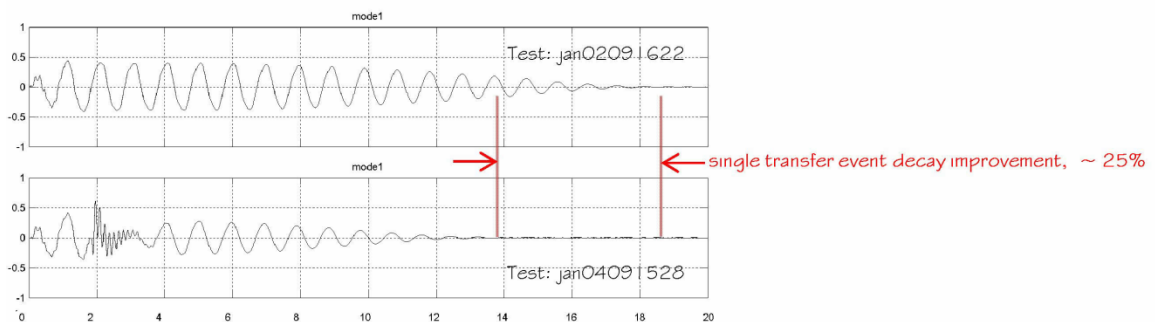
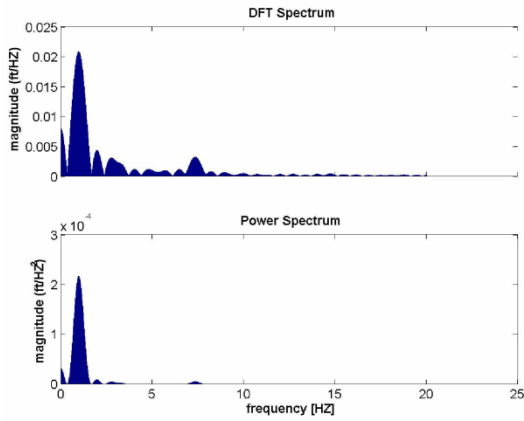


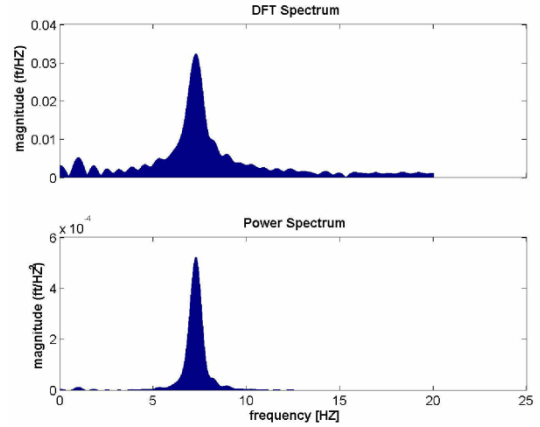
Figure 5-38 Settling Time Improvement [Single MD Event]

Figure 5-39 contains two Discrete Fourier Transforms of the Node-2 measured acceleration that attempt to illustrate the ability of the 3-point tendon to transfer energy to the 2nd vibration mode. The first DFT was computed over the time window of 2 to 3.5 seconds during a test when the system was allowed to decay naturally. The second DFT was taken over the same time window during a single Modal Damping event test.

37 tests were conducted to investigate the effectiveness of two sequential, or back-to-back, Modal Damping events, while 17 tests were conducted to investigate three sequential transfer events. Figure 5-40 compares the plots of measured and computed data collected for the system naturally damped with that of the system subjected to ‘three’ Modal Damping events.

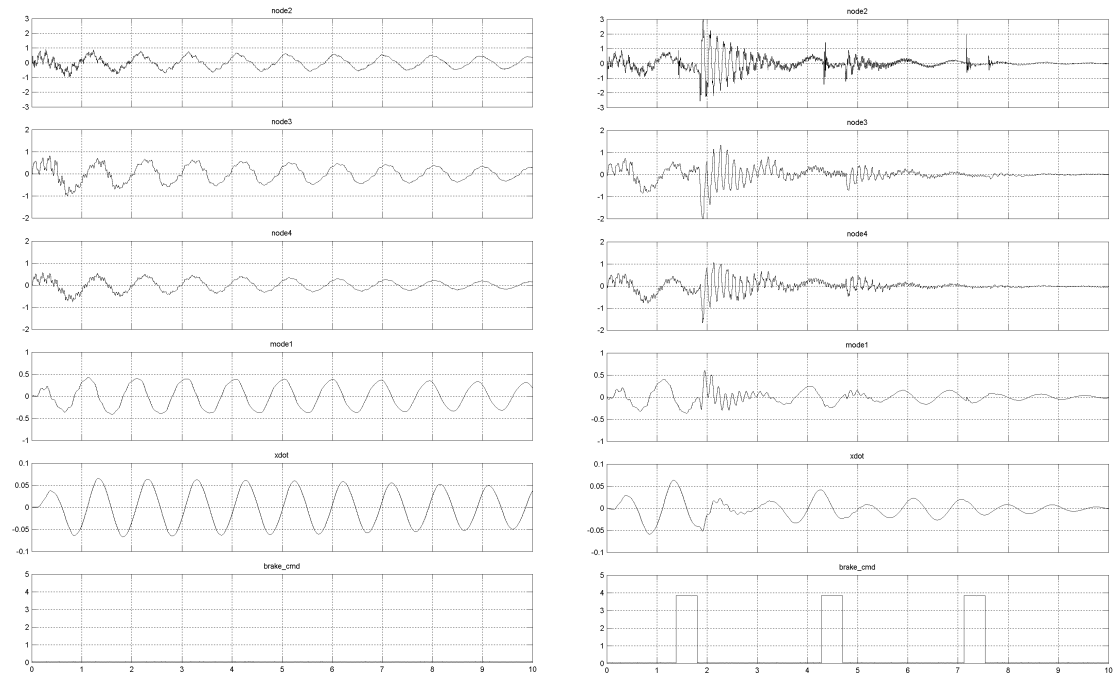


(a) Without Modal Damping
[test: feb04091516]



(b) With Modal Damping
[test: feb04091531]

Figure 5-39 Modal Damping DFT Effect [2 to 3.5 sec]



(a) No MD events [test: feb04091516]

(b) Three MD events [test: feb04091531]

Figure 5-40 Measured Test Data [Three MD Events]

The control logic was designed to allow three fundamental time periods to elapse between each Modal Damping event. This proved to be sufficient time to allow 2nd mode vibrations to decay. Energy transfer and 2nd mode excitation can be observed

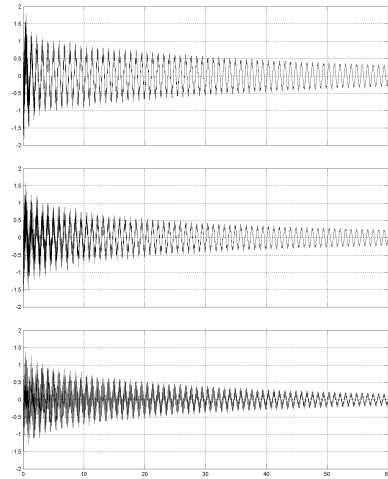
for all three Modal Damping events. The 2nd event was found to be effective based on the observed response and improved settling times measured. Likewise, an observable and measureable response was noted for the 3rd event as evident by its associated contributions found in Table 5-14 and Figure 5-40. However its effectiveness was comparatively low. At the time the 3rd event was executed, total system energy was reduced by approximately 75% and fundamental sway displacements were significantly smaller. These conditions exacerbate the design limitations of the control tendon. Being mechanical in nature, it has inherent non-linear hysteresis behavior associated with tendon slack. An improved design and implementation could potentially improve the efficiency of multiple Modal Damping events.

5.3 Simulation Validation

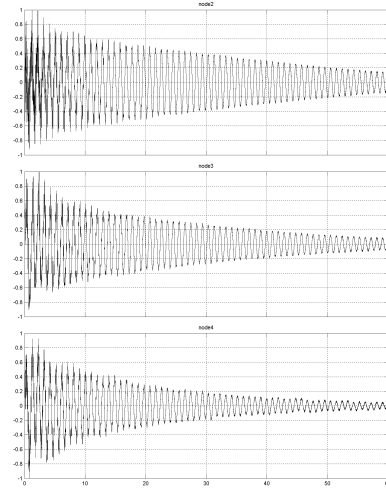
Significant effort was directed at developing the system model that became the central component in the dynamic simulation used to investigate, refine and evaluate the closed-loop Modal Damping control algorithm. The effort proved worthwhile as the transition and application of the control on the experimental model was performed with minimal difficulty. Comparing the measured results with those generated by the simulation provided an opportunity to validate the fidelity of :

1. The accuracy of the cantilever model.
2. The accuracy of the physical mechanisms associated with the control actuator interaction with the cantilever.
3. And, the validity of the control strategy that was designed to transfer energy from one vibration mode to another. Following are three sets of results that attempt to provide a qualitative comparison between the virtual world and the physical world.

Figure 5-41 compares the accelerometer data captured during a Pluck test when the system was allowed to dampen naturally. The measured data of Figure 5-41b is from the system configured without the control tendon attached. The tested system was composed of the dual cantilever elements with all the story hardware integrated. The two sets of accelerations are not identically scaled. The simulation predictions are scaled to acceleration due to gravity $(in/sec^2) / \left(32 ft \cdot 12 \frac{in}{ft} / sec^2 \right) = g$. The unit of the measured data is volts. It was decided that there was nothing to be gained for the time and effort that was required to calibrate and convert the measured data to different units. The damping information remained unchanged. Comparing the features of the two sets of responses reveals good correlation. The relative magnitudes of the fundamental mode as it decays are comparable between equivalent nodes of the two data sets. The modal complement among the nodes within a data set can be inferred by examining the decay envelopes. The envelopes between the two sets show similar characteristics. The experimental model was subjected to drag effects that were not included in the simulation model. The additional damping mechanism may explain what appears to be a minor damping increase particularly in Nodes 3 & 4 of the experimental model response. In general, the simulation response was thought to correlate well with the measured data for this test scenario.



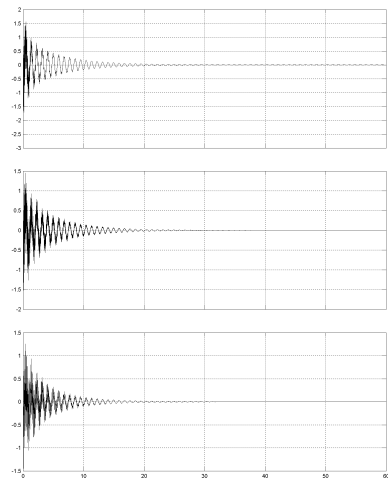
(a) Nodal accelerations [SIMULINK]



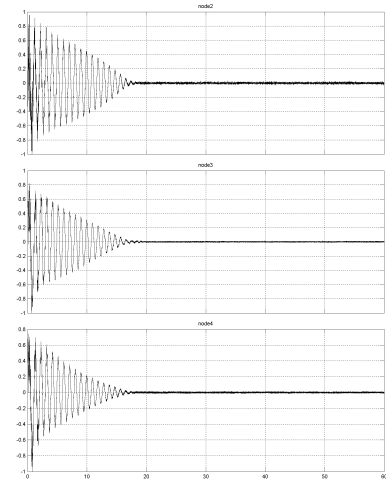
(b) Experimental data
[test: feb04091531]

Figure 5-41 Simulation Validation [Natural Damped Without Control Tendon]

Figure 5-42 again, compares the accelerometer data captured during a Pluck test when the system was allowed to dampen naturally. However, this test scenario includes the control tendon in the system configuration.



(a) Nodal accelerations [SIMULINK]

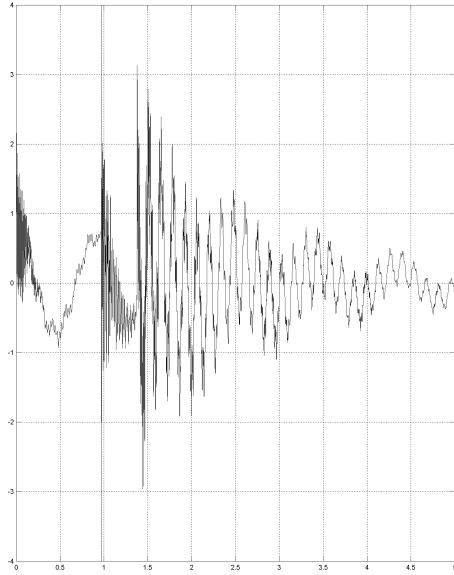


(b) Experimental data
[test: feb04091531]

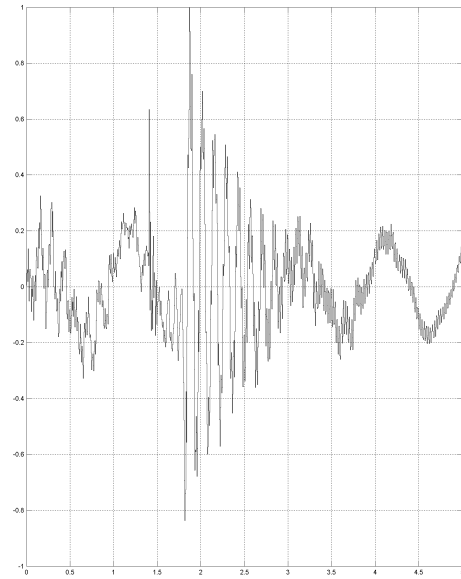
Figure 5-42 Simulation Validation [Natural Damped With Control Tendon]

As was described above, the experimental model response was found to be dominated by a frictional component that was not expected. The simulation model did not have a frictional damping mechanism. The viscous damping mechanism was adjusted to emulate the additional dissipation. Although settling times between the two sets are equivalent, the decay envelopes are clearly different. The absence of the frictional component did not affect the development and evaluation of the control algorithm.

Figure 5-43 was probably the most satisfying comparison between the two systems. It captures the dynamics of the energy transfer orchestrated by the Modal Damping control. Recall, that the control event is non-linear in nature. The two targeted vibration modes involved in the transfer are orthogonal. Linear state based control would not transfer the energy. A Bang-Bang non-linear algorithm was utilized. The event is clearly captured in both the simulated and measured responses. The absence of the frictional damping mechanisms explains a somewhat different decay profile. However, the simulated control event adequately captures the dynamics of the transfer. The measured response demonstrates the conceptual objective of the control strategy while validating the modeling approach utilized in the simulation. Furthermore the nearly identical response of the simulation was achieved with only the anelastic mechanism. It validates the effectiveness of Modal Damping regardless of the damping mechanism.



(a) Simulated nodal acceleration
[SIMULINK]



(b) Experimentally measured
acceleration
[test: feb04091531]

Figure 5-43 Simulation Validation [Modal Damping Energy Transfer Event]

CHAPTER VI

CONCLUSION

An alternative vibration energy damping approach that employs inter-modal energy transfer was developed to augment the natural dissipation capability of tall, flexible structures. The motivation behind the approach was established. An implementation strategy based on a simple 3-point tendon was selected and engineered. The mathematical basis supporting the implementation scheme was developed and culminated in a dynamic simulation (MATLAB/SIMULINK) of the full cantilever-tendon couple physics and Modal Damping control logic. The simulation results yielded the following findings:

1. Vibration energy could be transferred between the fundamental mode and the 2nd order mode using a relatively simple, controllable 3-point tendon. The tendon was controlled by an intelligent control law using simulated sampled measurements from basic accelerometers.
2. Modal Damping Augmentation improved the overall dynamic energy dissipation behavior of the subject structure. Improvements in the range of 30% to 70% were shown for the test scenarios investigated.
3. In general, nodal displacements were improved across the structure after the Modal Damping event, in some locations up to 40%. Nodal velocities lower in structure experience an increase in magnitude up to 100%. The increased velocities coincided

with increased structural deformation rates leading to increased energy dissipation by the anelastic damping mechanism.

The results of the Modal Damping simulation was used to design, fabricate, and assemble a Concept Demonstration experimental model. Both the control tendon configuration and the experimental model designs used in the concept demonstration evolved from their simulation counterparts. The Concept Demonstration implementation took on the look of a more practical, real-world configuration. Regardless, the improved configuration maintained the simple 3-point force distribution behavior. Test execution and data collection were accomplished by automated script that was run on a standard laptop computer. Summary results of the concept demonstration experimental testing were:

1. The designed, fabricated and assembled experimental model was characterized. Its mode shapes were derived analytically and its modal frequencies and damping properties were both derived analytically and measured experimentally.
2. Characterization testing revealed an unexpected dominant coulomb damping mechanism in the system response. The frictional damping was attributed to the implementation of the mechanical control actuation subsystem and was not predicted to the degree measured. Nevertheless, it did not have a significant impact on the conclusions established by the demonstration. Three natural damping mechanisms are inherent to the structures of interest to some degree: anelastic, drag, and coulomb. Even the simple roadside cantilever will contain frictional damping. Its typical mounting is by mechanical connection to a transformer/break away base. The cantilever/base interaction would naturally have some frictional damping properties. Impact dampers often hang inside the cantilever structure. The friction based interaction between the impact damper and the cantilever is vital to

- its effectiveness. Modal Damping was designed to exploit the increased damping impedance of higher order modes regardless to what mechanism the damping might be attributed.
3. Ninety-two (92) separate tests were completed and compiled into an Evaluation-Set that was statistically analyzed to assess general performance of the Modal Damping concept. A subset of sixty-six (66) tests was established as the Demonstration Set based on a perceived pseudo-optimized set of test parameters. Tests from the Demonstration Set included zero, one, two and three Modal Damping Events. The zero Modal Damping event test was established as the baseline to measure performance of the Modal Damping.
 4. Statistically combined results show that the single Modal Damping event improved settling time by approximately 24%. The two-Modal Damping event test improved settling time by approximately 38% overall. The three-Modal Damping event showed minor improvement over the two-event test, improved overall settling time by approximately 40% over the baseline.
 5. No additional energy was introduced into the vibrating structure to effect energy transfer between the vibrations modes. The forces required were self-powered by the kinetic energy associated with the fundamental mode.

The physics behind the anelastically damped energy distribution was examined to investigate the possible threats to the system imposed by Modal Damping. This investigation further shed addition insight to explain the improved damping performance demonstrated by Modal Damping. The investigation revealed the following for the conditions examined (equivalent modal vibration energies):

1. The damped energy densities developed by the 2nd mode immediately within the base region of the structure can potentially be nearly twice those of the fundamental mode.
2. Both the fundamental and the 2nd modes dissipate approximately the same energy over the bottom 50% of the structures height.
3. The 2nd mode utilizes the third quadrant of the structure's height (50→75%) more effectively to dissipate significantly vibration energy. The utilization of the third quadrant makes the 2nd mode significantly more efficient than the fundamental mode in terms of dissipating dynamic energy.

In conclusion, the analytical and the experimental results demonstrated that Modal Damping can potentially be a viable damping option for the tall, flexible structures of interest. It is reasonable to assume that the modal vibration analysis performed herein and the damping control design can be applied to terrestrial, space-based and other light and flexible structural topologies of interest.

6.1 Recommendations

Based on the conclusions stated above, Modal Damping lends itself to further study and advanced development that could lead to its application. Specifically,

1. The adaptation of Modal Damping to a larger scale, more sophisticated structural model can be investigated.
2. More complex stiffness distributions can be examined.
3. 'Real-world' actuation systems that lend themselves to increased structural mass distributions can be examined.
4. 'Real-world' control system requirements can be investigated.

5. Control algorithm optimization can be examined. The Modal Damping control law could be enhanced to allow the amount of energy transferred to be more robust. In doing so, the compromise between energy transferred and the resulting structural dynamics could be evaluated in real time. Improved energy dissipation could still be achieved yet maximum nodal velocities could be constrained.
6. Modal Damping can be studied and adapted to transfer energy to higher order modes; i.e. modes above the 2nd vibration mode.
7. Modal damping can be investigated for near term, real-world adaptation to HAPCO-like structures, enabling an enhancement to the impact damper.

BIBLIOGRAPHY

1. N. Satake, K. Suda, T. Arakawa, A. Sasaki, Y. Tamura, 'Damping evaluation using full-scale data of buildings in Japan', *Journal of Structural Engineering*, 2002, pp. 470-477
2. K. Suda, N. Satake, J. Ono, A. Sasaki, 'Damping properties of buildings in Japan', *Journal of Wind Engineering*, 59, 1996, pp. 383-392
3. ASCE Tall Buildings Committee, Damping Guidelines, <<http://www.nd.edu/~tallbldg/dampingguidelines.html>>, estimated access August 2004
4. K.W. Johns, R.J. Dexter, 'Fatigue testing and failure analysis of aluminum luminaire support structures', Final Report, ATLSS Report No. 98-06, May 1998, p. 4
5. K.W. Johns, R.J. Dexter, 'Fatigue testing', p. 1
6. Architectural Record, Issue 01-2004, p. 23
7. <<http://www.nyc-tower.com/image10/>>, accessed March 2009
8. <<http://www.nps.gov/archive/wamo/history/chap4.htm>>, estimated access January 2005
9. R.J. Nacheman, 'The empire state building: façade evaluation and repair of an engineering landmark', *Structure Magazine*, January 2006, pp. 39-43
10. <http://www.esbnyc.com/tourism/tourism_facts_2.cfm?CFID=14220&CFTOKEN=1408>, accessed October 2008
11. <<http://www.enm.bris.ac.uk/anm/tacoma/tacoma.html#mpeg>>, estimated access March 2005
12. K. Yamada, T. Kobori, 'Fundamental dynamics and control strategies for aseismic structural control', *International Journal of Solid and Structures*, 38, 2001, pp. 6079-6121
13. H. Bachmann, W. Ammann, *Vibration Problems in Structures: Practical Guidelines*, Birkhäuser Basel, 1994, p. 77
14. K. Yamada, T. Kobori, 'Fundamental dynamics and control strategies', p. 6081

15. T Kijewski, A. Kareem, 'Estimation and modeling of damping and engineering auxiliary damping systems in civil engineering structures: an overview', NatHaz Modeling Laboratory Report, 2000, pp. 4-5, <<http://www.mendeley.com/c/5731209/Kijewski-2000-Estimation-and-Modeling-of-Damping-and-Engineering-Auxiliary-Damping-Systems-in-Civil-Engineering-Structures-An-Overview>>, accessed March 2009
16. J.W. Tedesco, W.G. McDougal, C.A. Ross, *Structural Dynamics Theory and Applications*, Menlo Park CA, 1999, pp. 78-100
17. N. Satake, K. Suda, T. Arakawa, A. Sasaki, Y. Tamura, 'Damping evaluation', p. 472
18. K. Suda, N. Satake, J. Ono, A. Sasaki, 'Damping properties', pp. 387-388
19. Reprinted from Journal of Wind Engineering, 59, K. Suda, N. Satake, J. Ono, A. Sasaki, 'Damping properties of buildings in Japan', pg 388, 1996, with permission from Elsevier, License Number 2199441315829
20. N.E. Dowling, *Mechanical Behavior of Materials*, Upper Saddle River, New Jersey: Prentice Hall, Inc, 1999, pp. 757-765
21. D.J. Inman, *Engineering Vibration*, Upper Saddle River, New Jersey: Prentice Hall, 2001, p. 400
22. T. Kijewski, A. Kareem, 'Estimation and modeling', pp. 29-32
23. M. Symans, M. Constantinou, 'Semi-active control systems for seismic protection of structures: a state-of-the-art review', *Engineering Structures*, 21, 1999, pp. 469-458
24. N. Kurata, T. Kobori, N. Koshika; 'Performance-based design with semi-active structural control technique', *Earthquake Engineering and Structural Dynamics*, 31, 2002, pp. 445-458
25. Sakamoto, M., Kobori, T., 'Research, development and practical applications on structural response control of buildings', *Smart Material and Structures*, 4, 1995, pp. A58-A74
26. J.J. Conner, *Structural Motion Control*, Pearson Education, Inc, 2003, p. 220
27. T. Irvin, 'The citicorp building tuned mass damper', <www.vibrationdata.com/Newsletters/January2002_NL.pdf>, pp. 3-6, estimated access March 2005
28. <http://www.greatbuildings.com/buildings/Citicorp_Center.html>, accessed March 2009
29. <http://www.pbs.org/wgbh/buildingbig/wonder/structure/citicorp2_skyscraper.html>, accessed March 2009

30. Tuned Liquid Dampers and Tuned Liquid Column Dampers Research at NatHaz Modeling Laboratory,
<http://www.nd.edu/~nathaz/research/liquid/liq_damp.html>, accessed March 2009
31. S.K. Yalla, A. Karrem, J.C. Kantor, 'DISCUSSION OF PAPER: Tuned liquid dampers for controlling earthquake response of structures by P. Banerji et al', *Earthquake Engineering and Structural Dynamics*, 2002, 31, pp.1037-1039
32. A.A. Damatty, 'Studies on the application of tuned liquid dampers to up-grade the seismic resistance of structures', ICLR Research Paper Series – No. 17, April 2002
33. S.L.T. de Souza, I.L. Caldas, R.L. Viana, J.M. Balthzar, R.M. Brasil, 'Impact dampers for controlling chaos in systems with limited power supply', *Journal of Sound and Vibration*, 279, 2005, pp. 955-967
34. P. Frantisek, 'More detail view on the dynamics of the impact damper', *Mechanics, Automatic Control and Robotics*, 3, 2003, pp. 907-920
35. L. Caracoglia, N.P. Jones, 'Analysis of light pole failures in Illinois – final report', Department of Civil Engineering, University of Illinois at Urbana-Champaign, Report No. UILU-ENG-2004-2007, August 2004, pp. 33-46
36. Y.L. Xu, 'Parametric study of active mass dampers for wind-excited tall buildings', *Engineering Structures*, 18, 1996, pp. 64-76
37. Y. Ikeda et al, 'Active mass driver system as the first application of active structural control', *Earthquake Engineering and Structural Dynamics*, 30, 2001, pp. 1575-1595
38. J.P. Lynch, 'Active structural control research at Kajima Corporation', White paper for The National Science Foundation's Summer Institute in Japan Program, Sept 17, 1998
39. J.P. Lynch, 'Active structural control', p. 51
40. <<http://www.nd.edu/~nathaz/research/Gang.htm>>, accessed March 2009
41. J.J. Conner, Structural Motion Control, pg 397
42. T. Nasu et al, 'Active variable stiffness system with non-resonant control', *Earthquake Engineering and Structural Dynamics*, 30, 2001, pp. 1597-1614
43. T. Nasu et al, 'Active variable stiffness', pg 1603
44. E. Taylor, 'Vibration control for two dynamically similar structures', Colorado School of Mines Report in support of Research Experiences for Undergraduates in Japan in Advanced Technology 2003, <mase.wustl.edu/wusceel/reujat/2003>, estimated access June 2005

45. R.E. Christenson, B.F. Spencer, N. Hori, K. Seto, 'Coupled building control using acceleration feedback', *Computer Aided Civil and Infrastructure Engineering*, 18, 2003, pp. 4-18
46. H.P. Gavin, 'Design method for high-force electroheological dampers', *Smart Material and Structures*, 7, 1998, pg. 665
47. M.D. Symans, M.C. Constantinou, 'Semi-active control systems for seismic protection of structures: a state-of-the-art review', *Engineering Structures*, 21, 1999, p. 474
48. Y. Fujino, T.T. Soong, B.F. Spencer, 'Structural control: basic concepts and applications', *Proceedings of the 1996 ASCE Structures Congress*, Chicago, Illinois, April 1996, pp. 1-11
49. Kareem, T. Kijewski, Y. Tamura, 'Mitigation of motions of tall buildings with specific examples of recent applications', Notre Dame White Paper, <[http://www.nd.edu/~nathaz/journals/\(1999\)Mitigation_of_Motion_of_Tall_Buildings_with_Recent_Applications.pdf](http://www.nd.edu/~nathaz/journals/(1999)Mitigation_of_Motion_of_Tall_Buildings_with_Recent_Applications.pdf)>, accessed September 2005
50. J.J. D'Azzo, C.H. Houpis, *Linear Control System Analysis and Design*, New York: McGraw-Hill, 1981, p. 149
51. C.T. Chen, *Linear System Theory and Design*, Holt, New York: Reinhart and Winston, 1970, p. 77
52. C.C. Chang, L.O. Yu, 'A simple optimal pole location technique for structural control', *Engineering Structures*, 20, 1998, pp. 792-804
53. H. Sedarat, H. Sedarat, R. Kosut. 'Active Control in Structures', 13th ASCE Engineering Mechanics Division Conference, Baltimore, June 1999
54. J.J. D'Azzo, C.H. Houpis, *Linear Control*, p. 495
55. K. Yamada, T. Kobori, 'Fundamental dynamics and control strategies', pp. 6094-6104
56. L.L. Chung, 'Modified predictive control of structures', *Engineering Structures*, 21, 1999, pp. 1076-1085A
57. A. Preumont, *Vibration Control of Active Structures: An Introduction*, Dordrecht, The Netherlands, 2002, p. 205
58. K.S. Kim, Y. Park, 'Robust LQG controller design for lightly damped uncertain linear systems', *KSME International Journal*, Vol 12 No 2, 1998, pp. 199-205
59. P.C. Chandrasekharan, *Robust Control of Linear Dynamical Systems*, Academic Press, 1996,

60. L. Rollins, 'Robust control theory', Carnegie Mellon University White Paper, 1999, <http://www.ece.cmu.edu/~koopman/des_s99/control_theory/>, accessed April 2009
61. J.N. Yang, S. Lin, F. Jabbari, 'H₂-based control strategies for civil engineering structures', *Journal of Structural Control*, 10, 2003, pp. 205-230
62. J.C. Wu, J.N. Yang, W.E. Schmitendorf, 'Reduced-order H_∞ and LQR control for wind-excited tall buildings', *Engineering Structures*, Vol 20, 1998, pp. 222-236
63. S. Ankireddi, H.T.Y. Yang, 'Sampled-data H₂ optimal output feedback control for civil structures', *Earthquake Engineering and Structural Dynamics*, 28, 1999, pp. 921-940
64. K. Yamada, 'Fundamental dynamics and control strategies', p. 6083
65. K. Yamada, 'Fundamental dynamics and control strategies', p. 6113
66. M. Battaini, F. Casciati, L. Faravelli, 'Fuzzy control of structural vibration. An active mass system driven by a fuzzy controller', *Earthquake Engineering and Structural Dynamics*, 27, 1998, pp. 1267-1276
67. L.A. Zadeh, 'Fuzzy sets', *Information and Control*, 8, 1965, pp. 338-353
68. M. Aldawod, B. Samali, F. Naghdy, D. Kwok, 'Active control of along wind response of tall building using a fuzzy controller', *Engineering Structures*, 23, 2001, pp. 1512-1522
69. G.G. Yen, 'Distributed vibration control in flexible multibody dynamics', *Computers & Structures*, 61, 1996, pp. 957-965
70. S.M. Yang, C.J. Chen, W.L. Huang, 'Structural vibration suppression by a neural-network controller with a mass-damper actuator' *Journal of Vibration and Control*, 12, 2006, pp. 495-508
71. F.E. Udwandia, M. Hossenini, 'Distributed control of large-scale structural systems', *Computer-Aided Civil and Infrastructure Engineering*, 13, 1998, pp. 377-387
72. J.P. Lurch, K.H. Law, 'Market-based control of linear structural systems', *Earthquake Engineering and Structural Dynamics*, 31, 2002, pp. 1855-1877
73. C.T. Chen, *Linear Systems*, pp. 384-386
74. C.T. Chen, *Linear Systems*, pp.283-291
75. C.T. Chen, *Linear Systems*, pp. 395-400

76. H.F. VanLandingham, *Introduction to Digital Control Systems*, Macmillan Publishing Company, New York, 1985, pp. 78-80
77. J.J. D'Azzo, C.H. Houpis, *Linear Control Systems*, pp. 509-519
78. M. Aldawod, 'Active control', p. 1521
79. D.P. Atherton, *Nonlinear Control Engineering*, New York, 1982, pp. 16-68
80. D.A. Wang, Y.M. Huang, 'Application of discrete-time variable structure control in the vibration reduction of a flexible structure', *Journal of Sound and Vibration*, 261, 2003, pp. 483-501
81. P. Malatkare, A. H. Nayfeh, 'On the transfer of energy between widely spaced modes in structures', *Non-Linear Dynamics*, 31, 2003, pp. 225-242
82. L. Caracoglia, 'Analysis of light pole failures', pg. 42
83. Rockwell International Proposal RI/RD87-201P-2, *Space Station Electrical Power System Design, Development, and Production (Work Package 4)*, Volume II – Technical Proposal, submitted to NASA Lewis Research Center, 1987
84. F.A. Charney, 'Consequences of using Rayleigh damping in inelastic response history analysis', *Proceedings of the 17th Analysis and Computation Specialty Conference*, No A10-17, May 2006
85. T Kijewski, A. Kareem, 'Estimation and modeling', p. 9
86. Y.L. Xu, 'Parametric study of active mass dampers', p. 65
87. P. Malatkar, A. Nayafeh, 'On the transfer of energy between widely spaced modes in structures', *Non-Linear Dynamics*, 31, pp. 225-242
88. P.V. O'Neil, *Advanced Engineering Mathematics*, 4th Edition, PWS-Kent Publishing Company, Boston, 1995, p. 814
89. D.J. Inman, *Engineering Vibration*, pp. 255-267
90. J.J. D'Azzo, C.H. Houpis, *Linear Control*, p. 85
91. J.J. D'Azzo, C.H. Houpis, *Linear Control*, pp. 171-177
92. M.J. Crocker, *Handbook of Acoustics*, Toronto Canada: J. Wiley and Sons, Inc., 1998, pp. 569-572
93. C.W. De Silva, *Vibration: Fundamentals and Practice*, Boca Raton, Florida: CRC Press, 2007, pp. 277-278
94. K. Ogata, *Modern Control Engineering*, Upper Saddle River, NJ: Prentice Hall, 1997, p. 717

95. A. Papoulis, *The Fourier Integral and its Applications*, New York, NY: McGraw-Hill Book company, Inc., 1962, p. 25
96. J.M. Gere, S.P. Timoshenko, *Mechanics of Materials*, 4th Edition, PWS Publishing, Boston, 1997, p. 602
97. R. Larson, R. Hostetler, B. Edwards, *Calculus*, Boston, MA: Houghton Milton Company, 1998, pg 498
98. R. Larson, R. Hostetler, B. Edwards, *Calculus*, p. 281
99. D. Bernal, 'Extracting flexibility matrices from state-space realizations', COST F3 Conference, 2000, Madrid, Spain, pp. 127-135
100. J.J. Conner, *Structural Motion Control*, pp. 73-79
101. J. W. Tedesco, *Structural Dynamics Theory and Applications*, pp. 237-251
102. J.C. McCormac and J.K. Nelson, *Structural Analysis - A Classical and Matrix Approach*, 2nd edn, Reading, PA, 1997, p. 328
103. T. Kijewski, A. Kareem, 'Estimation and modeling', p. 9
104. D.J. Inman, *Engineering Vibration*, pp. 255-267
105. J.J. D'Azzo, C.H. Houpis, *Linear Control*, pp. 171-177
106. D. Mohammad, N.U. Khan, V. Ramamurti, 'On the role of Rayleigh damping', *Journal of Sound and Vibration*, 185, 1995, pp 207-218
107. MATLAB & SIMULINK Version R2007a, The MathWorks, Inc., Natick, MA
108. R.C.Minor, 'Hapco lighting pole first mode vibration test report', HAPCO white paper, June 2004
109. J. D'Azzo, C. Houpis, *Linear Control*, pp. 111-118
110. Wind Loads on Structure, Version 1.6, Standards Design Group, <<http://www.standardsdesign.com/WLS/Default.htm>>, accessed March 2009
111. ASCE/SEI 7-05, *Minimum Design Loads for Buildings and Other Structures*, pp. 21-30
112. <<http://rocky.digikey.com/WebLib/Measurement%20Specialties%20Inc/Web%20Data/Accelerometer%20ACH-01.pdf>>, accessed June 2008
113. <<http://vishay.com/strain-gages/gages-sensors/0.125/>>, accessed July 2007
114. <<http://sine.ni.com/nips/cds/view/p/lang/en/nid/14605>>, accessed September 2007

115. McMaster-Carr product number 3458T43,
<<http://www.mcmaster.com/#3458t43/=2nn4fl>>, accessed June 2008
116. National Instrumentation Specification Sheet
<<http://sine.ni.com/nifn/cds/view/comp/p/sn/n24:USB/pg/4/lang/en/nid/1036/ap/daq/sd/3a104a683cd42010VgnVCM100000940aa482RCRD>>,
accessed August 2008
117. National Instrumentation NI-DAXmx,
<<http://zone.ni.com/devzone/cda/tut/p/id/5409>>, accessed December 2008

APPENDICES

APPENDIX A

LIST OF VARIABLES, DEFINITIONS AND USAGE

Spatial Reference

x, y, z *generalized coordinate axis in the Cartesian Coordinate system*
 u, v, w *generalized displacements along the x, y, and z axis respectively*

Energy Reference

U *total system energy, Kinetic Energy (KE) + Potential Energy (PE)*
 W *total work energy done by (to) the system*
 $p(z, t)$ *instantaneous damped power density along the z axis of the structure*
 $w(z)$ *damped energy density along the z axis of the structure given the defined time interval*
 $dp(x, y, z, t)$ *differential instantaneous damped power associated with a differential element within the vibrating structure*

Mathematical Operators

$\dot{u} = \frac{d u}{dt}, \ddot{u} = \frac{d^2 u}{dt^2}$ *Newton notation for 1st and 2nd time derivative respectively*

$\dot{\mathbf{u}} = \frac{d \mathbf{u}}{dt}, \ddot{\mathbf{u}} = \frac{d^2 \mathbf{u}}{dt^2}$ *Newton notation for 1st and 2nd time derivative of the given vector*

$\|\mathbf{v}\|_2$ *L₂ or Euclidean norm*

$\|\mathbf{v}\|_\infty$ *L_∞ norm, $\max_{1 \leq i \leq n} |v_i|$*

$X(s), U(s), Y(s)$ *LaPlace transforms of the state variable, input and output signals*

$G(s), H(s)$ *LaPlace transforms of feedforward and feedback transfer functions*

Structural Dynamic Model Parameters

f_i *ith nodal force*

$y_i, \dot{y}_i, \ddot{y}_i$ *ith nodal displacement, velocity and acceleration*

m_i, c_i, k_i *scalar mass, damping and stiffness coefficients associated with the ith mode*

$\mathbf{y} = [y_1 \ \cdots \ y_n]^T$ *nodal displacement vector*

$\dot{\mathbf{y}} = [\dot{y}_1 \ \cdots \ \dot{y}_n]^T$ *nodal velocity vector*

$\ddot{\mathbf{y}} = [\ddot{y}_1 \cdots \ddot{y}_n]^T$	<i>nodal acceleration vector</i>
$\tilde{\mathbf{y}}, \tilde{\dot{\mathbf{y}}}, \tilde{\ddot{\mathbf{y}}}$	<i>nodal displacement, velocity, and acceleration vectors after basis transformation</i>
\mathbf{G}	<i>gravity influence matrix (developed and presented within)</i>
$\mathbf{L} = [l_1 \cdots l_n]^T$	<i>cantilever segment length vector</i>
$\mathbf{h} = [h_1 \cdots h_n]^T$	<i>nodal height vector given each node's height above the base support</i>
$\mathbf{M}, \mathbf{C}, \mathbf{K}$	<i>mass, damping and stiffness matrices</i>
\mathbf{S}	<i>flexibility matrix</i>
$\tilde{\mathbf{C}}, \tilde{\mathbf{K}}$	<i>mass normalized damping and stiffness matrices</i>
$\mathbf{f} = [f_1 \cdots f_n]^T$	<i>nodal force vector</i>
$d\mathbf{f} = [df_1 \cdots df_n]^T$	<i>differential nodal force vector representing the control tendon incremental feedback force correction on the cantilever</i>

State-Space Model and Control Parameters

$\mathbf{A}, \mathbf{B}, \mathbf{C}_{out}, \mathbf{D}$	<i>constant coefficient matrices forming the state-space model</i>
$\mathbf{x} = [x_1 \cdots x_n \cdots x_{2n}]^T$	<i>state variable vector, where n represents the DOF of the system model</i>
$\mathbf{u} = [u_1 \ u_2 \ \cdots \ u_m]^T$	<i>input/excitation vector, where m represents the number of unique input sources</i>
\mathbf{y}_{out}	<i>output vector</i>
$u_{-1}(t - \tau)$	<i>unit step function at time $t = \tau$</i>

Vibration/Modal Parameters

$\lambda_i = \omega_i^2$	<i>i^{th} modal eigenvalue</i>
$\mathbf{v}_i = [v_{1,i} \ \cdots \ v_{n,i}]^T$	<i>i^{th} vibration mode shape vector (approximate discretized)</i>
Λ	<i>diagonalized eigenvalue matrix</i>
$\mathbf{T} = [\mathbf{v}_1 \ \cdots \ \mathbf{v}_n]$	<i>modal matrix</i>
$Z_i(z)$	<i>i^{th} displacement mode shape (continuous function)</i>

Generalized Damping Parameters

ζ	<i>critical damping ratio</i>
ζ_i	<i>critical damping ratio of the i^{th} vibration mode</i>
σ	<i>damping coefficient</i>
σ_i	<i>damping coefficient of the i^{th} vibration mode</i>
m_d, c_d, k_d	<i>scalar mass, damping and stiffness coefficients for the secondary damper</i>

Material and Sectional Parameters

I	<i>Sectional Moment-of-Inertia</i>
E	<i>Modulus of Elasticity</i>

Generalized Structural Parameters

$m(z)$ *moment distribution function along the z axis of the structure*

$\kappa(z,t)$ *instantaneous curvature along the z axis of the structure*

All other specialized variable definitions and usages are defined and described in place within the document.

APPENDIX B

CONCEPT DEMONSTRATION TEST PARAMETERS AND RESULTS

test #	date	time	S/W build	delay count	hold count	reverse count	MD events	test duration [sec]	time to settle [sec]
1	26-Dec-08	15:39	1	235	12			20	dry-run
2	29-Dec-08	15:55	1	235	12			20	dry-run
3	29-Dec-08	16:03	1	230	12			20	dry-run
4	29-Dec-08	16:23	1	230	12			20	dry-run
5	30-Dec-08	15:21	1	230	12			20	dry-run
6	30-Dec-08	15:24	1	210	15			20	dry-run
7	30-Dec-08	15:26	1	200	20			20	dry-run
8	30-Dec-08	15:28	1	210	20			20	dry-run
9	30-Dec-08	15:36	1	205	20			20	dry-run
10	30-Dec-08	15:38	1	205	17			20	dry-run
11	31-Dec-08	15:12	1	230	12			20	dry-run
12	31-Dec-08	15:13	1						18.07
13	31-Dec-08	15:18	1						dry-run
14	31-Dec-08	15:23	1	230	12			20	dry-run
15	31-Dec-08	15:26	1	205	17			20	dry-run
16	31-Dec-08	15:28	1	205	25			20	dry-run
17	31-Dec-08	15:29	1	205	25			20	dry-run
18	7-Jan-09	14:10	1	230	12			20	dry-run
software build 2 completed with multiple events & 3 cycles between concurrent events									
19	7-Jan-09	14:12	2	1	1		1	20	18.53
20	7-Jan-09	14:13	2	55	12		3	20	dry-run
21	7-Jan-09	14:17	2	50	15		3	20	dry-run
22	7-Jan-09	14:20	2	55	20		1	20	dry-run
23	7-Jan-09	15:52	2	40	40		3	20	dry-run
24	8-Jan-09	12:28	2	40	40		3	20	dry-run
25	8-Jan-09	12:30	2	40	2		2	20	dry-run
26	8-Jan-09	12:32	2	40	4		3	20	dry-run
27	8-Jan-09	12:36	2	40	1		3	20	dry-run

test #	date	time	S/W build	delay count	hold count	reverse count	MD events	test duration [sec]	time to settle [sec]
28	8-Jan-09	12:38	2	40	1		3	20	dry-run
29	8-Jan-09	15:21	2	40	20		3	20	dry-run
upgraded brake electronics & software build 3 to include reverse brake current									
30	31-Jan-09	16:41	2				0	30	18.52
31	31-Jan-09	11:45	2	50	80		3	30	14.63
32	31-Jan-09	16:53	2	55	85		3	30	11.27
33	31-Jan-09	16:54	2	55	90		3	30	11.27
34	1-Feb-09	12:56	2	55	85		3	20	11.27
35	1-Feb-09	13:29	3	50	80	?	4	20	14.7
36	1-Feb-09	13:31	3	55	85	?	4	20	10.8
37	1-Feb-09	16:51	3	55	85	?	3	20	11.27
38	1-Feb-09	16:54	3	55	90	?	3	20	11.3
39	1-Feb-09	17:16	3	55	90	5	1	20	15.18
buffer output offsets eliminated									
40	1-Feb-09	17:24	3	55	90	5	1	20	13.13
41	1-Feb-09	17:25	3	50	85	5	2	20	10.8
42	1-Feb-09	17:26	3	55	85	5	3	20	10.24
43	1-Feb-09	17:28	3	55	75	5	3	20	9.8
44	1-Feb-09	18:01	3	55	80	5	1	20	12.9
45	1-Feb-09	18:04	3	55	80	5	2	20	10.64
46	1-Feb-09	18:05	3	55	80	5	3	20	10.47
47	1-Feb-09	18:06	3	55	80	5	4	20	10.2
48	2-Feb-09	14:29	3	0	80	0	1	20	18.9
49	2-Feb-09	14:32	3	55	85	0	1	20	12.81
50	2-Feb-09	14:34	3	55	85	0	2	20	11.16
51	2-Feb-09	14:35	3	55	85	0	3	20	10.57
52	2-Feb-09	14:44	3	55	85	5	1	20	12.74
53	2-Feb-09	14:46	3	55	85	5	2	20	10.38
54	2-Feb-09	14:48	3	55	85	5	3	20	9.8
55	2-Feb-09	14:49	3	50	85	5	1	20	13.36
56	2-Feb-09	14:50	3	50	85	5	2	20	11.2
57	2-Feb-09	14:51	3	50	85	5	3	20	10.28
58	2-Feb-09	14:53	3	50	75	5	1	20	13.79
59	2-Feb-09	14:54	3	50	75	5	2	20	11.36
60	2-Feb-09	14:55	3	50	75	5	3	20	10.35

test #	date	time	S/W build	delay count	hold count	reverse count	MD events	test duration [sec]	time to settle [sec]
61	2-Feb-09	14:57	3	50	75	10	1	20	14.81
62	2-Feb-09	14:58	3	50	80	10	1	20	13.83
63	2-Feb-09	15:00	3	50	80	15	1	20	14.79
64	2-Feb-09	15:01	3	50	80	15	2	20	12.34
65	2-Feb-09	15:03	3	50	80	15	3	20	11.31
66	2-Feb-09	15:07	3					60	[b]
67	2-Feb-09	15:10	3					20	18.16
68	2-Feb-09	15:14	3	50	80	10	1	20	13.83
69	2-Feb-09	16:16	3	50	75	10	1	20	14.26
70	2-Feb-09	16:19	3	50	75	10	2	20	10.86
71	2-Feb-09	16:21	3	50	75	10	3	20	10.35
72	2-Feb-09	16:22	3					20	18.51
73	2-Feb-09	16:24	3	50	75	15	1	20	15.15
74	2-Feb-09	16:25	3	50	75	15	2	20	13.05
75	2-Feb-09	16:26	3	50	75	15	3	20	10.89
76	2-Feb-09	16:28	3	50	65	15	1	20	16.6
77	2-Feb-09	16:29	3	50	65	15	2	20	15.07
78	2-Feb-09	16:53	3	50	75	15	2	20	11.86
software build 4 completed. 3 cycles between adjoining events									
79	3-Feb-09	14:18	4					20	19.11
80	3-Feb-09	14:20	4	50	80	15	1	20	14.33
81	3-Feb-09	14:22	4	50	80	15	2	20	12.62
82	3-Feb-09	14:23	4	50	80	15	3	20	11.69
83	3-Feb-09	14:25	4	30	80	15	1	20	16.99
84	3-Feb-09	14:26	4	40	80	15	2	20	13.75
85	3-Feb-09	14:27	4	50	80	12	1	20	13.73
86	3-Feb-09	14:29	4	50	80	12	2	20	12.16
87	3-Feb-09	14:30	4	50	80	12	3	20	11.63
88	4-Feb-09	15:16	4					20	18.89
89	4-Feb-09	15:20	4	50	75	15	1	20	14.69
90	4-Feb-09	15:21	4	50	75	15	2	20	12.64
91	4-Feb-09	15:22	4	50	75	15	3	20	11.71
92	4-Feb-09	15:24	4	50	80	15	1	20	14.08
93	4-Feb-09	15:26	4	50	80	15	2	20	12.03
94	4-Feb-09	15:27	4	50	80	15	3	20	11.16

test #	date	time	S/W build	delay count	hold count	reverse count	MD events	test duration [sec]	time to settle [sec]
95	4-Feb-09	15:28	4	50	85	15	1	20	13.65
96	4-Feb-09	15:29	4	50	85	15	2	20	11.67
97	4-Feb-09	15:31	4	50	85	15	3	20	11.19
98	4-Feb-09	15:32	4	50	80	18	1	20	13.76
99	4-Feb-09	15:34	4	50	80	15	2	20	11.71
100	4-Feb-09	15:35	4	50	80	15	3	20	10.8
change gap between brake electro-magnet and rotating disc									
101	4-Feb-09	15:39	4					20	19.23
102	4-Feb-09	15:41	4	50	80	15	1	20	18.52 ^[a]
103	4-Feb-09	15:48	4	50	80	15	2	20	11.58
104	4-Feb-09	15:49	4					20	19.15
105	4-Feb-09	15:50	4	50	80	15	1	20	13.51
106	4-Feb-09	15:52	4	50	80	15	2	20	11.73
107	4-Feb-09	15:53	4	40	80	15	3	20	12.62
108	4-Feb-09	15:56	4	40	80	15	2	20	13.62
109	9-Feb-09	16:05	4	50	80	15	2	20	11.5
110	9-Feb-09	16:08	4	50	80	15	2	20	11.77
111	9-Feb-09	16:09	4	50	80	15	2	20	11.26
112	9-Feb-09	16:16	4	50	80	15	2	20	11.42
113	9-Feb-09	16:28	4	50	80	15	2	20	11.69
114	9-Feb-09	16:30	4	50	80	15	2	20	11.66
115	9-Feb-09	16:32	4	50	80	15	2	20	11.68
116	9-Feb-09	17:44	4	50	80	15	2	20	11.17
117	9-Feb-09	17:46	4					20	18.96
118	13-Feb-09	12:28	4	55	80	15	2	20	10.79
119	13-Feb-09	12:30	4					20	18.99
120	13-Feb-09	12:35	4	55	80	15	2	20	10.81
121	13-Feb-09	12:37	4	60	80	15	2	20	11.24
122	13-Feb-09	12:46	4	55	80	15	2	20	10.8
123	13-Feb-09	14:25	4	55	80	15	2	20	11.55
124	13-Feb-09	14:27	4	55	80	15	2	20	11.24
125	13-Feb-09	14:31	4	55	80	15	2	20	11.15
126	13-Feb-09	14:31	4	55	80	15	2	20	11.17
127	22-Feb-09	15:35	4	55	80	15	1	20	13.51

test #	date	time	S/W build	delay count	hold count	reverse count	MD events	test duration [sec]	time to settle [sec]
128	22-Feb-09	15:37	4					20	19.34
129	22-Feb-09	15:39	4					30	19.73

[a] test 102. Gap was set too large to actuate breaking. Used as a free vibration test.

[b] test 66. Data collected for 60 second profile.